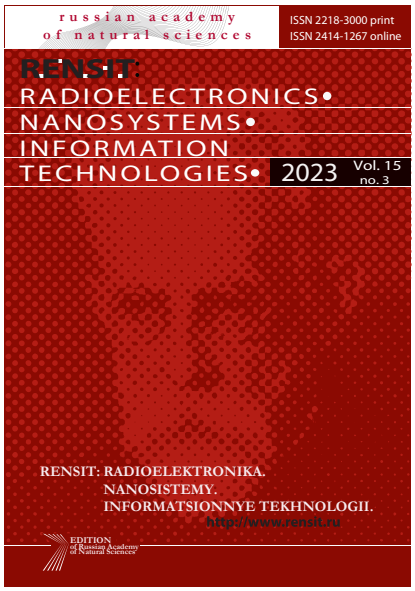

RENSIT:
RadioElectronics. NanoSystems. Information Technologies

Journal "Radioelectronics. Nanosystems. Information Technologies" (abbr. RENSIT)
publishes original articles, reviews and brief reports, not previously published, on topical problems in **radioelectronics (including biomedical) and fundamentals of information, nano- and biotechnologies and adjacent areas of physics and mathematics.**

Designed for **researchers, graduate students, physics students of senior courses and teachers**.
It turns out **2 times a year** (that includes 2 issues)

Authors of journal are academicians, corresponding members and foreign members of Russian Academy of Natural Sciences (RANS) and their colleagues,
as well as other russian and foreign authors on presentation of their manuscripts by the members of RANS, which can be obtained by authors before sending articles to editors.
And also after its receiving - on recommendation of a member of editorial board of journal, or another member of Academy of Natural Sciences, that gave her opinion on article at request of editor.
The editors will accept articles in both **Russian and English** languages.

Articles are internally peer reviewed (**double-blind peer review**) by members of the Editorial Board.
Some articles undergo external review, if necessary.

Journal RENSIT is included in the **DB SCOPUS, EBSCO Publishing,** in the international abstracts database - **Ulrich's International Periodicals Directory**,(USA, New York, http://www.ulrichsweb.com), in the **AJ and DB VINITI RAS** (http://www.viniti.ru), and DB **Russian Science Citation Index (RSCI** http://elibrary.ru/project_risc.asp). Included in the **List of Higher Attestation Comission** (No. 2204 dated July 17, 2023: K1 in 18 groups of specialties) **of Science and Higher Education Ministry of the Russian Federation**.
Full-text content is posted in the DB of the **Russian Scientific Electronic Library**
- information resource on the Internet http://elibrary.ru and is available for registered users.
And also - in Open Access **CyberLeninka NEB** of Russian Federation http://cyberleninka.ru.

On journal's website http://www.rensit.ru posted metadata publications
and **RENSIT: Radioelectronics. Nanosystems. Infomation Technologies - english version** (cover-to-cover translation) of journal, which is a party to **CrossRef.**

The founder - the **Russian Academy of Natural Sciences**
Publisher - Publishing Center of the Russian Academy of Natural Sciences
Publisher Address: 29/16, Sivtsev Vrazhek lane, Moscow 119002, Russian Federation

CONTENTS

RUSSIAN ACADEMY OF NATURAL SCIENCES

DEPARTMENT OF RADIOELECTRONICS, NANOPHYSICS AND INFORMATION TECHNOLOGIES PROBLEMS

RENSIT:

RADIOELECTRONICS. NANOSYSTEMS. INFORMATION TECHNOLOGIES.

2023, VOL. 15, № 3

FOUNDED IN 2009
4 ISSUES PER YEAR
MOSCOW

ISSN 2414-1267

The journal on-line is registered by the Ministry of Telecom and Mass Cjmmunications of the Russian Federation. Certificate El. no. FS77-60275 on 19.12.2014

EDITORIAL BOARD ADDRESS
218-219 of., 7 b., 11, Mokhovaya str., 125009 MOSCOW, RUSSIAN FEDERATION,
TEL. +7 495 629 3368
FAX +7 495 629 3678 FOR GRACHEV

DOI: 10.17725/rensit.2023.15.205

Electromagnetic wave localization and scattering parameters investigation in a partially absorbing medium depending on the output tract geometric configuration

Yaroslav V. Kravchenko
Prokhorov Institute of General Physics of Russian Academy of Sciences, http://www.gpi.ru/
Moscow 119991, Russian Federation
E-mail: kravch@kapella.gpi.ru

Dmitry V. Tsipenyuk
Moscow Polytechnic University, https://new.mospolytech.ru/
Moscow 107023, Russian Federation
All-Russian Institute of Scientific and Technical Information of RAS, http://www.viniti.ru/
Moscow 125190, Russian Federation
E-mail: dimat777@list.ru

Andrey V. Voropinov
Laser Graphic Art Ltd, http://www.lasergraphicart.com/
Moscow 105318, Russian Federation
E-mail: avv@lasergraphicart.com

Received May 9, 2023, peer-reviewed May 16, 2023, accepted May 23, 2023

Abstract: **The paper presents first results obtained on an experimental setup designed to study the parameters of localization, scattering and absorption of microwave radiation with a power of 1-4 mW at the 38 GHz when radiation propagates in variable-section waveguides. The parameters of localization and scattering of an electromagnetic wave in a partially absorbing medium were studied depending on the geometric configuration of the output tract. The interpretation of the obtained initial results was carried out within the framework of the (1+4)D extended space model (ESM). The extended space model is formulated in (1+4)-dimensional space time-coordinate-interval action. An additional spatial coordinate in the ESM is the interval, which in the ESM has the physical meaning of the action. In the dual (1+4)D space energy-momentum-mass, the interval (action) in the ESM corresponds to the mass. ESM considers the question of the emergence of a non-zero variable mass for a photon and its localization under the influence of an external field.**

Keywords: **electromagnetic field localization and scattering, radiation absorption, variable cross section waveguide, microwave radiation, (1+4)D extended space model**

PACS 11.10 KK, 03.50.-Z, 03.65. PM

For citation: Yuaroslav V. Kravchenko, Dmitry Yu. Tsipenyuk, Andrey V. Voropinov. Electromagnetic wave localization and scattering parameters investigation in a partially absorbing medium depending on the output tract geometric configuration. *RENSIT: Radioelectronics. Nanosystems. Information Technologies*, 2023, 15(3):205-214e. DOI: 10.17725/rensit.2023.15.205.

Contents

1. INTRODUCTION

In [1], published by us in 2021, we described the creation and testing of an experimental setup designed to study the localization parameters of electromagnetic microwave radiation with a power of 0.001-0.004 W in the range of 36.0-79.0 GHz when radiation propagates in metal waveguides of variable cross section filled with dielectrics with different refractive indices.

The results of measurements carried out on the created experimental stand, we will compare with the calculations of the electromagnetic field for microwave antennas, carried out using programs based on the method of moments (for example, NEC2, MININEC3 programs or using the HFSS electrodynamic modeling and design system (High Frequency Structure Simulator), IE3D, Microwave Office, Microwave Studio [2-5]).

In addition to comparing the obtained experimental results with generally accepted calculation models, we plan to evaluate the possibility of description using calculations based on the Extended Space Model (ESM) developed earlier in [6-10]. ESM is based on the physical hypothesis that the mass (rest mass) and its conjugate value – action (interval) are dynamic variables. The interaction of fields and particles determines the magnitude of these variables. Such a model is a generalization of the Special Relativity Theory (SRT). In SRT, the interval and rest mass of particles are invariants, while in the proposed ESM [6-10] they can change. For example, in ESM a photon can acquire mass (both positive and negative). Such a mass can appear and change due to electromagnetic interaction and generate gravitational forces. This allows us to consider gravity and electromagnetism as a single field in the ESM.

It should be noted that a five-dimensional model close to the ESM was developed by Paul Wesson et al. [11-14]. P.Wesson in his works proposed to use the "mass" as the fifth coordinate as an additional coordinate to the time and three spatial coordinates: [11] p. 10 "we ... consider mass on the same basis as time and space ..." and [11] on page 191 equation (7.40) "This means that the role of the uncharged 4D mass in 5D geometry is played by an additional coordinate". This approach to the introduction of the fifth coordinate seems to us illogical. For example, this leads to difficulties in generalizing the four-dimensional energy-momentum tensor to the five-dimensional energy-momentum-mass tensor in 5D space. In our opinion, the mass can be considered as the fifth coordinate, but not in the coordinate space. The mass must be considered in the momentum space, namely as an additional quantity to the energy and the three components of the momentum. In this case, in the coordinate space, the fifth coordinate must be a different value, which is associated with the mass. As a result of considering mass as the fifth coordinate, in addition to time and space, it was difficult in [11-13] to establish a connection between mass and experiments. Recently in [14] James Overduin (co-author Paul Wesson) and R.C. Henry proposed the same idea of introducing the fifth coordinate as Tsipenyuk D.Yu. and Andreev V.A. in 1999 [10].

An overview of various models on the topic of multidimensional fields can be found in the book [15]. The most famous pioneering approaches to the construction of five-dimensional models can be found in the works of Klein Felix [16], Einstein [17,22], Klein Oskar [18], Kaluza [19], Fock [20], Mandel [21].

In works on Rumer's 5-optics [23], the fifth coordinate is also introduced in the form of an action and a 5-dimensional space with metric (1;4) is considered. However, Rumer does not consider any transformations in this space that would confuse the coordinate with the other four coordinates of the Minkowski space. Therefore, in the conjugate to the 5-dimensional coordinate space, the mass in Rumer's five-optics remains

constant and is not converted into energy and momentum.

In this paper, we present the first experimental results of measuring the localization parameters of microwave radiation with a frequency of 38 GHz and a power of 4 mW when propagating in waveguides of variable cross section filled with a dielectric material with a high refractive index and also compare the magnitude of the signal attenuation effect in a dielectric sheet absorber of microwave radiation of variable thickness. depending on the shape of the waveguides (convergent or rectangular in cross section). A qualitative interpretation of the results was carried out on the basis of previously published works on the possibility of overcoming the Coulomb barrier in the framework of ESM [24].

2. LOCALIZATION AND TRANSFORMATIONS OF FIELDS AND PARTICLES WITHIN THE ESM APPROACH

The localization of fields and particles, their transformations within the framework of the ESM approach are considered in detail in [6-10,24]. Some of the results of these works related to the topic of this article are briefly outlined below.

The extended space model makes it possible to describe the process of electromagnetic field localization when an electromagnetic wave enters from vacuum into an external space-variable field (for example, an electron) or into a converging (expanding) waveguide.

The ESM considers a generalization of Einstein's special relativity theory (SRT) to a 5-dimensional space, or rather to a (1+4)-dimensional space (*T, X, S*) with the metric (+ - - - -). The physical basis for such a generalization is the fact that in SRT the masses of particles are scalars and do not change under their elastic interactions. However, it is well known that a photon can be considered a massless particle and described by a plane wave only in infinite empty space. If a photon enters a medium or finds itself in a limited space, for example, in a resonator or waveguide, then it acquires a nonzero mass. This mass can appear and change due to electromagnetic interaction and generate gravitational forces. It is this circumstance that allows us to consider gravity and electromagnetism as a single field.

ESM is based on the assumption that the relationship between energy, momentum and mass is 5-dimensional if we take into account the possibility of changing mass in physical processes

$$E^2 - c^2 p_X^2 - c^2 p_Y^2 - c^2 p_Z^2 - m^2 c^4 = 0. \quad (1)$$

At the same time, in the ESM, the length of the Lorentz-covariant 5-vector corresponding to objects satisfying (1) is equal to zero:

$$(ct)^2 - x^2 - y^2 - z^2 - s^2 = 0. \quad (2)$$

It seems natural to expand the space of parameters characterizing the particle, taking into account the fact that its mass can change during the interaction. Let's take a simple analogy. A free particle moves in a straight line, so to describe its behavior, we can restrict ourselves to the (1+1)-dimensional space formed by the time *T* and the direction of its movement *X*, since the other *Y* and *Z* coordinates remain constant. If the particle begins to interact with other objects, so that it can leave the straight line and start moving also in the (*YZ*) plane, then this space is no longer enough and it has to be expanded to (1+3)-dimensional. Similarly, in our case, as long as the mass of the particle does not change, we can restrict ourselves to the 4-dimensional Minkowski space M(1,3), but if it starts to change, the space M(1,3) has to be extended to the 5-dimensional *G*(*T; X, Y, Z, S*).

An isotropic 5-dimensional mass energy-momentum vector is introduced in this space:

$$\tilde{p} = (E/c; p_X, p_Y, p_Z) \quad (3)$$

and a 5-dimensional isotropic current vector generating a unified electromagnetic-gravitational field:

$$\vec{\rho} = (j_0, \vec{j}, j_4) = \left[\frac{emc}{\sqrt{1-\beta^2}}, \frac{em\vec{v}}{\sqrt{1-\beta^2}}, emc \right]. \quad (4)$$

Similarly, a 5-vector potential A is introduced into the ESM:

$$A = (\varphi, \vec{A}, A_S) = (A_T, A_X, A_Y, A_Z, A_S). \quad (5)$$

The components of such a 5-dimensional vector potential are related in the ESM by the system of equations:

$$\Diamond_{(5)} A_T = -4\pi\rho, \quad (6)$$

$$\Diamond_{(5)} \vec{A}_{X;Y;Z} = \frac{-4\pi}{c} \vec{j}, \quad (7)$$

$$\Diamond_{(5)} A_S = \frac{-4\pi}{c} j_S, \quad (8)$$

$$\Diamond_{(5)} = \frac{\partial^2}{\partial x^2} + \frac{\partial^2}{\partial y^2} + \frac{\partial^2}{\partial z^2} + \frac{\partial^2}{\partial s^2} - \frac{1}{c^2}\frac{\partial^2}{\partial t^2}. \quad (9)$$

On the basis of the vector potential (5) in the ESM, one can construct the usual electric and magnetic fields $\vec{E}$ and $\vec{H}$,, as well as two new fields – the scalar Q and the vector $\vec{G}$ components of which are determined similarly to the construction of fields in the four-dimensional Minkowski space:

$$\left\| F_{ik} \right\| = \frac{\partial A_i}{\partial x_k} + \frac{\partial A_k}{\partial x_i}; \; i,k = t,x,y,z,s, \quad (10)$$

$$\left\| F_{ik} \right\| = \begin{pmatrix} 0 & -E_X & -E_Y & -E_Z & -Q \\ E_X & 0 & -H_Z & H_Y & -G_X \\ E_Y & H_Z & 0 & -H_X & -G_Y \\ E_Z & -H_Y & H_X & 0 & -G_Z \\ Q & G_X & G_X & G_X & 0 \end{pmatrix}. \quad (11)$$

The external action in the ESM is described using rotations of three hyperbolic rotations (*T, X*), (*T, Y*), (*T, Z*) corresponding to the Lorentz transformations in the four-dimensional Minkowski space M(1,3) and new types of rotations – one hyperbolic (*T, S*) and three Euclidean (*X, S*), (*Y, S*), (*Z, S*) in the extended space *G*(1,4).

Rotations in *G*(1,4) have a clear physical meaning, so for example, hyperbolic rotations (*T, X*), (*T, Y*), (*T, Z*) are simply, according to (1) and (2), the change in particle velocity in corresponding *X, Y* or *Z* direction.

In the case of hyperbolic rotations in the plane (*TS*), according to (2), there is a simultaneous change in the mass and energy of the particle. For example, the dependence of the photon mass on the rotation angle θ is determined by the formula $mc^2 = \hbar\omega \mathrm{sh}\theta$ [6-10]. Expression for the localization parameter l in terms of the angle θ:

$$l = \frac{2\pi c}{\omega \cdot sh\theta}. \quad (12)$$

For Euclidean rotations in the plane (*XS*), the dependence of the photon mass on the rotation angle ψ is determined by the formula $mc^2 = \hbar\omega \sin\psi$, from which follows the expression for the localization parameter l in terms of the angle ψ:

$$l = \frac{2\pi c}{\omega \cdot \sin\psi}. \quad (13)$$

The speed of wave propagation c in vacuum is related to the propagation of speed in a medium or waveguide v refractive index n by the relation $v = c/n$.

In the case of rotations (*XS*), a photon under the influence of an external field acquires a mass related to the refractive index by the relation:

$$m_{(XS)} = \frac{\hbar\omega}{c^2} \cdot \sin\psi = \frac{\hbar\omega}{c^2 n}. \quad (14)$$

Rotation (*XS*) corresponds in ESM to a transition from a space with one optical density to a space with another optical density. In this case, no time processes occur, everything is considered at the same moment in time. Therefore, the energy of the particles is conserved, and all processes occurring with them are reduced to internal rearrangements. Conventionally, this can be understood in such a way that a particle entering a denser medium is deformed elastically, and leaving it, restores its characteristics.

In the case of hyperbolic rotations (*TS*), a photon under the influence of an external field acquires a mass related to the refractive index by the relation:

$$m_{(TS)} = \frac{\hbar\omega}{c^2} \cdot sh\theta = \frac{\hbar\omega}{c^2}\sqrt{n^2 - 1}. \quad (15)$$

The physical meaning of rotations (*TS*) is that we do not perform spatial movements, we are always at the same point, but the optical density at this point changes over time. In this case, the transformation (*TS*) means the transition to a different point in time and a different optical density. This can be interpreted in such a way that an external field arises in space, which, acting on a particle and doing work, changes its energy and mass.

From the point of view of ESM, the transition from a medium with one refractive index to a medium with another refractive index can be interpreted as a movement along the fifth coordinate of the Extended Space. This (1+4)-dimensional space can be understood as a set of 1+3-dimensional Minkowski spaces, each of which is characterized by some parameter, such as the refractive index *n*. And the transition from a medium with an index of n_1 to a medium with a refractive index of n_2 can be interpreted as a transition in a (1+4)-dimensional space from one (1+3)-dimensional subspace to another (1+3)-dimensional subspace. Thus, the geometry of the Expanded space turns out to be connected with the physics of those processes that we study in each specific problem. Namely, with the fields and environments that participate in these processes. The distribution of these media and fields in our ordinary Minkowski space determines the distribution of the "refractive index" in the Extended space, i.e. its geometry.

In [8] the solution of the system of equations (6)-(8) was found in the form

$$U(s,x,y,z,t) = u(s,x,y,z) \cdot e^{-iks} \cdot e^{i\omega \cdot t}, k = \frac{2\pi}{\lambda}. \quad (16)$$

Assuming that the desired function is stationary in time and changes slowly along the s axis compared to the change along the *x, y, z* axes. In this case, the solution has the form of a 3-dimensional Gaussian wave

$$u = u_0 \left(\frac{w_0}{w}\right)^{3/2} \times \times \exp\left[-i(ks+\varphi) - (x^2+y^2+z^2)\left(\frac{1}{w^2} + \frac{ik}{2R}\right)\right]. \quad (17)$$

Here w_0, the minimum wave radius at the point $s = 0$; w – is the wave diameter at point s_1 and *R* is the wavefront curvature radius at this point.

When a plane electromagnetic wave enters a medium or an external field, ESM predicts that, in accordance with (20), taking into account the above assumptions, the plane wave is localized into a sphere with radius w_0.

We also note that it was shown in [24] that the fields (11) transform into each other upon rotations in *G*(1,4), which leads to the possibility of overcoming the Coulomb barrier in the framework of the ESM.

1. Hyperbolic rotations in the plane (T,X) lead to the following field transformation:

$$\vec{E}' = \vec{E} + \frac{1}{c}[v, \vec{H}],\ \vec{G}' = \vec{G} + \frac{v_S}{c}\vec{E}, \quad \vec{H}' = \vec{H},\ Q' = Q. \quad (18)$$

2. Hyperbolic rotations in the plane (T,S) lead to:

$$\vec{E}' = \vec{E} + \frac{v_S}{c}\vec{G},\ \vec{G}' = \vec{G} + \frac{v_S}{c}\vec{E}, \quad \vec{H}' = \vec{H},\ Q' = Q. \quad (19)$$

3. Euclidean rotations in the plane (X,S) lead to:

$$\vec{E}' = \vec{E} - \vec{u}Q,\ \ \vec{G}' = \vec{G} + [\vec{u}, \vec{H}], \quad \vec{H}' = \vec{H} + [\vec{u}, \vec{G}],\ \ Q' = Q + \frac{1}{c}(\vec{u}, \vec{E}). \quad (20)$$

here *v*, v_S, *u* are the velocities corresponding to the motion along the corresponding axis in *G*(1,4).

It was shown in [24] that, within the framework of ESM, the field of a plane electromagnetic wave $\vec{E}, \vec{H}$, when turning in the $\varphi^{YS} + \varphi^{ZS}$ planes by specially selected angles, can completely transform into the fields *G* and *Q*, which will make it possible to overcome the Coulomb barrier.

3. DESCRIPTION OF THE INSTALLATION AND THE RESULTS OF THE FIRST MEASUREMENTS

3.1. Description of the installation

A detailed description of the created experimental setup is given in [1].

The results of measurements obtained at the facility will be compared with the results of calculations based on existing models of microwave radiation propagation and predictions based on ESM. The facility also assumes the measurement of microwave localization parameters when radiation enters dielectric media with a refractive index greater than unity.

The installation diagram is shown in **Fig. 1**.

Microwave radiation with a frequency of 38 GHz is generated by generator 1 of the G4-141 brand (generation region 36-55 GHz). The output signal power is adjustable from 1 to $4 \cdot 10^{-3}$ W, the range of the output power level is 30 dB. The instability of the output frequency is not more than 10^{-3}. The limit of instability of the output power level is ±0.3 dB. After the microwave generator, the radiation propagates along a silver-plated copper output waveguide 2 30 mm long, having a rectangular cross section $a \times b = 5.5 \times 2.5$ mm.

Inside the waveguide 2, a dielectric rod 4 is installed, made of Teflon, which completely fills the waveguide and extends 135 mm outward from the waveguide. We used two types of dielectric Teflon rods of different profiles: No. 1 with a cross section from 5.5×2.5 mm at the beginning to 0.1×2.5 mm at the end of a rod 180 mm long and No. 3 with the same cross section of 5.5×2.5 mm along the entire rod 200 mm long.

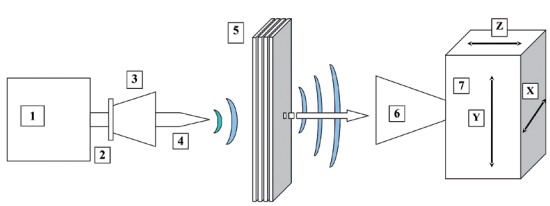

Fig. 1. *Installation diagram. 1 - microwave radiation generator 38 GHz, 2-output horn antenna, 4 - Teflon dielectric insert of constant or variable cross section, 5 - dielectric sheet absorber of microwave radiation of variable thickness 0-50 mm, 6 - receiving horn with a microwave radiation receiver connected to the ADC and control computer, 7 - system of 3-dimensional X-Y-Z positioning of the receiver.*

The installation has the ability to install a horn antenna 3 (output diameter 45 mm and length 75 mm), as well as a waveguide 2 with a wall thickness of 1.2 mm, made of copper and silver-plated from the inside.

The receiver 6 combined with a horn antenna (inlet diameter 35 mm, length 55 mm) can be precisely moved in three spatial directions (movement accuracy 0.1 mm in the range 0-140 mm) using the 3-dimensional positioning system of the receiver 7. Further, the signal is the received microwave signal processed by the ADC and transmitted to the control computer.

To study the possible difference in the absorption of microwave radiation depending on the degree of localization between the emitter 4 with a Teflon core installed with a constant profile No. 1 or a variable profile No. 3 and the receiver 6, a dielectric sheet absorber of electromagnetic microwave radiation 5 was installed, consisting of a set of dielectric plates with a thickness of 2 to 16 mm. The maximum thickness of the inlaid sheet dielectric absorber was 55 mm. The measured absorption coefficient of 38 GHz microwave radiation with a change in the total thickness of the inlaid sheet dielectric absorber from 2 to 55 mm was from 5 to 90% of the output signal. When setting the maximum level of the output power of the signal at the level of $4 \cdot 10^{-3}$ W, the amplitude of the recorded useful signal reaches the level of 350 mV at a distance of about 150 mm.

3.2. Measurement results.

Fig. 2 shows the first results of measuring the shape of the vertical profiles of a microwave wave with a frequency of 38 GHz emerging from a rectangular waveguide with a cross section of

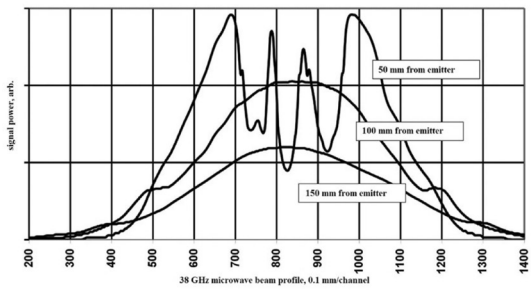

Fig. 2. *Comparison of the shape of the 38 GHz microwave beam profiles (without taking into account the relative magnitude of the signal), depending on the distance from the transmitter to the receiver 50, 100 and 150 mm. Output horn diameter 45 mm, horn length 60 mm and input horn 35 mm, horn length 50 mm.*

5.5×2.5 mm, combined with an output horn with a diameter of 45 mm and a horn length of 60 mm. The input horn combined with the radiation sensor had a diameter of 35 mm and a horn length of 50 mm.

Vertical profiles were measured both in the middle of the beam in the horizontal direction and with detuning every 5-10 mm from the middle section. Presented in Fig. 2 vertical wave profiles were measured at different distances of 50, 100, and 150 mm between the output and input sections of the horns.

On Fig. 2 are presented to compare the wave profile shape at different distances without taking into account the real value of the received signal. It can be seen that at a distance of 50 mm the wave has not yet formed completely, which corresponds to the near Fresnel diffraction zone for radiation with a frequency of 38 GHz (wavelength 7.89 mm). Already at a distance of 100 mm, the wave front is practically formed, which corresponds to the far Fraunhofer diffraction zone.

These results are in good agreement with theoretical ideas about the formation of a wave front during the emission of electromagnetic radiation, depending on the distance along the direction of radiation propagation.

At distances corresponding to the near diffraction zone, the theoretical calculation of the shape of the wave front presents significant difficulties; therefore, we carried out most of the measurements at distances of more than 100 mm between the transmitter and receiver. At the same time, we were limited in the ability to measure the wavefront at large distances, since the maximum possible precision movement of the receiver 6 used on the setup was limited to 140 mm with a positioning accuracy of the system 7 of 0.1 mm, see Fig. 1.

For an experimental assessment of the presence or absence of differences in the degree of absorption of electromagnetic waves with different degrees of localization in stacked dielectric absorbers of various thicknesses, the installation shown in Fig. 1 was assembled. A different form of the emitted electromagnetic wave was created by Teflon absorbers 4 having a constant or variable cross-sectional profile. Depending on the profile of the Teflon insert No. 1 or No. 3 in the output waveguide 2, the shape of the radiation wavefront at the half-intensity level was different. At a distance of 100 mm from the outer cut of the Teflon insert, after passing through the 18 mm thick dielectric absorber, the value of the vertical profile of the signal from the rectangular insert No. 1 is 316±3 mm at half-height of the maximum value. At the same time, from insert No. 3, which has a converging signal profile, the value at half height was 424±3 mm.

On **Fig. 3** the results of one of the conducted experiments on the absorption of microwave radiation with a frequency of 38 GHz in a dielectric absorber of variable thickness are presented. In this experiment, a Teflon insert with a converging profile No. 3 (from 5.5×2.5 mm at the beginning to 0.1×2.5 mm at the end) was inserted into the output waveguide 2 and protruded from it by 125 mm, while the output horn 3 was absent. see Fig. 1. An input horn of rectangular section 36×30 mm, 60 mm long, combined with receiver 6, was installed at a distance of 100 mm from the end of the Teflon insert. A stacked Teflon absorber with

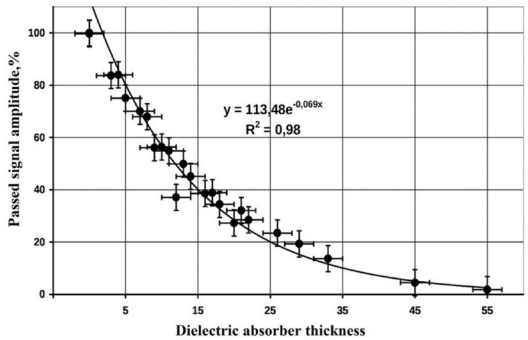

Fig. 3. *Dependence of the relative value of the transmitted signal of microwave radiation with a frequency of 38 GHz on the thickness of the stacked dielectric absorber.*

a thickness of 2 to 55 mm was adjusted in the range of 0.1–4 mm from the end of the Teflon insert so that the signal level in the receiver 6 from the radiation transmitted through the absorber was maximum. To reduce the level of interference from microwave waves scattered by the installation equipment, special absorbers of microwave radiation were attached at the emitter output and receiver input, which made it possible to significantly reduce the noise level in the receiving path.

On Fig. 3 in addition to the experimental data on the dependence of the transmitted signal when using a Teflon insert of a converging profile No. 3, an approximation based on the exponential formula of the data obtained and the value of the reliability of this approximation R^2 are given. Comparison of the obtained approximation formulas for Teflon inserts No. 1 (rectangular section) and No. 3 (converging section) showed a difference in the exponents at the level of 4-5% (–0.069 versus –0.074). At the same time, the exponent in the trend formula corresponding to the absorption of the localized wave emerging from the converging waveguide No. 3 is less than the exponent obtained by approximating the results of the Teflon rod No. 1 with a rectangular constant profile by the exponential law.

The accuracy of the data of the first experimental results and the total amount of measurements carried out so far only allows estimating and limiting the magnitude of the obtained effect of the difference in the absorption of electromagnetic microwave waves in the region of 35-50 GHz with different degrees of localization from above by a value of about 3-4% for a given experiment geometry.

4. DISCUSSION OF THE RESULTS AND CONCLUSIONS

The first qualitative results have been obtained, which make it possible to compare the absorption of electromagnetic waves of different degrees of localization in a dielectric absorber. Within the framework of ESM, the propagation of an electromagnetic wave along the *Z* axis in a waveguide of variable cross section converging along the *X* and *Y* axes filled with a dielectric with a refractive index greater than 1 corresponds to the case of a combination of rotations , and in the *XS, YS* and *ZS* planes [6,24]. With a combination of rotations in different planes, according to the ESM formalism, a plane electromagnetic wave consisting only of components passes partially (and under certain conditions, completely) into new fields.

So, for example, when rotating, the following changes occur in the components

$$E'_Y = \cos\varphi^{YS} E_Y + Q\sin\varphi^{YS};\ H'_X = H_X\cos\varphi^{YS} - G_Z\sin\varphi^{YS};$$
$$Q = Q\cos\varphi^{YS} - \sin\varphi^{YS} E_Y;\ G'_X = G_X\cos\varphi^{YS} - H_Z\sin\varphi^{YS}.$$

When and turning in the *XS* and *ZS* planes, according to the ESM, similar field transformations also occur [6-7].

According to the qualitative estimates obtained in the ESM of the processes occurring during the passage of a plane electromagnetic wave through a converging dielectric waveguide of variable cross section (wave localization), a new field object arises in which, due to the partial transformation of the initial fields into new fields, due to which it is possible to more effectively overcome the Coulomb material barrier. As a result, less efficient scattering of such localized waves in comparison with

nonlocalized electromagnetic radiation should be observed in experiments according to ESM [24].

In our series of experiments, we obtained an estimate of the scattering of microwave radiation with a frequency of 38 GHz in dielectric absorbers of variable thickness for different shapes of the incident wave wavefront (different degrees of localization). If the initial microwave radiation from the generator passes through a converging dielectric waveguide, a smaller scattering of radiation during propagation through a dielectric absorber is recorded in comparison with experiments in which the microwave from the generator passed through a Teflon rod of constant cross section.

To compare the obtained experimental data with the results of model calculations, we plan to carry out calculations based on existing software packages, such as NEC2, MININEC3 and HFSS (High Frequency Structure Simulator), IE3D, Microwave Office, Microwave Studio [2-5].

In order to more fully study the expected effect, measurements will be carried out using silicone dielectric materials, which have a significantly higher refractive index for electromagnetic waves in the microwave range.

REFERENSES

1. Tsipenyuk DYu, Derzhavin SI, Kravchenko YV, Bogdanov MR. Installation for studying the parameters of localization of an electromagnetic wave in a waveguide of variable cross-section in the framework of the predictions of the 5-d extended space model. *RENSIT: Radioelectronics. Nanosystems. Information technologies*, 2021, 13(4):407-418; doi: 10.17725/rensit.2021.13.407.
2. Description of the basic MMANA-GAL. Website of the developer of the MMANA-GAL program. DL2KQ & DL1PBD, http://gal-ana.de/basicmm/en/.
3. Goncharenko IV. HF and VHF antennas. Part 1. Computer simulation. MMANA. Moscow, IP RadioSoft, Journal "Radio", 2004. 126 p. (in Russ.).
4. High Frequency Structure Simulation. *Manuals,* Agilent, 2000.
5. Sirkeli AI, Drach VE, Review of CAD modeling of microwave devices. *Interactive Science*, 2017, 1(11):139-141, doi: 10.21661/r-116149.
6. Andreev VA, Tsipenyuk DYu. Electromagnetic field in the extended space 5-dimensional model, its localization and interaction with waveguide. *RENSIT: Radioelectronics. Nanosystems. Information technologies*, 2019, 11(2):93-102; doi: 10.17725/rensit.2019.11.093.
7. Andreev VA, Tsipenyuk DYu. The Mass and Size of Photons in the 5-Dimensional Extended Space Model. *Journal of Modern Physics,* 2016, 7(11):1308-1315; doi: 10.4236/jmp.2016.711116.
8. Andreev VA, Tsipenyuk DYu. The 5-dimensional Extended space model. Localization of a plane wave and its interaction with a point charged particle. *Pramana-J. Phys.*, 2021, 95:196; https://doi.org/10.1007/s12043-021-02233-7.
9. Tsipenyuk DYu. Non-isotropic objects in extended space. *Engineering Physics,* 2017, 6:20-26; http://infiz.tgizd.ru/en/arhiv/16434.
10. Tsipenyuk DYu, Andreev VA. Elektrodinamika v rasshirennom prostranstve [Electrodynamics in extended space]. *Preprint IOFAN*, 1999, No 9, 26 p.; doi: 10.24412/FhlTben9-y4 (in Russ.).
11. Wesson PS. *Space, Time, Matter: modern Kaluza-Klein theory*. Singapore, World Scientific Publ., 1999, 209 p. Available: https://archive.org/details/ spacetimematterm0000wess.
12. Wesson PS. *Five-Dimensional Physics. Classical and Quantum Consequences of Kaluza-Klein Cosmology.* Singapore, World Scientific Publ., 2006, 232 p.

13. James Overduin, Paul Wesson. KaluzaKlein Gravity. *Physics Reports,* 1997, 283:303-378.
14. Overduin J, Henry RC. *Physics and the Pythagorean Theorem*. arXiv:2005.10671v2; 2020.
15. Vladimirov Yu.S. *Space-time: explicit and hidden dimensions*. Moscow, LIBROKOM Publ., 2010, 208 p.
16. Klein Felix. Über neuere englische Arbeiten zur Gesammelte matematische Abhandlungen. *Zeitschrift für Mathematik und Physik,* 1901, 46:375.
17. Einstein A. Die Grundlage der allgemeinen Relativitätstheorie. *Annalen der Physik*, 1916, 49:769-822.
18. Klein Oskar. Quantentheorie und fünfdimensionale Relativitätstheorie. *Zeitschrift für Physik,* 1926, 37(12):895-906; doi: 10.1007/BF01397481.
19. Kaluza Th. Zum Unitätsproblem in der Physik. *Sitzungsberichte der Koniglich Preussischen Akademie der Wissenschaften, Berlin,* 1921, 966-972.
20. Fock VA. Über die invariante Form der Wellen und der Bewegungsgleichungen für einen geladenen Massenpunkt. *Zeitschrift für Physik,* 1926, 39:226-232.
21. Mandel H. Über den Zusammenbang zwischen der Einsteinischen Theorie des Fern. Parallelismus und der Fünfdimensionalen Fieldtheorie. *Zeitschrift für Physik,* 1926, 39:136-145.
22. Einstein A, Bergmann P. Generalization of Kaluza's Theory of Electricity. *Ann. Math., Ser. 2,* 1938, 39:683-701.
23. Rumer UB. *Research in five-dimensional optics*. Moscow, URSS Publ., 2010, 152 p.
24. Andreev VA, Tsipenyuk DYu. Tunneling of the potential barrier and particle's size in the Extended Space Model. *Proc. Int.Conf. PIRT-2015*, 2015, 20-32; doi: 10.18698/2309-7604-2015-1-20-32.

DOI: 10.17725/rensit.2023.15.215

Methods and features of measuring the thermal resistance of integrated microwave amplifiers on heterojunction bipolar transistors

[1]Vyacheslav A. Sergeev, [1,2]Vitaliy I. Smirnov, [1]Andrey A. Gavrikov

[1]Kotelnikov Institute of Radioengineering and Electronics of RAS, Ulyanovsk Branch, http://www.ulireran.ru/
Ulyanovsk 432071, Russian Federation

[2]Ulyanovsk State Technical University, https://www.ulstu.ru/
Ulyanovsk 432027, Russian Federation

E-mail: sva@ulstu.ru, smirnov-vi@mail.ru, a.gavrikoff@gmail.com

Received May 9, 2023, peer-reviewed May 16, 2023, accepted May 23, 2023

Abstract: **The method of measuring the thermal resistance (TR) of semiconductor devices (SD) according to OST 11 0944-96 and the original modulation method implemented in the hardware and software package developed by the authors are described. In both methods, the SD is heated by pulsed power, and the temperature of its active region (transition) is determined by a change in the temperature–sensitive parameter (TSP) - the voltage at the SD at a low current passed through the SD in the pauses between the pulses of the heating current. The measurement error of the vehicle by the standard method strongly depends on the choice of the duration of the heating current pulses and the delay time when measuring the voltage at the SD after switching off the heating current. In the modulation method, the duration of the heating current pulses is changed according to the harmonic law, and according to the results of measuring the voltage at the SD during the passage of the heating and measuring current, the modulus of the thermal impedance of the SD is determined as the ratio of the first harmonic of the transition temperature to the first harmonic of the heating power. According to the frequency dependence of the thermal impedance module, the components of the vehicle of the object are determined, while the requirements for maintaining the temperature of the device body are significantly reduced and, as a result, the measurement error of the vehicle is reduced. The results of comparative measurements of the TR of integrated microwave amplifiers (amplifying cascades) on InGaP/GaP HBT by the standard and modulation method at different values of the amplitude of the heating current are presented. It is shown that the results of measuring the TR of integrated microwave amplifiers by both methods are in good agreement with each other. It is established that with an increase in the amplitude of the heating current, the TR junction-case of integrated microwave amplifiers decreases, which is due to the alignment of current distribution in the structure of the GBT during heating.**

Keywords: **integrated microwave power amplifiers, heterobipolar transistors, thermal parameters, measurement, modulation method**

UDC 621.382.32

Acknowledgments: The work was supported by the Russian Science Foundation (project No. 22-29-01134).

For citation: Vyacheslav A. Sergeev, Vitaliy I. Smirnov, Andrey A. Gavrikov. Methods and features of measuring the thermal resistance of integrated microwave amplifiers on heterojunction bipolar transistors. *RENSIT: Radioelectronics. Nanosystems. Information Technologies,* 2023, 15(3):215-222e. DOI: 10.17725/rensit.2023.15.215.

Contents

1. INTRODUCTION

Microwave power amplifiers based on heterojunction bipolar transistors (HBT) are widely used in various radioelectronic systems operating in the *S*- and *L*-bands [1,2]. One of the key problems for this devices class is heat removal from dies, since the microwave power amplifiers efficiency is much less than unity [1,2]. At the same time, the real thermal parameters of the microwave power amplifier modules can differ significantly from the calculated ones, therefore, it is necessary to control their thermal parameters both at manufacturing enterprises and at the input control of electronic equipment manufacturers using such devices.

To control the microwave power amplifiers thermal parameters, the methods of IR thermometry [3,4], Raman thermometry [5], or photoconductivity spectroscopy [6] are used. These methods are not very accurate, and obviously unsuitable for fully finished products in closed cases.

The purpose of this work was to test methods for indirect measurement of the integrated microwave power amplifiers thermal parameters based on HBT by the standard and modulation methods at various currents and to analyze the obtained dependencies.

2. METHODS FOR MEASURING THE THERMAL RESISTANCE OF INTEGRATED MICROWAVE AMPLIFIERS

The thermal properties of semiconductor devices are usually characterized by the thermal resistance (TR) "junction-to-case" R_{Tjc}, defined as the ratio of the temperature increment ΔT_j of the HBT *p-n*-junction to the thermal power dissipated in it:

$$R_{Tjc} = \frac{T_j - T_c}{P} = \frac{\Delta T_j}{P},$$

where T_j – *p-n*-junction temperature of the transistor, included in the amplifier; T_c – fixed case temperature; P – power dissipated in the amplifier.

According to OST 11 0944-96 [7] for BT and HBT, a measurement object pulsed heating mode is used, which is connected according to the circuit with a common base. The junction temperature T_j is determined in the pauses between heating current pulses I_{heat} by measuring a temperature sensitive parameter (TSP) that is linearly dependent on the junction temperature T_j. As a TSP for BT and HBT, a direct voltage U_{eb} is used at the emitter junction when a small fixed measuring current flows through it. The measurement error of TR by this method according to estimates [7] is more than 12% with a confidence level of 0.95. One of the reasons for this is the transient electrical process that occurs when switching the BT or HBT from the heating mode to the TSP measurement mode [8]. Another reason is the uncertainty in setting the duration of heating pulses, which, according to the standard [7], should be 3–5 times higher than the "transition-to-case" thermal constant τ_{Tjc}, but the standard does not provide a method for measuring τ_{Tjc}.

These shortcomings are absent in the modulation method with the object heating by heating current pulses, the duration of which is changed according to the harmonic law [9]:

$$\tau(t) = \tau_{av}(1 + a\sin 2\pi ft),$$

where τ_{av} – average pulse duration; a, f – coefficient and frequency of heating power modulation.

The heating power modulation causes sinusoidal oscillations of the transition temperature T_j, averaged over the period, with a phase shift φ relative to the variable power:

$$T_j(t) = T_{j0} + T_m\sin(2\pi ft - \varphi),$$

where T_{j0} – junction temperature constant; T_m – variable component amplitude of the junction temperature at the modulation frequency *f*.

Thermal impedance is defined as the amplitudes ratio of the junction temperature variable components and the heating power The thermal impedance dependence on the modulation frequency of the heating power has features in the form of flat sections and inflection points determined by the components of the TR of the object [10]. The modulation method has a advantages number compared to the standard method [11]: it allows measuring the TS components, and this method significantly reduces the requirements for maintaining the temperature of the object body constant. Both methods are implemented in a hardware-software complex, which includes a microprocessor-based thermal resistance meter, a computer, and specialized software [11].

3. HARDWARE-SOFTWARE COMPLEX FOR MEASURING THERMAL RESISTANCE

The modulation method for measuring TR is implemented in a hardware-software complex (HSC), the functional diagram of which is shown in **Fig. 1**. The HSC works as follows. The operator enters data on the measurement modes and parameters, which are transferred to the microcontroller via the USB interface. The microcontroller, together with a digital potentiometer (DP) and a heating current source

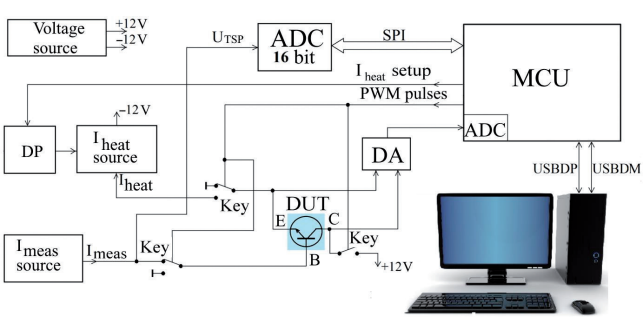

Fig. 1. *Functional diagram of the hardware-software complex.*

Iheat, generates pulses with the amplitude, repetition period and pulse-width modulation frequency set by the operator. The heating current pulses passing through the collector-emitter circuit of the transistor heat the object of measurement with a power that varies according to the harmonic law. The amplitude of the variable power component is determined based on the amplitude of the heating current pulses set by the operator and the measured voltage at the object, which is fed through a differential amplifier (DA) to the input of the analog-to-digital converter (ADC) built into the microcontroller.

The impact on the object of variable power, which changes according to a harmonic law, causes a change in the temperature of the active region of the transistor die (*p-n*-junction) according to the same law, but with a phase shift relative to the heating power. The measurement of the junction temperature is carried out indirectly based on the measurement of a temperature-sensitive parameter (TSP), which is used as a direct voltage U_{eb} between the emitter and the base of the transistor when a fixed measuring current Imeas flows through the emitter junction. The transition temperature is measured in pauses between heating pulses with a time delay relative to their trailing edge, which is necessary to complete transient electrical processes. The junction temperature is measured by a 16-bit ADC that communicates with the microcontroller via the SPI (Serial Peripheral Interface) serial peripheral interface. To ensure the flow of heating current pulses through the transistor through the collector-emitter circuit, and in the pauses between pulses through the base-emitter circuit, electronic switches Key on field-effect transistors controlled by a microcontroller are used.

By the HSC it is possible to measure the TR not only by the modulation method, but also by the standard method according to OST 11 0944-96, using heating of the object

by a series of heating current pulses with a constant duration. Since the duration of the heating pulses must be such that the die has time to reach a stationary temperature regime, while the case temperature remains unchanged, a special regime is provided in the HSC to determine this optimal duration. It is based on the measurement and analysis of the transient thermal characteristic (TTC), that is, the dependence of $Z_T(\tau)$ of the transient TR on the duration τ of the heating current pulses and includes the passage of heating pulses through the object with a duration increasing according to a logarithmic law. In this case, the pause between pulses exceeds the pulse duration by a factor of 4–5, which is quite sufficient for the die temperature to return to its initial value after each pulse. After each heating pulse with a certain time delay, the response to this effect is measured – the change in the transition temperature. To determine the optimal pulse duration, smoothing and differentiation of the measured TTC is applied.

4. MEASUREMENT OF THE MICROWAVE AMPLIFIER THERMAL RESISTANCE BY THE STANDARD METHOD

The objects of study were integrated microwave amplifiers based on InGaP/GaP HBT type MMG3014NT1 with a limiting frequency of 4 GHz and a maximum operating current of 300 mA [12]. During measurements, the object was connected to a source of heating pulses according to a common-base circuit. Heating was carried out by a series of heating current pulses flowing through the "collector-emitter" circuit. The voltage U_{eb} used as the TSP was measured with a time delay of 40 μs relative to the end of each heating current pulse. The temperature coefficient of the forward voltage drop was measured by the standard method and for the HBT MMG3014 is – 1.78 mV/K.

To determine the optimal duration of the heating current pulses, the transient thermal characteristic (TTC) was first measured by passing heating current pulses, with a change in duration τ from 0.1 to 300 ms with a step constant on a logarithmic scale of 50 pulses per decade. The results of the PTC measurements are presented in the upper window in **Fig. 2**. The features of the TTC were identified by calculating $[dZ_T/d\tau]^{-1}$ as a function of the pulse duration τ. The result of such processing of TTC is shown in the lower window in Fig. 2. The maximum of the graph in the lower window corresponds to the optimal pulse duration, the value of which for the studied HBT MMG3014 turned out to be 5.5 ms. At the pulse duration determined in this way, the measurements were carried out by the standard method. The thermal resistance R_{Tjc} was determined by calculating the temperature difference of the die before and after the heating pulse, followed by averaging over all pulses. To eliminate the influence of the delay time on the measurement results, extrapolation of the TSP values by the end of each heating pulse was used; it was assumed that the process of object die cooling is described by a root dependence [8].

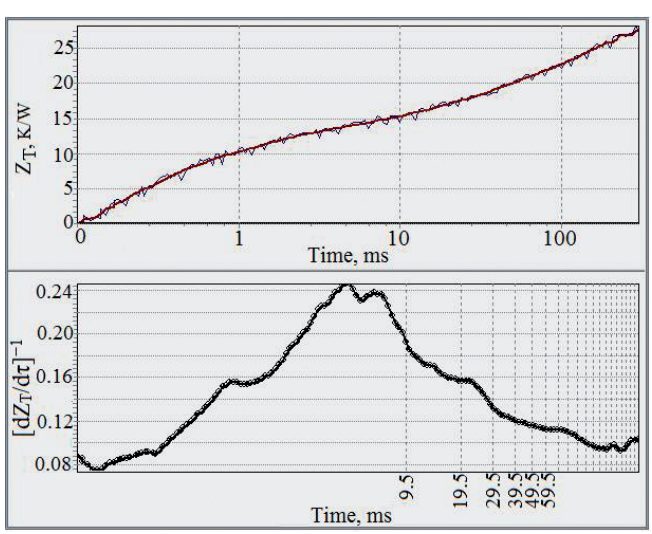

Fig. 2. *Transient thermal characteristic (top) and the result of its processing (bottom).*

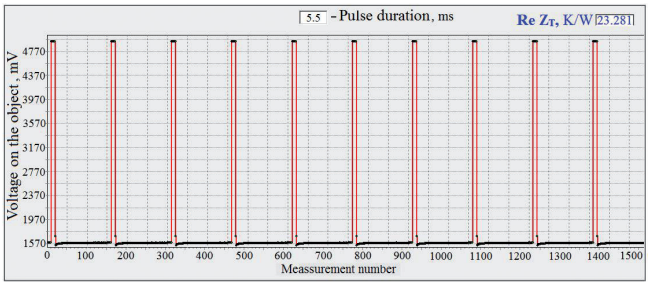

Fig. 3. *The shape of the voltage on the object when measuring the TC of the microwave amplifier MMG3014 standard method at I_{heat} = 200 mA.*

The result of measuring the TR of the MMG3014 microwave amplifier at I_{heat} =200 mA is shown in **Fig. 3**. Regardless of the set pulse duration, the voltage at the top of the pulses was measured 10 times with subsequent averaging. To determine the change in the junction temperature caused by the heating pulse, the TSP value was measured 10 times before each heating pulse and 130 times after it. The interval between adjacent TSP measurements was 13 μs, which was determined by the capabilities of the external ADC and SPI interface. The measured value of TC at I_{heat} = 200 mA turned out to be 23.28 K/W. TC measurements at various I_{heat} values showed that with an increase in the I_{heat} amplitude, the value of R_{Tjc} decreases significantly.

5. MEASUREMENT OF THERMAL RESISTANCE BY THE MODULATION METHOD

In this method, the object is heated by a sequence of heating current pulses with a given repetition period and a duration that varies according to a harmonic law. To determine R_{Tjc}, the dependence of the real part Re $Z_T(f)$ of the thermal impedance on the modulation frequency of the heating power f was measured (upper window in **Fig. 4**). The inflection point on the dependence Re $Z_T(f)$ is determined by the thermal resistance "junction-to-case" R_{Tjc}. To determine this component, a plot of the dependence of the inverse derivative Re $Z_T(f)$ on frequency from Re

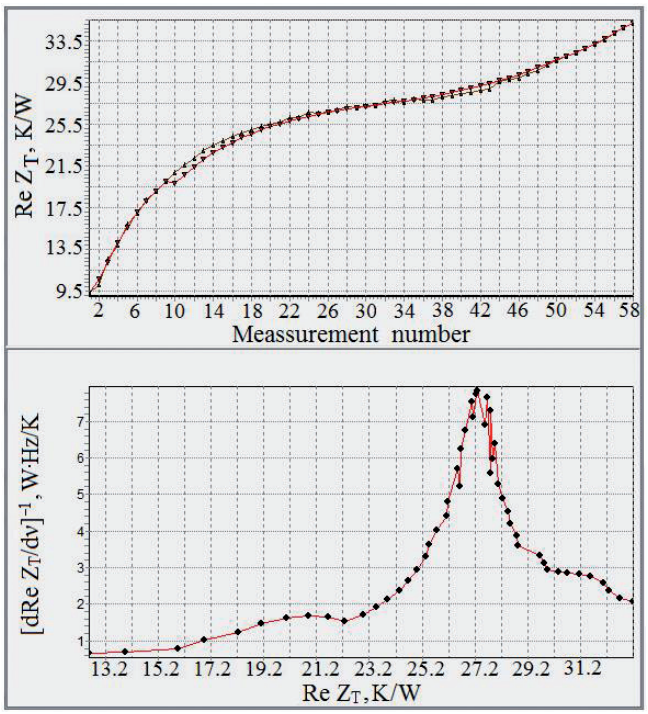

Fig. 4. *Frequency dependence of the real part Re $Z_T(f)$ thermal impedance of the MMG3014 microwave amplifier.*

Z_T was plotted (lower window in Fig. 4). The maximum on the graph corresponds to the TR R_{Tjc} component.

To assess the inhomogeneity of the distribution of the heating current over the die structure of the MMG3014 microwave amplifier, the dependence Re $Z_T(f)$ was measured at different values of the amplitude of the heating current pulses. The results of processing the obtained dependences are shown in **Fig. 5.** For the convenience of

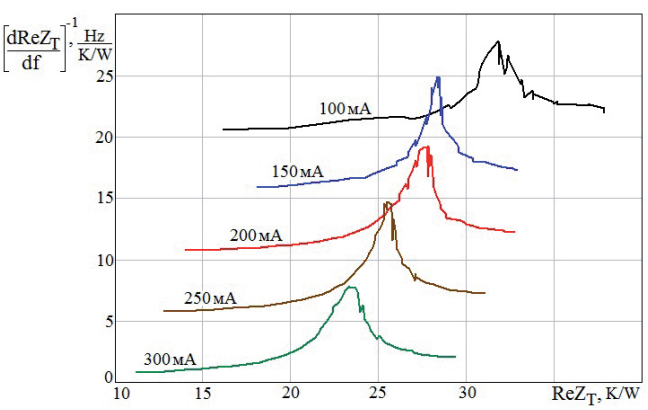

Fig. 5. *Dependence of $(dReZ_T/df)^{-1}$ on the real part of the thermal impedance Re Z_T microwave amplifier MMG3014 at different amplitudes of I_{heat}.*

perceiving the graphs, all of them are shifted relative to each other along the ordinate axis by 5 units. It can be seen that with an increase in Iheat from 100 to 300 mA, the maxima, whose position relative to the Re Z_T axis determines the thermal resistance R_{Tjc}, shift to the beginning of the abscissa axis. This indicates that with an increase in the amplitude of the heating current pulses, the values of the thermal resistance R_{Tjc} of the microwave power amplifier based on the HBT significantly decrease.

The results of measurements of R_{Tjc} at different values of RTjc, obtained by the modulation method, are shown in **Fig. 6.** The solid line 1 shows the result by the least squares method. Line 2 shows the result of processing the R_{Tjc} values obtained by the standard method. It can be seen that the nature of the dependence of R_{Tjc} on Iheat for both methods is the same, but there is a significant difference between the measured values of R_{Tjc}. The reason for this difference is that, in addition to the die in which the HBT is formed, the power amplifier has matching elements with active and capacitive resistance. When using the modulation method, the object is heated by a sequence of pulses with a repetition period of about 100 μs, and when using the standard method, by single pulses with a duration of several milliseconds. Due to the different nature of the current flow through the matching capacitive elements, the HBT die is heated by a series of short current pulses more than when heated by single pulses.

In addition, it can be seen from the figure that the thermal resistance R_{Tjc} of the MMG3014 HBT microwave amplifier noticeably decreases with an increase in the heating current amplitude. One of the most probable mechanisms of such a decrease is the equalization of the current distribution in the comb structure of the HBT during heating [13,14]. One of the main reasons for the inhomogeneous current distribution in the comb structures of BT and HBT in the active mode of operation is the voltage drop across the resistance of the current-carrying emitter tracks of metallization in relation to the thermal potential [14]. With an increase in the structure temperature and thermal potential, the effect of the voltage drop on the metallization resistance decreases and the inhomogeneity of the current density in the structure decreases. Thus, the steepness of the current dependence R_{Tjc} can serve as an indirect diagnostic parameter of the resistance of current-carrying metallization and the inhomogeneity of the current distribution in the HBT structure.

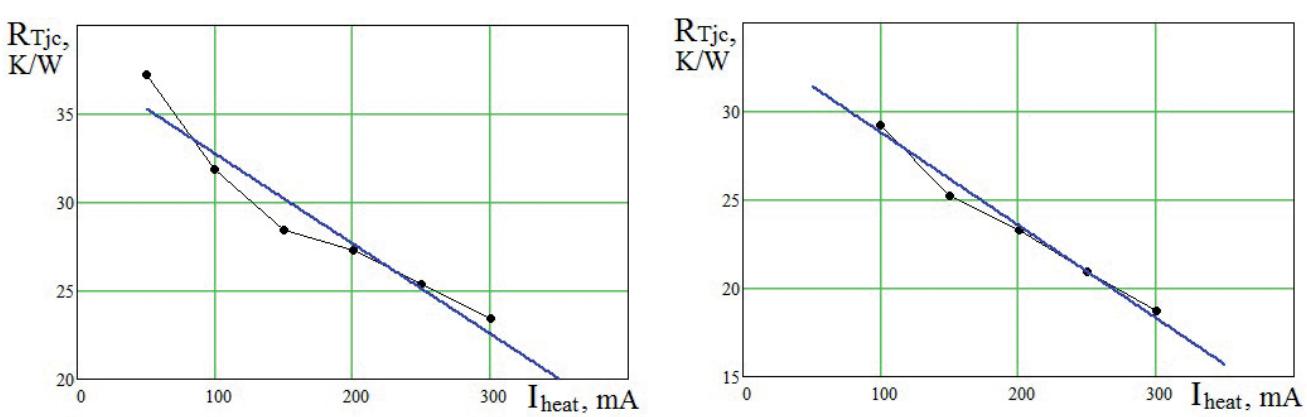

Fig. 6. *Dependence of the thermal resistance of the MMG3014 microwave amplifier, measured by various methods, on the amplitude of the heating current pulses: 1– standard method; 2 –modulation method.*

6. CONCLUSION

The results of comparative measurements of the junction-to-case TR of integrated microwave amplifiers (amplifier stages) based on InGaP/GaP HBT by the standard and modulation methods at different values of the heating current amplitude are presented. It is shown that the results of measuring the junction-case TR of integrated microwave amplifiers by both methods are in good agreement with each other. It has been established that with an increase in the amplitude of the heating current, the TS of the junction-case of integrated microwave amplifiers decreases, which is probably due to the alignment of the current distribution in the HBT structure during heating.

Thus, the steepness of the current dependence R_{Tjc} can serve as an indirect diagnostic parameter of the inhomogeneity of the current distribution in the HBT structure.

REFERENCES

1. Sechi F, Bujatti M. *Moshchnyye tverdotel'nyye SVCH-usiliteli* [Power solid-state microwave amplifiers]. Moscow, Tekhnosfera Publ., 2015, 416 p.
2. Retnyuk V. Vybor tekhnologii SVCH-transistorov dlya ispol'zovaniya v usilitelyakh moshchnosti [The choice of microwave transistor technology for use in power amplifiers]. *SVCH-elektronika*, 2018, 2:4-6, (in Russ.).
3. Sergeev VA, Tarasov RG, Hodakov AM. Raschet i izmerenie teplovyh parametrov monolitnyh integral'nyh shem SVCH-usilitelej v sostave vyhodnyh usilitelej moshnosti X-diapazona [Calculation and measurement of thermal parameters of monolithic integrated circuits of microwave amplifiers as part of X-band output power amplifiers]. *Zhurnal radioelektroniki* [*elektronnyj zhurnal*], 2019, 8. Access mode: http://jre.cplire.ru/jre/sep19/1/text.pdf, (in Russ.).
4. Mahalingam M, Mares E. Infrared temperature characterization of high power RF devices. *Proc. IEEE MTT-S International Microwave Sympsoium Digest,* 2001, 3:2199-2202.
5. He J, Mehrotra V, Shaw MC. Ultra-high resolution temperature measurement and thermal management of RF power devices using heat pipes. *Proc. 11th International Symposium on Power Semiconductor Devices and ICs* (*ISPSD'99*), p. 145-148, 1999.
6. Cinà L, Di Carlo A, Reale A. Thermal Model of High-Power Amplifiers Based on Time-Dependent Temperature Profiles Measured by Photoconductance. *IEEE Transactions on Electron Device,* 2018, 65(5):1739-1744.
7. OST 11 0944-96. Mikroskhemy integral'nyye i pribory poluprovodnikovyye. Metody rascheta, izmereniya i kontrolya teplovogo soprotivleniya [Integrated circuits and semiconductor devices. Methods of calculation, measurement and control of thermal resistance]. Moscow, SUE NPP Pulsar, 1997, 110 p., (in Russ.).
8. Blackburn DL, Oettinger FF. Transient Thermal Response Measurements of Power Transistors. *IEEE Transactions on Industrial Electronics. Control Instruments*, 1976, 2:134-142.
9. Smirnov VI, Sergeev VA, Gavrikov AA, Shorin AM. Modulation method for measuring thermal impedance components of semiconductor devices. *Microelectronics Reliability,* 2018, 80:205-212.
10. Smirnov VI, Gavrikov AA, Shorin AM. Metod izmereniya komponent teplovogo soprotivleniya poluprovodnikovykh priborov i ego prakticheskaya realizatsiya [Method of measuring components of thermal resistance of semiconductor devices and its practical implementation]. *Avtomatizatsiya protsessov upravleniya*

[Automation of control processes], 2017, 2(48):98-105, (in Russ.).

11. Smirnov VI, Sergeev VA, Gavrikov AA, Tarasov RG. Sravnitel'nyj analiz metodov izmereniya teplovyh parametrov SVCH-usilitelej moshnosti na bipolarnyh tranzistopah [Comparative analysis of methods for measuring thermal parameters of integrated microwave power amplifiers on bipolar transistors]. *Zhurnal radioelektroniki* [*elektronnyj zhurnal*], 2022, 8. Access mode: http://jre.cplire.ru/jre/aug22/11/text.pdf, (in Russ.).
12. Freescale Semiconductor Technical Data: *Document Number: MMG3014NT1 Rev. 5*, 3/2016.
13. Sergeev VA, Khodakov AM. Two-Section Model of the Current Distribution in Strip Layouts of Bipolar and Hetero-Bipolar Microwave Transistors. *Journal of Communications Technology and Electronics*, 2022, 67(11):1400-1405.
14. Sergeev VA, Hodakov AM. Thermoelectric model of a heterojunction bipolar transistor taking into account the voltage drop on the current-carrying metallization. *RENSIT: Radioelectronics. Nanosystems. Information technologies*, 2022, 14(2):103-110e. DOI: 10.17725/rensit.2022.14.103.

DOI: 10.17725/rensit.2023.15.223

Specific of microwave radiometers operation on the external distortions conditions

Igor A. Sidorov, Alexander G. Gudkov, Sergey V. Chizhikov, Vitaly Yu. Leushin
Bauman Moscow State Technical University, https://bmstu.ru/
Moscow 105005, Russian Federation
E-mail: igorasidorov@yandex.ru, profgudkov@gmail.com, chigikov95@mail.ru, ra3bu@yandex.ru

Received May 27, 2023, peer-reviewed June 5, 2023, accepted June 13. 2023

Abstract: **The influence of external disturbances on the sensitivity and dynamic range of the microwave radiothermograph is considered. The results of an experimental study of the interference situation in the range up to 3 GHz are presented. The diagram of the spectral density of interference adjacent to radio astronomy windows is analyzed. The features of real observed disturbances are investigated. The classification of possible disturbances according to their characteristics is given. Algorithms for discrimination of various types of interference are considered. The sensitivity and dynamic range of the microwave radiometer are evaluated using the pulse noise suppression algorithm.**

Keywords: **microwave radiothermography, pulse interference, narrowband interference, radiometer sensitivity, dynamic range**

UDC 612.087

Acknowledgments: The study was carried out with a grant from the Russian Science Foundation (project No. 19-19-00349P).

For citation: Igor A. Sidorov, Alexander G. Gudkov, Sergey V. Chizhikov, Vitaly Yu. Leushin. Specific of microwave radiometers operation on the external distortions conditions. *RENSIT: Radioelectronics. Nanosystems. Information Technologies*, 2023, 15(3):223-234e. DOI: 10.17725/rensit.2023.15.223.

Contents

1. INTRODUCTION

A microwave radiometer is a highly sensitive receiver of the own radiothermal radiation from various physical bodies, environments or space objects. Microwave radiometers are mainly used in radio astronomy [1], for remote sensing of the Earth's surface and atmosphere from space [2], from an airplane or unmanned aerial vehicle [3], as well as from various ground carriers [4]. Of particular interest is the use of microwave radiometers in medicine, for non-invasive measurement of the internal temperature of the human body in order to detect malignant neoplasms in the early stages of development, when their therapy is especially effective [5-9]. The probing of the human body by microwave radiometers

simultaneously in several frequency ranges makes it possible to visualize the 3*D* distribution of the internal thermal field of a person [10]. The input signal of the microwave radiometer is a broadband noise signal - radiothermal radiation, the spectral density of which is described by the well–known Planck formula and Planck's law for blackbody radiation. The distribution of thermal noise amplitudes obeys Gaussian statistics and in the reception band of the microwave radiometer has an almost uniform spectral density, i.e. it represents white noise. For the case of low frequencies, Planck's formula reduces to the Rayleigh-Jeans formula, according to which the intensity of thermal radiation is directly proportional to body temperature. Therefore, the intensity of thermal radiation is usually expressed in units of temperature – degrees on the Kelvin scale. In degrees Kelvin, both the input measured signal of the microwave radiometer and the sensitivity of the radiometer, which is understood as the minimum detectable signal, are expressed.

The sensitivity or minimally detectable signal of an ideal (excluding fluctuations in the gain of a microwave amplifier) full-power radiometer is proportional to the sum of the noise temperatures of the antenna T_{A} and the first stage of the microwave amplifier T_{n} and is inversely proportional to the radiometric gain representing the square root of the product of the equivalent width of the input receiving band Δf at the time of accumulation, or integration of the detected signal τ [1].

$$\delta T = \frac{T_a + T_n}{\sqrt{\Delta f \cdot \tau}}. \quad (1)$$

Sensitivity is the most important characteristic of a microwave radiometer along with the dynamic range, which is understood as the ratio of the maximum undistorted measured signal T_{max} to the value of the minimum detectable signal δT:

$$\text{D}_d = \frac{T_{\text{MAX}}}{\delta T}. \quad (2)$$

Dynamic range is a dimensionless quantity, which is usually expressed in decibels:

$$D_d\left[dB\right] = 10lg\left(D_d\right). \quad (3)$$

The presence of artificial or natural distortions in the reception band of the microwave radiometer degrades the sensitivity and dynamic range of the radiometer.

The purpose of this article is to evaluate the effect of artificial or natural distortions in the reception band of a microwave radiometer on the sensitivity and dynamic range of the radiometer. And also to evaluate these parameters when using algorithms for discrimination of some special types of distortions, for example, pulse or narrowband distortions.

2. INFLUENCE OF EXTERNAL INTERFERENCE ON THE MICROWAVE RADIOMETER OPERATION

By external distortions, we will understand any signals of natural or artificial origin, other than thermal radiation, falling into the receiving band of the radiometer. Electromagnetic radiation that occurs during spark discharges in the atmosphere – lightning – refers to interference of natural origin. As well as radiation caused by solar flares. Artificial distortions refers to any radiation of artificial origin during arc discharges (electric welding), spark discharges, for example, from candles of a running internal combustion engine, as well as any type of radio transmitters, Bluetooth and Wi-Fi devices and others. Every active

or passive radio user works in the frequency band allocated to him. The distribution of radio airwaves between users is regulated by national legislation, taking into account international agreements. Thus, in the Russian Federation, such distribution is determined by the table approved by the Decree of the Government of the Russian Federation No. 1203-47 dated September 18, 2019 "On Approval of the Table of distribution of Radio Frequency Bands between the Radio Services of the Russian Federation and the Recognition of Certain Resolutions of the Government of the Russian Federation as Invalid". According to the Table, a number of frequency ranges are allocated for the operation of passive means, radiometers and radio telescopes, therefore these ranges are sometimes called "radio astronomy windows". The operation of any active emitters in these ranges is prohibited. But the allocated radio astronomy windows are rather narrow, so frequencies from 1400 to 1427 MHz, that is, only 27 MHz, are allocated in the *L*-band for radio astronomy.

According to the formula (1), the sensitivity of the radiometer is inversely proportional to the square root of the reception bandwidth. Therefore, to increase sensitivity, radio astronomers have only two ways to increase sensitivity:

1) reducing receiver noise by reducing the temperature of the microwave amplifier by cooling to the temperature of liquid helium, by using special cryogenic technology, and

2) increasing the accumulation time.

For radiometers of remote sensing of the earth from unmanned aerial vehicles, the use of cryogenic technology and an increase in accumulation time are unacceptable. It remains to expand the receiving band, but at the same time, distortions created by active means will inevitably get into the receiving band of the radiometer. In addition, the dedicated radio astronomy windows are constantly narrowing. So in the *C*-band recently there was a radio astronomy window with a width of more than 200 MHz. According to the latest edition of the "Radio Frequency Band Distribution Table ...", only 10 MHz remained from 200 MHz from 4990 to 5000 MHz. The released frequencies were given for testing of communication facilities according to the 5*G* standard. So radiometers manufactured before 2019 for the *C*-band now work in distortions conditions.

For medical radiometers – radiothermographs, the situation with external distortions is even worse. Thus, to obtain information about the thermal fields of the human body at a depth of up to 7-10 cm, it is necessary to work in the 700 MHz range with a bandwidth of about 200 MHz. There are no distortions-free bands in this range. The problem is solved with the help of passive anti-distortions devices, either by using special noise-proof antenna applicators, or by conducting analyses in special shielded cameras with a degree of shielding of more than 60 dB. It should be noted that the cost of a shielded camera is almost an order of magnitude higher than the cost of the radiothermograph itself. In addition, there are problems with its placement, assembly and maintenance, which limits the applicability of the method. But even the funds listed are not enough. In addition, the use of shielded cameras is unacceptable both in radio astronomy and in remote radiometric sensing. Therefore, the task of searching for algorithms and methods of operation of radiometers in conditions of external distortions becomes very urgent.

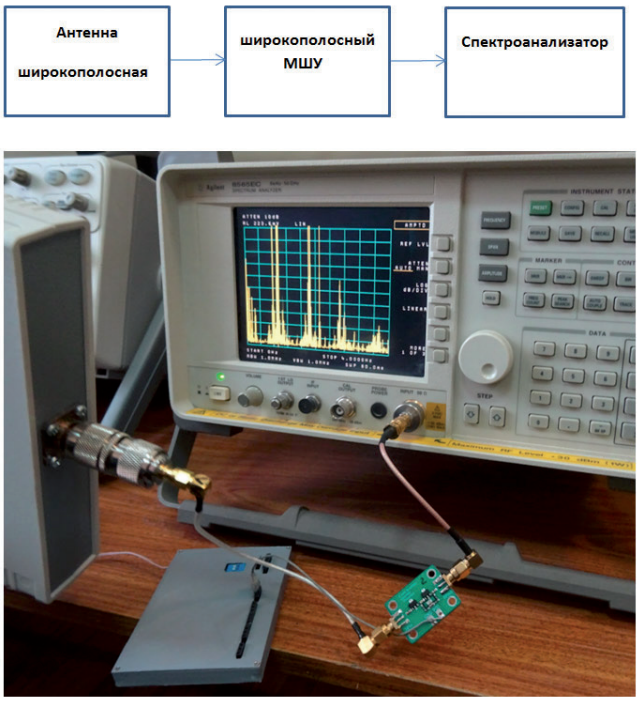

Fig. 1. *Distortions spectrum diagram.*

To find effective algorithms for the operation of radiometers in distortions conditions, it is necessary to investigate possible types of distortions encountered in practice. To study the frequency distribution of the distortions in the range up to 4 GHz, an experiment was conducted, the scheme of which is shown in **Fig. 1**.

The signal from the broadband antenna was amplified by 40 dB by a low-noise broadband amplifier and fed to the spectrum analyzer. The distortions spectrogram is shown in **Fig. 2**.

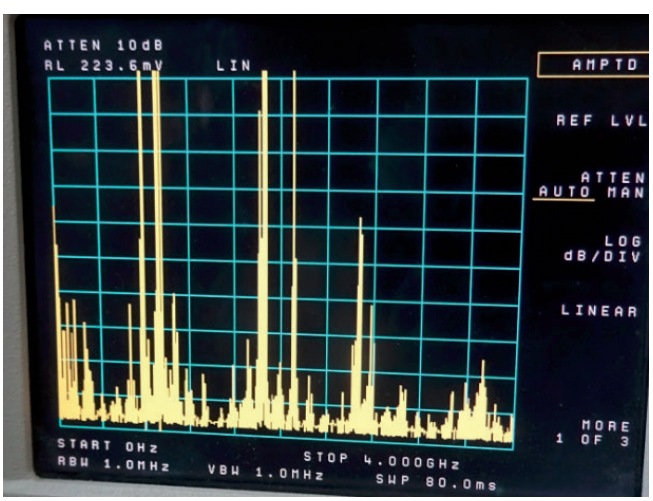

Fig. 2. *Distortions spectrogram diagram in the range from 0 to 4 GHz.*

The analysis of the spectrogram shows that the entire ether in the range is quite densely filled with distortions (signals of active means). A small window is observed in the *L*-band and especially strong distortions in the 900 and 1800 MHz bands – interference from GSM cellular networks. Due to the fact that there are practically no free gaps between the distortions, the use of notch filters to filter distortions will be ineffective. The use of known distortions suppression algorithms by digital distortions filtering will also be ineffective.

To study the characteristics of distortions in the time domain, a microwave radiometer with two-references *C*-band modulation was used. The scheme of such a radiometer is known and published [11]. The signal from the output of the power detector was fed to the first channel of the two-channel oscilloscope, a modulation control signal was fed to the second channel, from which the oscilloscope was synchronized. The antenna of the radiometer was either directed into the sky to check for the presence and recording of distortions, or was covered with an absorbing material to register the noise track in the absence of distortions.

At the same time, the output signal of the radiometer was recorded after the synchronous filter and the synchronous detector at an accumulation time of one second.

The view of the noise track (the waveform of the noise signal at the output of the quadratic detector) in the absence of external interference is shown in **Fig. 3**. The modulation control signal is shown against the background of the noise track. The noise signal represents a normally distributed random process. The distribution function

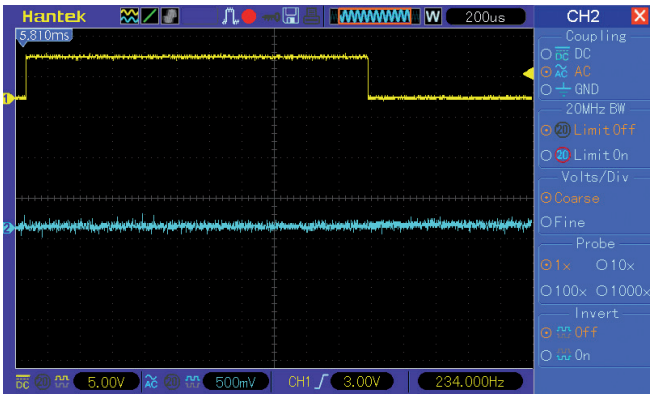

Fig. 3. *Noise track view in the absence of external distortions.*

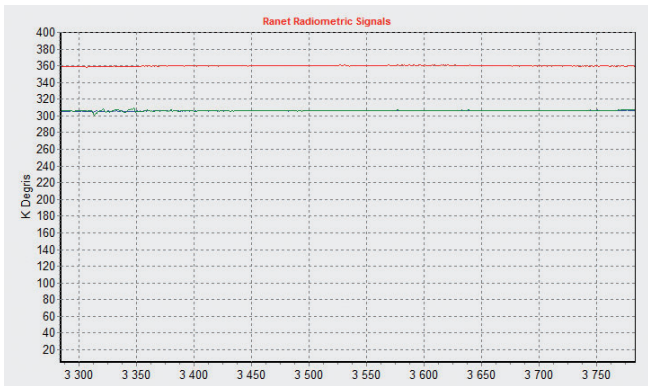

Fig. 4. *Radiometer output signal diagram after a second integration.*

of a random process is described by the Gauss formula (4).

$$f(U)=\frac{1}{\sqrt{2\pi\sigma^2}}e^{-\frac{(U-U_m)^2}{4\sigma^2}}, \quad (4)$$

U_{mn} – the average value of the signal or mathematical expectation, σ is the standard deviation or variance.

The signal realization function *U*, shown in Fig. 3, represents the voltage dependence on time. The voltage is measured in units of Volts, but can be converted to degrees on the Kelvin scale, due to the presence in the radiometer circuit of two internal reference loads with different and known temperatures. It is known that 99.7% of the samples of a normally distributed signal fit into the range ± 3 *σ*. The magnitude of the noise track shown in Fig. 3 can be estimated approximately at 200 mV, which corresponds to a noise temperature of approximately 600 K

The view of the corresponding output signal of the radiometer (Fig. 3) is shown in **Fig. 4** as a copy of the screen of the digital processing program, obtained after integrating the signal for one second.

Fig. 4 shows graphs of three values. The upper line in red represents a graph of the values of the "hot" reference load, heated by 50 degrees relative to the "cold" load (blue line), which has a temperature equal to the ambient temperature. The temperature of the "black" body that covered the antenna from distortions is equal to the temperature of the "cold" load (green line). Therefore, their graphs in Fig.4 practically coincide at the level of 305K. At the scale of the graph, the fluctuations of the output signal are not noticeable, since they do not exceed 1 K.

The presence of external distortions significantly changes the picture. Since the power of natural radiothermal signals is extremely small (about – 60 dB), a low-noise microwave amplifier with a large gain is required (about 80 dB with a 50 MHz reception band) so that the amplified noise would significantly exceed the power detector's own noise. With such an amplification, almost any external artificial signal exceeds in magnitude the thermal radiation noise track shown in Fig. 3. An external distortions signal, in the worst case, can overload the amplifier of the first stage when the amplitude of the amplified distortion signal reaches the maximum value of the output signal of the amplifier. In this case, it makes no sense to talk about the sensitivity of the radiometer. It is impossible to work in conditions of such great distortions. But in practice, there are often situations when saturation of the microwave amplifier does not

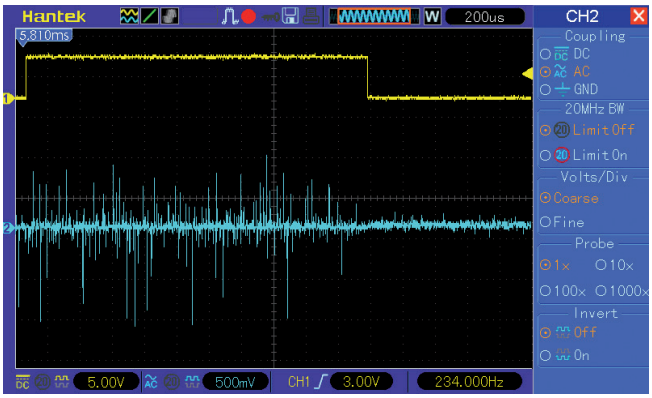

Fig. 5. *The power detector output external distortions diagram.*

occur, although the distortions exceeds the magnitude of the noise track. An example of a detected signal under such conditions is shown in the oscillogram **Fig. 5**.

The type of radiometer output signal in the presence of external distortions is shown in **Fig. 6**.

The range of fluctuations of the output signal in the conditions of external distortions exceeds 300K.

В этом случае минимально обнаружимый сигнал определяется не столько параметрами радиометра, сколько параметрами помехи.

The analysis of the signal shown in Fig. 5 shows that the distortions is not a continuous signal, but a non-periodic sequence of short pulses with different amplitudes. The pulse distortions will be considered short if its

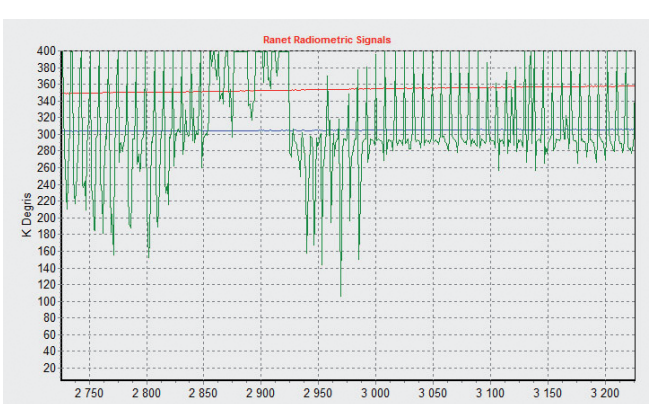

Fig. 6. *Radiometer output signal in the conditions of external.*

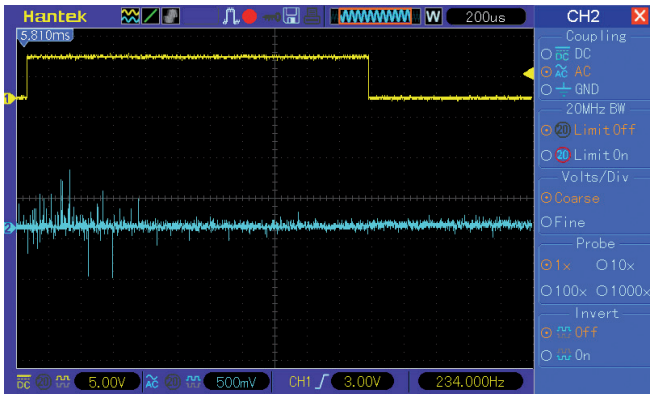

Fig. 7. *Example of short pulse interference.*

duration is less than the sampling period of the detected signal. In this case, the distortions falls into only one ADC count. This type of distortions is typical for some digital communications and radars for various purposes. If pulse distortions, as in Fig. 5, is received continuously throughout the entire time of signal accumulation, then it is very difficult to take into account their influence and, if possible, eliminate it. Perhaps this is a topic for future research. If the distortions is received only part of the signal accumulation time, then algorithms for detecting, accounting for and suppressing distortions of this type can be proposed. An example of a short pulse distortions is shown in **Fig. 7**.

It should be noted that in practice there are not only short pulse distortions, but also longer ones, for example, as in **Fig. 8**. This type of distortions can probably also be

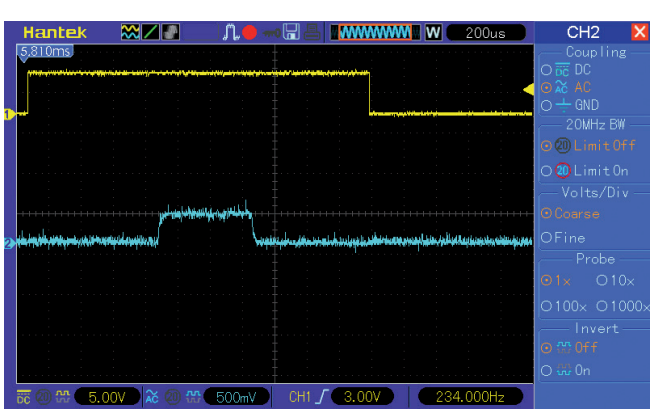

Fig. 8. *Example of the long pulse interference.*

taken into account and suppressed, but this is the topic of a separate study.

3. ALGORITHM FOR EXTERNAL IMPULSE NOISES DISCRIMINATION

As noted above, the search for effective methods and algorithms for the operation of microwave radiometers in conditions of external distortions is an urgent task. Dissertations and numerous articles are devoted to it solving (for example [12]). But the task is so complex and multifaceted that no common solution has been found so far. The algorithm for taking into account the influence of external distortions for the special case of pulsed non-continuous external distortions is considered below. The algorithm involves detecting the presence of external distortions , filtering out samples containing pulse distortions , further processing the remaining samples to calculate the antenna temperature. It should be noted that in order to apply the algorithm, it is necessary to have registered samples of the signal from the detector output for at least one second. The implementation of the algorithm is possible in two variants: in a pseudo-real time scale and with post-experimental processing of the registered signal.

Post-detector processing of the radiometer signal involves the integration of an analog signal for a sufficiently long time, compared with the modulation period, or the summation of discrete digital samples after converting the analog signal into digital form. When summing N independent samples, the variance of a normal random process decreases by the square root of N times. The actual radiometric gain, represented by the denominator of formula (1), is the square root of the number of independent signal samples, in accordance with V.A.Kotelnikov's theorem, up to a constant coefficient of 2.

After summing the samples, it is impossible to separate the samples containing distortions from the sum. Therefore, the algorithm must be applied before integrating (summing) the signal. To do this, we need to remember all the samples for the accumulation time. The rate of receipt of samples is determined by the band of the detected signal. It usually does not exceed 50 kHz. Then the sampling frequency will be 100 kHz (in accordance with V.A.Kotelnikov's theorem), and the sampling period is 10 micro seconds. A modulation radiometer with meander modulation receives only half of the time of the modulation period a signal from the antenna, and the second half - signals from internal standards. It is necessary to remember only the samples of the signal from the antenna, since the signals of the standards do not contain external distortions and can accumulate according to a known algorithm. Usually, the isolation between the antenna channel and the reference channels is determined by the quality of the microwave modulator and exceeds 20 dB. If the distortions is so great that it penetrates the channels of the standards, then the microwave amplifier will definitely be overloaded in the antenna channel, and, as noted above, in this case, the distortions suppression algorithms are not effective.

The proposed distortions discrimination algorithm at the first stage involves determining the signal parameters – the average value and dispersion, for a certain short period of time (up to 0.1 of the modulation period) in the absence of distortions . The presence of distortions is determined by the presence of samples, the

value of which deviates from the average value by the amount of tripled dispersion walue. If this condition is not met, then other counts are taken for the same period of time. If the desired "reference" interval could not be detected, then the algorithm is not applicable in this situation.

At the second stage, samples are detected throughout the signal accumulation interval, the value of which deviates from the average value by the value of the tripled dispersion and more (the average value and dispersion are determined at the first stage). Further, all detected samples are excluded from the data array.

At the third stage, the summation (averaging) of the remaining samples in the array is performed.

It should be noted that after applying the algorithm, the sensitivity of the radiometer (and, accordingly, the dynamic range) will deteriorate somewhat due to a decrease in the number of independent signal samples summed during the accumulation time. The greater the degradation, the greater the number of samples with distortions (the greater the intensity of the distortions). But this degradation is still less than the deterioration of sensitivity in the presence of distortions and without the use of the algorithm.

The block diagram of the external pulse distortions discrimination algorithm is shown in **Fig. 9**.

In case of inapplicability of this algorithm, two methods are proposed that work in the constant presence of distortions.

The first method is based on iterative distortions suppression. To test the effectiveness of the algorithm, a special program was developed and, based on it, a computer simulation of the distortions

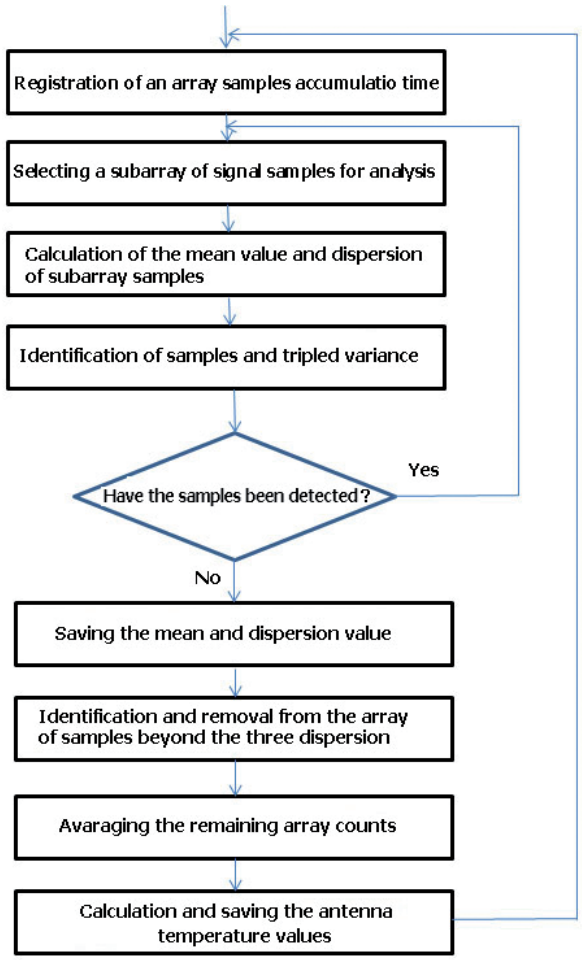

Fig. 9. *The external pulse distortions discrimination algorithm.*

filtering process was carried out. An array of data with parameters close to the parameters of the noise signal at the output of the power detector of the radiometer with a frequency band of about 50 kHz was used as the initial data. The modulation period consists of four intervals of 256 samples. The sampling period is 10 msec. The average value of the simulated signal was taken at the level of 300K, and the variance at the level of 10 degrees. An additional noise process was mixed into the generated data array, simulating a pulse interference with the parameters: the average value (mathematical expectation) at the level of 300K and a variance of 100 degrees. A parameter characterizing the intensity of interference was introduced, numerically equal to the

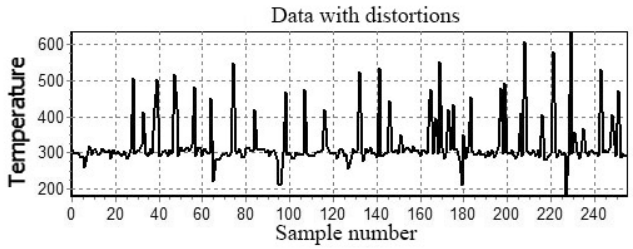

Fig. 10. *Generated data with pulse distortions.*

number of distortions pulses (counts) for one modulation period of 256 counts. The generated data for the distortions parameter of 50 pulses for the modulation period are shown in the graph **Fig. 10**, which are similar to the real recorded data shown in Fig. 7. Different algorithms were used to calculate the mathematical expectation and variance. The iterative algorithm turned out to be the most effective, in which:

1. The mean M and dispersion D are calculated for 256 points.
2. Signal values are revealed ai, for which $|a_i - M| > kD$ replaced by M.
3. Checking that D has reached the specified value.
4. Skip to step 1 if the value is not reached.

Calculations show that the best result is achieved when $k = 3$.

When noise pulses are added to the original signal, the values of the mathematical expectation and variance of the noise process change. When calculating iterations according to the presented algorithm, after 3-4 iterations, the values of the mathematical expectation and the variance of the noise process return to the set values. A graph of the dependence of the expectation value and the variance of the noise process on the number of iterations is shown in **Fig. 11**.

As can be seen from the graphs, the distortions is almost completely filtered out in five iterations. Of course, the number of

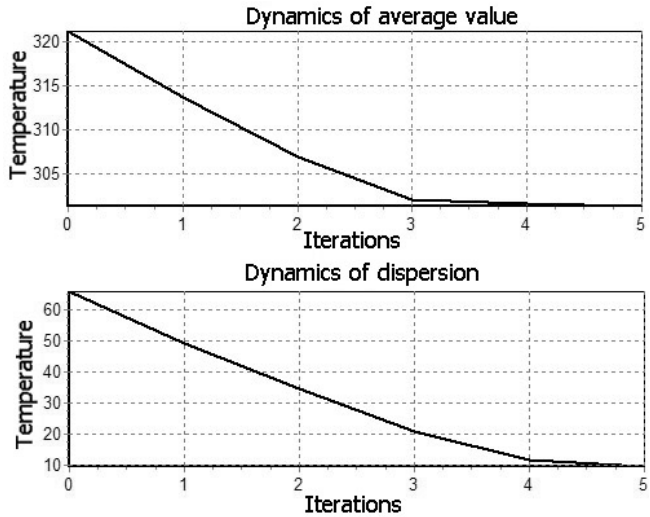

Fig. 11. *The mean value and dispersion changes dynamics.*

iterations required depends on the intensity of the interference.

Another algorithm is based on the analysis of the sample histogram, which leads to the separation of data with distortions and without distortions.

1. A data histogram is being constructed. (**Fig. 12**). As expected, the largest amount of data has accumulated in a cell that corresponds to real data without distortions. It can be seen that 134 values out of 256 have accumulated in this cell.
2. These data are selected, and the average value and variance are calculated.
3. This set is supplemented with those ai data for which $|a_i - M| < kD$

It follows from **Table 1** that the number of useful signal values has increased to 190. If we take into account that according to

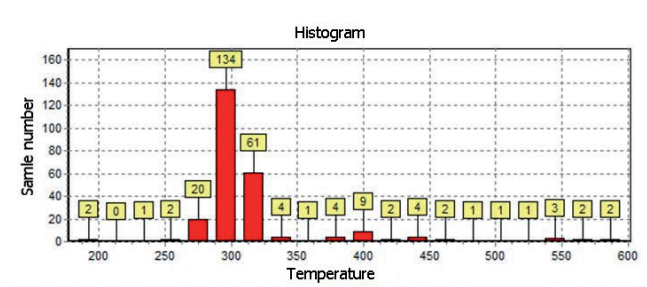

Fig. 12. *Data histogram.*

Table 1

Useful signal

Iteration	Number	Mean	Dispersion
1	256	318.8793	58.2905
2	134	297.9854	5.7277
3	190	299.5555	8.3838

the parameters of the model, only 50 points were replaced by interference, then we can conclude that these points were removed. They can be replaced by an average value.

The type of signal with filtered interference is shown in **Fig. 13**.

Second sensitivity – the sensitivity of the radiometer with a signal accumulation time of one second, is one of the main parameters of the radiometer that determines the accuracy of measurements and dynamic range. For the signal parameters in the considered model, the second sensitivity, provided there no distortions, would be 0.3 degrees. And in the presence of pulse distortions with the above parameters, the sensitivity would deteriorate by 10 times – up to 3 degrees. Accordingly, the dynamic range will deteriorate by 10 times. When using the proposed interference suppression algorithms, the sensitivity will improve, but will not reach the value obtained for a signal without distortions. The deterioration of sensitivity in this case is not due to an increase in the equivalent noise temperature of the signal, but to a decrease in the number of independent samples of the signal, since part of the samples was removed or replaced by a constant as a result of the application of

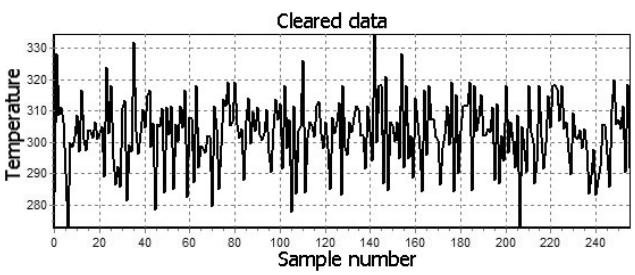

Fig. 13. *Data cleared of distortions.*

algorithms. In this case, the sensitivity after filtering distortions will be 0.37 degrees. The degradation will be 23% and this is significantly better than if the interference was not filtered out. At the same time, the dynamic range will decrease from 43 dB to 42 dB. In the presence of distortions and without the use of distortions suppression algorithms, the dynamic range would be reduced to 33 dB. Of course, the degradation of sensitivity and dynamic range depends on the intensity of distortions.

4. DISCUSSION

The obtained experimental spectrograms and waveforms of a signal with pulse interference, as well as the results of modeling distortions filtering algorithms, allow us to hope for the practical possibility of working in conditions of external pulse distortions. The presented distortions filtering algorithms require testing on real equipment in real conditions. To solve this problem, it is required to digitalize the analog signal from the output of the power detector of the radiometer with a sampling frequency of about 100 kHz and store the data in non-volatile memory. Further processing is carried out in a personal computer using a specialized program. This article discusses distortions received by specialized medical radiothermograph equipment, and it does not consider classical methods of dealing with pulse interference (for example, the median method).

Currently, the conducted research has shown the prospects of these algorithms. However, the use of algorithms requires additional research, including experimental ones, followed by their introduction into data processing programs of the radiothermograph hardware. In case of successful introduction of new devices and

algorithms into the equipment of medical radiothermographs, it will be possible to conduct medical tests and procedures in a regular office without using a special shielded camera, the cost of which significantly exceeds the cost of the radiothermograph itself. Due to the exclusion of the cost of a special shielded camera from the total cost of the necessary equipment, the method of microwave radiothermography using a radiothermograph will become more accessible and widespread.

5. CONCLUSIONS

As a result of experimental studies, calculations and modeling, the following new results were obtained:

- waveforms of real external pulse interference of a microwave radiometer in the C-band were obtained;
- the analysis of the operation of the microwave radiometer in the conditions of pulse distortions was carried out;
- the influence of external pulse distortions on the sensitivity and dynamic range of the microwave radiometer was evaluated;
- the algorithm of detection, accounting and discrimination of pulse distortions is proposed;
- the sensitivity and dynamic range of the microwave radiometer were evaluated, taking into account the suppression of external pulse interference.

REFERENCES

1. Yesepkina NA, Korolkov DV, Pariyskiy YuN. *Radio telescopes and radiometers.* Moscow, Nauka Publ., 1973, 416 p.
2. Kerr YH, Waldteufel P, Wigneron, J-P, Martinuzzi J-M, Font J, Berger M. Soil moisture retrieval from space: The soil moisture and ocean salinity (SMOS) mission. *IEEE Trans. Geosci. Remote Sens.*, 2001, 39(8):1729-1735; doi: 10.1109/36.942551.
3. Verba VS, Gulyaev YuV, Shutko AM, Krapivin VF (Eds.). *Microware Radiometry of Land and Water Surfaces: From Theory to Practice.* Sofia, Marin Drinov Academic Publishing, 2013, 296 p.
4. Sidorov IA, Gudkov AG, Oblivantsov VV, Ermolov PP, Novichikhin EP, Leushin VYu, Agandeev RV. Radiometric remote determination of soil moisture portraits in a vineyard in Crimea. *Electromagnetic waves and electronic systems,* 2022, 27(5):65-70; https://doi.org/10.18127/j15604128-202205-09.
5. Evgeny P. Novichikhin, Igor A. Sidorov, Vitaly Yu. Leushin, Svetlana V. Agasieva, Sergey V. Chizhikov. Detection of a local source of heat in the depths of the human body by volumetric radiothermography. *RENSIT: Radioelectronics. Nanosystems. Information Technologies,* 2020, 12(2):305-312. DOI: 10.17725/rensit.2020.12.305.
6. Ahmed M Hassan, Magda El-Shenawee. Review of Electromagnetic Techniques for Breast Cancer Detection. *IEEE Reviews in biomedical engineering,* 2011, 4:103-118. DOI: 10.1109/RBME.2011.2169780.
7. Vesnin S, Turnbull AK Dixon JM, Goryanin I. Modern Microwave Thermometry for Breast Cancer. *J. Mol. Imaging Dyn.,* 2017, 7(2):136-141. DOI: 10.4172/2155-9937.1000136.
8. Gudkov AG; Leushin VY, Sidorov IA, Vesnin SG, Porokhov IO, Sedankin MK, Agasieva SV, Chizhikov SV, Gorlacheva EN, Lazarenko MI et al. Use of Multichannel Microwave Radiometry for Functional Diagnostics of the Brain. *Biomed. Eng.*, 2019, 53:108-111.
9. Sedankin M, Chupina D, Vesnin S, Nelin I, Skuratov V. Development of a miniature

microwave radiothermograph for monitoring the internal brain temperature. *East. Eur. J. Enterp. Technol.,* 2018, 3:26-36.

10. Sidorov IA, Gudkov AG, Leushin VY, Gorlacheva EN, Novichikhin EP, Agasieva SV. Measurement and 3D Visualization of the Human Internal Heat Field by Means of Microwave Radiometry. *Sensors,* 2021, 21:4005, doi: 10.3390/s21124005.
11. Sidorov IA, Gudkov AG, Agasieva SV, Khokhlov NF, Chernikov AS, Vagapov Y. A portable microwave radiometer for proximal measurement of soil permittivity. *Computers and Electronics in Agriculture.* 2022, 198(2):107076. DOI: 10.1016/j.compag.2022.107076.
12. Fedoseeva EV, Shchukin GG, Rostokin IN, Rostokina EA. Compensation of interference in the operation of microwave radiometric systems. Radio engineering and telecommunication systems, 2014, 1(13):50-62.

DOI: 10.17725/rensit.2023.15.235

Extended orthogonal feedback precoding for spatial multiplexing systems

Mikhail G. Bakulin, Vitaly B. Kreyndelin
Moscow Technical University of Communications and Informatics, http://mtuci.ru/
Moscow 111024, Russian Federation
E-mail: m.g.bakulin@gmail.com, vitkrend@gmail.com
Andrey A. Reznev
Scientific-Technical Center "Atlas", http://www.stcnet.ru/
Moscow 127018, Russian Federation
E-mail: andrey.reznev@gmail.com
Received May 19, 2023, peer-reviewed May 26, 2023, accepted June 02, 2023

Abstract: **Various methods of generating of space-time codes and algebraic structures for increasing noise immunity of MIMO communication systems with a large number of transmitting and receiving antennas are considered. The possibility of generation of an orthogonal precoding matrix in MIMO systems depending on changing reception conditions in a radio channel using feedback from a transmitter to a receiver is shown. It is obtained that to transmit such a precoding matrix in MIMO systems with 4×4, 8×8, 16×16 antenna configurations, feedback is required with the ability to transmit only 2 bits on the reverse link at an energy gain of 1.5 dB... 2.5 dB compared to an open loop system. The precoding matrices obtained in the article and their formation algorithms can be used in the development of new MIMO mobile communication systems.**

Keywords: **MIMO, spatial multiplexing, algebraic codes, precoding, Golden code, maximum likelihood, ML, MMSE**

UDC 621.396

For citation: Mikhail G. Bakulin, Vitaly B. Kreyndelin, Andrey A. Reznev. Extended orthogonal feedback precoding for spatial multiplexing systems. *RENSIT: Radioelectronics. Nanosystems. Information Technologies,* 2023, 15(3):235-242e. DOI: 10.17725/rensit.2023.15.235.

Contents

1. INTRODUCTION

Shannon–Hartley theorem modification for the channel capacity defined that MIMO channel is more effective than SISO due to independent communication channels between transmitters and receivers [1]. The number of communication channels is $\min(N_{tx}, N_{rx})$ [1,2], where N_{tx} – is the number of transmitting antennas and N_{rx} – is the number of receiving antennas.

Diversity on both sides of the system and coherent signal processing are the special features of MIMO systems. Those features together with increasing of number of independent communication channels allows to improve noise immunity [1,3,4].

The fact that the number of independent communication channels for MIMO

systems is $N_{tx} \cdot N_{rx}$ but the real number of communication channels which used for one symbol transmission is N_{rx}. That is the reason why different symbols received with different quality [1,5].

Spatial multiplexing is used in MIMO systems when one symbol transmits via one antenna per one timeslot. Improving noise immunity of the system we may combine symbols in special space algebraic codes which are presented in matrix format [6,7]. One of these codes used for 2×2 MIMO systems is so called Golden code for two transmitting and two receiving antennas [8,9]. Golden code performance gain is 1.5-2 dB [8,10,11]. The breaking factor for widespread of algebraic codes for massive MIMO systems is high computational complexity of optimal demodulation [10,12]. For example, computational complexity of Maximum Likelihood demodulator in algebraic codes is growing in line with $2^{k_b N_{tx}^2}$, where k_b – is the number of bits per modulated symbol.

In those papers [13,14,15] offered extended orthogonal precoding method for MIMO systems with full diversity reception using special orthogonal matrices with dimensions $\left(N_{tx}^2 \times N_{tx}^2\right)$. The method demonstrates that resulted orthogonal matrices give us the minimum of maximum variance of *QAM* symbols for linear demodulation method [16].

The other way to impact on noise immunity of the system to get the information about the channel to have the chance of choosing the space time code. There is a popular way to have the control closed loop to transmit the information [1,17,18] within the system. The key factor for the efficiency of the method is precise information about the channel and the capacity of reverse closed loop [17,19,20].

This paper offers the combination of orthogonal precoding and channel state information for choosing appropriate precoding matrices. The necessary minimum value of reverse channel information is only few bits. As shown below for MIMO 8×8 it's only 3 bits are enough.

2. MIMO SYSTEM MODEL

MIMO spatial multiplexing system model describes the connections between the transmitter and receiver and might be expressed as [1,2]:

$$\mathbf{y}_n = \mathbf{H}\mathbf{x}_n + \boldsymbol{\eta}_n, \quad (1)$$

where $\mathbf{y}_n = \left[y_n^{(1)} \quad y_n^{(2)} \quad \cdots \quad y_n^{(N_{rx})} \right]^T$ – $(N_{rx} \times 1)$-dimensioned vector of received signal; $\mathbf{H}$ – $(N_{rx} \times N_{tx})$-dimensioned MIMO channel matrix which consist of scalar channel parameters (complex transmission coefficients) $h^{(i,j)}$ which are non-correlated zero mean Gaussian with the variances $E\left\{\left|h^{(i,j)}\right|^2\right\} = \frac{1}{N_{tx}}$, which means that the channel is independent Rayleigh fading channel; $\boldsymbol{\eta}_n$ – $(N_{rx} \times 1)$-dimensioned Gaussian noise vector with covariance matrix $\mathbf{R}_\eta = E\left\{\boldsymbol{\eta}_n \boldsymbol{\eta}_n^H\right\}$, which are mostly diagonal [1].

In such MIMO system where N_{tx} – is the number of transmitting antennas and N_{rx} – is the number of receiving antennas the input modulated symbols stream divided into number of $(N_{tx} \times 1)$-dimensioned vectors $\mathbf{x}_n = \left[x_n^{(1)} \quad x_n^{(2)} \quad \cdots \quad x_n^{(N_{tx})} \right]^T$, where every m-element of n-vector is $x_n^{(m)} = s_{(n-1)N_{tx}+m}$, $m = \overline{1, N_{tx}}$, $n = 1, 2, \ldots$ Every modulated symbol is zero mean $E\{s_i\} = 0$, and unit power $E\left\{|s_i|^2\right\} = 1$.

Let's take the same approach as it was in [13,14,15], when using the transmission of extended vector of modulated symbols $\tilde{\mathbf{x}} \triangleq \left[\mathbf{x}_1^T \quad \mathbf{x}_2^T \quad \cdots \quad \mathbf{x}_L^T \right]^T$, which is one structure of L – vectors and size of this vector is $(LN_{tx} \times 1)$. Extended channel model for this vector is

$$\tilde{\mathbf{y}} = \tilde{\mathbf{H}}\tilde{\mathbf{x}} + \tilde{\boldsymbol{\eta}}, \quad (2)$$

where

$$\tilde{\mathbf{y}} \triangleq \begin{bmatrix} \mathbf{y}_1^T & \mathbf{y}_2^T & \cdots & \mathbf{y}_L^T \end{bmatrix}^T,$$

$$\tilde{\boldsymbol{\eta}} \triangleq \begin{bmatrix} \boldsymbol{\eta}_1^T & \boldsymbol{\eta}_2^T & \cdots & \boldsymbol{\eta}_L^T \end{bmatrix}^T,$$

$$\tilde{\mathbf{H}} \triangleq \begin{bmatrix} \mathbf{H} & \mathbf{O} & \cdots & \mathbf{O} \\ \mathbf{O} & \mathbf{H} & \cdots & \mathbf{O} \\ \vdots & \vdots & \ddots & \vdots \\ \mathbf{O} & \mathbf{O} & \cdots & \mathbf{H} \end{bmatrix}$$

– is $(LN_{rx} \times LN_{tx})$-dimensioned block diagonal extended channel matrix.

Let's have new matrix $\tilde{\mathbf{F}}$, which is $(LN_{rx} \times LN_{tx})$-dimensioned and use it for precoding our extended vector $\tilde{\mathbf{x}}$. We may get new vector $\mathbf{z}$ which is $\mathbf{z} = \tilde{\mathbf{F}}\tilde{\mathbf{x}}$. New channel model has the form:

$$\tilde{\mathbf{y}} = \tilde{\mathbf{H}}\tilde{\mathbf{F}}\tilde{\mathbf{x}} + \tilde{\boldsymbol{\eta}}. \quad (3)$$

MMSE-based demodulated vector and covariance matrix for this vector are given below:

$$\tilde{\mathbf{x}} = \left(\tilde{\mathbf{F}}'\tilde{\mathbf{H}}'\tilde{\mathbf{H}}\tilde{\mathbf{F}} + \frac{1}{\rho}\mathbf{I}_{LN_{tx}} \right)^{-1} \tilde{\mathbf{F}}'\tilde{\mathbf{H}}'\tilde{\mathbf{y}}$$

$$\tilde{\mathbf{V}} = \left(\rho\tilde{\mathbf{F}}'\tilde{\mathbf{H}}'\tilde{\mathbf{H}}\tilde{\mathbf{F}} + \mathbf{I}_{LN_{tx}} \right)^{-1}. \quad (4)$$

Than we have

$$\tilde{\mathbf{x}} = \left(\tilde{\mathbf{F}}'\tilde{\mathbf{H}}'\tilde{\mathbf{H}}\tilde{\mathbf{F}} + \frac{1}{\rho}\mathbf{I}_{LN_{tx}} \right)^{-1} \tilde{\mathbf{F}}'\tilde{\mathbf{H}}'\tilde{\mathbf{y}} =$$

$$= \tilde{\mathbf{F}}' \left(\tilde{\mathbf{H}}'\tilde{\mathbf{H}} + \frac{1}{\rho}\mathbf{I}_{LN_{tx}} \right)^{-1} \tilde{\mathbf{H}}'\tilde{\mathbf{y}} = \tilde{\mathbf{F}}'\hat{\mathbf{z}}, \quad (5)$$

$$\tilde{\mathbf{V}} = \tilde{\mathbf{F}}' \left(\rho\tilde{\mathbf{H}}'\tilde{\mathbf{H}} + \mathbf{I}_{LN_{tx}} \right)^{-1} \tilde{\mathbf{F}} = \tilde{\mathbf{F}}'\tilde{\mathbf{V}}_z\tilde{\mathbf{F}},$$

where $\hat{\mathbf{z}} = \left(\tilde{\mathbf{H}}'\tilde{\mathbf{H}} + \frac{1}{\rho}\mathbf{I}_{LN_{tx}} \right)^{-1} \tilde{\mathbf{H}}'\tilde{\mathbf{y}}$ – is MMSE-based vector for $\mathbf{z}$, $\tilde{\mathbf{V}}_z = \left(\rho\tilde{\mathbf{H}}'\tilde{\mathbf{H}} + \mathbf{I}_{LN_{tx}} \right)^{-1}$ – covariance matrix for $\mathbf{z}$ vector.

In that transformation the resulted covariance matrix is block diagonal matrix, as given below:

$$\tilde{\mathbf{V}}_z = \begin{bmatrix} \mathbf{V}_{MMSE} & \mathbf{O} & \cdots & \mathbf{O} \\ \mathbf{O} & \mathbf{V}_{MMSE} & \cdots & \mathbf{O} \\ \vdots & \vdots & \ddots & \vdots \\ \mathbf{O} & \mathbf{O} & \cdots & \mathbf{V}_{MMSE} \end{bmatrix}, \quad (6)$$

$$\mathbf{V}_{MMSE} = \left(\rho\mathbf{H}'\mathbf{H} + \mathbf{I}_{N_{tx}} \right)^{-1}, \quad (7)$$

where $\mathbf{V}_{MMSE}$ is $(N_{rx} \times N_{tx})$-dimensioned MMSE-based covariance matrix for symbol vector in the system with simple spatial multiplexing, for channel model (1).

3. ORTHOGONAL PRECODING USING INCOMPLETE EXTENDED VECTOR

As we may see in [13], orthogonal precoding of transmitted symbols does not affect the trace of covariance matrix of estimation errors. It means that average values of SNR after linear demodulation have not been changed but in same time the probability distribution is changed, which means that noise immunity of the system is getting better due to the minimum of maximum variance criteria [16]. Next important point in [13] is that we may choose types of orthogonal matrices which give us the way to reduce the variety of minimum and maximum variance in covariance matrix and reduce the mean error probability. When we apply our extended vector with $L = N_{tx}$ size there are no variety between minimum and maximum variance and all variances are equal to the mean. The other side of the approach is negative because we must operate with large size vectors and matrices. It would be good to have the approach which operates with smaller vectors and matrices. For example, two vectors with $(N_{tx} \times 1)$ size give us one extended vector with $(2N_{tx} \times 1)$ size and orthogonal precoding matrix will be $(2N_{tx} \times 2N_{tx})$ size.

Let's take system with N_{tx} and $L = 2$, choose the precoding matrix as following:

$$\tilde{\mathbf{F}} = \frac{1}{\sqrt{2}}\begin{bmatrix} \mathbf{I}_4 & e^{-j\varphi}\mathbf{P}_4' \\ -e^{j\varphi}\mathbf{P}_4 & \mathbf{I}_4 \end{bmatrix}, \quad (8)$$

where φ – is rotation angle for symbol constellation; $\mathbf{P}_4$ – is (4×4)-dimension permutation matrix where every element is 0 except one which is equal to 1 and it means that $\tilde{\mathbf{F}}$ is orthogonal matrix.

For the maximum diversity gain, we should have 0 at main diagonal for matrix $\mathbf{P}_4$. This is the situation when every symbol transmits via two different antennas.

Considering new covariance matrix of estimation errors according to (5) - (7)

$$\tilde{\mathbf{V}} = \tilde{\mathbf{F}}'\tilde{\mathbf{V}}_z\tilde{\mathbf{F}} = \\ = \frac{1}{2}\begin{bmatrix} \mathbf{V}_{MMSE} + \mathbf{P}_4'\mathbf{V}_{MMSE}\mathbf{P}_4 & \ddots \\ \ddots & \mathbf{V}_{MMSE} + \mathbf{P}_4'\mathbf{V}_{MMSE}\mathbf{P}_4 \end{bmatrix}. \quad (9)$$

Since we are interested in variances of error of estimation only which are located at main diagonal and then we do not have any concerns about the rest of block matrices inside. Having our permutation matrix $\mathbf{P}_4$ we may get new vector of diagonal elements of matrix $\tilde{\mathbf{V}}$:

$$\tilde{\mathbf{v}} \triangleq \mathrm{diag}\left(\tilde{\mathbf{V}}\right) = \frac{1}{2}\begin{bmatrix} \mathbf{v}_{MMSE} + \mathbf{P}_4\mathbf{v}_{MMSE} \\ \mathbf{v}_{MMSE} + \mathbf{P}_4\mathbf{v}_{MMSE} \end{bmatrix}, \quad (10)$$

where diag(**A**) is the operator which creates vector from diagonal elements of **A** matrix, $\mathbf{v}_{MMSE} \triangleq \mathrm{diag}\left(\mathbf{V}_{MMSE}\right)$ – N_{tx}-dimensioned vector of diagonal elements of MMSE-based covariance matrix.

Considering the example of following permutation matrix:

$$\mathbf{P}_4^{(1)} = \begin{bmatrix} 0 & 0 & 0 & 1 \\ 0 & 0 & 1 & 0 \\ 0 & 1 & 0 & 0 \\ 1 & 0 & 0 & 0 \end{bmatrix}. \quad (11)$$

In that case for the first half of diagonal vector $\tilde{v}$ we can write the following expressions:

$$\begin{aligned} \tilde{v}_1 &= \frac{1}{2}\left(v_{MMSE,1} + v_{MMSE,4}\right) \\ \tilde{v}_2 &= \frac{1}{2}\left(v_{MMSE,2} + v_{MMSE,3}\right) \\ \tilde{v}_3 &= \frac{1}{2}\left(v_{MMSE,3} + v_{MMSE,2}\right) \\ \tilde{v}_4 &= \frac{1}{2}\left(v_{MMSE,4} + v_{MMSE,1}\right). \end{aligned} \quad (12)$$

The second half of diagonal vector $\tilde{v}$ is the same as the first one.

As the result of orthogonal precoding (12) there are vector with two variances instead of four different variances for MMSE-based algorithm and maximum of those new variances guaranteed less than original ones. We should note that chosen permutation matrix does not realize that maximum of new variances would be minimal because there no all combinations located at main diagonal.

We may choose other permutation matrices with different locations of "1", for example:

$$\mathbf{P}_4^{(2)} = \begin{bmatrix} 0 & 0 & 1 & 0 \\ 0 & 0 & 0 & 1 \\ 1 & 0 & 0 & 0 \\ 0 & 1 & 0 & 0 \end{bmatrix}, \mathbf{P}_4^{(3)} = \begin{bmatrix} 0 & 1 & 0 & 0 \\ 1 & 0 & 0 & 0 \\ 0 & 0 & 0 & 1 \\ 0 & 0 & 1 & 0 \end{bmatrix}. \quad (13)$$

For these matrices, we obtain the following variance values of estimation errors using orthogonal precoding:

$$\begin{aligned} \tilde{v}_1^{(2)} &= \frac{1}{2}\left(v_{MMSE,1} + v_{MMSE,3}\right) & \tilde{v}_1^{(3)} &= \frac{1}{2}\left(v_{MMSE,1} + v_{MMSE,2}\right) \\ \tilde{v}_2^{(2)} &= \frac{1}{2}\left(v_{MMSE,2} + v_{MMSE,4}\right) & \tilde{v}_2^{(3)} &= \frac{1}{2}\left(v_{MMSE,2} + v_{MMSE,1}\right) \\ \tilde{v}_3^{(2)} &= \frac{1}{2}\left(v_{MMSE,3} + v_{MMSE,1}\right) & \tilde{v}_3^{(3)} &= \frac{1}{2}\left(v_{MMSE,3} + v_{MMSE,4}\right) \\ \tilde{v}_4^{(2)} &= \frac{1}{2}\left(v_{MMSE,4} + v_{MMSE,2}\right) & \tilde{v}_4^{(3)} &= \frac{1}{2}\left(v_{MMSE,4} + v_{MMSE,3}\right). \end{aligned} \quad (14)$$

Using three variants of permutation matrices $\mathbf{P}_4^{(1)}, \mathbf{P}_4^{(2)}, \mathbf{P}_4^{(3)}$ we may search the whole set of combinations for diagonal

vector. We may transmit the information selecting the right combination for transmission with minimum of maximum variance. For our system with $N_{tx} = 4$ it is only 2 bits needed in the feedback loop to transmit the information about the view of precoding matrix.

Large scale configurations for MIMO systems may use the same approach (see (11), (13)) and the number of those matrices to search the whole set of combinations is $(N_{tx} - 1)$ when $N_{tx}=2^m$. The number of bits is needed to transmit the information is m.

Those kinds of systems when we may select the precoding matrix and transmit that information via reverse link, are the systems with the control closed loop.

4. SIMULATION RESULTS

The section offers simulation results for proposed orthogonal precoding algorithm with matrix selection for various MIMO configurations. The simulation has been done with following conditions:

- MIMO channel with independent Rayleigh fading;
- QPSK modulation;
- MMSE-based demodulation.

In **Fig. 1** we show bit-error rates (BER) for 4×4nMIMO configuration for the following modes:

- SMx – is ordinary spatial multiplexing;
- SMx + OrtPr – is spatial multiplexing for two time slots;
- SMx + CL-OrtPr – is spatial multiplexing with proposed orthogonal precoding for time slots and close loop (Close Loop Orthogonal Precoding).

We may see that the orthogonal precoding with close loop increases noise immunity in 2-3 dB for BER range 0.01-0.001 with comparison to ordinary spatial multiplexing system. Compared to a MIMO system using orthogonal open-loop (uncontrolled) precoding, the proposed method provides a gain of ~ 1 dB.

For the configuration MIMO 8×8 see **Fig. 2**, the gain compared to conventional multiplexing is 1.6-4.1 dB, and compared to orthogonal open-loop precoding, the gain is 0.5-1.5 dB.

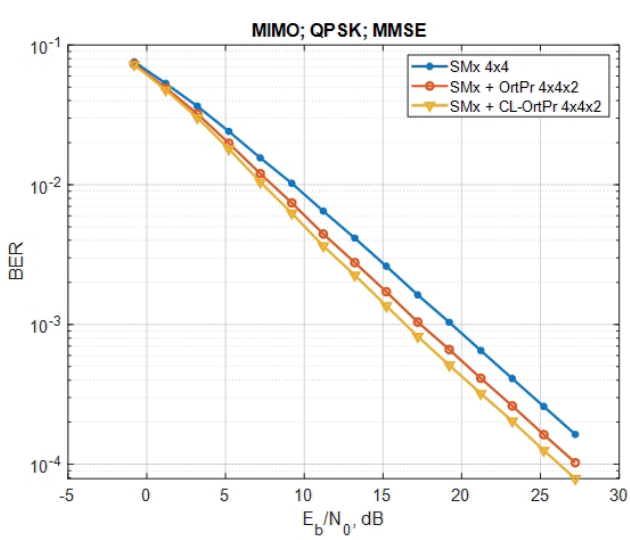

Fig. 1. *BER vs. SNR per bit for proposed system with orthogonal precoding and orthogonal precoding with closed loop for 4×4 MIMO system.*

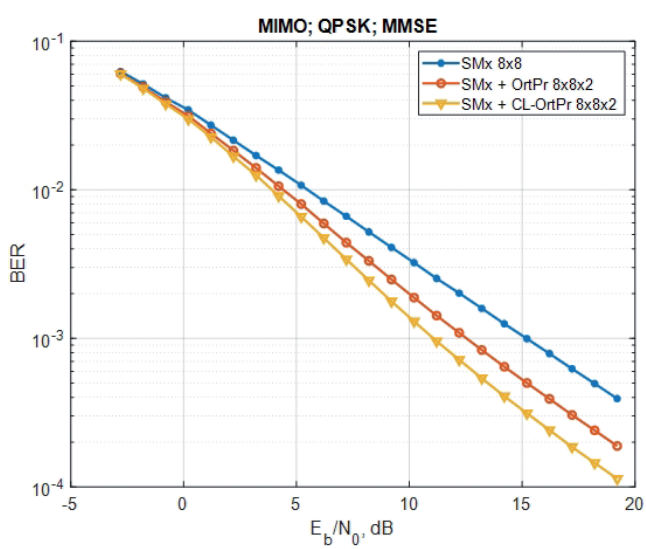

Fig. 2. *BER vs. SNR per bit for proposed system with orthogonal precoding and orthogonal precoding with closed loop for 8×8 MIMO system.*

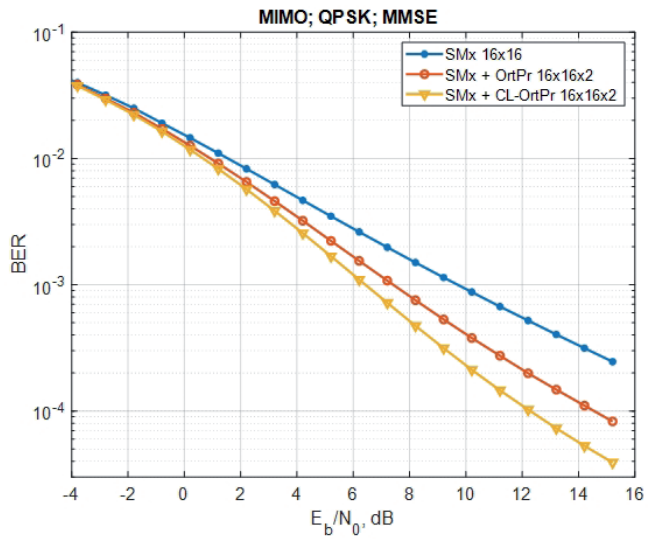

Fig. 3. *BER vs. SNR per bit for proposed system with orthogonal precoding and orthogonal precoding with closed loop for 16×16 MIMO system.*

Fig. 3 shows performance curves for is 16×16 MIMO configuration. Here, there are gains of 0.9-3.3 dB and 0.3-1.0 dB compared to systems with conventional spatial multiplexing and an orthogonal precoding system without control, respectively.

Note that for all configurations, the gain increases as the signal-to-noise ratio increases.

5. CONCLUSION

The orthogonal precoding method, which uses a closed reverse channel control loop to select a precoding matrix, improves the performance of a multi-antenna MIMO communication system by increasing the diversity order. Our precoding algorithm based on minimum of maximum variances optimal criteria which operate with elements of main diagonal of covariance matrix for MMSE-based demodulation algorithm.

Close loop utilizes for transmission the information about precoding matrices demonstrating the better diversity effect using part of extended vector with modulated symbols. The volume of the information needed for 4×4 MIMO system is only 2 bits. The combination of orthogonal precoding for strong sparse matrices and using only part of extended vector with modulated symbols do not increase computational complexity at transmitting and receiving sides of MIMO systems.

The simulation results for orthogonal precoding with close loop provide us with 1-4 dB gain which depends on dimensions of MIMO system and required BER interval.

As the signal-to-noise ratio increases, the gain from using the proposed orthogonal precoding method with a closed control loop increases.

REFERENCES

1. Bakulin MG, Varukina LA, Kreindelin VB. *MIMO technology: principles and algorithms*. Moscow, Hotline-Telecom Publ., 2014, 244 p.
2. Sibille A, Oestges C, Zanella A. *MIMO From Theory to Implementation*, 2011, Elsevier, USA, p. 350.
3. Durgarao T, Naga Lakshmi TJ. Wireless-Powered Relaying Communication based on MIMO-OFDM: A Comprehensive Survey. *5th Intern. Conf. on Smart Systems and Inventive Technology (ICSSIT)*, Tirunelveli, India, 2023, pp. 1-8, doi: 10.1109/ICSSIT55814.2023.10060888.
4. Hori Y, Nakajima A, Higashinaka M, Aruga H. A New Transmit Diversity Technique for FSK Exploiting its Orthogonality. *IEEE Communications Letters*, 2021, 25(9):3094-3098, doi: 10.1109/LCOMM.2021.3089709.
5. Pankratov DY, Stepanova AG. Nonlinear Iterative Chebyshev Based Demodulation Algorithm With Eigenvalues Estimates Of The Channel Matrix For Massive MIMO Systems. *Systems of Signal Synchronization, Generating*

and Processing in Telecommunications (SYNCHROINFO), Russia, Svetlogorsk, 2020, pp. 1-5, doi: 10.1109/SYNCHROINFO49631.2020.9166003.

6. Dayal P, Varanasi MK. Algebraic space-time codes with full diversity and low peak-to-mean power ratio. *IEEE Global Telecommunications Conference* (IEEE Cat. No. 03CH37489), 2003, 4:1946-1951, doi: 10.1109/GLOCOM.2003.1258577.
7. Damen MO, Abed-Meraim K, Belfiore J. Diagonal algebraic space-time block codes. *IEEE Transactions on Information Theory*, 2002, 48(3):628-636, doi: 10.1109/18.985979.
8. Belfiore J, Rekaya G, Viterbo E. The golden code: a 2×2 full-rate space-time code with non-vanishing determinants. *Proc. International Symposium on Information Theory,* 2004, pp. 310-310, doi: 10.1109/ISIT.2004.1365347.
9. Viterbo E, HongY. Applications of the Golden Code. *Information Theory and Applications Workshop*, USA, CA, La Jolla, 2007, pp. 393-400, doi: 10.1109/ITA.2007.4357609.
10. Xu H, Pillay N. An Alternative Encoding of the Golden Code and its Low Complexity Detection. *IEEE Access*, 2022, 10:30147-30156, doi: 10.1109/ACCESS.2022.3159682.
11. Lee SJ et al. A Space–Time Code with full Diversity and Rate 2 for 2 Transmit Antenna Transmission. *IEEE C* 802.16e – 04/434r2. WWW.IEEE802.ORG/16.
12. Imamura T, Sanada Y. Low Complexity Belief Propagation based MIMO Detection with MMSE Pre-cancellation for Overloaded MIMO systems. *IEEE 92nd Vehicular Technology Conference (VTC2020-Fall)*, Canada, Victoria, BC, 2020, pp. 1-5, doi: 10.1109/VTC2020-Fall49728.2020.9348702.
13. Bakulin MG, Kreindelin VB, Reznev AA. Orthogonal Precoding for Systems with Spatial Multiplexing with a Linear Receiver. *Journal of Communications Technology and Electronics,* 2021, 66(12):1346-1353. DOI 10.1134/S1064226921120020.
14. Kreyndelin VB, Bakulin MG, Reznev AA. Improved Space Time Codes through Orthogonal Transformation. *Systems of Signals Generating and Processing in the Field of on Board Communications,* 2022, pp. 1-5, doi: 10.1109/IEEECONF53456.2022.9744302.
15. Deng T, Zhang L, Feng Y, Jiang Y. A Double Full Diversity Unitary Space Time Precoded V2V MIMO Communication System. *IEEE/CIC International Conference on Communications in China (ICCC)*, China, Sanshui, Foshan, 2022, pp. 99-104, doi: 10.1109/ICCC55456.2022.9880809.
16. Reznev AA, Kreindelin VB. New optimality criterion for space-time matrices. *Elektrosvyaz'*, 2020, 2:59-62 (in Russ.).
17. Zia MU, Xiang W, Vitetta GM, Huang T. Deep Learning for Parametric Channel Estimation in Massive MIMO Systems. *IEEE Transactions on Vehicular Technology*, doi: 10.1109/TVT.2022.3223896.
18. Jianchi Zhu, Jingxiu Liu, Xiaoming She and Lan Chen. Investigation on precoding techniques in E-UTRA and proposed adaptive precoding scheme for MIMO systems. *14th Asia-Pacific Conference on Communications*, Japan, Akihabara, 2008, pp. 1-5.
19. Prata A, Sveshtarov J, Pires SC, Oliveira ASR, Carvalho NB. Optimized DPD Feedback Loop for m-MIMO sub-6GHz Systems. *IEEE/MTT-S*

International Microwave Symposium, USA, PA, Philadelphia, 2018, pp. 485-488, doi: 10.1109/MWSYM.2018.8439268.

20. Krishnamoorthya A, Schober R. Downlink Massive MU-MIMO With Successively-Regularized Zero Forcing Precoding. *IEEE Wireless Communications Letters,* 2023, 12(1):114-118, doi: 10.1109/LWC.2022.3218597.

DOI: 10.17725/rensit.2023.15.243

3D image formation of the earth surface relief in the aperture synthesis mode when rotating the receiving antenna phase center and the transceiver module diversion

Boris G. Tatarsky, Nazhzhar Tammam
Moscow Aviation Institute, http://www.mai.ru/
Moscow 125993, Russian Federation
E-mail: boris-tatarsky@inbox.ru, tnajjar23551@gmail.com

Andrey I. Panas
Shokin Research and Production Center "Istok", http://www. istokmw.ru/
Fryazino 141190, Moscow region, Russian Federation
E-mail: aipanas@istokmw.ru

Received June 05, 2023, peer-reviewed June 12, 2023, accepted June 19, 2023

Abstract: **The features of 3D radar image formation during the synthesis of an artificial aperture due to rotation of the phase center of the receiving antenna and stationary diversed transceiver module have been considered during the interferometric interpretation of incoming data. The main mathematical relations, associated with determination of the relief height are given, the algorithm for processing the trajectory signal based on the interferometric approach, as well as the results of evaluating the efficiency of the proposed algorithm, obtained by computer simulation, are presented.**

Keywords: **radar system, antenna aperture synthesis, antenna phase center, interferometer base, interferometric processing, radar image, point target, antenna phase center rotation, transceiving module, receiving module, distributed radar system**

UDC 621.396.9

For citation: Boris G. Tatarsky, Andrey I. Panas, Nazhzhar Tammam. 3D image formation of the earth surface relief in the aperture synthesis mode when rotating the receiving antenna phase center and the transceiver module diversion. *RENSIT: Radioelectronics. Nanosystems. Information Technologies,* 2023, 15(3):243-252e. DOI: 10.17725/rensit.2023.15.243.

Contents

1. INTRODUCTION

The development of theoretical foundations and technical capabilities for the creation of synthetic aperture radar systems (SAR) makes it possible to receive radar images (RI) of observed objects with a resolution of the order of meters or less [1-4]. At the same time when solving a number of practical problems airborne radars require great information capabilities, which can only be provided by obtaining 3D RIs. In particular, obtaining 3D RIs of the observed surface makes it possible to reduce errors in determining coordinates of the observed ground objects due to their

height, and consequently, to increase the accuracy of determining the location of the radar carrier relative to ground radar-contrast landmarks when using image data. Besides, the formation of 3D RIs allows to obtain information about the relief of the observed area in any weather conditions and time of day, which allows the radar carrier to solve the problems of following the terrain in the conditions of poor optical visibility. The issues of the formation of 3D RIs were previously considered in the scientific and technical literature [5-6]. So, the formation of 3D RIs during the translational movement of the carrier (the antenna phase center (APC) of the radar) is considered in [5], and a possibility of forming 3D RIs during the rotation of the APC of the radar transceiving module is shown in [6].

The purpose of the article is to consider the features of forming 3D RIs in a distributed radar system, consisting of a receiving module (Rx), the antenna phase center of which rotates around a circle, and a stationary receiving-transmitting (Rx-Tx) module.

2. PROBLEM STATEMENT

Let us assume that there is a distributed radar in which the phase centers of the Rx and Rx-Tx modules are separated in space. The antenna phase center of Rx-Tx radar module is located in point A (**Fig. 1**) and it has the following coordinates: $x_{pc} = 0$, $y_{pc} = 0$, $z_{pc} = H$. But the APC of the receiving module is located in point B, it rotates strictly around the circle with a radius r with a constant angular velocity ω_{rot} in a plane (M, X', Y') relative to the center of rotation (p. M). The plane of rotation (M, X', Y') is parallel to the horizontal plane (O, X, Y). As a result the APC coordinates of the Rx module can be represented as

$$x_{rrm}(t) = r\cos(\omega_r t + \varphi_0), \quad (1)$$

$$y_{rrm}(t) = r\sin(\omega_r t + \varphi_0), \quad (2)$$

$$z_{rrm} = H + d, \quad (3)$$

where φ_0 – the initial phase of APC rotation of the receiving antenna, $\Omega_r(t) = \omega_r t + \varphi_0$ – a current angle of APC rotation relative to axis X', d – a distance between the APC of the receiving-transmitting module and the center of the APC rotation of the receiving module in the vertical plane of the module (Fig. 1).

The study of the probing signal is carried out by the Tx module (p. A) and the reception is carried out by both Rx-Tx module (p. A) and Rx module (p. B). The processing of the trajectory signal is carried out jointly in p. A and B, realizing an interferometric processing system. Under these conditions the interferometer base $\|\overrightarrow{AB}\|$, which we denote as I, does not change with the angle change $\Omega_r(t)$ and can be presented as

$$I(t) = \sqrt{\left(x_{pc}(t) - x_{rrm}(t)\right)^2 + \left(y_{pc}(t) - y_{rrm}(t)\right) + d^2}, \quad (4)$$

$$I = \sqrt{\left(r\cos\left(\Omega_r(t)\right)\right)^2 + \left(r\sin\left(\Omega_r(t)\right)\right)^2 + d^2} = \sqrt{r^2 + d^2}. \quad (5)$$

It is known [6], that with interferometric processing of signals in the process of aperture synthesis due to APC rotation, it is possible to form 3D RIs. Based on the described situation we will consider the process of forming 3D RIs during the rotation of APC of the receiving module and separated in space but stationary located APC of the Rx-Tx module. First, let's consider the basic mathematical relationships that determine the possibility of indicating the height of the observed object using the example of a point target (Fig. 1).

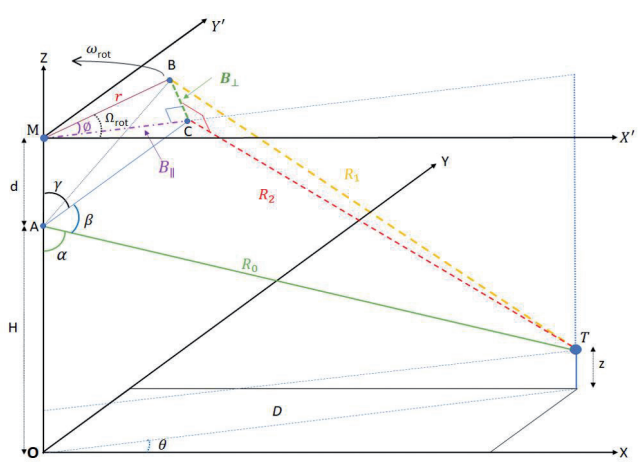

Fig. 1. *The geometry of location of the APC and the target in 3D space.*

3. DETERMINING THE OBJECT HEIGHT BY RADAR OBSERVATION

The registration will be done relative to the point where APC of Rx-Tx module is located (p. A). Then the height of the target Z_t can be presented as

$$Z_t = H - R_0 cos(\alpha), \quad (6)$$

where H – the distance between the horizontal plane OXY and the point of APC of Rx-Tx module location (height); R_0 – distance from APC of Rx-Tx module to the point target (point T); α – antenna look angle.

Consider the MOT plane in Fig. 1, which includes the OZ axis and the target location point (p. T). Taking into account this consideration, the expression (6) can be written as

$$Z_t = H + R_0 cos(\beta + \gamma), \quad (7)$$

where β – the angle between R_0 and vector $\overrightarrow{AC}$, which determines the point of APC of Rx module location relative to R_0 direction, and γ – the angle between $\overrightarrow{AC}$ vector and OZ axis. In the general case, p. C determines the position of APC Rx module projection on the MOT plane. Both angles $\beta(t)$, $\gamma(t)$ are functions of time, since the APC location of Rx module changes in time and accordingly its projection on the (MOT) plane changes. But at the same time, the sum of these angles does not depend on time and, accordingly, angle α – antenna look angle – does not change when observing a single point target (PT).

To define the PT height Z_t, it is necessary to know the following information: the value of the signal phase at the output of interferometer $\psi_z(t)$, formed by Rx-Tx and Rx modules; the slant distance to the target R_0; the radius rotation value r of APC Rx module; distance d between the APC of Rx-Tx module and antenna rotation plane of Rx module; the antenna look angle θ in the azimuth plane; the angular position Ω of the APC Rx relative to the X axis.

Based on geometry in Fig. 1, the phase $\psi_z(t)$ of the signal at the output of interferometer can be presented as:

$$\psi_z(t) = \frac{2\pi}{\lambda}\left(R_1(t) - R_0\right), \quad (8)$$

where $R_1(t)$ – distance from the APC of Rx module to PT, λ – probing oscillation wavelength, R_0 – distance from PT to APC of Rx-Tx antenna.

Basing on ΔTAC (see Fig. 1), one can write down:

$$\left(R_2(t)\right)^2 = R_0^2 + \left(\|AC\|(t)\right)^2 - 2R_0\|AC\|(t)cos\left(\beta(t)\right). \quad (9)$$

From equation (9), it follows that angle β can be presented as

$$\beta(t) = arccos\left(\frac{R_0^2 + \|AC\|^2 - R_2(t)^2}{2R_0\|AC\|(t)}\right). \quad (10)$$

Then from the right triangle ΔBCT, we get the following:

$$R_2(t)^2 = R_1(t)^2 - B_\perp(t)^2 = \left(\frac{\lambda\psi_z(t)}{2\pi} + R_0\right)^2 - B_\perp(t)^2, \quad (11)$$

where $B_\perp = \left\|\overrightarrow{CB}\right\|$ – distance from the APC of Rx module to MOT' plane. As $\|AC\|^2 = d^2 + B_\|^2$, $I^2 = B_\perp(t)^2 + \|AC\|(t)^2$, we can write:

$$\beta(t) = arccos\left(\frac{I^2 - \left(\left(\frac{\lambda\psi_z(t)}{2\pi}\right)^2 + \frac{\lambda\psi_z(t)}{\pi}R_0\right)}{2R_0\sqrt{d^2 + B_\|(t)^2}}\right), \quad (12)$$

where $B_\| = \left\|\overrightarrow{MC}\right\|$ – projection of APC of Rx module location point on MOT plane equal to:

$$B_\|(t) = r\cos(\phi(t)), \quad (13)$$

$\phi(t)$ – angle between the directions $\overrightarrow{MB}$ and $\overrightarrow{MC}$, which can be presented as:

$$\phi(t) = \omega_r t - \theta. \quad (14)$$

Then, taking into account expressions (14) and (13), we can write

$$B_\| = r\cos(\omega_r t - \theta). \quad (15)$$

From expression (15) it follows that the value of angle β can be defined as

$$\beta(t) = arccos\left(\frac{I^2 - \left(\left(\frac{\lambda\psi_z(t)}{2\pi}\right)^2 + \frac{\lambda\psi_z(t)}{\pi}R_0\right)}{2R_0\sqrt{d^2 + \left(r\cos\left(\omega_r t - \theta\right)\right)^2}}\right). \quad (16)$$

In its turn it follows from Fig. 1 (see ΔMAC) that angle γ is equal to the following

$$\gamma(t) = arctan\left(\frac{B_{\parallel}(t)}{d}\right) = arctan\left(\frac{r\cos(\omega_r t - \theta)}{d}\right). \quad (17)$$

Basing on (16) and (17), the expression (7), determining the point target height Z_t, can be presented as:

$$Z_t = H + R_0 \cos\left(arccos\left(\frac{I^2 - \left(\left(\frac{\lambda\psi_z(t)}{2\pi}\right)^2 + \frac{\lambda\psi_z(t)}{\pi}R_0\right)}{2R_0\sqrt{d^2 + \left(r\cos(\omega_r t - \theta)\right)^2}}\right) + arctan\left(\frac{r\cos(\omega_r t - \theta)}{d}\right)\right). \quad (18)$$

The expression (18) makes it possible to determine the PT height at its various positions, defined by angle θ.

Fig. 2 shows the results of simulating the nature of the change in angles α, β and γ. The simulation was conducted under the following conditions: d = 3 m, r = 8 m, λ = 3 cm, D = 10 km, H = 500 m, $\omega_r = 10\pi$ rad/s, $\varphi_0 = 0$, Z_t = 10 m, $\theta = 0°$ (Fig. 2*a*); $\theta = 45°$(Fig. 2*b*).

The presented results show that angles β and γ change with time when the PC of a real Rx antenna rotates. At the same time the antenna look angle of the point target α, equal to $[\pi - (\beta + \gamma)]$, remains unchanged in time. The results also show, that the nature of the change in angles β, γ does not depend on the location of a PT and d, r, z, H and R_0 parameters.

4. CONDITIONS FOR UNAMBIGUOUS DETERMINATION OF THE OBSERVATION OBJECT HEIGHT

When using interferometric processing to determine the height of the relief an ambiguity problem arises, which is due to the fact that the phase of the output signal of the phase detector, which compares the phases of the received signals, varies in the range from $-\pi$ to π: $\psi(t) \in [-\pi, \pi]$. This fact must be taken into account when determining the target height, basing on the phase change of the interferometer output signal.

Let us determine the conditions under which the unambiguous measurements of the PT height will be ensured. To do this, let's consider how the phase $\psi(t)$ changes at the maximum given value of the height $\psi_h(t)$ and at the height corresponding to the zero level $\psi_0(t)$, and find their difference.

$$\psi_h(t) - \psi_0(t) = \frac{2\pi}{\lambda}\left(\Delta R_h(t) - \Delta R_0(t)\right), \quad (19)$$

where $\Delta R_0(t) = R_{1,0} - R_{2,0}(t)$; $\Delta R_h(t) = R_{1,h_{uniq}} - R_{2,h_{uniq}}(t)$; $R_{1,0}$ – the distance from the PC of the receiving-transmitting antenna to PT_0; PT_0 is a point target, the height of which is considered to be zero;

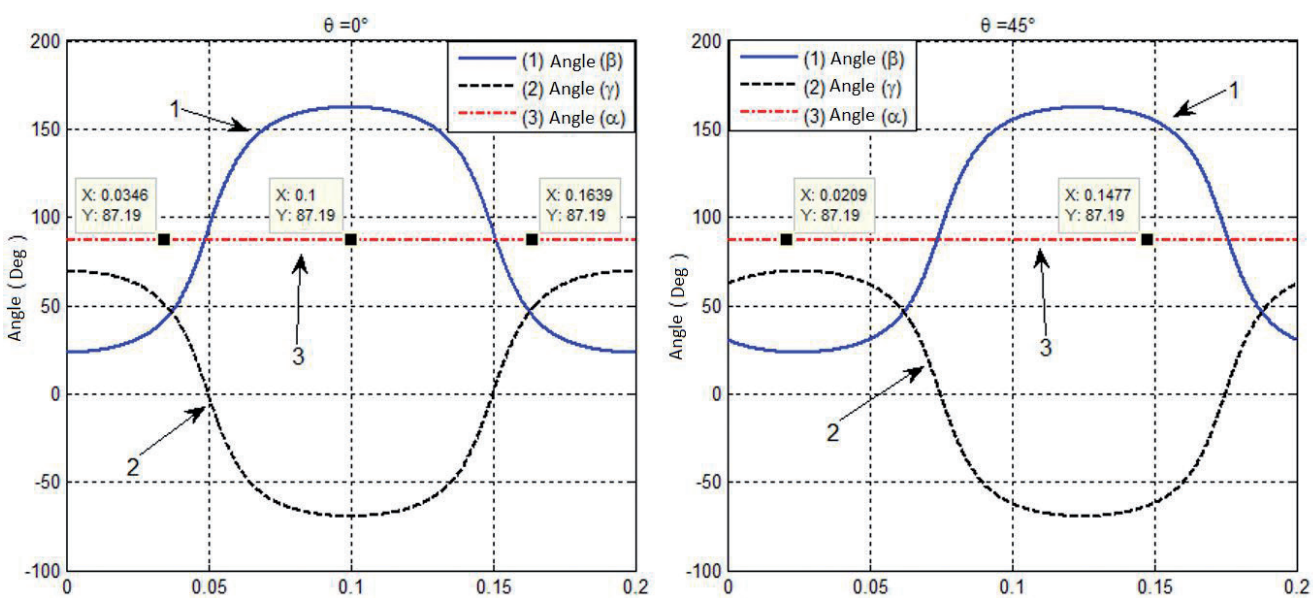

Fig. 2. *The nature of the change in angles β (curve 1), γ (curve 2) and a (curve 3) when rotating APC Rx module.*

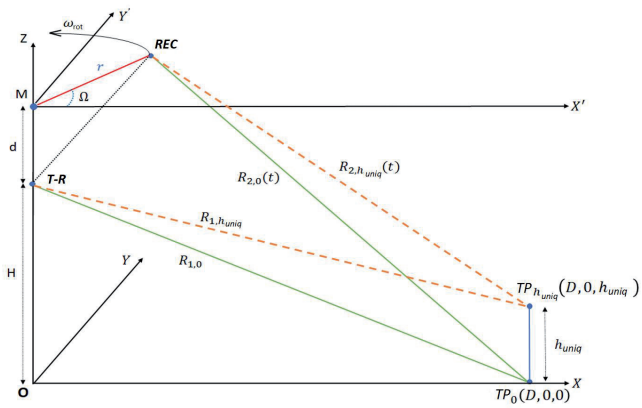

Fig. 3. *Geometric positions of APC and PT with zero height and the height corresponding to the maximum value within the unambiguous measurement.*

$R_{2,0}$ – the distance from the PC of the receiving antenna to PT_0; $R_{1,h_{uniq}}$ – the distance from the PC of the receiving-transmitting antenna to $PT_{h_{uniq}}$, $PT_{h_{uniq}}$ – a point target, the height of which is set within the range of unambiguous measurement; $R_{2,h_{uniq}}$ – the distance from the PC of the receiving antenna to $PC_{h_{unit}}$ (see **Fig. 3**). The expression (19) can be rewritten as follows

$$\Delta\psi_h(t)-\Delta\psi_0(t)= \\ =\frac{2\pi}{\lambda}\left[\left(R_{1,h_{uniq}}-R_{1,0}\right)+\left(R_{2,0}(t)-R_{2,h_{uniq}}(t)\right)\right]. \quad (20)$$

Taking into account the expansion $\sqrt{1+x}=1+\frac{1}{2}x-\frac{1}{8}x^2...$ and the fact that $H, d, r << D$; $\varphi_0 = 0°$, and $R_{1,0}=\sqrt{D^2+H^2}$, we get

$$R_{1,h_{uniq}}-R_{1,0}\cong\frac{h_{uniq}^2}{2R_{1,0}}-\frac{Hh_{uniq}}{R_{1,0}}-\frac{(h_{uniq}^2-2Hh_{uniq})^2}{8R_{1.0}^3}, \quad (21)$$

$$R_{2,0}(t)-R_{2,h_{uniq}}(t)\cong\frac{h_{uniq}^2-2(H+d)h_{uniq}}{2R_{1.0}}- \\ -\frac{r\cos(\omega_r t)[h_{uniq}^2-2(H+d)h_{uniq}]\sqrt{R_{1,0}^2-H^2}}{2R_{1,0}^3}. \quad (22)$$

At the same time taking into account that $h_{uniq}^4 \ll 8R_{1,0}^3$, and relying on (20)-(22), the expression (19) can be represented as

$$\psi_h(t)-\psi_0(t)= \\ =\frac{2\pi}{\lambda}\left[\frac{dh_{uniq}}{R_{1,0}}+\frac{(H+d)\left(\sqrt{R_{1,0}^2-H^2}\right)r\cos(\omega_r t)h_{uniq}}{R_{1,0}^3}\right]. \quad (23)$$

To ensure unambiguous height measurement the phase difference of the output signal of the interferometric processing system must satisfy the condition $[\psi_h(t) - \psi_0(t) \le \pi]$. When solving (23) we obtain the measured value of the unambiguous height of the observed target. It follows from the expression (23) that the unambiguous measured height is related to the rotation of the PC of the receiving antenna. In this case the unambiguous height depends on variables λ, r, H, d, ω_r and $R_{1,0}$ as follows

$$h_{uniq}(t)\cong\frac{\lambda R_{1,0}^3}{2\left[dR_{1,0}^2+r(H+d)\cos(\omega_r t)\sqrt{R_{1,0}^2-H^2}\right]}. \quad (24)$$

The nature of the change $h_{uniq}(t)$ when varying variables d, r, H is shown in **Fig. 4-6**.

From the results, presented in Fig. 4-6 one can see that the unambiguous measured height changes according to the periodic law. Moreover, the interferometer base, i.e., the vertical distance

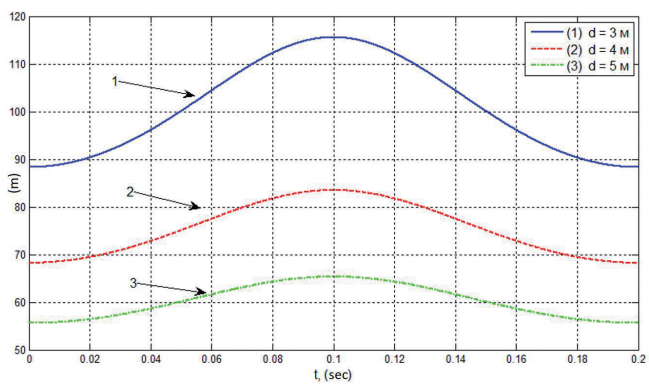

Fig. 4. *The change in the unambiguously measured height in the process of rotation at H = 500 m, r = 8 m, D = 10 km and varying the vertical distance between the PCs of the real antennas: d = 3, 4, 5 m.*

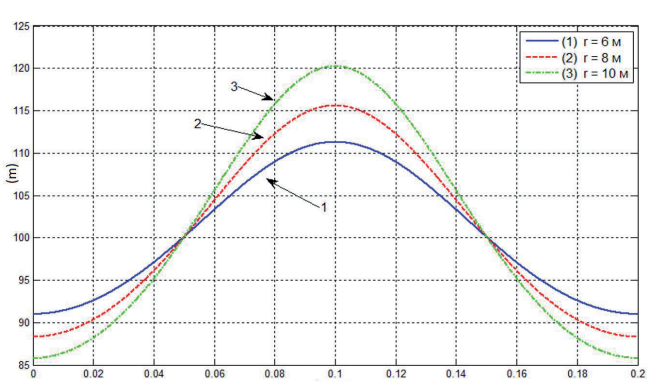

Fig. 5. *The change in the unambiguously measured height in the process of rotation at H = 500 m, d = 3 m, D = 10 km and varying the PC rotation radius value of the receiving antenna.*

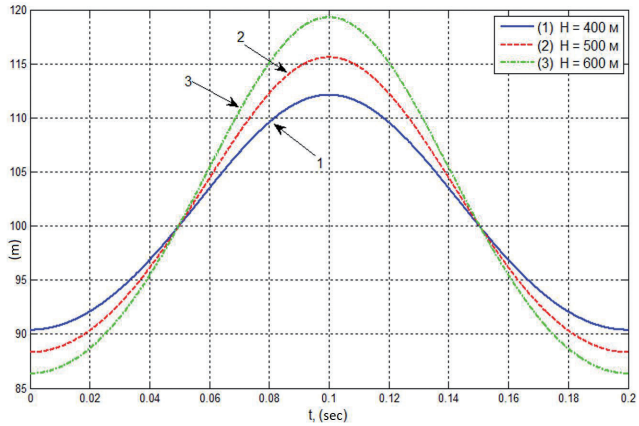

Fig. 6. *The change in the unambiguously measured height in the process of rotation at d = 3 m, r = 8 m, D = 10 km and variation of the radar carrier height: H = 400, 500, 600 m.*

between the PCs of real Rx and Rx-Tx antennas has the greatest influence on the result of height evaluation. In this case the maximum value of $h_{uniq}(t)$ is reached at $t = 0.5\ T$, where T – is the time corresponding to one rotation turn of the APC of Rx module, at which the angle between the direction to the PT and the position of the receiving antenna is π rad. In this situation the distance from the PT to the PC of the Rx antenna will be the maximum possible and, accordingly, the difference $[\psi_h(t) - \psi_0(t)]$ – the minimum.

One can also see from **Fig. 5** and **6**, that the maximum value of $h_{uniq}(t)$ is reached at $t = 0.5\ T$, when $\omega_r t = \pi$. At the values of $\omega_r t = \pi/2$ и $\omega_r t = 3\pi/2$ (i.e., when the angle between the PT and Rx antenna is $\pi/2$ and $(-\pi)/2$ accordingly), the height of the unambiguous measurement is defined by one and the same value, which makes it possible to state: the radius of rotation r and the height H of the radar carrier do not influence $h_{uniq}(t)$ at $t = 0.25\ T$ and $0.75\ T$.

From the obtained results we can conclude that in order to eliminate the phase shift, caused by the rotation of the APC Rx it is necessary to choose $t = 0.25\ T$. In this case the expression (24) can be presented as

$$h_{uniq} \cong \frac{\lambda}{2d} R_{1,0}. \qquad (25)$$

The expression (25) shows, that the height of an unambiguous measurement is inversely proportional to the value d – the vertical distance between the PCs of real antennas and is directly proportional to the wavelength of the probing signal λ and distance to the target $R_{1,0}$. In particular, at $\lambda = 3$ cm, $d = 3$ m, $D = 10$ km, $H = 500$ m we get $h_{uniq}(t)$ 50 m.

In future we will assume that the height report is carried out at $t = 0.25\ T$ or $\omega_r t =$ rad. In this case the expression (18) can be written as

$$Z_c = H - \frac{\left(\left(\frac{\lambda\psi_z(T_1)}{2\pi}\right)^2 + \frac{\lambda\psi_z(T_1)}{\pi} R_0\right) - I^2}{2d}, \qquad (26)$$

where $T_1 = 0.25\ T$. Expression (26) directly implies the following: what information it is necessary to have in order to be able to determine the height of the surface object of observation.

5. ALGORITHM FOR DETERMINING THE HEIGHT OF THE OBSERVED EARTH'S SURFACE RELIEF

It follows from the obtained results that in order to determine the height H of the observed surface relief it is necessary to do the following steps:

1. Determine the phase difference $\psi_h(m,n)$ of the received signals from the observed object (relief) at the output of the processing system (at the output of phase detector PD) in each resolution element in azimuth and range, where m,n are the current numbers of resolution elements in range and azimuth, respectively. As $\psi_h(m,n) = \varphi \pm 2\pi N$ is periodical, it is necessary to determine the number of the whole periods of N phase reversal.
2. Determine the phase difference $\psi_0(m,n)$ of the output signals corresponding to the zero height for each resolution cell

$$\psi_0(m,n) = \frac{2\pi}{\lambda}\left(R_{1,0}(m,n) - R_{2,0}(m,n)\right).$$

In view of the fact that the distance $R_{1,0}(m,n)$ is unknown in practice, we calculate it using $R_{1,h}(m,n)$, and get the following in the result

$$\psi_0(m,n) \cong \frac{\pi}{\lambda}\left(\frac{I^2 + 2dH}{R_{1,h}(m,n)}\right), \qquad (27)$$

where I – interferometer base. This phase is also a periodic function, so it's necessary to

estimate the number of the whole periods of phase reversal.

3. Determine the relief height $h(m,n)$, based on (26) in the assumption that $\omega_r t = \pi/2$ and $\theta = 0$ degrees, we get

$$h(\mathrm{m},\mathrm{n}) = \mathrm{z}_h(\mathrm{m},\mathrm{n}) - \mathrm{z}_0(\mathrm{m},\mathrm{n}), \quad (28)$$

$$h(m,n) \cong \frac{\lambda^2}{8\pi^2 d}\left(\psi_0^2(m,n) - \psi_h^2(m,n)\right) + \frac{\lambda}{2\pi d}\left(\psi_0(m,n) - \psi_h(m,n)\right) R_{1,h}(m,n), \quad (29)$$

$$h(m,n) \cong \frac{\lambda}{2\pi d}\left(\psi_0(m,n) - \psi_h(m,n)\right) R_{1,h}(m,n). \quad (30)$$

Expression (30) actually contains the whole information necessary to determine the relief height during the PC rotation of the receiving antenna and the antenna diversity of Rx-Tx module, namely: the distance to the target $R_{1,h}(m,n)$, phase difference $\psi_h(m,n)$ of the received signals at the output of the processing system and parameters r, d, H, λ, that define the observation conditions.

The determination of an unambiguous phase (disclosure of the phase difference) is performed using the algorithm presented in [8], the essence of which is to integrate the phase difference between two adjacent resolution elements provided that this difference does not exceed the value of π, and there are no sharp changes in height relief. Otherwise a large number of phase turns occurs. More details about this algorithm can be found in [9].

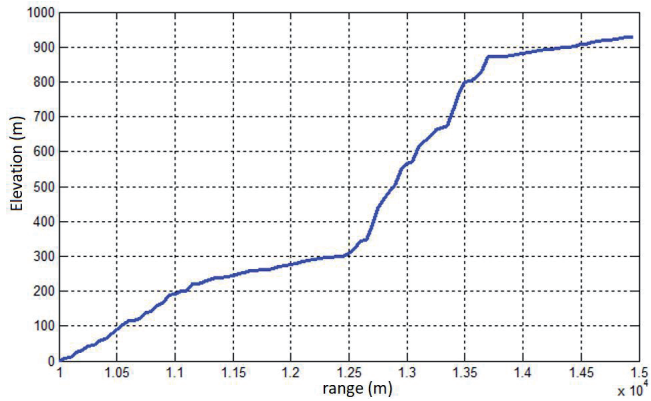

Fig. 7. *Modeled earth relief.*

The algorithm operability was tested by computer simulation. Initially the relief of the earth surface section was formed in the modeling environment, which is shown in **Fig. 7.** The relief has height jumps from 0 m up to 50 m within the range scale from 10 km to 15 km with a range step of 50 m. The height measurement range corresponds to half of its unambiguous measurement.

During modeling it was assumed that d = 3 m, H = 500, r = 8 m, λ = 3 cm, then in accordance with previously described algorithm the formation of the RI of the observed relief was carried out.

At the first step of the algorithm the phase difference $\psi_h(m,n)$ of the received signals was determined within each resolution element (**Fig. 8***a*), and then the unambiguous phase was determined using the algorithm presented

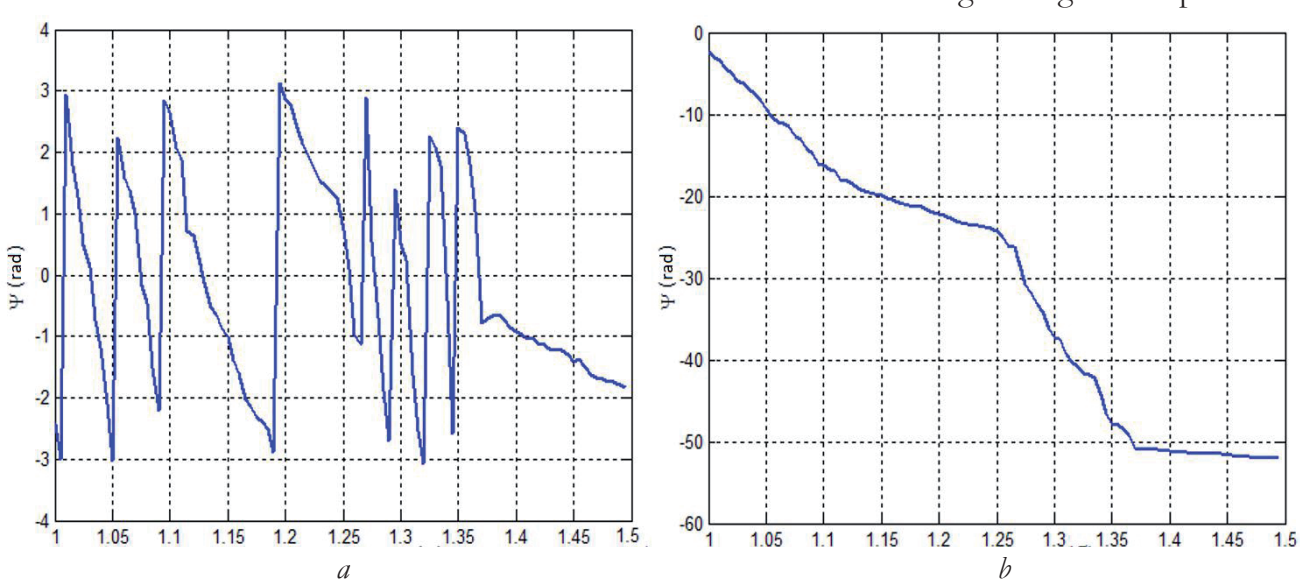

Fig. 8. *Phase difference $\psi_h(m,n)$ of the received signals at the PD output before (a) and after (b) the processing.*

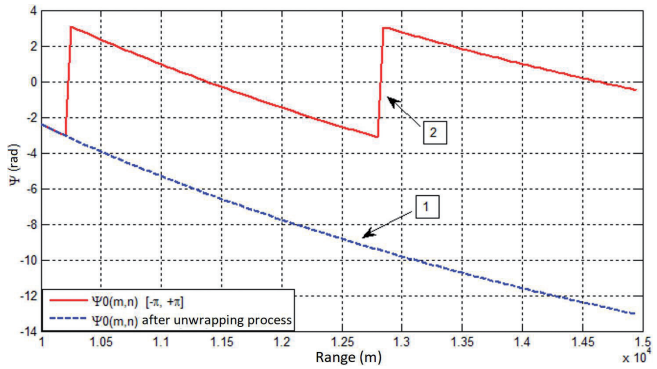

Fig. 9. *Phase difference $\psi_0(m,n)$ of the reflected signals, corresponding to the flat earth surface before (curve 1) and after the processing (curve 2).*

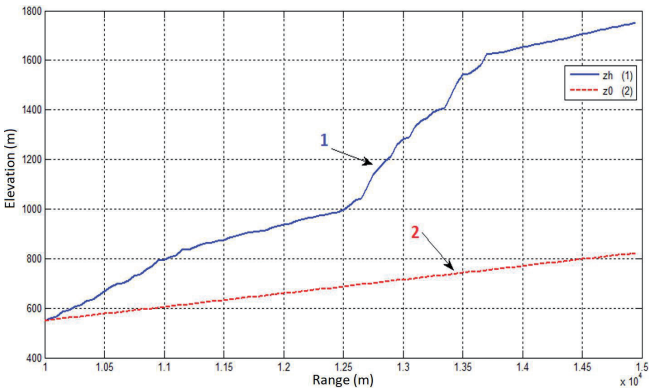

Fig. 10. *The relief of terrain $z_h(m,n)$ (1) and the component $z_0(m,n)$, corresponding to the zero height of the earth surface (2), along the range scale from 10 km to 15 km for one azimuth bin.*

in [8]. The results of processing are shown in Fig. 8*b*.

At the second step the phase difference was determined for the flat earth surface in each element of resolution at the given range on the basis of the expression (27) and the unambiguous phase $\psi_0(m,n)$ was determined too. The results of the algorithm work at the second step are given in **Fig. 9**.

At the third step, using the expression (18), the relief height was determined as the difference of heights $z_h(m,n)$ and $z_0(m,n)$ within the resolution elements in range and azimuth. In this case it was believed that the instant of time $t = 0.25\ T$ (i.e. $\omega_r t = \pi/2$). In this case the expression for $z_h(m,n)$ and $z_0(m,n)$ can be represented as

$$z_h(m,n) = \mathrm{H} - \left(\frac{\left(\left(\frac{\lambda \psi_h(m,n)}{2\pi} \right)^2 + \frac{\lambda \psi_h(m,n)}{\pi} R_{1,h}(m,n) \right) - I^2}{2d} \right), \quad (31)$$

$$z_0(m,n) = \mathrm{H} - \left(\frac{\left(\left(\frac{\lambda \psi_0(m,n)}{2\pi} \right)^2 + \frac{\lambda \psi_0(m,n)}{\pi} R_{1,h}(m,n) \right) - I^2}{2d} \right). \quad (32)$$

Fig. 10 shows the results of calculating $z_h(m,n)$ (curve 1) and $z_0(m,n)$ (curve 2) within the fixed element of resolution in azimuth.

Fig. 11 shows 3D image of the terrain relief, formed in the antenna aperture synthesis mode with rotation of the receiving antenna and the fixed position of the APC of Rx-Tx module when using the considered algorithm.

To assess the accuracy of the relief formation, the developed algorithm determined the error in calculating the height of the relief relative to the model used. The results of determining the error in the relief formation are presented in **Fig. 12**, where the nature of the change in this error on the range scale within the variation of the model relief height is shown.

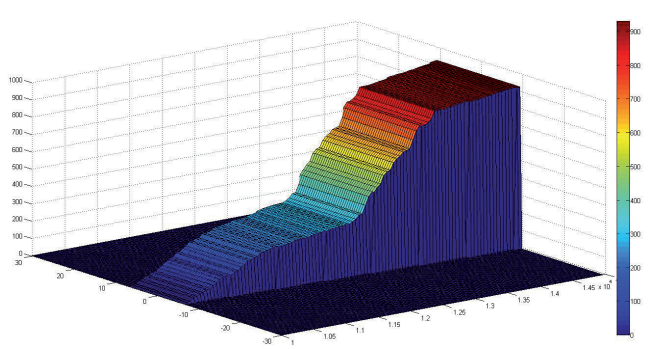

Fig. 11. *3D image of the simulated relief of terrain.*

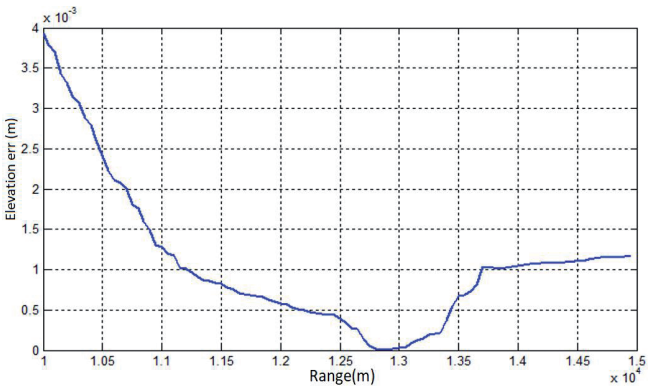

Fig. 12. *Changes in the error of relief formation along the range scale from 10 km to 15 km.*

Fig. 12 shows that the error in the restoring the relief height corresponds to the thousandths of a meter, which allows us to state that the developed algorithm adequately restores the relief of the observed surface. At the same time it should be noted that the obtained results correspond to a situation in which observation noise and possible errors in determining parameters *r,d* and *H* were not taken into account.

6. CONCLUSION

Thus, the results presented in the article, show that when synthesizing the antenna aperture due to rotation of the APC of the receiving module and the spaced but stationary position of antenna Rx-Tx module, it is possible to form 3*D* images of the observed earth surface. The formation of 3*D* images is provided by interferometric processing of the received signals in two reception points spaced relative to each other. In this case the errors in the restoration of the relief correspond to thousandths of a meter. The study of the influence of parameters *r, H* and *d* on unambiguity of the height measurement as well as the simulation results, showed that the vertical distance *d* between the PC of the receiving-transmitting antenna and the plane of rotating the PC of the receiving antenna has the greatest influence on the process of restoring the relief of the observed surface.

REFERENCES

1. Kondratenkov GS, Frolov AYu. *Radiovidenie. Radiolokatsionnye sistemy distantsionnogo zondirovaniya Zemli.* Kondratenkov GS (ed.). Moscow, Radiotekhnika Publ., 2006, 368 p. ISBN 588070-071-2.
2. Antipov VN, Vikentyev FYu, Koltyshev EE, Kondratenkov GS, Lavrov AA, Frolov AYu, Yankovskiy VT. *Aviatsionnye sistemy radiovideniya.* Kondratenkov GS (ed.). Moscow, Radiotekhnika Publ., 2015, 648 p. ISBN 978-5-93108-105-2.
3. Verba VS, Tatarskiy BG, Maistrenko EV. Novye tekhnologii radiolokatsionnogo monitoringa zemnoi poverkhnosti dlya nositelei vertolyotnogo tipa. *Zhurnal radioelektroniki* [elektronnyi zhurnal, ISSN 1684-1719], 2018, №2:1-18. Access mode: http//jre.cplire.ru/jre/feb18/4/text/pdf.
4. Koshelev VI, Kirdyashkin VV, Sychev MI, Yasentsev DA. *Aktualnye voprosy radiolokatsii.* Bakulev PA (ed.). Moscow, MAI Publ., 2016, 215 p. ISBN 978-5-4316-0353-2.
5. Shimkin PE. Odnoprokhodnyi bortovoi interferometricheskiy radiolokator s sintezirovannoi aperturoi antenny perednebokovogo obzora dlya otsenki reliefa podstilayushchei poverkhnosti. *Dissertatsiya na soiskanie uchonoi stepeni kandidata tekhnicheskih nauk.* Moscow, MEI Publ., 2018.
6. Verby VS, Tatarskii BG (eds.). *Kompleksy s bespilotnymi letatelnymi apparatami v 2 knigah: Kn. 1. Printsypy postroeniya i osobennosti primeneniya kompleksov s BLA.* Moscow, Radiotekhnika Publ., 2016, 502 p. ISBN 978-5-93108-135-9.
7. Dvite GB. *Tablitsy integralov i drugie matematicheskie formuly.* Moscow, Nauka Publ., 1983, 228 p.

8. Goldstein RM, Zebker HA, Werner CL. Satellite radar interferometry: Two-Dimensional Phase Unwrapping. *Radio Science*, 1988, 23(4):713-720. DOI: 10.1029/RS023i004p00713.
9. Ian Herszterg, Marcus Poggi, Thibaut Vidal. Two-Dimensional Phase Unwrapping via Balanced Spanning Forests. *Informs Journal on Computing,* 2019, 31(3):527-543. DOI: 10.1287/ijoc.2018.0832.

DOI: 10.17725/rensit.2023.15.253

Algorithm for detecting epileptiform EEG activity in delayed cerebral ischemia

Yuriy V. Obukhov, Ivan A. Kershner

Kotelnikov Institute of Radioengineering and Electronics of the Russian Academy of Sciences, http://www.cplire.ru/

Moscow 125009, Russian Federation

E-mail: yuvobukhov@mail.ru, ivan.kershner@gmail.com

Irina V. Okuneva, Mikhail V. Sinkin

N.V. Sklifosovsky Research Institute of Emergency Medicine, Department of Emergency Neurosurgery, https://sklif.mos.ru/

Moscow 129090, Russian Federation

E-mail: okunevaiv@mail.ru, mvsinkin@gmail.com

Received August 15, 2023, peer-reviewed August 18, 2023, accepted August 21, 2023

Abstract: **An algorithm for automatic detection of epileptiform activity in EEG monitoring data with delayed ischemia after hemorrhage in the subarachnoid space of the brain is proposed and described. The algorithm is based on the formalization of the visual characteristics of epileptiform activity in the form of a peak-wave discharge pattern and analysis of the mutual correlation of multichannel EEG signals with the selected pattern. Fragments of epileptiform activity in each pair of bipolar electrodes were determined from three conditions according to the description of peak-wave discharges of epileptiform activity: 1) the value of positive mutual correlation at the peak of the correlation function should be greater than 0.4; 2) a positive peak of mutual correlation should be followed by a peak with a negative correlation; 3) the width of the peak of negative mutual correlation at half-altitude should be at least 2 times greater than that of the previous positive peak of positive mutual correlation. As with the visual detection of epileptiform activity, the neurophysiologist selected simultaneous peak-wave discharges in several bipolar electrodes. The results of testing the algorithm on an hour-long EEG recording of a patient with delayed ischemia are presented. Fragments with epileptiform activity during the hour under review were identified 17 in the right hemisphereand 2 in the left. Interhemispheric asymmetry is caused by a right-sided aneurysm in patient. The operating time of the algorithm on a modern personal computer is no more than 5 minutes to process 16 bipolar signals, so it can be used to calculate the hourly amount of epileptiform activity in almost real time of the manifestation of this indicator of delayed ischemia after aneurysmal subarachnoid hemorrhage.**

Keywords: **electroencephalogram, long-term monitoring, epileptiform activity, mutual correlation function, delayed cerebral ischemia**

UDC **519.67, 612.1, 53.083, 519.24, 004.93**

Acknowledgments: The study was funded by a grant from the Russian Science Foundation No. 22–69-00102, https://rscf.ru/en/project/22-69-00102/.

For citation: Yuriy V. Obukhov, Ivan A. Kershner, Irina V. Okuneva, Mikhail V. Sinkin. Algorithm for detecting epileptiform EEG activity in delayed cerebral ischemia. *RENSIT: Radioelectronics. Nanosystems. Information Technologies*, 2023, 15(3):253-262e. DOI: 10.17725/rensit.2023.15.253.

Contents

1. INTRODUCTION

Delayed cerebral ischemia usually occurs 4 to 14 days after the onset of a non-traumatic or traumatic hemorrhage in the subarachnoid space of the brain. The objectives of conservative treatment of patients with subarachnoid hemorrhage (SAH) are stabilization of the patient's condition, prevention of recurrence of SAH, prevention and treatment of vascular spasm and delayed cerebral ischemia. Intensive treatment is carried out in the conditions of monitoring the main indicators characterizing the state of the cerebrovascular system and vital functions. After admission of a patient with suspected non-traumatic or traumatic SAH to the intensive care unit of a neurosurgical hospital, a detailed neurological examination, an assessment of the severity of the condition, computer tomography (CT scan) and magnetic resonance imaging (MRI studies), transcranial and extracranial Doppler ultrasonography to assess the severity of angiospasm, electroencephalography to assess the severity of changes in the bioelectrical activity of the brain are performed.

Clinical neurological examination is the "gold standard" for diagnosing delayed cerebral ischemia, but it requires good speech contact with the patient, which is impossible in the case of severe SAH, accompanied by depression of wakefulness before coma. Neuroimaging methods, which include CT and MRI, remain the "gold standard" of instrumental diagnosis of delayed ischemia, but their main drawback is the need to transport the patient to the tomograph, which makes it impossible to use them in the monitoring mode.

Electroencephalography (EEG) records the bioelectrical activity of the brain, so any change in its functional state is immediately reflected in the indicators of the curves. Changes in EEG are directly related to volumetric blood flow [1]. Signs (indicators) of cerebral ischemia are manifested on the EEG in real time, which makes this method indispensable for intraoperative monitoring during operations on the brachiocephalic arteries, and in the intensive care unit for early diagnosis of delayed cerebral ischemia after SAH.

If brain damage due to hemorrhage has led to depression of wakefulness before coma and clinical neurological examination is difficult, and CT requires transportation of the patient to the device, continuous EEG monitoring becomes the main way to diagnose and predict the development of delayed cerebral ischemia. An alternative approach is Doppler ultrasonography monitoring. This method allows you to accurately diagnose vasospasm, but the very fact of narrowing the vessel does not always lead to cerebral ischemia, and the technical feature of ultrasound measurement of blood flow velocity allows you to determine it only at one small point

not exceeding a few millimeters, while the spasm can be localized elsewhere.

EEG monitoring is the only method by which continuous round-the-clock monitoring of the functional state of the brain of a patient with SAH in the intensive care unit can be carried out to diagnose and predict the development of delayed cerebral ischemia. In combination with periodic studies using neuroimaging methods, it allows for early detection and prediction of the development of delayed ischemia, which makes it possible to begin intensive treatment and stop its development. In principle, long-term monitoring of EEG in real time of the manifestation of indicators makes it possible to diagnose and predict the development of delayed ischemia and evaluate its dynamics even before its heart attack develops, and further evaluate restoration of cerebral perfusion even before clinical improvement [2-4].

Existing EEG monitoring systems provide real-time recording of EEG in the disk memory in the presence of instrumental artifacts and artifacts of the patient's vital activity and at the same time display multi-channel EEG on the monitor for visual observation and analysis by the doctor. To highlight time intervals with artifacts caused by the patient's vital activity and the care of his medical staff, it is advisable to analyze video recordings synchronous with EEG.

Usually, the analysis of the results of long-term video-EEG monitoring is carried out retrospectively offline by viewing multichannel EEG and video fragments. The methodology for EEG analysis of delayed ischemia is traditionally based on visual analysis of curves, with the allocation of artifact-free recording areas and analysis of its background structure, single special graphic patterns, spectral energy in a certain time interval (usually 1 hour) in various frequency ranges alpha (8-13 Hz), beta (14-40 Hz), theta (4-8 Hz), delta (0.5-3 Hz), and their ratio in the delta/alpha and (delta + theta)/(alpha + beta) ranges, possessing specificity in relation to various clinical conditions. This analysis is an extremely time-consuming and time-consuming work of highly qualified neurophysiologists and, in addition, the objectivity of such a diagnosis varies significantly between individual specialists. Given the required 10–14-day duration of monitoring in patients with SAH, the use of the generally accepted analysis of graph elements visually by EEG in offline mode is almost impossible and does not allow for prompt medical decision-making in case of unfavorable development of delayed ischemia.

Therefore, for the widespread use of quantitative EEG (qEEG), it is necessary to develop an automated system for detecting indicators of delayed ischemia as a result of subarachnoid hemorrhage, which makes it possible to detect, classify and predict indicators of delayed ischemia in real time [3]. In addition, due to the artifacts of the patient's vital activity and his service by medical personnel, the automated calculation of EEG diagnostic parameters without a priori selection of data segments without artifacts or manual review by trained neurophysiologists is an unsolved problem of automatic algorithms for detecting delayed ischemia.

Numerous studies have made it possible to identify EEG patterns, which are sometimes called "malignant" in the literature, since they are characteristic of an unfavorable prognosis of survival and restoration of consciousness [2-4]. These include sustained suppression of the amplitude of background activity below 10 μV, disruption of the continuity of EEG curve oscillations with the development of the flash-suppression pattern, registration of generalized periodic discharges with the same interval between digits and monomorphic graphic patterns, etc. The main diagnostic and prognostic indicators of delayed ischemia in EEG monitoring are (1) focal and regional slowing, index decrease, and cessation of rapid activity; (2) a decrease in the variability of the EEG power averaged over the frequency range and leads separately in the left and right hemispheres of the alpha rhythm power; (3) a decrease in the ratio of the average power of alpha/delta rhythms; (4) epileptiform graphic patterns, including sporadic epileptiform discharges, lateralized rhythmic delta activity, lateralized periodic discharges, or generalized periodic discharges. Lateralized periodic discharges are sharp oscillations, such as spikes and sharp waves, that occur more or less periodically [5]. Recent studies of epileptiform anomalies have demonstrated their diagnostic and prognostic potential in monitoring delayed ischemia after SAH [3,4].

In [6], the results of a retrospective study of the values of the hourly number of epileptiform discharges, determined visually, were published to predict the development of delayed ischemia after SAH. Using visual offline analysis of EEG graphic patterns using the Persyst EEG Analysis Support System (https://www.persyst.com/), it was found that in many patients with SAH, the hourly number of epileptiform discharges per hour increases during the first 3 to 10 days after cerebral hemorrhage, the main risk period for delayed ischemia. In patients with developing delayed ischemia, hourly epiactivity for 3.5–6 days is significantly higher after SAH compared to those who do not develop ischemia (area under the ROC curve AUC = 0.72).

Finally, individual trends in the dynamics of epileptiform discharges over time, assessed using a group analysis of the trajectory of hourly load – the number of epileptiform discharges per hour, also help to stratify the risk of delayed ischemia. Similar results were obtained in studies of rats with pharmacological provoking of mild, moderate, and severe stroke [7]. The maximum AUC within 5 days after SAH is 0.61, and within 10 days it is 0.68. These are the results showed that the hourly number of epileptiform discharges is a useful parameter for identifying individuals at higher risk of developing delayed cerebral ischemia after SAH. These studies were performed by neurophysiologists retrospectively "manually" using the analysis of diagnostic parameters offline, using, as a rule, the Persyst EEG Analysis Support System (https://www.persyst.com). Fragments of multichannel ones lasting 5–15 seconds were analyzed. Such an analysis, firstly, is extremely time-consuming, secondly, it depends on the qualifications of neurologists [8] and, thirdly, in principle, changes in the hourly number of epileptiform discharges cannot be applied in real time. As a result, a 2022

review [3] on the diagnosis of delayed cerebral ischemia concluded that it was necessary to develop algorithms for the automatic detection of indicators of delayed cerebral ischemia after SAH.

This article proposes and describes an algorithm for automatic detection of time fragments of EEG with epileptiform activity, based on the analysis of the functions of cross correlation of EEG with a characteristic fragment of epileptiform activity and the results of its testing on clinical EEG data – monitoring of a patient after SAH.

2. ALGORITHM FOR DETECTING EPILEPTIFORM ACTIVITY

In **Fig. 1** shows the layout of the electrodes in accordance with the international standard 10–20%. For long-term EEG monitoring, bipolar mounting (differential recording scheme) Fp1-F7, F7-T3, T3-T5, T5-O1, Fp1-F3, F3-C3, C3-P3, P3-O1 – left hemisphere and Fp2-F4, F4-C4, C4-P4, T5-O1, P4-O2, Fp2-F8, F8-T4, T4-T6, T6-O2 – right hemisphere are used. Bipolar EEG recording is used to reduce trends and other artifacts. The signal is recorded at a sampling rate of 250 Hz. Signal filtering was carried out in the Matlab programming environment using filters: notch (iirnotch function) at a frequency of 50 Hz, 8th order Butterworth bandpass filter (butter function) in the frequency range 0.5-70 Hz, removal of the linear trend (detrend function).

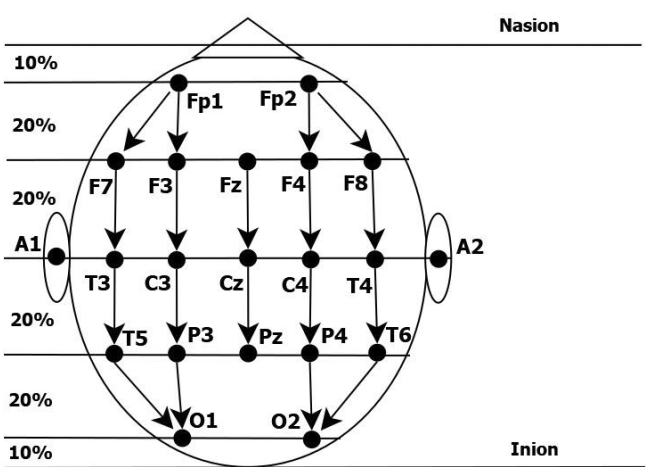

Fig. 1. *Arrangement of EEG electrodes on the scalp in accordance with the international scheme of 10-20%. Even electrodes are on the right hemisphere, odd electrodes are on the left, A1 and A2 are reference electrodes. The arrows indicate pairs of electrodes in bipolar EEG recording.*

In **Fig. 2** shows an example of a 5-second fragment of a bipolar EEG of a patient with delayed ischemia after SAH in the frontal part of the right hemisphere, recorded on 10/14/2022.

From Fig. 2 shows that the characteristic features of the graph element of epileptiform activity (see, for example, recording in a pair of channels C4-P4) is the presence of a high-amplitude (100 μV) acute negative peak with a duration of 90 msec at a half-altitude and a wave following it with a duration of more than 2 times. To detect a fragment of epileptiform activity, we used the analysis of the cross correlation of the function (Matlab xcorr function) of EEG recording in each pair of bipolar electrodes with a negative peak sample, which was chosen as a negative EEG peak in a pair of C4-P4 electrodes in a time interval of about 3.5 seconds. The green dots indicate the maximum and zero correlation values.

In **Fig. 3** shows the function of cross correlation of the bipolar signal of the EEG fragment shown in Fig. 2, with selected sample. A fragment of epileptiform activity is highlighted in red, which was determined from three conditions according to the description

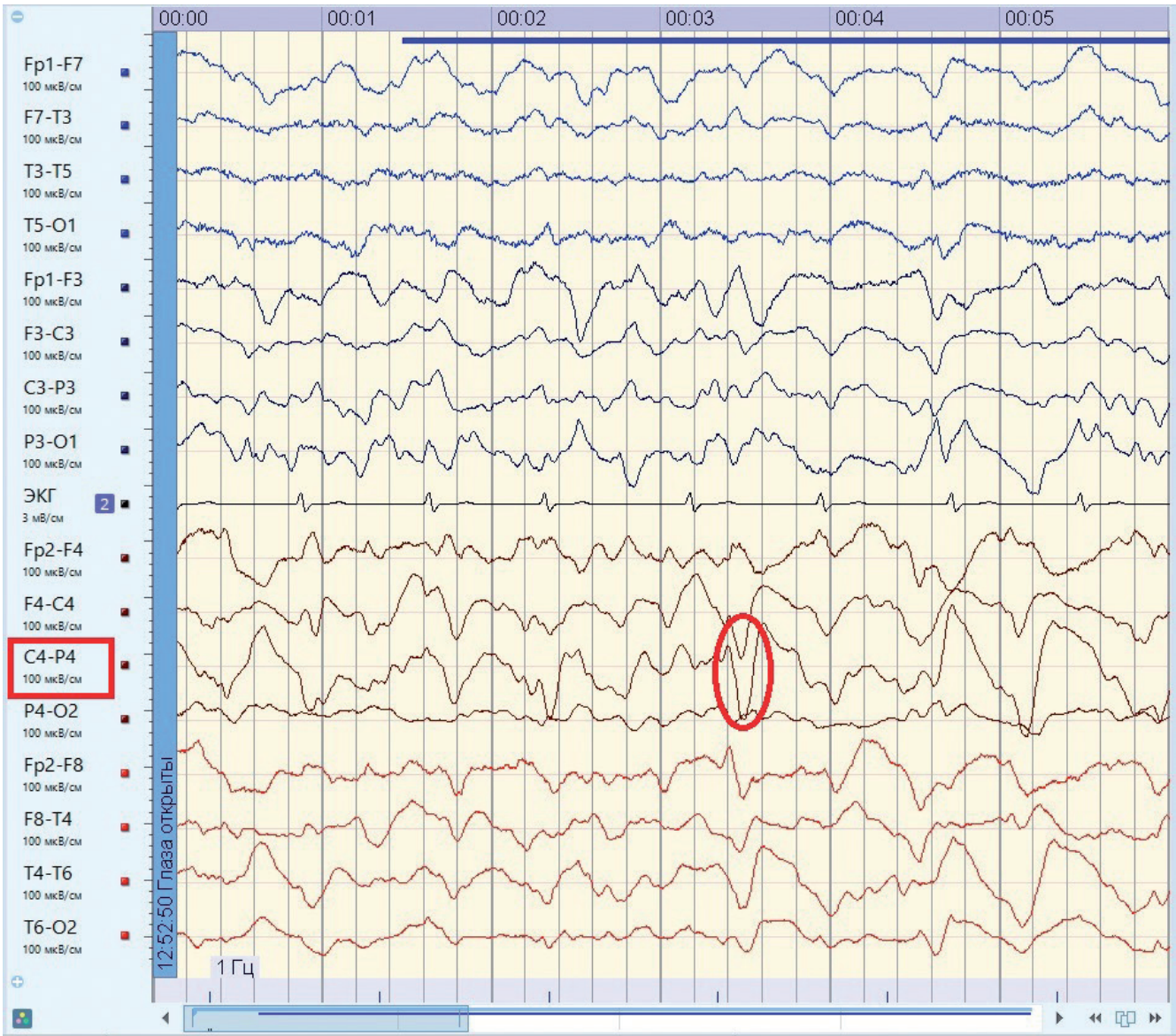

Fig. 2. *A 5-second fragment of an EEG recording with epileptiform activity indicated by a red circle.*

of peak-wave discharges of epileptiform activity:

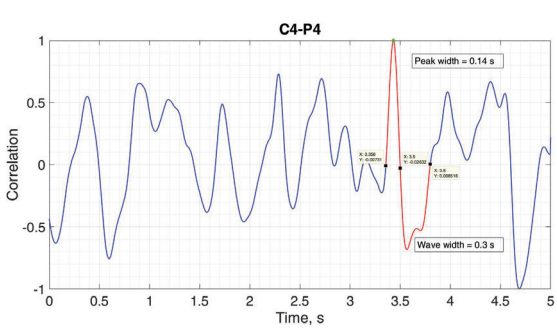

Fig. 3. *Cross correlation of a 5-second EEG fragment with a negative EEG peak in a pair of C4-P4 electrodes in a time interval of about 3.5 sec from Fig. 2.*

1) the value of positive cross correlation at the peak of the correlation function should be greater than 0.4;

2) a positive peak of cross correlation should be followed by a peak with a negative correlation;

3) the width of the peak of negative cross correlation at half-altitude should be at least 2 times greater than that of the previous positive peak of positive cross correlation.

3. RESULTS OF PROCESSING CLINICAL EEG RECORDINGS

An hour-long EEG recording was analyzed at a 3-hour daily recording on 12.10.2023 before CT examinations in patient D., who had a ruptured aneurysm of the right internal carotid artery. On CT on 10/15/2023, a hematoma was found in the area of surgery in the right front temporoparietal region. CT scan dated 10/18/2023 diagnosed ischemia in the right temporal and occipital lobes of part of the right hemisphere. It should be noted that the EEG fragment in which the sample of epileptiform activity presented in Fig. 2 was selected was recorded on another day of EEG monitoring.

In **Fig. 4** as an example is a fragment of the EEG of patient D. in the time interval of 2 hours 45 minutes 38 seconds – 2 hours 45 minutes 41 seconds, which visually determines the epileptiform activity.

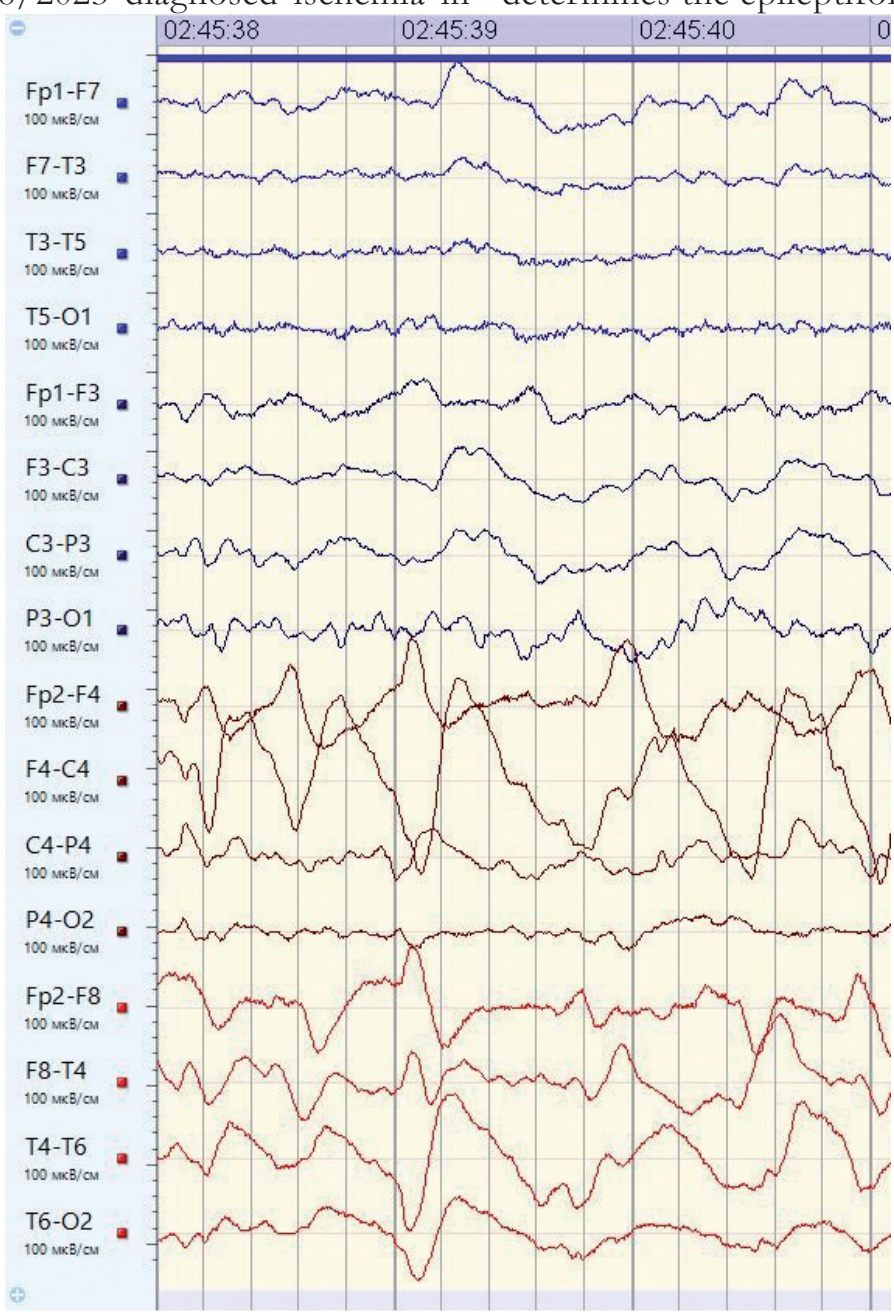

Fig. 4. *Fragment of the EEG of patient D. in the time interval 2 hours 45 minutes 38 seconds – 2 hours 45 minutes 41 seconds.*

In **Fig. 5** shows the functions of the cross correlation of the EEG with the sample described in section 2. The peaks corresponding to epileptiform activity simultaneously in 3 bipolar pairs of F4-C4, T4-T6 and T6-O2 electrodes at about 39 seconds of the fragment and the peak in one bipolar pair of F4-C4 electrodes at 41 seconds are highlighted in red.

With the visual detection of epileptiform activity, the neurophysiologist distinguishes simultaneous peak-wave discharges in several electrodes. To exclude the artifact genesis of discharges, taking into account the phenomenon of volumetric propagation of bioelectric activity generated by the cerebral cortex, it is advisable to allocate time fragments with simultaneous graphic elements in 2 or more closely spaced bipolar pairs of electrodes. During the hour under review, 17 such fragments were identified in the right hemisphere and 2 in the left. This interhemispheric asymmetry is due to a right-sided aneurysm in patient D.

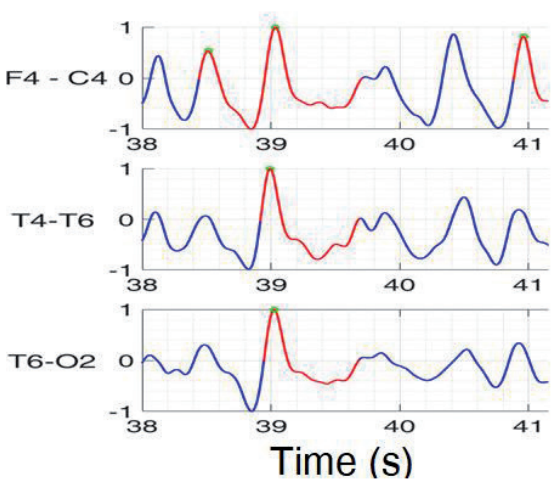

Fig. 5. *Cross correlation of EEG, peaks corresponding to epileptiform discharges are highlighted in red. On the chart, the time is indicated in seconds, the countdown starts from 2 hours 45 minutes and the 38th second.*

The operating time of the algorithm on a modern personal computer is no more than 5 minutes to process 16 bipolar signals, so it can be used to calculate the hourly amount of epileptiform activity in almost real time of the manifestation of this indicator of delayed ischemia after SAH.

4. CONCLUSION

Usefulness of quantitative EEG in detecting delayed cerebral ischemia after aneurysmal subarachnoid hemorrhage. It provides a non-invasive, continuous assessment of brain activity in real time and requires a relatively short time to determine the diagnostic indicators of delayed ischemia compared to a medical assessment of the baseline EEG. With the increasing availability of software capable of calculating these EEG functions in real time, it has great clinical potential for the timely treatment of delayed ischemia. EEG can also be used as a screening tool for patients with qEEG features to assess the high risk of inclusion in clinical trials testing new treatments to mitigate and prevent delayed ischemia. The development of a multifunctional algorithm based on all the above-mentioned functions of the EEG, including epileptiform activity, is the next step in optimizing the algorithm for predicting delayed ischemia, which can be clinically implemented. Ultimately, qEEG is a promising modality implemented in everyday practice, allowing for non-invasive real-time monitoring with global whole-brain coverage. At the same time, it has the potential advantage of cost- and time-effectiveness, especially given the future development of automated systems

that could facilitate rapid detection and early intervention in delayed ischemia.

This article describes the proposed algorithm for automatic detection of EEG epileptiform activity, based on the formalization of the description of peak-wave discharges of epileptiform activity and its visual detection by neurophysiologists. Testing of the algorithm on clinical data showed its adequacy to the neurophysiological description of epileptiform activity in delayed ischemia after hemorrhage in the subarachnoid space of the brain.

The operating time of the algorithm on a modern personal computer is no more than 5 minutes to process 16 bipolar signals, so it can be used to calculate the hourly amount of epileptiform activity in almost real time of the manifestation of this indicator of delayed ischemia after aneurysmal subarachnoid hemorrhage. Therefore, we believe that the application of the developed algorithm will solve the problem of detecting epileptiform activity and assessing its development with delayed ischemia in real time of the manifestation of this indicator.

REFERENCES

1. Brandon Foreman, David Albers, J Michael Schmidt, Cristina Maria Falo, Angela Velasquez, E Sander Connolly, Jan Claassen. Intracortical electrophysiological correlates of blood flow after severe SAH: A multimodality monitoring study. *Journal of Cerebral Blood Flow & Metabolism*, 2018, 38(3):506-517, doi: 10.1177/0271678X17700433.
2. Eric S Rosenthal, Siddharth Biswal, Sahar F Zafar, Kathryn L O'Connor, Sophia Bechek, Apeksha V Shenoy, Emily J Boyle, Mouhsin M Shafi, Emily J Gilmore, Brandon P Foreman, Nicolas Gaspard, Thabele M Leslie-Mazwi, Jonathan Rosand, Daniel B Hoch, Cenk Ayata 8, Sydney S Cash, Andrew J Cole, Aman B Patel, M Brandon Westover. Continuous Electroencephalography Predicts Delayed Cerebral Ischemia after Subarachnoid Hemorrhage: A Prospective Study of Diagnostic Accuracy. *Ann Neurol.*, 2018, 83:958-969, doi: 10.1002/ana.25232.
3. Hae Young Baang, Hsin Yi Chen, Alison L Herman, Emily J Gilmore, Lawrence J Hirsch, Kevin N Sheth, Nils H Petersen, Sahar F Zafar, Eric S Rosenthal, M Brandon Westover, Jennifer A Kim. The Utility of Quantitative EEG in Detecting Delayed Cerebral Ischemia After Aneurysmal Subarachnoid Hemorrhage. J*ournal of Clinical Neurophysiology,* 2022, 39(3):207-215, doi: 10.1097/WNP.0000000000000754.
4. Carlos F Muniz, Apeksha V Shenoy, Kathryn L O'Connor, Sophia C Bechek, Emily J Boyle, Mary M Guanci, Tara M Tehan, Sahar F Zafar, Andrew J Cole, Aman B Patel, Michael B Westover, Eric S Rosenthal. Clinical development and implementation of an institutional guideline for prospective EEG monitoring and reporting of delayed cerebral ischemia. *Journal of Clinical Neurophysiology,* 2016, 33(3):217-226, doi: 10.1097/WNP.0000000000000281.
5. Sinkin MV, Krylov VV. Rhythmic and periodic EEG patterns. Classification and clinical significance. *S.S. Korsakov Journal of Neurology and Psychiatry,* 2018, 118(10-2):9-20 (in Russ.).

6. Kim JA et al. High epileptiform discharge burden predicts delayed cerebral ischemia after subarachnoid hemorrhage. *Clinical Neurophysiology*, 2022, 141:139-146.
7. Hyun-Joon Yoo, Jinsil Ham, Nguyen Thanh Duc, Boreom Lee. Quantification of stroke lesion volume using epidural EEG in a cerebral ischaemic rat model. *Scientific Reports*, 2021, 11(1):2308, doi: 10.1038/s41598-021-81912-2.
8. Mark L. Scheuer, Anto Bagic, Scott B. Wilson. Spike detection: Inter-reader agreement and a statistical Turing test on a large data set. *Clinical Neurophysiology*, 2017, 128(1):243-250.
9. Bazhenov M, Timofeev I, Fröhlich F, Sejnowski TJ. Cellular and network mechanisms of electrographic seizures. *Drug Discovery Today Disease Models*, 2008, 5(1):45-57.

DOI: 10.17725/rensit.2023.15.263

A Neoteric View of sp^2 Amorphous Carbon

Elena F. Sheka

Peoples' Friendship University of Russia, https://www.rudn.ru/
Moscow 117198, Russian Federation
E-mail: sheka@icp.ac.ru

Received March 26, 2023, peer-reviewed April 03, 2023, accepted April 10. 2023

Abstract: **Presented is a concentrated synopsis of facilities of empirical and virtual analytics that, once applied, have provided a fully new vision of sp^2 amorphous carbons. This study proved that the solids are multilevel structures, started with the first-level basic structural units (BSUs) and accomplished as macroscopic agglomerates of globular structures, consisting, in its turn, of stacked BSUs. BSUs present necklaced graphene molecules, size, and shape of which are governed by the relevant graphene domains while chemical composition in addition to basic carbon is controlled with heteroatoms of the necklaces. This study shows that BSUs and stacks of BSUs determine the short-range order of the solids and are the main subject of the applied analytics. The synopsis consists of two parts related to empirical and virtual analytics. The former is composed of sections related to structural determination, total and atomic chemical content evaluation and elicitation of the covalent bond composition. The second presents new analytic approaches based on the Digital Twins concept and virtual vibrational spectrometry. The synopsis is configured as an atlas composed of generalized pictures accompanied with necessary explanations to be discussed in detail in the extended references.**

Keywords: **sp^2 amorphous carbons; molecular short-range order; necklaced graphene molecules; structural and compositional analytics; virtual spectrometry analytics**

UDC 004.942, 547.022.1

Acknowledgments: The author is thankful to colleagues, without collaboration with whom this atlas presentation would not be possible. My deep gratitude to I. Natkaniec, N.N. Rozhkova, Ye.A. Golubev, the late B.S. Rasbirin, Ye.N. Kabachkov, Ye.U. Ipatova, the late K. Holderna-Natkaniec, K. Druzhbicky, Y.M. Shul'ga, V.M. Mel'nikov, D.K. Nelson, A.N. Starukhin, V. Tkachev. M.F. Budyka. I greatly appreciate fruitful discussions with M.L. Terranova, S.P. Gubin, and A.Tadger. My invaluable gratitude to N.A. Popova, V.A. Popova for assistance with calculations and results treatment. This paper has been supported by the RUDN University Strategic Academic Leadership Program.

For citation: Elena F. Sheka. A Neoteric View of sp^2 Amorphous Carbon. *RENSIT: Radioelectronics. Nanosystems. Information Technologies,* 2023, 15(3):263-294e. DOI: 10.17725/rensit.2023.15.263.

Content

1. A CONCISE HISTORICAL INTRODUCTION

The last two decades have seen a profound breakthrough in our understanding of sp^2 amorphous carbon (aC). First, this was due to the epoch-making development of graphenics – a new material science. The new scientific trend revived a huge interest in solid carbon in general, and gave rise to the first, and then subsequently more convincing guesses that the history of graphenics did not begin in 2010 but goes back centuries ago, and that it is precisely aC that shows the way. The second important circumstance, which stimulated a new interest in amorphous carbon, is the highly elevated level of research into the structure and chemical composition of materials. In the rays of these two illuminations, sp^2 aC began to play with completely new facets. The purpose of this review is to introduce readers to a new vision of this old material.

My first personal encounter with sp^2 aC was in 2005. Being engaged in fullerenes at that time, I was puzzled by the search for evidence of the presence of this sp^2 nanocarbon in nature. Having heard about its possible observation in a natural mineral called shungite carbon, huge deposits of which are located within Russian Karelia, I went to sort it out on the spot. Scholars from the Institute of Geology of the Karelian Scientific Center of the Russian Academy of Sciences, who worked on these deposits, told me many interesting things about this mineral, but its connection with fullerenes has not been confirmed. However, fairy tale-like stories about its outstanding properties, its belonging to the family of nanoscale solid carbons, and the high degree of carbonization reaching more than 98%, did not allow for forgetting this amazing substance. Throughout the formation and further development of the radical concept of sp^2 nanocarbons, which then included fullerenes, carbon nanotubes, and first new graphene materials, such as graphene oxide and reduced graphene oxide (rGO), my attention again and again turned to shungite carbon. After a deep analysis in collaboration with N.N. Rozhkova it was suggested that the mineral is of a complex multilevel structure based on molecular-like compositions, which are nanosize graphene domains framed along the perimeter by heteroatoms that provide complete and/or partial termination of dangling valence bonds of the domain edge atoms [1]. This assumption was in line with fundamentals of chemical processes in nanoscale systems presented in a conceptual article by R. Hofmann, Nobel Prize winner in chemistry [2]. Thus, the idea arose that the basic structural unit (BSU) of shungite carbon is a necklaced graphene molecule (NGM). Analyzing the available chemical content data, we assumed that hydrogen and oxygen are the main components of this BSU's heteroatom necklace.

At the same time, all geophysicists share common opinion that shungite carbon belongs to amorphous solids, i.e., is a member of the aC family. In turn, this body belongs to covalent solids, in which the short-range order [3] is evidently determined by a particular configuration of covalent sp^2 C–C bonds. Chemistry teaches us that covalent bonds are extremely persistent, are characterized with a well-defined local topology, and tend to strongly resist changing their lengths and angles to ensure a stable chemical composition of substances. Therefore, it seems reasonable to assume that, within the limits of the short-range order space, sp^2 C–C bonds retain their standard topology, thereby separating the graphene domain limited in size from the total massif of an extended honeycomb structure. A further variation in the domain arrangement ensures the disorder of the solid. In this sense, shungite carbon is analogous to covalent molecular amorphics, in which the short-range order is determined with the basic standard molecules [4]. Accordingly, it is natural to assume that the NGMs, suggested to explain the structure of shungite carbon, can be considered as BSUs of sp^2 aC of any origin. Moreover, the well-studied multilevel structure of shungite carbon can be taken as the basis for all aCs of this type.

The first bridge, uniting shungite carbon with other sp^2 aCs was built when comparing vibrational spectra of shungite carbon and one of the synthetic rGOs [5]. It would seem that there was nothing to prevent the idea of NGMs as BSUs from being a fundamental concept for the entire

class of sp^2 aCs. However, one day, on the desk of one of my colleagues, I saw two flasks filled with black powder, with manufacturer's labels pasted on, saying "C 100%", and with CB624 and CB632 inscriptions indicating SIGMA-ALDRICH MERCK as producers. Both products were synthetic sp^2 aC known as black carbon [6]. The indisputable authority of the manufacturer and the high price of the products did not leave a shadow of doubt about its quality, and none of my arguments based on the quantum nature of the matter and asserting the impossibility of the existence of C 100% nanoscale graphene domains were heard. The only way to solve the problem of the 100% nature of the carbons was to conduct a thorough study of a set of sp^2 aC using as many available analytical methods as possible. Seven samples listed in **Table 1** were selected. All of them were of the maximum carbonization [7-12]. The first three are natural sp^2 aCs, the next two are synthetic technical graphenes – rGOs [13] obtained in various ways, and the last two are the above-mentioned black carbons from the SAM. All samples were analyzed by the same set of methods under equal conditions. Three groups of analytic techniques were used: 1) structural one, 2) evaluating the overall atomic composition of the samples, and 3) determining the atomic composition of covalent C–A bonds (A = C, H, O).

The results obtained allowed us to solve the main problem and obtain indisputable evidence that BSUs of sp^2 aCs have a unified nature and are NGMs, the size of whose domains and atomic composition of the relevant necklaces are determined by the chemical history of the amorphics' origin. The next result showed that all the studied aCs have a multilevel structure based on zero-level BSUs with subsequent aggregation of the units into stacks, globules, and micro- and/or macroscopic agglomerates of higher levels. The third result is that, due to the structural and compositional complexity of sp^2 aCs, analytical testing of samples cannot be single-technique and requires the use of a set of methods. Last, when the multi-technique analytics of sp^2 aCs is mastered, quantum–chemical modeling of the structure, composition, and properties of their BSUs becomes possible. Thus obtained model BSUs open the way to new analytics of the sp^2 aCs that is a virtual one and is based on the Digital Twins concept [14].

The current review presents a consolidated view on these multi-technique analytics applied to a representative set of sp^2 aCs. Since discussed results are too numerous, an atlas-like format was chosen to facilitate the presentation. Although the results, obtained with the participation of the author, make the main contribution to the figures and tables presented below, those obtained in other groups were also taken into account when compiling the review. Nevertheless, the author apologizes in advance for the possible omission of other important results unknown to her and expresses her gratitude for the relevant indications.

2. GENERAL CHARACTERISTICS OF THE CARBON AMORPHICITY

As mentioned earlier, sp^2 aCs present only a part of aCs that form a large allotropic class of solids, both natural and synthetic. Many books and reviews are devoted to the issue, among which [15–31], but a few, allow the reader to create his/her own idea of the complexity and high science intensity of the touched issue. Natural amorphics are products of nature's laboratory for geological billion-million-year time. Geologists' examinations suggest a few classification schemes of carbon species [32–35]. One of which, presenting a continuous evolution of aC as increasing

Table 1

sp^2 Amorphous carbons selected for a joint study

No	Samples	Abbreviation	Origin	References
1	Shungite carbon	ShC	Shun'ga deposit of Karelia, Russia	[7]
2	Anthraxolite	AnthX	Pavlovsk deposit of Novaya Zemlya, Russia	[8]
3	Anthracite	AnthC	Donetsk deposit, Russia	[9]
4	rGO	Ak–rGO	Institute of the Inorganic Chemistry, RAS, Moscow, Russia	[10]
5	rGO	TE–rGO	Institute of the Chemical Physics, RAS, Moscow, Russia	[11]
6	Black carbon	CB632	Sigma-Aldririch-Merk company, USA	[12]
7	Black carbon	CB624	Sigma-Aldririch-Merk company, USA	[12]

carbonization rank of pristine carbonaceous masses into ordered crystalline graphite thus exhibiting the main stream of carbon life in nature [36], is shown in **Fig 1***a*. As seen in the figure, a general motion is split into two gloves, the left of which starts with plants and sediments, proceeds through sapropels to brown coals, and later to convenient coals and anthracite, finishing with graphite. As for the right glove, it covers carbonization of pristine gas and distillate oil and proceeds through petroleum and naphthoids, to asphalts, and then to kerites, anthraxolites, and shungites. As in the previous case, graphite is the endpoint. This scheme is related to sp^2 aC that actually dominates in nature [36]. Natural sp^3 aC is not as largely distributed, due to which diamond-like amorphous solids have only recently become top issues of the carbon mineralogy [37,38].

The family of synthetic aCs is quite large, covering species different not only by the carbonization rank, but also by a mixture of sp^2 and sp^3 components. Analogously to natural species, synthetic amorphics were classified as well [36,39,40] and the relevant classification scheme is presented in Fig. 1*b*. Previously ternary, it was completed to a rhombic one to take into account oxygen as another important ingredient [36]. Comparing schemes presented for natural and synthetic aCs, it becomes evident that if natural aCs belong to sp^2 carbon family and are carbonization-rank characterized, synthetic aCs are mainly sp^3-configured solid carbons. The sp^2 group

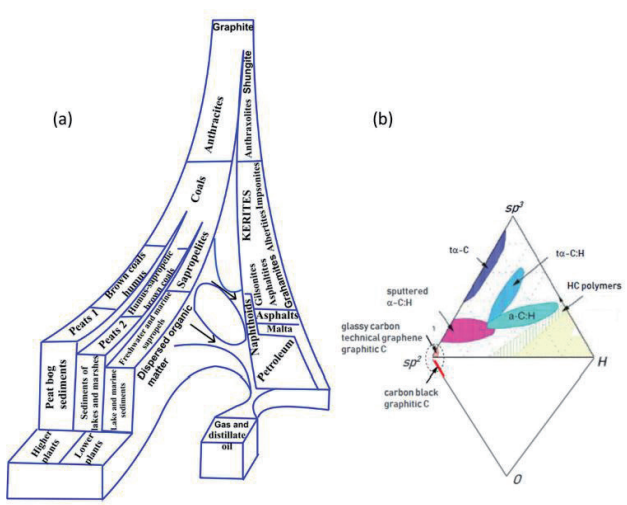

Fig. 1. *General classification of amorphous carbon. (a) Carbon life path in nature according to the Uspenskiy's classification. (b) Rhombic diagram of synthetic amorphous carbon-hydrogen-oxygen system.*

of the synthetic species, characterized by the highest carbonization, takes only a small oval-mapped place. Because of the small amount of sp^3 solid aC in nature, special technologies to produce ta–C, ta–CH (t means tetragonal), and sputtered sp^2 & sp^3 mixed a–C:H products were developed. It is necessary to complement this part of carbon solids by graphite oxide (GO), which corresponds to sp3 configured carbon with up to ~ 40% of oxygen in the case of complete oxygenation. As for sp^2 synthetic aCs, for a long time they were presented by multi-tonnage industrial production of glassy carbon, covering graphitic, black, activated, and other highly carbonized products [41]. However, the graphene era called to life a new high-tech material—technical graphenes, or rGOs [13], which are the final product of either oxidation-reduction [10,42] or oxidation-thermally-shocked exfoliation [11,43] of nanosize graphite. Two new members of this community are on the way—laser-induced graphene (LIG) manufactured by multiple lasing on cloth, paper, and food [44] and extreme quality flash graphene (FG) [45], closest in ordering to graphite.

Despite aCs having been the object of study and practical use for hundreds of years, only recently have they been considered from the general concept of the solid-state physics [36] basing on fundamentals of the amorphicity of solids accumulated in monographs [3]. The first conceptual issue concerns a considerable degree of amorphous solid ordering that is subdivided into short-range (local) and medium-range ones, the boundary between which passes around a few nm. The second issue is related to the direct interconnection of the solids' properties and their local ordering due to which establishing a short-range structure has always been the main goal of study. The peak development of this topic of solid-state physics was reached in the third quarter of the previous century. Historically, the most attention has been given to monoatomic Si and Ge, which, it would seem, is quite conducive to our study, since carbon, silicon, and germanium form a common tetrel's family of the Mendeleev's table so that a similar behavior could be expected of all the members. As was found, tetrahedrally bonded sp^3 configured atoms form the short-range order of Si and Ge amorphous solids. However, in the case of carbon, as seen in Fig. 1*b*, similar amorphous compositions of carbon are concentrated only near

sp^3 corner and are related to the ta–C phase. This internal protest of carbon atoms against the sp3 hybridization of their electrons in the solid state is confirmed by extremely severe conditions for the formation of diamonds (40 GP and 960–2000°C) [46]. In contrast to Si and Ge, the main part of the pure C-solids is sp^2-configured. A comprehensive discussion of this peculiarity related to the tetrel's family members is outside the topic of the current review and can be found in monograph [28]. Thus, monoatomic solid carbon has the unique ability to form amorphous (as well as crystalline) states of two types, characterized by fundamentally different short-range orders presented by either tetrahedral sp^3 groups of bonded atoms or an sp^2 honeycomb network of benzenoid units, graphene domains, thus strongly differentiating sp^3 and sp^2 aCs. Throughout this review, we will mainly talk about sp^2 aCs.

Recent comparative studies [47–50], taken together with a large pool of individual data, have shown that the general architecture of both natural and synthetic sp^2 aCs is common and can be characterized as a multilevel fractal structure [36,51,52], albeit differing in detail at each level. The structure of the first level is similar in all the cases and is presented by necklaced graphene BSUs introduced earlier. The necklacing plays a decisive role, ensuring the formation and stability of short-range order, on the one hand, and preventing graphitization, on the other [1,2], thus allowing the attribution of the sp^2 aCs origination to the reaction amorphization [3]. The second-level structure is provided with nanometer-thick BSU stacks, which were confidently recorded by X-ray and neutron diffraction structural studies of sp^2 aCs of all types [48]. Once standard, BSU stack pattern forces us to expand the amorphics' short-range order, completing individual BSUs with their stacks and thus distinguishing sp^2 aCs from routine molecular amorphics [4,53,54]. The third-level structure of the amorphics reliably follows from the porous structure evidently observed experimentally [52,55]. It is constructed from the BSU stacks but the final compositions depend on the stacks' lateral dimension. When the latter is at the first nanometers level, the composition presents globules of ~10 nm in size, which well correlates with pores, the size of which is first nanometers as well [52,56]. Further aggregation of globules leads to the formation of micro-nanosize agglomerates with pores of tens nm and more [52]. Such a structure is typical to natural sp^2 aCs such as shungite carbon, anthraxolite, anthracite, as well as black carbon coating of diamonds [57], mixed carbon-silica spherical 'sweets' [58], black carbon in meteorites [59,60] and metamorphosed polymictic sandstones [61], biogenic carbon, originated from anaerobic oxidation of methane [62], and none of the exclusions have been known so far. **Fig. 2** presents the evolution of the structure of this kind of sp^2 aC from a single BSU to macroscopic rocks. A schematic structure of a globule, shown in the figure, is designed on the data related to shungite carbon. Molecule $C_{66}O_4H_6$ constitutes one of the possible models of the BSUs based on the graphene domain

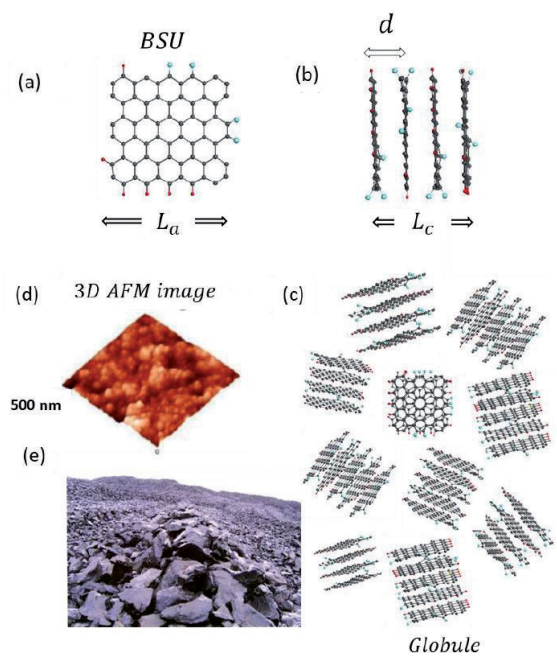

Fig. 2. *Multi-level structure of sp^2 amorphous carbons, BSU size of which constitutes first nanometers. (a) Single necklaced-graphene BSU ($C_{66}O_4H_6$ for shungite carbon* [36]*). (b) Four-layer BSU stack. L_a and L_c are linear size of BSU and BSU stack thickness of 1.2 nm and 1.4 nm, respectively; d is interlayer distance of 0.35 nm. (c) Planar view on a model globule composed of different stacks, the latter consisting of BSU layers from 4 to 7, differently oriented to each other, with total linear dimensions of ~ 6 nm [1]. Gray, red and blue balls depict carbon, hydrogen, and oxygen atoms, respectively. (d) 3D AFM image of globular structure of shungite carbon powder* [36]*. (e). Karelian shungite carbon deposit* [63]

C_{66} [49]. The model is commensurate by size with real BSU and its heteroatom necklace is composed basing on chemical data of the species established in [48]. Combined into four-, five-, and six-layer stacks in accordance with empirical structural data [47–50], the molecules create a visible picture of the nanoscale globules, further agglomeration of which provides the final nanostructured view of the species presented by the 3*D* AFM image in the figure. In contrast to natural bodies, synthetic amorphics are characterized by a large dispersion of BSU size from units to tens and/over first hundreds of nanometers. At the low-limit end of the dispersion, their structure is similar to that of natural species described above. At the high-limit end, the BSU size does not prevent from BSU packing in nanosize-thick stacks while the latter laterally extended are further packed in a paper-like structure. The above concept concerning sp^2 aCs structure is based on planar BSUs. The latter are indeed characteristic of real structures, evidence of which are numerous. However, from time-to-time images of natural solids exhibit bent fragments. The issue will be discussed in Section 3.2.

As mentioned earlier, sp^2 aCs do not match any of the known types of disorder that are characteristic for monoatomic covalent solids [3]. Considering this, the sp^2 carbon amorphization can be attributed to enforced fragmentation of graphite [36]. Obviously, fragmented product can be obtained from both the top and bottom. In the first case, it means the disintegration of pristine graphite, while in the second case, it concerns stopping the graphitization of pristine graphene lamellas. There might be various reasons for fragmentation, including mechanical impact, chemical reaction, temperature shock, exposure to hard radiation, etc. However, each fragmentation act is completed with a chemical reaction providing stabilization of necklaces around fragmented graphene domains. Thus formed BSUs, mainly, and their stacks, additionally, ensure the short-range order of the sp^2 aCs. They are characterized by large variety with respect to not only different classes of aCs, but to the same class as well. The variety concerns the BSU size, shape, variation of necklace chemical content, and, most importantly, the local distribution of heteroatoms in the BSU necklaces at fixed atomic percentage on average. Thus, to complete empirical analytics of sp^2 aCs with a virtual one, a large family of NGMs should be associated with each real sample [64]. A single member of the family, shown on the top of Figure 2, is only 'one snapshot' of communities related to one of the possible permutations of hydrogen and oxygen atoms in the framing area.

Completing the introduction, a few words should be added about the radical nature of the sp^2 aCs BSUs. The latter is provided with chemical activity of valence uncompensated sp^2 carbon atoms, among which non-terminated edge atoms of graphene domains (these atoms of the NGM $C_{66}O_4H_6$ are clearly seen on the top of Figure 2) are the most active. In spite of this, the BSUs remain stable radicals due to the spin-delocalized character of the molecule radicalization provided by the conjugation of unpaired sp2 electrons over the total number of carbon atoms, nearly degenerated spin-triplet energy gap E_{ST}, incorporation of heteroatoms (O, N, S) inside benzenoid units or outside the latter [65]. The sleeping activity of the bodies can be stimulated by the additional fragmentation [66], as is in the case of the sp^2 aCs catalytic application [67].

3. STRUCTURE OF SP² AMORPHOUS CARBONS

3.1. Short Foreword

Once started as classical continuous bulks, today's sp^2 aCs unhesitatingly take their place among nanotechnological materials. Their scientific perception was developing alongside the growing material science, receiving at each turn of the progression a stimulating pulse of a deeper penetration into the understanding of their nature. This development, support, and stimulation would not have been possible without simultaneous progress of instrumental analytical technology. Such a coordinated movement clearly manifested itself to be applied to the structural studies of sp^2 aCs. A perfect historical review on the structure of carbon materials explored by local transmission electron microscopy and global powder diffraction probes [68] presents this growth in the best way. A set of modern techniques, suitable for studies of the structure of nanomaterials, includes atomic force microscopy (AFM), scanning electron (SEM), scanning transmission electron microscopy (STEM), high-resolved transmission electron microscopy (HRTEM), X-ray powder diffraction (XRPD), and thermal neutron powder diffraction (NPD). All these

methods have their advantages and disadvantages, and none of them is sufficient to completely disclose the sp^2 aCs structure. The best success is achieved with the joint use of electron microscopy (EM) and powder diffraction (PD) [68]. It is this combination which will be the focus of this review as well.

Structural studies of sp^2 aCs are obviously complicated by the multilevel structure of a real object. Starting from the bottom, the amorphic structure gradually becomes more complex from individual BSUs to BSU stacks, then to globules of aggregated stacks, and finally to micro- and/or macro-scopic agglomerates. None of the analytical methods described above "sees" the structure of the matter in its entirety. Thus, individual BSUs, which are molecular entities, are not atomically seen by any of the methods. Only HRTEM makes it possible to detect the presence of individual BSUs of first nm in size as bar-like images of vertical projections of the areas occupied by carbon atoms. Simultaneously, HRTEM reveals the presence of BSUs' stack structure thus making possible to estimate the degree of turbostraticity in the latter [69,70]. If the corresponding microscope is equipped with a console that provides fixation of the electron beam diffraction on the sample, then it may determine the interlayer distance d inside the stacks of BSUs [13]. In the number of cases related to medium-resolution either TEMs or STEMs, it is possible to reveal well-structured globules of 10–20 nm in size. Images obtained with submicron-resolution EM instruments, as well as with AFM, represent the samples under study in the form of microscopic agglomerates. It should be taken into account that all EM methods deal with a strictly limited part of the object under consideration. All the obtained results are local and may change, sometimes significantly, when passing to another place of the studied sample.

XRPD and NPD are powerful techniques related to samples as a whole. However, they concern the stack structure only, but allow determining not only interlayer distance d inside the stacks, but linear dimension L_a of BSUs, that constitute the stacks, as well as thickness of the latter L_c (see the description of the values in Fig. 2). Because of significant variability of the sample amorphous structure, the obtained data are statistically averaged and may differ from local ones, obtained microscopically.

Summarizing this short foreword in terms of amorphous state physics, we may state that the modern structural techniques can distinguish short- and middle-range order of solid sp^2 aCs, but in different way. Thus, HRTEM sees the former quite definitely, both as individual BSUs and as stacks of them, but quite locally with respect to the sample body. STEMs of high resolution may visualize the second one as globules of stacks, also locally. Both PD techniques visualize the short-range order in statistically averaged values of the interlayer distanced d in stacks, the stack thickness L_c, and linear dimension of BSUs L_a, composing the stacks [69]. In what follows, a representative set of sp^2 aCs will be presented in light of EM an PD techniques applied together. This investigation concerns a set of samples listed in Table 1.

3.2. Electron Microscopy

Fig. 3 presents a collection of EM results that demonstrate the analytics ability. A comparative view of the images presented in Fig. 3*a–c* allows seeing that microscopic particles of the solids have a common inner structure based on nanosize elements. At the same time, the structures themselves are quite different, apparently evidencing different characteristics of aggregation that precede the solidification. Evidently, the latter occurs differently in nature (cf. Fig. 3*a,b*) while being similar in nature

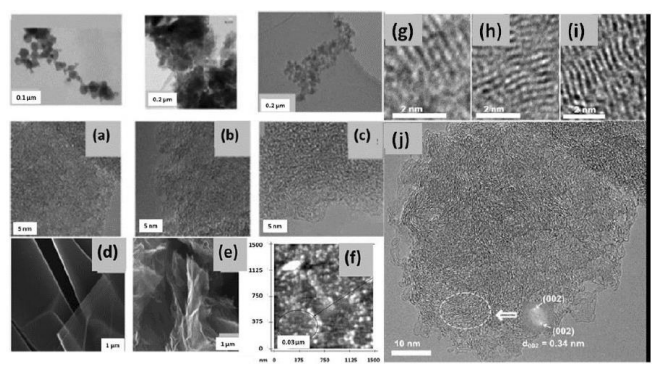

Fig. 3. *Multilevel structure of sp^2 amorphous carbons in light of electron microscopy. (a–c) STEM (top) and HRTEM (bottom) images of ShC (a), AnthX (b), and CB of Sigma-Aldrich-Merk (c). (d) and (e) SEM images of paper-like technical graphenes Ak-rGO (d) and TE-rGO (e). Adapted from Ref. [49]. (f) SEM image of globules' aggregates [7]. (g–j) HRTEM images of the atomic structure of ShC: stacks of flat (g-h) and bent (i) BSU layers. General view of a ShC particle (j), for which Fourier diffraction pattern of the indicated area (see inset) was obtained. Adapted from Ref.* [13]

and industry (cf. Fig. 3*a,c*), and again differently when going from industrial production of carbon black to chemically synthesized Ak-rGO and TE-rGO (cf. Fig. 3*c–e*). In the latter case, both GO and rGO often present paper-like solids [42]. At the same time, HRTEM studies of these solids reveal a picture similar to those shown in Fig. 3*a–c*.

When EM, used earlier to study shungite carbon [71,72] in particular, did not allow for establishing the multilevel structure of sp^2 aC unambiguously, today the possibility of using it with different magnifications makes it possible to reliably verify this. This can be traced when looking at Fig. 3*a,f*. As the resolution increases, the structure of microparticles (conditional fourth level of the ShC structure) in Fig. 3*a* is replaced by aggregation of globules with an average size of tens nm (third-level structure) in Fig. 3*f* and then by a set of elements of the first nanometers in size (second- and first-level structure) in Fig. 3*a*. Similar globular images were observed for anthraxolites as well [73,74].

Fig. 3*g–j* present a detailed view of the first two-level structure of shungite carbon [13]. Bars from several fractions of a nanometer to several nanometers long are clearly visible in these images. They are the projections of carbon atom planes oriented almost parallel to the electron beam. It is clearly visible that these structural fragments are grouped into stacks. The distance between fragment planes in the stacks was estimated using a tight connection between the HRTEM image and diffraction of the electron beam providing Fourier diffraction patterns of the former [75]. Thus, the selected region in the HRTEM image in Fig. 3*j* has a Fourier diffraction spot pattern, which corresponds to the interlayer spacing (d = 0.34 nm) of a disordered graphite-like material [13].

The atomic planes grouped into stacks of 4–7 layers are clearly visible in Fig. 3*g–i*. As is seen, flat fragments are indeed characteristic of the real structure and are numerous. However, the images also contain bent fragments. Since interlayer spacing d for bent fragments is usually 0.34–0.38 nm, any chemical modification of BSUs within their basal planes, which might cause the bending, should be excluded. Accordingly, it was suggested to explain the bending of primary flat BSUs by the existence of various mineral inclusions outside the units. In fact, such impurities accompany ShC formation (from silica micro- and nanoparticles to metal nanoparticles

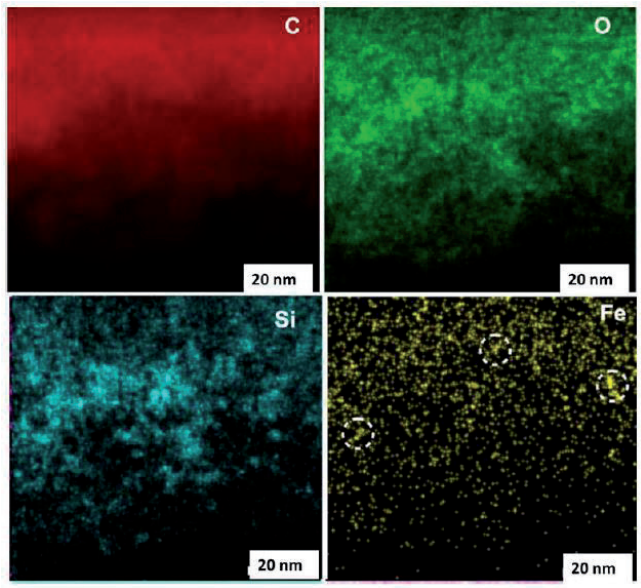

Fig. 4. *HRTEM element mapping of sp^2 amorphous carbons. Shungite carbon in the light of C, O, Si, and Fe elements. The circles in the iron map indicate nanoclusters.*

[7]). Proving the suggestion has revealed a unique opportunity of HREELS to study the atomic structure and the elemental composition of the substance under study. The latter can be disclosed when EM is combined with point-like energy dispersive spectral (EDS) analysis. **Fig. 4** presents an example of the ShC elemental composition mapping with respect to C, O, Si, and Fe constituents. It is seen that only carbon is uniformly distributed throughout the sample, whereas other elements are heterogeneously dispersed. The iron map attracts a particular attention revealing cluster segregation of fractions of a nanometer in size. Similar clusters, containing other metals, are observed as well. Primary BSUs may willingly cover metal nanoparticles and bend, similarly to graphene sheet placed on a heap of gold nanoparticles [76].

3.3. X-Ray and Neutron Powder Diffraction

X-Ray diffraction and elastic neutron scattering are widely applied to determine short-range order parameters of amorphous materials [77–79]. **Fig. 5** presents a typical set of data that provide such structural data relating to sp^2 aCs that concern BSU stacks and BSUs themselves. As is known, diffractogram reflexes Gr (*00l*) are mainly sensitive to the interlayer distance in graphite-like bodies while Gr (*hk0*) ones involve information related to graphite-like structure in the layer plane [68]. As seen in Figure 5*a,b*, all the plottings are similar and

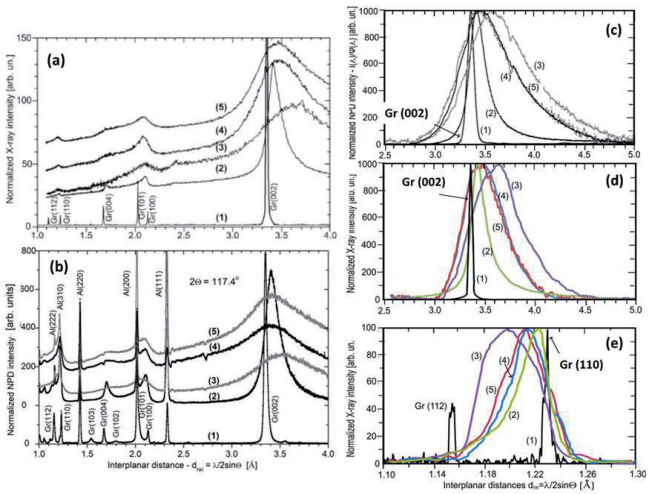

Fig. 5. *Powder diffraction in the service of short-range structure determination of sp^2 amorphous carbons. (a) Panoramic views of XRPD plottings of sp^2 aCs and graphite. (b) The same related to NPD. (c) Normalized intensities of the NPD Gr (002) reflexes. (d) The same concerning XRPD. (e) Normalized intensities of the XPRD Gr (110) reflexes. (1)–(5) mark Gr, CB624, CB632, ShC, and AntX. See the sample nomination in Table 1 and plottings details in Ref. 48. Graphite of Botogol'sk deposit* [81] *was used as standard.*

quite scarce, once expectedly concentrated around reflexes Gr (*002*). The abandon richness of NPD spectrograms is usually provided with numerous additional reflexes caused by neutron scattering in crystalline aluminum of a cryostat (see detailed comments in Ref. [80]). Gr (*002*) reflexes are located in the region of 3.3–3.5 Å, which determines interlayer distance d along c axis between the neighboring layers in graphite thus pointing to undoubted graphite-like stacking of the relevant BSUs. No less important are reflexes Gr (*110*), located in the region of 1.1–1.3 Å, which characterize the size of BSU stacks in lateral directions [69,70]. As seen in the figure, for all the studied sp^2 aCs Gr (*002*) and Gr (*110*), reflexes are shifted (up and down, respectively), as well as considerably broadened, pointing convincingly to a considerable size restriction for the relevant BSUs in both directions.

The broadening of diffraction reflexes is usually attributed to the narrowing of the coherent scattering region (CSR) of a scatterer in the relevant direction [82–84]. According to Scherrer's formula, the full width at half maximum (FWHM) of diffraction peak B and the CSR length L_{CSR} are inversely connected:

$$L_{CSR} = k\lambda/B\cos\Theta. \quad (1)$$

where λ and Θ are the neutron and/or X-ray wavelength and scattering angle while k is a factor depending on the reflex under study [82]. The factor determination is a permanent problem of a quantitative diffraction study of nanosize objects. However, when the study is performed for a set of samples under the same conditions, L_{CSR} can be addressed to the reference one as [80]:

$$L_{CSR} = (B_{ref} / B)(\lambda / \lambda_{ref})L^{ref}_{CSR}, \quad (2)$$

where, L^{ref}_{CSR}, evidently attributed to crystalline graphite, constitutes ~20 nm along both c and a directions [85].

A comparative view of Gr (*002*) and Gr (*110*) reflexes of sp^2 aCs is presented in Fig. 5*c–e*. As seen in Fig. 5*c,d*, NPD and XRPD reflexes Gr (*002*) are similar. Gr (*110*) reflexes are less intense and quite noisy due to which the usual abandon richness of NPD seriously prevents accurate working in the place while XRPD reflections remain accessible. **Table 2**

Table 2

Parameters of the short-range structure of sp^2 amorphous carbons[1].

Samples	d (Å)	L_c, nm	Number of BSU layers	L_a nm	Ref
ShC	3.47(n); 3.48(X)	2.5(n); 2.0(X)	7(n); 5–6(X)	2.1(X)	[48]
AnthX	3.47(n); 3.47(X)	2.5(n); 1.9(X)	7(n); 5–6(X)	1.6(X)	[48]
AnthC (Donetsk)	3.50(X)	2.2(X)	5–6(X)	2.1(X)	[49]
Ak-rGO	3.50(n)	2.4	7(n)	>20	[5]
TE-rGO	3.36(n)	2.9	8(n)	>20	[12]
CB632	3.57(n); 3.58(X)	2.2(n); 1.6(X)	6(n); 4–5(X)	1.4(X)	[48]
CB624	3.40(n); 3.45(X)	7.8(n); 4.1(X)	23(n); 12(X)	2.5(X)	[48]
μncr Gr	3.35	>20	~100	>20	[48]

[1]Notations (*n*) and (*X*) indicate NPD and XRPD data, respectively; [2]The definition "> 20 nm" marks the low limit of the dimension pointing that it is bigger than the CSR of crystalline graphite equal to ~20 nm along both a and c directions. Actual dimensions are of micrometer range.

accumulates L_c and L_a data, determined by applying Equation (2) to the obtained data. As seen in the Table, maximum positions, *d*, of Gr (*002*) reflexes, provided by NPD and XRPD measurements of the studied aCs convincingly evidence that all the samples consist of stacks formed by graphene-like BSUs. The average interlayer distance in the stacks constitutes $d = 3.47 \pm 0.10$ Å, thus remarkably exceeding *d* in graphite crystals. This was to be expected, since the components of the BSU stacks are not flat one-atom-thick bare graphene domains, but NGMs. The van der Waals thickness of the necklace heteroatoms and their possible deviation from the domain plane is the main reason for the increase in this standard graphite parameter.

4. GENERAL ATOMIC CONTENT OF SP2 AMORPHOUS CARBONS

4.1. Short Foreword

Since BSUs are responsible for the short-range order of sp^2 aCs, it is these bodies that govern the chemical content of the whole solid. Evidently, the presence of BSUs' necklaces determines the unavoidable heterogeneity of the latter. The necklace contribution into the total atomic content is structure-sensitive. It gradually decreases from a few at % to a negligible amount when the BSU size grows from the first nanometers to micrometers. As seen in **Table 2,** BSUs of the selected set of sp^2 aCs are nanosize to be proper for heterogeneous chemical analysis. Modern analytic techniques are usually specified for the determination of particular sets of elements. Carbon, hydrogen, and oxygen are the main triad of organic chemistry, so that their dominant presence in the aCs is fully expected. Analyzing the available assortment of analytic techniques, one can make sure that practically all of them are able to fix carbon. As for hydrogen and oxygen, the techniques are distinctly divided into {C,H}, {C,O}, and {C,H,O} groups. Following this division, we subordinate further description to this grouping.

4.2. {CH} Analytics

Analytic techniques are qualitative, quantitative, or mixed. The first are those based on chemical or physical properties that reveal a strong dependence on the chemical entity under study. In the case of sp^2 aCs, combustion and incoherent inelastic neutron scattering (IINS) of hydrocarbons are widely used for detecting hydrogen. The former lays the foundation of differential thermal analysis (DTA) and differential scanning calorimetry (DSC) [86], the latter, less popular, presents inelastic incoherent neutron scattering (IINS) vibrational spectra [87].

The DTA/DSC analysis mainly concerns the *brutto* content of sample carbon, so called *fixed carbon* following the equation

$$\% \text{ Fixed Carbon} = 100 - (\%\text{Adsorbed Water} + \%\text{Ash} + \%\text{Volatile Matter}) \quad (3)$$

The fixed carbon is definitely not carbon-pure and must at least include hydrogen and oxygen components, which are highly combustible constituents in addition to carbon. As occurred, DSC thermograms of a set of sp^2 aCs, obtained at the same conditions, are quite different [48] while the carbonization of all the samples is over 90%. **Fig. 6***a* presents the data collection, which evidently

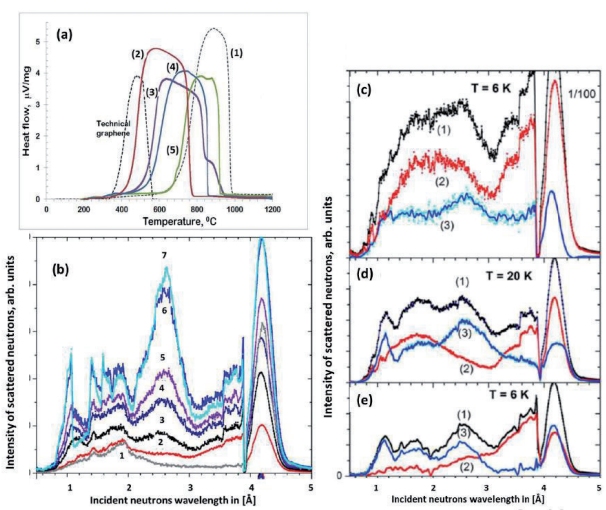

Fig 6. *Hydrogen detection in sp^2 amorphous carbons. (a) DSC thermograms of as prepared solids: spectral Gr (1), ShC (2), AntX (3), CB632 (4), and CB624 (5) [48]. DSC curve of the lab rGO is reconstructed from experimental data presented in Ref. [88]. (b) Time-of-flight IINS spectra of water gradually added to CB632. 1, 2, 3 mark scattering from Al-cryostat, dry and as prepared samples, respectively. (4–6) Spectra of water loaded in 100g of as prepared CB632 sample in ml: 0.5 (4), 1.0 (5) and 2.0 (6). (7) 2.5 ml of water loaded in as prepared CB624 sample. (c)–(e) Normalized TOF IINS spectra of sp^2 amorphous carbons after subtracting the Al-cryostat background: AntX (c), ShC (d), CB632 (e). Digits mark spectra of as prepared (1) and dry (2) samples as well as adsorbed water (3), the latter obtained as the difference between spectra (1) and (2) (see details in* [47]).

reveals changes in the temperature of the process onset T_{ost}, from 370°C to 720°C. Thus, as seen in the figure, T_{ost} of graphite is the largest. In contrast, on the opposite side of the observed series of the DSC thermograms, there is one related to a lab-produced rGO [88], Tost for which constitutes 370°C. As is known, rGOs, both natural and synthetic, usually contain a few wt% of hydrogen. Accordingly, the presented DSC series may evidence a gradual depletion of hydrogen content in the sp^2 aCs series from ShC to CB624 and graphite. In this case, the T_{ost} below 720°C obviously indicates the hydrogen presence in the solid, therewith, the lower the T_{ost}. DTA/DSC are fully qualitative techniques. However, a comparative study of a set of samples under equal conditions allows for disclosing a solids' comparable series following the decrease in hydrogen content, such as the following:

rGO > ShC > AntX > CB632 > CB624 > Gr.

In its turn, protium is a peculiar hydrogen isotope of the largest cross-section for the IINS among all the elements, making the relevant techniques highly protium sensitive. The abundance of a real hydrogen isotope family with protium readdresses the statement to chemical hydrogen [87]. Thus, water is willingly adsorbed with both natural and synthetic sp^2 aCs, which is evidently caused by their porous structure and hydrophilic nature of the BSUs necklaces that cover inner walls of pores. Expectedly, Fig. 6*b* presents a strong reaction of IINS spectra on the gradual hydration of CB632. As shown in Fig. 6*c–e*, each as-prepared sp^2 aCs involves a large quantity of adsorbed water and must be freed from it before analysis for the hydrogen content. In their turn, dry samples of the latter still remarkably scatter neutrons, thus exhibiting the hydrogen presence in the solids related to the necklaces of their BSUs. So far, none of IINS' quantitative analyzes for hydrogen in sp^2 aCs has been developed, leaving it mainly qualitative. However, when a study of a solids' set under equal conditions is possible, a comparative analysis of the obtained IINS spectra, as is in the case presented for dry samples in Figure 6*c–e*, allows a confident conclusion that the hydrogen content in the AntX and ShC BSUs is comparable, while that one for the CB632 is much lower. The relevant comparative series of samples looks like the following:

ShC ≈ AntX > CB632 > Gr.

This tendency is quite similar to the one followed from the DSC data in Figure 6*a*, while not identical. Apparently, it may be caused by the fact that DSC results were obtained for as-prepared samples that could not be fully freed from the adsorbed water.

In contrast to the above techniques, a combustion-based elemental analysis (EA) can provide a qualitative hydrogen analysis of sp^2 aCs. Standard CHNS EA involves determination of carbon and hydrogen contents supplemented with the detection of nitrogen and sulfur. It does not determine oxygen content directly and the relevant data are just residual content of 100 wt% samples mass after excluding all other contributions. The hydrogen data related to the solids listed in Table 1 are presented in **Table 3.** The comparative sample series looks as follows:

AntC > AntX > TE-rGO ≈
≈ Ak-rGO > ShC > CB632 > CB624.

There is much common and different in the triad of comparative series evidencing that obtaining exact values of hydrogen content even in the same samples of sp^2 aCs is hardly possible. None of the

Table 3

Chemical content of BSUs of sp^2 amorphous carbons

Samples	Elemental analysis, wt%						XPS analysis, wt%			
	C	H	N	O	S	Ref.	C	O	Minor Impurities	Ref.
ShC	94.44	0.63	0.88	4.28	1.11	[48]	88.5	8.6	2.9	[48]
AnthX	94.01	1.11	0.86	2.66	1.36	[49]	89.5	7.7	2.8	[48]
AnthC	90.53	1.43	0.74	6.44	0.89	[49]	89.6	8.1	2.3	[49]
TE-rGO	84.51	1.0	0.01	13.5	1.0	[49]	82.3	14.8	2.9	[49]
Ак-rGO	89.67	0.96	0.01	8.98	0.39	[49]	89.5	7.6	2.9	[49]
CB624	89.67	0.18	0	0.15	-	[48]	93.1	5.9	1.0	[48]
CB632	97.94	0.32	0.04	1.66	0.68	[48]	90.7	7.8	1.5	[48]

techniques are free from particular limitations related to both the performance and interpretation of the results obtained. However, all of them are highly important and useful.

4.3. {CO} ANALYTICS

Since CHNS EA does not provide the determination of the oxygen content, EDS and X-Rays photoelectron spectroscopy (XPS) take on the main role. Both techniques are qualitative and quantitative, thus detecting the oxygen presence in samples and determining its atomic percentage. **Fig. 7** presents a general view on these techniques' abilities. Qualitative EDS, known as EDS mapping, allows for registering of the distribution of a selected element over the sample by monitoring its monochromatic X-ray emission [89]. Typical EDS maps for ShC are presented in Fig. 7*c–e*. As seen in Fig. 7*e*, oxygen is largely presented in the solid. The quantitative EDS analysis (Fig. 7*a*) concerns a comparison of the intensity of element-wave-dependent X-ray emission with that of a standard reference element registered at identical conditions. A characteristic feature of EDS is the localized

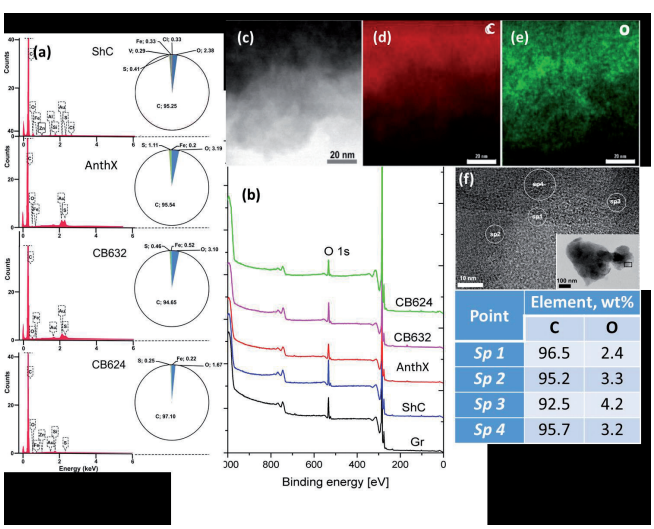

Fig. 7. *Oxygen detection in sp^2 amorphous carbons. (a) EDS spectra and content diagrams of dry sp^2 amorphous carbons. Spherical diagrams visualize the samples chemical content, details of which are given in Ref.* [48]. *(b) XPS survey spectra of as prepared amorphous carbons and graphite GSM2 at room temperature* [48]. *(c)–(d) Dark-field HRTEM of an edge fragment of ShC particle (c) and its element EDS mapping for C (d) and O (e) elements. (f) Localization of EDS point elemental analysis of ShC, the data of which are listed in table below. The inset marks the region under study. Details are given in* [13].

character of its data. The measurements are usually performed at inclusion-free sites controlled by EDS maps, similar to the O-map in Fig. 7*e*. The data should be averaged over those determined at several different places for each sample. As shown in Fig. 7*f*, the data related to different places of the sample scatter quite remarkably. Fig. 7*a* presents a collection of EDS spectra of a set of dry sp^2 aCs samples while partitioned chemical components are presented by spherical diagrams. As seen in the figure, the emission spectra are presented by main signals related to carbon, the amount of which covers the region of 95.05÷97.44 wt%, and oxygen of 1.7÷3.3 wt%. In addition, a variable set of minor impurities is usually obtained. EDS analysis confirms that sp^2 aCs are not carbon-pure but involve a few percentages of oxygen and ~1.5 wt% of minor impurities.

In contrast to EDS, XPS data are statistically space-averaged. A general panorama of the survey XPS spectra of a set of sp^2 aCs is presented in Fig. 7*b*. It is usually assumed that a high degree of vacuum provides the release of the studied samples from the adsorbed water. Quantification of atomic content is provided using sensitivity factors from the elemental library of CasaXPS [90]. The XPS spectra of the studied samples look quite similar, evidencing the C1s and O1s spectra of the main chemical components and allowing for the evaluation of atomic percentage of the observed elements by standard technique. The obtained data are given in Table 3. As seen in the table, all the studied sp^2 aCs contain a considerable amount of oxygen.

Concluding the chemical testing, is necessary to pay attention to the following: all the methods allow for the direct determination of carbon content. The dispersion of the latter occurs quite largely and constitutes 95.2÷88.5 wt% for ShC, 95.6÷89.5 wt% for AntX, and 97.94÷90.7 wt% and 99.67÷93.1 wt% for CB632 and CB624, etc., respectively. This feature clearly evidences the multi-elemental character of the species, on the one hand, and the different sensitivity of the used analytical techniques to chemical elements that accompany carbon in the studied samples, on the other. It is important to note as well that all the reference carbons unavoidably used in testing are not pure carbons as well. Oxygen is the main impurity, which may point to a heightened propensity of pure carbons to

oxygenation. Hydrogen is the next contributor. In addition, the hydrogen weight content is comparable with that of other minor impurities involving sulfur, nitrogen, chlorine, silicon, and different metals. The role of the latter is particularly important in the geochemistry of carbon [91,92] or the engineering technology of highly carbonized products [93]. Once concentrated on disclosing the BSU atomic structure, we shall restrict ourselves in what follows by the consideration of carbon–hydrogen–oxygen triad that present necklaced graphene oxyhydrides. The latter are covalent species characterized by a large variety of covalent bonds between the triad elements, attribution of which to particular atomic pairs is provided with the {CHO} analytics of sp^2 aCs.

4.4. {CHO} Analytics

There are many methods for the direct or indirect determination of the composition of covalent bonds. As applied to sp^2 aCs, the most successful are vibrational spectroscopy in the first case and XPS in the second. Vibrational spectroscopy includes a wide range of different methods based on the inelastic scattering of elementary particles (photons, neutrons, electrons, γ particles, neutrinos, etc.). Each of these methods is characterized by its own way of extracting information about the covalent bonds of a scattering substance from the corresponding spectra. Methods for the indirect study of the bonds are based on the reaction of the binding energy of atoms to the presence of other atoms bound to them, the most prominent representative of which is XPS. This method is widely used in the analytics of sp^2 aCs, and that is why we will begin the review of {CHO} analytics with it.

4.4.1. XPS analysis

In contrast to IINS, which is a 'hydrogen tool' and which provides a reliable qualitative test of the hydrogen presence in sp^2 aCs, XPS in general, and its O1s spectra in particular, is considered as the main 'oxygen tool' of the solids. The determination of O/C content, exhibited in Figure 7*b*, is usually followed with a detailed analysis of covalent bonds, formed by the element within the bodies' BSU necklaces. **Fig. 8** presents a general view on a massive set of XPS results, for a selected set of sp^2 aCs listed in Table 1. As mentioned earlier, XPS analysis of chemical bonding is based on

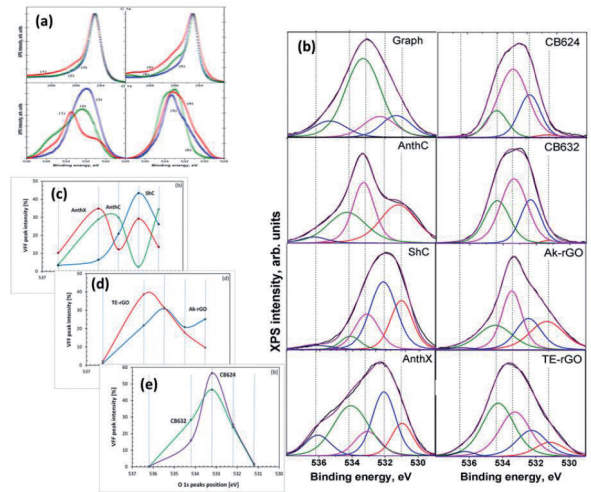

Fig. 8. *sp^2 Amorphous carbon chemical bonds configuration in view of XPS. (a) C1s (top) and O1s (bottom) XPS spectra of AnthC (1); AnthX (2); ShC (3); TE-rGO (4), Ak-rGO (5) and CB632 (6) at room temperature. (b) Expanded O1s XPS spectra and fraction-distributions of Voigt-fitting-function (VFF) peaks of O1s spectra over peaks number of natural (left) and synthetic (right) sp^2 amorphous carbons at room temperature. (c)–(e) Distribution of the VFF peaks intensity over group binding energies for natural (c), synthetic (d) and industrial (e) sp^2 aCs. Details are presented in* [49].

two fundamental facts: (1) the atom-dependent value of binding energy (BE_A) of electrons on internal orbits of the *i–th* atom, BE_{iA}; and (2) the BE_{iA} value's dependence on the *i–th* atom neighboring, which allows disclosing the type of chemical bonding of the atom to other ones. Both features are clearly visible in the case of sp^2 aCs carbon (C1s) and oxygen (O1s) XPS spectra shown in Fig. 8*a*. The tailing of C1s spectra and broad O1s ones are commonly associated with the multi-variable response of carbon and oxygen atoms to their surroundings. For a long time, the relevant XPS spectra have been analyzed in terms of the 'four peaks' approximation that involves groups C–C, C–O, C=O, and COO of C1s spectra and C–O, C=O, C(=O)O, and O=C(O) groups of O1s spectra [94–104]. In the latter case, the corresponding components are usually associated with the simplest oxygen containing groups (OCGs) such as hydroxyls, epoxides, carbonyls, and carboxyls. The approach resulted from the extended XPS study of numerous different polymers of known structures, which laid the foundation for atomic group assignment

Table 4

Group binding energies of O1s XPS spectra attributed to BSUs of sp^2 amorphous carbons (composed from the published data [113]).

GBEs	BE, eV	Assignments
1	531.2	C=O, O=C-O-C=O, O=C-O-C (lactones and pairs of lactones)
2	532.2	O=C-O-C (lactones); O=C-C=O (o-quinones); O=C-OH; C=O in aggregated cyclic ethers with lactone
3	533.2	sp^2C-OH; C-O-C in cyclic ethers; C-O-C-OH (hydroxypyrans: singles and pairs); O=C-O-C (lactones and pairs of lactones); O=C-OH; C-O-C in aggregated cyclic ethers with lactones
4	534.2	C-O-C in aggregated cyclic ethers; C-O-C-OH (hydroxypyran: singles and pairs); C-O-C in aggregated cyclic ethers with lactones
5	536.2	O=C-O-C-O-C-O-C-O-C=O in aggregated cyclic ethers with lactones

to characteristic XPS peaks [105]. However, this approach happened to conflict with IR absorption studies, which revealed much more complicated OCGs, including benzenoid heterocycles such as ketones and quinones, cyclic ethers, lactones and acid anhydrides, furan and pyrans, as well as hydroxypyrans and so on [106–111]. Evident questions were raised in the case of XPS [112], the answers to which were collected in a profound review [113]. Thus, a 'five peaks' approach was suggested to decompose O1s spectra, which was realized with respect to spectra shown in Fig. 8*a* [48,49]. The modified asymmetric Voigt functions [114] were adopted to separate waveforms of XPS spectra following the group binding energies listed in **Table 4**. A full collection of the decomposed data is presented in Fig. 8*b*, while a comparative view of them relating to natural, synthetic, and industrial sp^2 aCs is shown in Fig. 8*c–e*, respectively. Thus, the revealed OCGs related to the BSUs of a selected set of sp^2 aCs are summarized in **Table 5**.

4.4.2. IINS Analysis

A high efficiency of IINS spectroscopy as an H-tool is clearly seen in Fig. 6. Original IINS spectra depend on the instrumentational peculiarities of the spectral devices in use. Accordingly, the spectra recorded either on the NERA spectrometer of the high flux pulsed IBR-2 reactor of the Frank Laboratory of Neutron Physics of JINR, or on the TFXA spectrometer at the ISIS pulsed-neutron source, Rutherford Appleton Laboratory, and on IN6 spectrometer of the ILL should be and, actually are, different. However, evidently, common information related to the vibrations of a scatterer involved in the action can be provided by converting the original data to the generalized density of vibrational states (GVDOS) by the relevant standard programs [87]. A collection of such GVDOS spectra, related to a set of sp^2 aCs listed in Table 1 [49], is shown in **Fig 9**. The spectra concern dry samples after removing adsorbed water. They are provided

Table 5

XPS-revealed oxygen-containing groups related to BSUs of sp^2 aCs, based on data of Refs, 48 and 49.

Samples	Assignments
ShC	carbonyls sp^2 C=O; acid anhydride O=C-O-C=O; o-quinone O=sp^2C-sp^2C=O, carboxyls sp^2C=OOH.
AntX	hydroxyls sp^2-OH; C-O-C-OH (hydroxypyran-HP) and pairs of HPs; C=OOC(lactone) and pairs of lactones; aggregated cyclic ethers with lactones.
AntC	carboxyls sp^2C-COOH; cyclic ethers; aggregated cyclic ethers; pyran and hydroxypyran.
Ak-rGO	aggregated cyclic ethers and aggregated cyclic ethers with lactones; lactones and pairs of lactones.
TR-rGO	aggregated cyclic ethers and aggregated cyclic ethers with lactones; hydroxypyrans and lactones, both singles and pairs.
CB632	C-O-C in cyclic ether and aggregated cyclic ether; C-O-C of pairs of cyclic ether and aggregated cyclic ether with lactone.
CB624	C-O-C in cyclic ether, aggregated cyclic ether and aggregated cyclic ether with lactone

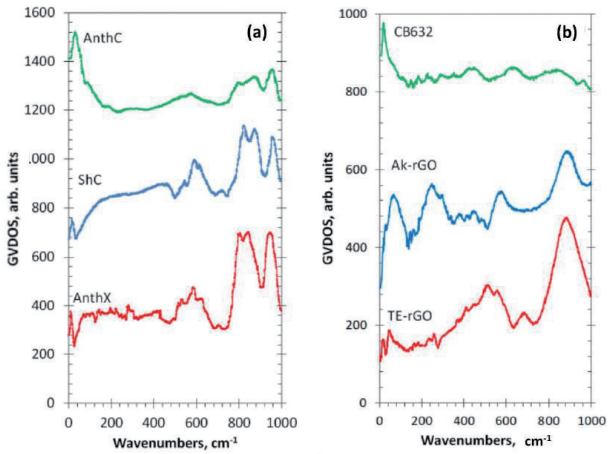

Fig. 9. *Generalized density of state of the hydrogen-involved vibrations of sp^2 amorphous carbons. (a) GVDOS spectra of dry natural solids, derived from IINS spectra at T = 20 K. (b) The same but for industrial and synthetic solids. See details in Ref.* [49].

with both direct scattering from hydrogen atoms, chemically bound with the edge atoms of the BSUs' graphene domains, as well as with enhanced scattering from the carbon atoms of the relevant graphene domains due to the 'riding effect'. The latter is caused by the contribution of hydrogen atoms to the eigenvectors of vibrations related to carbon atoms through the BSU molecules (see detailed discussion of both effects in [5]). The spectra are fine-structured enough to be attributed to particular vibrations, thus establishing the chemical bonding of hydrogen atoms in the solids [87]. As is typical for any vibrational spectroscopy of molecules, group frequencies (GFs) lay the foundation of the covalent bonds analysis [115]. Presented in **Table 6**, GFs correspond to atomic bonding inside (C,X) groups (X = C, H) [49].

The GVDOS spectra in Fig. 9 are definitely divided into two parts. Thus, all the spectra in Fig. 9*a* have much in common in the regions of 960 cm^{-1}, 800 cm^{-1}, and 600 cm^{-1} in spite of being recorded on different spectrometers, namely, ShC and AnthX on NERA [121][1] and AnthC on TFXA [122]. Characteristic spectral features are clearly visible in all the spectra, thus indicating a similar involvement of hydrogen atoms in the scattering. Table 6 accumulates group frequencies widely used in the analysis of vibrational spectra of hydrocarbons [116]. According to the table, first two features are attributed to the in- and out-of-plane bending vibrations of sp^2C-H bonds of methyne groups, while the third one represents ip bendings of carbon atoms of the benzenoid units of the BSU graphene domains enhanced by the 'riding effect'. Therefore, the IINS study of natural sp^2 aCs reveals that, in addition to the similarity in molecular spatial structure of their BSUs, hydrogen atoms in their necklaces predominantly form sets of methyne

Table 6

Group frequencies of aromatic molecules required for the hydrogen-content analysis of vibrational spectra of sp^2 amorphous carbons.

Spectral Region, cm^{-1}	Group Frequencies[1]			
	(C, C)[2]	(C, H_1)[2]	(C, CH_2)[3]	(C, CH_3)[4]
400–700	404 δ *op* C-C-C	673 δ *op* in phase	711 δ CH_2	210 *r* CH_3
	606 δ *ip* C-C-C	846 δ *op*, C_6 libration		344 δ CH_3
	707 C-C-C puckering	967 δ *op*		900 ν C-CH_3
700–1200	993 ring breathing	990 δ op, trigonal	948 ϱ CH2	1041 ϱ CH_3
	1010 δ C-C-C	1037 δ ip		
	trigonal	1146 δ ip, trigonal		
		1178 δ ip		
1200–1600	1309 ν C-C Kekule	1350 δ ip in phase	1409 δ internal CH_2	1333 δ CH3
	1482 ν C-C	3056 ν C-H		1486 δ internal CH_3
	1599 ν C-C	3057 ν trigonal C-H		
2800–3200	-	3064 ν C-H	3114 ν CH_2	2950 ν CH_3
		3073 ν in phase C-H		

[1]Greek symbols ν, δ, ϱ, r, τ mark stretching, bending, rocking, rotational, and torsion modes, respectively; [2]GFs notifications of fundamental vibrations of benzene molecule [116]; [3]GFs notifications of fundamental vibrations of benzyl radical [117,118]. Hereinafter, GFs, additional to the benzene pool of vibrations, will be shown only; [4]GFs notifications of fundamental vibrations of toluene [119,120].

sp^2C–H bonds. An intense peak below 100 cm^{-1} in the AnthC spectrum indicates that besides sp^2C–H bendings, torsions of hydroxyls take part in the scattering. A further support of the latter suggestion is given in Section 5.3.2.

In contrast to natural amorphics, their synthetic and industrial analogues are characterized by significantly different GVDOS spectra, as seen in Fig. 9*b*. A comprehensive analysis of the spectra [49] showed that the formation of methylene sp^2C–CH_2 bonds in the BSU necklaces of the solid was the main motive of the H/C bonding in TE-rGO, while the formation of sp^2C–CH_3 methyls dominates in the Ak-rGO solid. In both cases, the chemical bonding of the BSU necklaces was a direct consequence of chemical reactions that accompanied the reduction of parental graphene oxide [49]. As for the spectrum of industrial CB632, it is very weak while that of CB624 cannot be distinguished over the background at all. This feature points to a practical absence of hydrogen in their BSU necklaces and is evidently connected with the high-temperature pyrolytic conditions of the solids production, which does not maintain the existence of hydrogen-containing radicals in the chemical surrounding. The hydrogen content in CB632 is at the limit of the technique sensitivity due to which only a sharp feature below 100 cm^{-1} marks the presence of hydrogen atoms in the species BSU necklace. Apparently, it may be attributed to the presence of hydroxypyran in the area.

4.4.3. IR Absorption Analysis

Organic chemistry is unthinkable without the widespread use of IR spectroscopy as the main analytical technique. The molecular nature of BSUs of sp^2 aCs undoubtedly puts the latter on par with other objects in the field. The special significance of this type of analysis of sp^2 aCs became apparent after it was found that the heteroatoms of the BSU necklaces, chemically bonded to the graphene domain, make the main contribution to the solids IR absorption spectra [64]. This feature will be discussed in more detail in Section 5.3.2. FTIR and DRIFT techniques are usually used to record the IR absorption spectra of the solids.

DRIFT spectra of sp^2 aCs listed in Table 1 are presented in the top panels of **Fig. 10**. They are combined in groups related to natural, synthetic, and industrial solids. A large variety of the spectra shape convincingly evidence a drastic variation of the chemical content of BSU necklaces of the solids. Evidently, to proceed with the spectra features assignment, a list of GFs related to the (C, O) bonding is needed. Such a list, based on the assignment of frequencies in the experimental spectra of graphene oxides [106,109,113,123] and extended calculations [64,124], is given in **Table 7**. As seen in the Table, practically each spectral region of the spectra is quite ambiguous, which complicates the assignment. However, a combined analysis of IR and XPS spectra greatly facilitates the job. The bottom panels in Fig. 10 present the distribution of the intensity of the Voigt fitting function (VFF) peaks (see Fig. 8*b*) over group binding energies related to oxygen O1s state. The relevant GBEs are listed in Table 4.

A joint DRIFT-XPS analysis of the studied sp^2 aCs shows that the features of these spectra can be described by taking into account the hydrogen and oxygen components of the BSUs' necklaces only [49]. As for the former, it dominates in natural aCs (Fig. 10*a*), and is still significant, but is much less intense in synthetic ones (Fig. 10*b*) and is practically absent in industrial carbon blacks, approaching nil for CB624 (Fig. 10*c*). This tendency is clearly evidenced with a considerable decrease in vertical scales in the figures. In full agreement with the results of the IINS analysis, the main contribution is provided with ip and op bendings of methyne, methylene, and methyl units. It should be noted as well that the

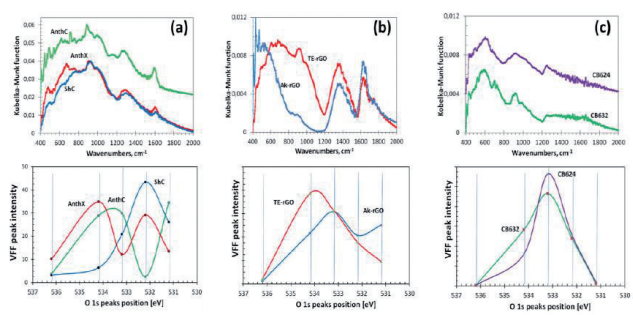

Fig. 10. *Joint DRIFT-XPS spectral analysis of sp^2 amorphous carbons. Top. DRIFT spectra of amorphous carbons at room temperature: natural (a), synthetic (b), and industrial (c) solids. Bottom. Distribution of intensities of VFF peaks of the O1s spectra of the solids presented in Figure 8b over group binding energies listed in Table 4. Adapted from* [49].

Table 7

Group frequencies required for the oxygen-content analysis of BSUs of sp^2 amorphous carbons[1], cm^{-1}.

300–1000	1000–1200	1200–1300	1300–1500	1500–1600	1600–1700	1800–1900	2600–3000	3000–3600
δ *op*², δ *ip*³, τ C-OH sp^2C-O-C and sp^2C-OH δ *op* sp^2C-C-C⁴ δ *ip*, puckering, ring breathing, δ trigonal sp^2C-C-C⁴, collective vibrations of graphene domain atoms⁵	ν sp^2C-O-C in cyclic ether, aggregated cyclic ether and acid anhydride	ν·sp^2C-OH, in lactone, hydroxyl pyran and acid anhydride	δ *ip* sp^2C-OH, ν sp^2C-O-C in cyclic ether and acid anhydride δ *ip*O-C=O in acid anhydride	δ *ip* sp^2C-OH, ν sp^2C-C	ν sp^2C =O in acid anhydride and lactone, aggregated cyclic ether with lactone pair, pairs of lactones	ν sp^2C =O in *o*-quinone, COOH	ν sp^3C-O-H in COOH ν sp^3C-H	ν sp^3C-O-H

[1]Greek symbols τ, δ and ν mark the molecule torsions, bendings and stretchings, respectively; [2]Out-of-plane bendings; [3]In plane bendings; [4]Benzene molecule data [116]; [5]Virtual data for nanographene [125].

hydrogen contribution to DRIFT spectra of natural solids is three–five times more than that of synthetic ones, while the hydrogen contents of the bodies (see Table 3) are quite comparable. This feature evidences that hydrogen atoms, directly attached the graphene domain edge atoms in the former case via sp^2C-H chemical bonds, are optically much more active than those ones involved in either methylene or methyl units via sp^2C –CH_2 and sp^2C –CH_3 bonds, once distant from the BSU domains. This issue was observed in virtual IR spectra of necklaced graphene molecules as well [64,126][2].

As seen in Fig. 10, the oxygen component of the studied solids varies quite drastically, while remaining similar in the samples of each of the three types. Thus, a joint DRIFT-XPS analysis, based on the GBEs and GFs listed in Tables 4 and **Table 7**, allowed for concluding of the following [49]: the oxygen component of the BSU necklaces of ShC may mainly involve carbonyls sp^2C=O and o-quinone O=sp^2C-sp^2C=O bonds. That one of AnthX is of lactone character consisting of C=OOC (lactone) and pairs of lactones, as well as of aggregated cyclic ether with lactone. The oxygen content of AnthC is the richest, involving carboxyls sp^2C-COOH, cyclic ethers, aggregated cyclic ethers, pyran, and hydroxypyran. Aggregated cyclic ethers, aggregated cyclic ether with lactone, and lactones are common for both Ak-rGO and TE-rGO, once completed with lactone pairs in the former case and with hydroxypyrans in the second. Similarly, C–O–C in cyclic ether and aggregated cyclic ethers with lactone form the ground of CB632 and CB624, completing the former case with lactones and/or hydroxypyrans. Obtained data led to the foundation of molecular models suggested for BSUs of the studied sp^2 aCs that are discussed in Section 5.2.

4.4.4. Raman Scattering Analysis

Raman scattering analysis has become a champion among a variety of analytic techniques applied to graphene-like materials, not excluding sp^2 aCs. No articles can be published without referring to the Raman spectra of such materials. This extraordinary situation is caused by the evident exclusiveness of the spectra, a general view of which for a set of sp^2 aCs listed in Table 1 is presented in **Fig. 11**. As seen in the figure, the spectra of samples, characterized by different short-range orders and chemical contents of the relevant BSUs, are practically identical by shape consisting of three characteristic regions named *D, G,* and 2*D* [127,128]. Following the assignment suggested for Raman spectra of crystalline graphite [129], the doublet of *D* and *G* bands corresponds

to a one-phonon contribution, while 2*D* marks the region of two-phonon events.

These one-phonon and two-phonon parts of the Raman spectra in Fig. 11 are not exactly identical, as shown by detailed consideration of the spectra structure [50]. However, a characteristic doublet *D*–*G* remains highly universal. For a long time, there has not been a convincing explanation for both the deep similarity of the spectra as a whole and the exclusive character of the *D*–*G* doublet. Starting from the spectra of crystalline graphite and graphene, consisting of two narrow bands *G* and 2*D*, spectroscopists looking for the band broadening and the appearance of *D* were divided into two groups. The first group members tried to explain the features remaining in the framework of crystal spectrum concepts. This is how the idea arose about the defective origin of the *D*-band [129,130] and about the double-resonance nature of the 2D

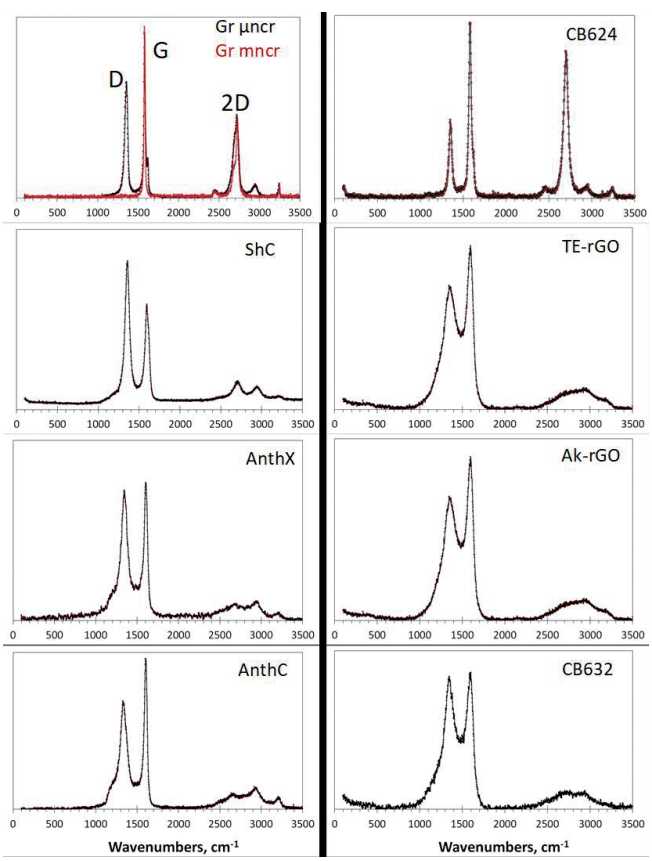

Fig. 11. *Raman spectra of sp^2 amorphous carbons at room temperature: shungite carbon (ShC), anthraxolite (AnthX), anthracite (AnthC), technical graphene TE-rGO and Ak-rGO, carbon blacks CB632 and CB624, as well as mono- (mncr) and micronanocstructured (μncr) Botogol'sk graphites, respectively (see details in* [50]).

one [131,132]. An exclusive role to two parameters of the spectra, namely the ratio of the intensity of the *D* and *G* bands, I_D/I_G , and the corresponding bands half-widths, Δω, was given to characterize the size and defect structures of the relevant graphene domains. Established theoretically for graphene crystal, this relationship was transferred to the molecular BSUs of amorphous substances by default [133,134]. However, as was shown lately [50], such a transfer turned out to be incompetent, which, nevertheless, has not stopped the efforts of the "theoretical description of the defectiveness" of the studied BUSs until now.

The molecular nature of sp^2 aCs underlies the position of scholars of the second group [135–141]. Information presented in previous sections of this article convincingly proves the issue, which makes all the crystal-based theoretical approach practically not applicable. It was shown that the polarizability tensor of a polyaromatic hydrocarbon, to which BSUs evidently belong, depends on the dynamic characteristics of the multimode vibrational spectrum. As occurred, the main contribution to the intensity of the spectra is made by sp^2C–C stretchings, due to which the observed *D*–*G*–2*D* set of bands is mainly characteristic of the network of sp^2C–C bonds. This is the first reason explaining the similarity of Raman spectra of different sp^2 aCs, since similar graphene domains constitute the main atomic part of the relevant BUSs. The second reason concerns the sp^2C–C stretching modes, which are responsible for the bands. It was found that the *G*-band is originated from the $e2_g$ vibration of benzene, while the modes responsible for the *D*-band come from the e1u mode of the molecule. The former provide simultaneous in-plane stretchings of all sp^2C-C bonds, while the latter concern both stretching and contraction of these bonds when carbon atoms move out-of-plane. A final decision of the problem has been obtained recently in the framework of virtual vibrational spectrometry [64]. As occurred, *D*-bands are, actually, caused by out-of-plane sp^2C–C stretchings that provide formation of a dynamically stimulated sp^3C–C bond between the adjacent layers of BSUs' stacks, thus being a characteristic test of a particular short-range order structure of the amorphics. Intensity of the *D*-band increases when the number of layers grows up to 4–5 and then markedly slows down when the total

thickness of stacks exceeds ~15 nm [142]. As for 2*D* region, the same out-of-plane sp^3C–C stretchings are responsible for the features, thus revealing the strongest anharmonicity among other vibrations.

A particular doublet pattern of the spectra strongly depends on the linear size of the BSU and is transformed from a broad-band-doublet one to a narrow-band one with drastic domination of the *G*-band when the size of graphene domain exceeds the free path of graphene optical phonons L_{ph} ~15 nm [143]. Therefore, the characteristic *D*–*G* doublet structure of the NGMs' Raman spectra is of structural origin, evidencing the stacked nature of the corresponding solid structure. Thus, the analysis of the structural and chemical content data, particularly, of the Raman spectra, of the cosmogenic carbon brought to Earth by the Chelyabinsk meteorite [60,144], leads to a confident conclusion about the graphite-like stacked structure of this carbon with a stack thickness of ~ 10–15 nm and more.

5. VIRTUAL ANALYTICS OF NECKLACED GRAPHENE MOLECULES

5.1. Short Foreword

Analysis of sp^2 aCs, performed using the analytic techniques described above, undoubtedly establishes the molecular nature of these solids, determines the solid-forming molecular BSUs as flattened necklaced-graphene type, estimates the average statistical linear size of them and the parameters of their primary stacking, and determines the atomic content of the BSUs' compositions. However, all these methods taken together do not allow us to describe BSUs using atomic structural forms such as $C_xH_yO_z(Imp)_{minor}$, so familiar for material science, beyond the general idea that they are graphene domains in a necklace of heteroatoms. Obviously, the numbers *x, y, z*, minor represent the realization of the chemical composition of substances, analytically determined as weight or atomic percentage, in atomic structural form. Taking into account the statistically averaged nature of the determined structural and compositional data (cf. Tables 2 and 3), the high complexity of constructing such a formula becomes evident. The first step towards solving this problem is the reduction of statistically averaged empirical data to point ones. The second step requires determining the formula-generating element and setting the absolute number of its atoms. In the case of sp^2 aCs, carbon atoms of number *x* evidently play the role. Further steps depend on which part of the BSUs is covered by this number. In the simplest case, it refers only to the graphene domain, due to which *y, z* and minor numbers determine the heteroatoms located in the BSU's necklace. If the heteroatom necklace includes carbon atoms such as those involved in carboxyl, methylene and methyl groups, or domain atoms are partially replaced by heteroatoms as in the case of, say, aggregated ethers and lactones, these numbers are determined by successive approximation. Naturally, chemical formulas $C_xH_yO_z(Imp)_{minor}$, constructed in this way and related to the same set of empirical chemical-content data, depend on the number of carbon atoms, i.e., on the size of graphene domains.

However, the presence of chemical formula does not allow for visualizing the BSU atomic structure. The problem is that a huge number of various-shaped graphene domains correspond to a given number of carbon atoms *x*. In its turn, a different number of edge atoms, subjected to targeting with heteroatoms, characterize shape-different domains. Moreover, the arrangement of heteroatoms over a set of the domain edge atoms is a difficult problem due to the large variability of multi-targeting, which is complicated by the high radicalization of these carbon atoms [145]. Therefore, in view of a practically infinite number of potential structural variations, none of the molecular structure of the $C_xH_yO_z(Imp)_{minor}$ chemical content, either drawn voluntarily by pen or designed by following particular algorithms, can take the place of an exact BSU view and is only one of a great number of possible 'snapshots'. Once so restricted with respect to real structures, the constructed BSUs are nevertheless useful, being the only structural images that allow for distinguishing the BSUs of different sp^2 aCs at the atomic level, immersing into the solids chemistry, exhibiting alive and silent chemical problems associated with the BSUs, disclosing the grounds and potentiality of different applications of sp^2 aCs, and so forth. Moreover, starting as molecular models of real solids, these virtual BSUs are easily transformed into Digital Twins [5,146] laying the foundation for reliable virtual analytics of the solids. Virtual vibrational spectrometry has so far been the first technique for the latter.

5.2. Molecular Models and Digital Twins of

BSUs of sp^2 Amorphous Carbons

In due course of the comprehensive analysis of the set of sp^2 aCs listed in Table 1 presented in the previous sections, a sufficient amount of data were obtained to enable the construction of BSUs models of the studied solids. Following general instructions, described in the previous section, rectangular graphene domains (5,5)NGr and (9,9)NGr with linear dimensions of 1.12×1.22 nm^2 and 1.97×2.20 nm^2, consisting of 66 and 190 carbon atoms, respectively, were chosen for modeling. According to the data in Table 2, the first domain is commensurate with the BSUs of natural solids and CB632, while the second is much bigger to be closer in size to the BSUs of CB624 and synthetic solids. Since the {CHO} triad evidently dominates in the chemical content in Table 3, we restricted ourselves with these elements only. Associated with the two domains mentioned above, the relevant BSU models listed in **Table 8** are presented in **Fig. 12***a–g*. We remind readers that the structures represent only instantaneous snapshots of numerous potential configurations of the same composition for each of the solids. It turned out that the analysis of numerical data on the chemical composition of BSUs from the viewpoint of XPS only is insufficient for a narrow choice of suitable structures [48]. It was necessary to plug DRIFT absorption spectra as well, which made it possible to significantly narrow the choice of structures to the set shown in the figure. A detailed discussion of building these models can be found in [49]. All structures are stable radicals [65] with temporarily quenched chemical activity. In the same way, BSU models can be built, which include, in addition to the triad of main components, minor impurities of nitrogen and sulfur [66] (see Fig. 12*h–j*). Evidently, these models, although not being exact imprints of the structure, make it possible to deal with sp^2 aCs with open eyes, understanding what the commonality and difference between natural amorphics are, and how the latter differ from synthetic and industrial ones. The difference in their behavior in catalysis [66], optics [147], medicine [148], etc. has the opportunity to become clearer.

Table 8

Chemical formulas of analytically provided models of basic structural units of sp^2 amorphous carbons.

No	Samples	Chemical formula
1	ShC	$C_{66}H_6O_4$
2	AnthX	$C_{66}H_{10}O_4$
3	AnthC	$C_{66}H_{14}O_4$
4	Ak-rGO	$C_{181}H_{27}O_{11}$
5	TE-rGO	$C_{185}H_{28}O_{19}$
6	CB632	$C_{66}H_2O_4$
7	CB624	$C_{181}O_9$

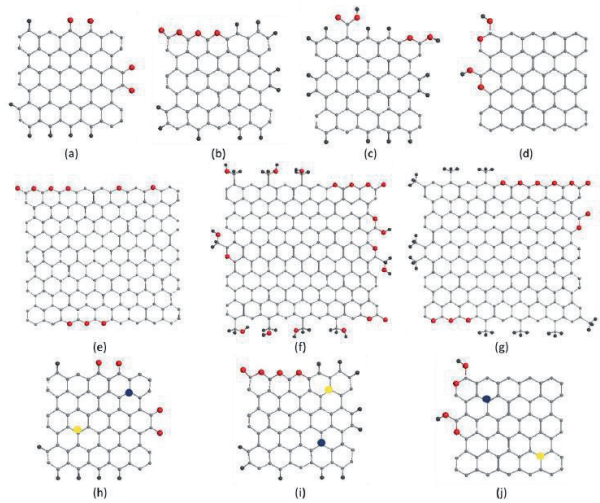

Fig. 12. *Molecular models of basic structure units of sp^2 amorphous carbons. Equilibrium structures of {CHO}-triad species: ShC (a), AnthX (b), AnthC (c), CB632 (d), CB624 (e), TE-rGO (f) and Ak-rGO (g). {CHO}-triad species complemented with nitrogen and sulfur additives: ShC (h), AnthX (i) and CB632 (j). Atomic content of the models follows the data listed in Table 3. Gray, red, black (a–g), completed with dark blue, yellow (h–j) balls depict carbon, hydrogen, oxygen, nitrogen and sulfur atoms, respectively.*

This first attempt at building empirically based models of NGMs opened up the possibility for a new direction of analytical research of sp^2 aCs aimed at moving from substances based on BSUs with an empirically unattainable structure, to those built from the NGMs of voluntary modified structure. Thus, going from individually different while not exactly determined empirical BSUs to a class of NGMs, undoubtedly having properties common to the whole class. This transition is possible within a new modeling concept known as the Digital Twins (DTs) [5,146]. The design of DTs is now subordinated not to the reproduction of the structure of empirical BSUs, but to respond to a series of questions aimed at elucidating one or another feature of the NGM class. In fact, when applied to a large set of NGMs [64,124,126], the approach has revealed many of the molecular commonalities, which are of practical interest, and which form the grounds of virtual

analytics of sp^2 aCs. First, this concerns virtual vibrational spectrometry that happened to be highly adaptive to a new analytic role.

5.3. Virtual Vibrational Analytics of sp² Amorphous Carbon

In molecular science the DT concept can be schematically presented as the following:

Digital twins → Virtual device → IT product.

This scheme connects three constituents of the approach [15]. Here, DTs are the molecular models under study, virtual device is a carrier of a selected software, and IT product covers a large set of computational results related to the DTs under different actions in the light of the soft explored. The quality of the IT product depends highly on how broadly and deeply the designed DTs cover all the knowledge concerning the object under consideration and how adequate the virtual device is to the peculiarities of this object. Applying virtual vibrational spectrometry, the virtual device is a virtual spectrometer. It should not contradict with the object nature and will perform calculations providing for the establishing of equilibrium structure of the designed DTs and obtaining their spectra of IR absorption and Raman scattering related to $3N–6$ vibrational modes. Virtual spectrometers differ by the software in grounds and are of HF (Hartree–Fock), DFT (density of functionals) or MD (molecular dynamics) type, since only semi-empirical programs based on the mentioned approximations can cope with the large volume of cumbersome calculations that are needed. As for quantum approaches, the radical nature of sp^2 aCs, caused by the open-shell electronic systems of their BSUs, forced us to abandon DFT- and MD-based softwares and pay particular attention to programs based on the unrestricted Hartree–Fock approximation. All the results illustrated below were obtained by using the virtual vibrational spectrometer HF Spectrodyn [149].

5.3.1. IINS Virtual Analytics

A standard model aimed at 'reading out' the empirical vibrational spectra of sp^2 aCs started far before the DT concept was introduced. The main problem preventing the issue from developing concerns the difficulty in building proper models. The situation changed appreciably when the first proposals to use NGMs as such models appeared. The models were initially applied for virtual IINS analytics of sp^2 aCs. Its main goal is to reproduce the solids behavior in the relevant empirical experiments. One-phonon GVDOS was the subject of calculations [87]. Two virtual experiments have been performed so far. The first mainly concerned adsorbed water in CB632, the empirical IINS spectrum of which is shown in Fig. 6*b*. A simplified BSU model, slightly different from the more detailed model that is shown in Fig. 12*d*, served as a carbon substrate immersed in the cloud of water molecules [2]. The second is related to a comparative analysis of empirical IINS spectra of sp^2 aCs presented in Fig. 9 using the first BSUs models, similar to those presented in Fig. 12 [47].

As seen in **Fig. 13**, the obtained virtual GVDOS is in line with the empirical data related to adsorbed water. In the second case, a set of virtual GVDOSs presented in **Fig 14** quite satisfactorily reproduced empirical data in the part related to the dependence of the spectra intensity on the hydrogen content of the relevant BSUs. Nearly linear dependence of the total spectrum intensity on the number of hydrogen atoms in the necklaces of the model BSUs was obtained [47], which follows the tendency of the hydrogen content of real sp^2 aCs listed in Table 3. A large width of the real IINS spectra does not allow for performing a more refined search of the BSUs models suitable for the spectra description [49].

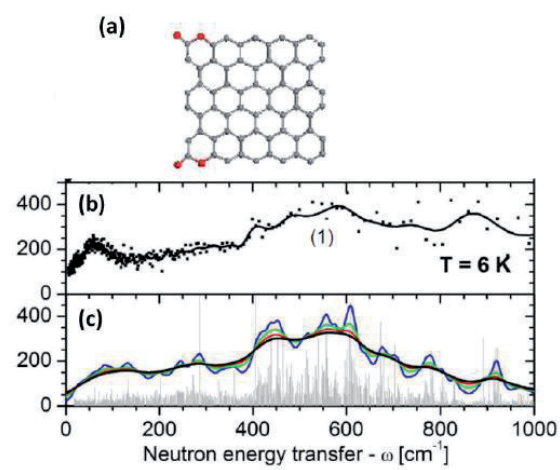

Fig. 13. *Adsorbed water in sp^2 amorphous carbon. (a) NGM model of BSUs of carbon blacks. (b) IINS-spectra-derived GVDOS of adsorbed water in as prepared CB632. (c) Virtual GVDOS of four-hydrogen-bond configured molecules of retained water. Gray and red balls depict carbon, and oxygen, respectively.*

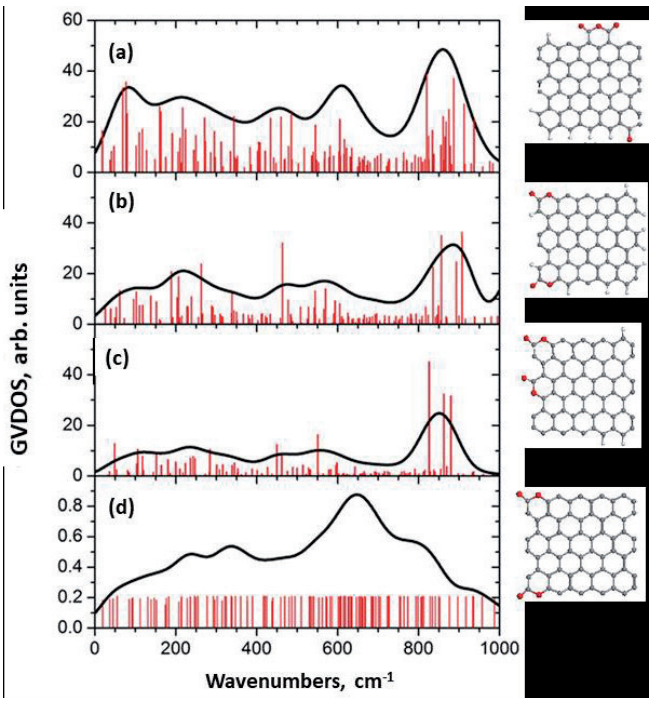

Fig. 14. *Virtual GVDOS spectra of graphene oxyhydrides related to the following BSUs' models: (a) ShC - $C_{68}O_4H_6$, (b) AnthX - $C_{64}O_4H_{10}$, (c) CB632 - $C_{64}O_4H_3$, and (d) CB624 - $C_{64}O_4$. Original bars are convoluted by Gaussian of 80 cm^{-1} half-width. Gray, white and red balls depict carbon, hydrogen and oxygen atoms, respectively.*

5.3.2. IR Absorption Virtual Analytics

The germination of virtual IR absorption analytics of sp^2 aCs has coincided with the beginning of transition of standard modeling of their individual molecular BSUs to the DT concept that concerns the class of NGMs [15,64,124,126]. A set of relatively reliable structural BSU models made it possible to penetrate their chemistry and begin to understand the main features of NGMs. In turn, the latter circumstance opened the way to recognize which information about molecules of this class can be obtained by asking the right questions. The latters should be formulated in the form of particular DT structures, whose treatment is aimed at receiving a clear answer to a particular inquiry. Referring the reader to the publications mentioned above for details, we confine ourselves to a brief enumeration of the answers received.

In terms of the DT concept, all the data discussed below were obtained using a virtual device-vibrational spectrometer HF Spectrodyn [149]. The obtained IT products present one-phonon harmonic spectra of IR absorption and Raman scattering. Their deviation from empirical analogues concerns the lack of anharmonicity and a considerable blue frequency shift. The former is highly important empirically, leading to a remarkable change in the optical spectra with respect to harmonic ones [150]. Nevertheless, the main features of both IR and Raman empirical spectra of the molecular sp2 nanocarbons are of harmonic origin. Accordingly, harmonic IT product reproduces the latter well enough. As for the unavoidable blue shift of virtual harmonic frequencies [151], it is quite considerable and constitutes ~200–500 cm^{-1} in the 1000–3500 cm^{-1} region. However, it is the same for all the studied DTs and can be ignored when comparing the virtual data of the species but should be taken into account at the final stage of comparing virtual and experimental data.

Digital Twins in place of real objects, and virtual spectrometers in place of real spectrometers, are real instruments of virtual vibrational spectrometry that provides the realization of many different goals. Comparative analysis, leading to the revealing of trends, common to both virtual and experimental spectra, is the strong point of the spectrometry. The unavoidable discrepancy of obtained individual virtual spectra and experimental data is its vulnerability. Obtaining the data presented below required consideration of several tens of DTs. Their design was carried out on the original graphene domains (5,5)NGr, (9,9)NGr, and (11,11)NGr. Digital Twins were conditionally divided into 'monochromic' and 'heterochromic' ones with respect to the chemical compositions of their necklaces. The former are carriers of highly distinguished identical chemical bonds while the latter are more adaptive to the varied chemical compositions of, say, empirical BSUs. Monochromic DTs with fully terminated edge atoms of the relevant graphene domains are of particular interest, presenting the effect of maximum contribution of the necklace heteroatoms into both the IR and Raman spectra of the molecules.

Fig. 15 presents a comparative view on the spectra of monochromic DTs based on the same graphene domain. As seen in the figure, the presence of heteroatoms drastically violates the DTs' IR spectra while leaving the Raman spectra practically unchanged. A thorough analysis of the data shown in the figure revealed that the following commonalities are inherent to all the NGMs, as well as to all of the sp^2 aCs BSUs.

1. Vibrational spectra of NGMs are determined by the pool of chemical bonds, among which sp^2C–C bonds configure graphene domains while sp^2C–A ones (A = H, O, N, S, and so forth) shape the NGMs' necklaces.
2. One-quantum harmonic vibration spectra of the NGMs, constituting of *N* atoms, cover 3*N*–*6* vibrational modes spread over the region of 0–1800 cm^{-1}, characterized for the excitation of sp^2C–C bonds, and of 0–3400 cm^{-1} depending on the sp^2C–A CBs configuration related to the NGM necklaces.
3. As seen in Fig. 15, all the NGMs' vibrational spectra contain a well-defined region of stretching vibrations of sp^2C–C bonds in the range of 1200–1800 cm^{-1} provided with the presence of graphene domains. The stretchings are slightly disturbed in Figure 15*c*–*e* due mainly to their reaction on the oxygen atoms presence in the NGMs' circumference (see detailed discussion of the feature in [124]).
4. The two communities of the NGMs' chemical bonds participate in their IR and Raman spectra quite differently. Covalent homopolar sp^2C–C bonds are not IR active due to a nil static dipole moment. Accordingly, IR absorption of graphene domains is extremely weak (Fig. 15*a*) while heteropolar sp^2C–A bonds show considerable absorption and are highly individually dependent on the chemical composition of the NGMs' necklaces (Fig. 15*b*–*e*). In contrast, activity of the Raman scattering is provided with sp^2C–C bonds in all the cases due to which the Raman signatures of bare graphene domains as well as NGMs are similar (Fig. 15*a*–*e*).
5. IR spectra, strongly dependent on the chemical composition of NGM necklaces, depend on the size of the latter rather weakly.
6. Analysis of virtual IR spectra of monochromic DTs allows for suggesting a definite set of group frequencies to be used for assignment of the spectra features to particular chemical bonds formed in the NGM necklaces.

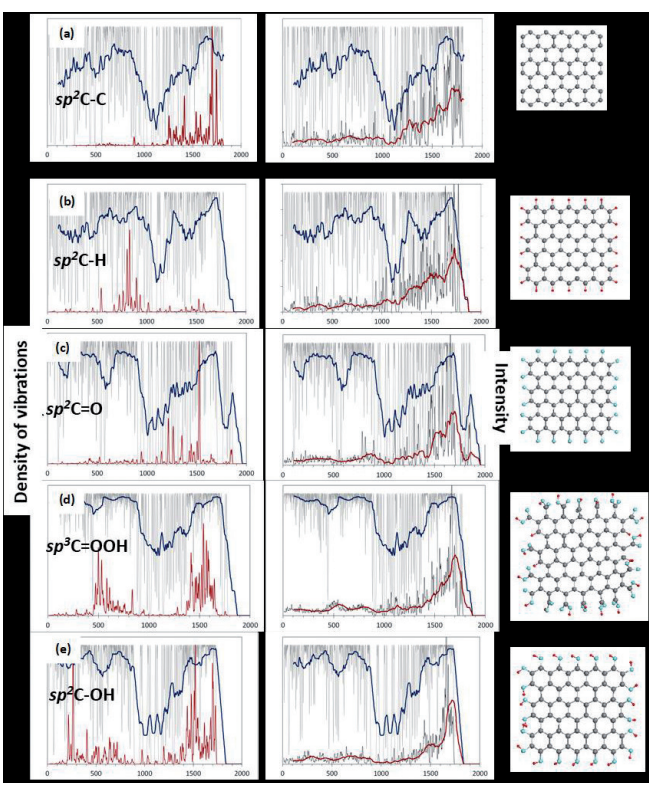

Fig. 15. *Virtual vibrational spectra (light gray) as well as one-phonon IR absorption and Raman scattering spectra (gray) of a set of the (5,5)NGr-based monochromic digital twins with fully terminated edge atoms of the graphene domains (a-e) [64]. Original sticks of the spectra are convoluted with Gaussian bandwidth of 10 cm^{-1}. Plottings of densities of vibrations and Raman spectra are accompanied with trend lines corresponding to 50–point linear filtration, dark blue and red, respectively. HF Spectrodyn virtual spectrometer. Equilibrium DT structures supplied with chemical formulas are presented on the right.*

In addition to exhibiting common trends of IR virtual spectrometry of NGMs discussed above, the first attempts were made to compare DTs' virtual spectra with the experimental ones of the relevant sp^2 aCs. Such a comparison related to TE-rGO is shown in **Fig. 16***a*. As seen in the figure, at first glance, the DRIFT spectrum of the object (red potting) differs drastically from the virtual one. However, once upshifted by 500 cm^{-1}, the three-band spectrum (blue plotting) correlates well with the similar three-band virtual one, reliably supporting the atomic configuration of the DT shown in the figure. Naturally, it is impossible to speak about the complete adequacy of the proposed model to the real BSU structure, but the fact of reproduction of the main components of the latter is obvious. Thus, the evidence, provided earlier with IINS as well as with DRIFT and XPS [49] spectra, is supported with virtual spectrometry.

A completely different situation is presented in Fig. 16*b*. In contrast to the previous case,

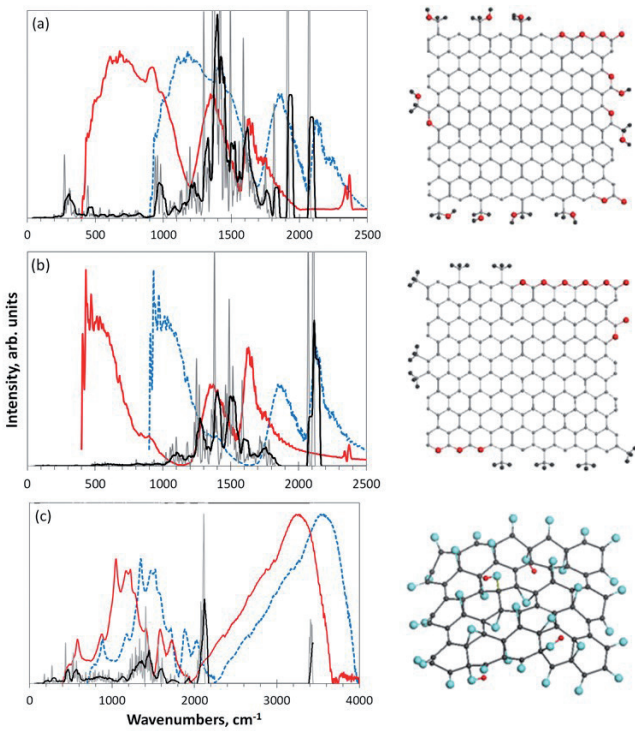

Fig. 16. *Digital twins' analytics of IR spectra of reduced and parental graphene oxides. (a,b) Virtual one-phonon (gray, supplemented with black trend lines corresponding to 50–point linear filtration, HF Spectrodyn) as well as original (red) and 500 cm^{-1} blue-shifted (blue) experimental IR absorption spectra of TE-rGO and Ak-rGO, respectively* [64]. *(c) The same but original and 300 cm^{-1} blue-shifted experimental IR spectra of graphene oxide* [124]. *Equilibrium structures of rGO's DTs $C_{185}H_{28}O_{19}$ and $C_{181}H_{27}O_{11}$ (see Table 8) as well as of GO's DT $C_{66}O_{40}H_4$ are shown on the right.*

the experimental spectrum of Ak-rGO, which deviates significantly from that for TE-rGO, is different from the virtual spectrum of DT as well. As can be seen, a similar upshift does not reveal any similarity between the real and virtual spectra, except for the band at ~1700 cm^{-1}. This band is perhaps the only evidence of the presence of quinones in the structure of both real Ak-rGO BSU and DT. As for the low-frequency part of the real spectrum in the region of 500–800 cm^{-1}, analysis of virtual spectra of monochromic DTs in Fig. 15 as well as many others point to its attribution to hydrogen atoms in the nearest vicinity to edge atoms of the NGMs' graphene domains. Such atoms are not presented in the DT chemical structure, which might explain the drastic discrepancy between the empirical and virtual IR spectra. As for reality, adsorbed water is the first candidate to be examined. Obviously, the presence of this water in TE-rGO may improve the fit between the empirical and virtual spectra in this region as well. The DT concept, worked out by example of NGMs [64,126], has recently been applied to the graphene oxide IR spectrum [124], positive result of which is shown in Fig. 16*c*.

5.3.3. Raman Scattering Virtual Analytics

The main features of NGMs' Raman spectra are presented in **Fig. 17** in a compressed way. The Digital Twins' analytics of Raman scattering spectra of NGMs [64,126] has revealed the following commonalities:

1. As evidenced in Figs 15 and 17, the graphene domain sp^2C-C stretchings determine the main pattern of the NGMs' Raman spectra.
2. The Raman spectra of NGMs respond to the presence of heteroatoms in the molecules' circumference due to the frequency difference of the sp^2C–C and sp^2C–C(A) stretchings [124] (see Fig. 15). However, the violation is not critical to significantly disturb the general similarity of the

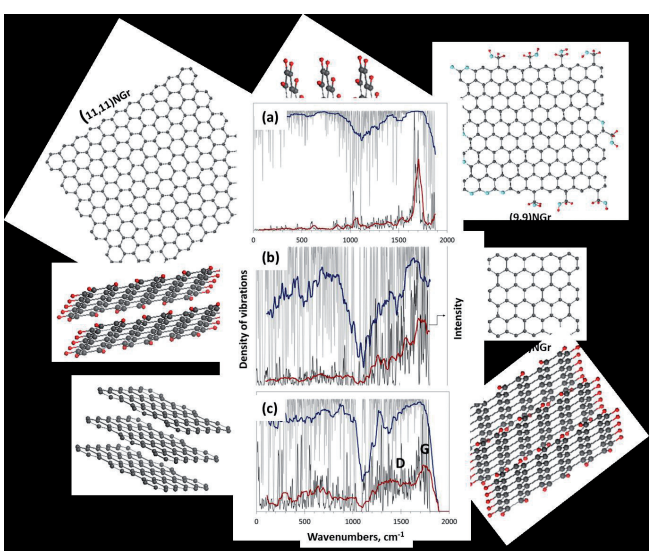

Fig. 17. *Digital twins' analytics of Raman spectra of individual and layered NGMs of different size and compositions. (a,b). Virtual densities of vibrations (light gray) and one-phonon Raman spectra (gray) of one-layer TE-rGO ($C_{192}O_{19}H_{44}$) and bare domain (5,5) NGr (C_{66}), respectively. (c) The same but two layers of hydrogenated domain (5, 5) NGr ($C_{132}H_{44}$). Original sticks of the spectra are convoluted with Gaussian bandwidth of 10 cm^{-1}. Both densities of vibrations and Raman spectra are accompanied with 50-points trend lines, dark blue and red, respectively. HF Spectrodyn. Adapted from Refs.* [64,126].

Raman spectra appearance of the different sp^2 aCs presented in Fig. 11.

3. The Raman spectra of individual NGMs of any chemical composition are not characterized with a standard *D*–*G* doublet as seen in Figs 15.
4. The Raman spectra of individual NGMs strongly depend on their linear dimensions and are transformed from a broad-band (see Fig. 17*b*) to narrow-band with a total domination of G-band when the size of the latter approaches the free path of graphene optical phonons L_{ph} ~15 nm [143] (see Fig 17*a*). The effect, which is typical size effect of phonon spectra of molecular amorphous solids [152], strengthens when (9,9) graphene domain is substituted with (11,11) [64].
5. The appearance of the *D*-band and formation of the *D*–*G* doublet is a particular feature attributed to NGM layering (see Fig. 17*c*). The effect becomes more pronounced when a double layer NGM is substituted with a three-layer one [64]. It is provided with the generation of dynamically stimulated sp^3C–C bonds between the carbon atoms of adjacent NGM layers [124] due to the exact van der Waals contact between them. A high activity of out-of-plane stretchings of benzenoid units [116,137] makes the sp3C–C stretchings active enough to generate the D-band.
6. The D-band's intensity increases when the number of NGM layers grows up to 4–5 nm and then markedly slows down when the stack thickness exceeds ~15 nm [142].

6. EXPRESS ANALYSIS OF SP^2 AMORPHOUS CARBONS BASED ON IR AND RAMAN SPECTRA

Evidently, all the above concerns the Raman spectra of real sp^2 aCs, particularly, the solids' short-range order presented with the relevant BSUs and their stacks and can be applied for analysis of empirical spectra of the solids, in general, and for their express analysis, in particular. Results of the latter, applied to a randomly selected sample [153], are demonstrated in **Fig. 18**. Starting from the Raman spectrum in Fig. 18*a*, one has to be convinced first in dealing with a sp^2 aC, but not with graphene oxide, whose Raman spectrum looks exactly as shown in the figure [124]. Convinced by the XRPD test, we move on to read out the Raman spectrum of the rGO solid. It tells us that the solid has a stacked structure consisting of 4–5 BSUs layers, BSUs linear size being its first nanometers. A considerable width of *D*- and *G*-bands allows for suspecting a turbostratic nature of the layer packaging. Evidently, the presence of the BSUs' necklaces is one of the reasons for both this disordering and slight increasing of the interlayer distance, as shown in Table 2. In its turn, the IR absorption spectrum in Fig. 18*b* shows that this rGO's necklace is mainly oxygenated, since none of the prominent sp^2C–H models, which are concentrated below 1000 cm^{-1}, are revealed. No traces of adsorbed water (region below 400 cm^{-1}) are fixed as well. Following the group frequencies listed in Table 7, it is possible to suggest the oxygen-containing contributions indicated in the figure. A rather scares fine structure of the IR spectrum is in line with the attribution of marked bands below 2000 cm^{-1} to cyclic ethers, while the band at 3400 cm^{-1} evidences traces of small amount of hydroxyls in the sample. The presented express analysis of the Raman and IR absorption spectra of an rGO sample is only the beginning of the in-depth analysis and is given as an example. Nevertheless, it provides a reliable entry level of analysis requiring further confirmation using all the advanced methods of analytical chemistry and spectroscopy.

7. CONCLUSIVE REMARKS

The first atlas of empirical and virtual analytics of sp^2 amorphous carbons is over. It opens the way

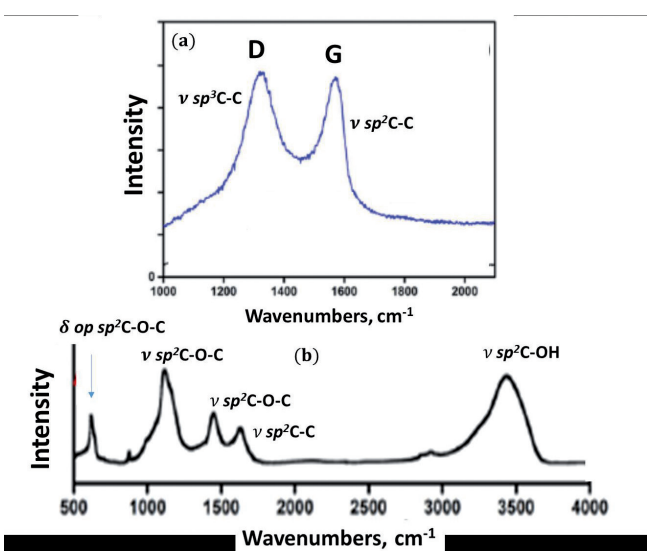

Fig. 18. *Express analysis of sp^2 amorphous carbon. Raman scattering (a) and IR absorption (b) spectra of a lab-fabricated reduced graphene oxide [153] in notations of vibrational analytics (see text).*

for further development, extension, sophistication, routing, substitution and suggests new visions and approaches. Both analytics are based on the molecular nature of the solids and are aimed at the disclosure and characterization of short-range order of the latter. The two analytics are not perfect and there are still questions to be raised and answered. What is presented for the reader's judgment is only the first attempt to summarize the currently available ideas about sp^2 amorphous carbon and offer a systematic way to check and analyze them.

Funding: This research receives no external funding.

Institutional Review Board Statement: Not applicable.

Informed Consent Statement: Not applicable.

Data Availability Statement: Any data or material that support the findings of this study can be made available by the corresponding author upon request.

Conflicts of Interest: The author declares no conflict of interests.

List of abbreviations

aC amorphous carbon
AFM atom-force microscopy
Ak-rGO lab rGO product
AnthC anthracite
AnthX anthraxolite
BSU basic structural unit
CB carbon black
DFT density functional theory
DRIFT Diffused-reflection IT Fourier determined spectrometer
DT digital ywin
DTA differential thermal analysis
DSC differential scanning calorimetry
EDS energy dispersion spectroscopy
EA elemental analysis
EM electron microscopy
FTIR Fourier determined IR spectroscopy
FWHM full width at half maximum
GBE group bending energy
GF group frequency
GO graphene oxide
GVDOS generalized vibrational density of states
HF Hartree-Fock approximation
HREELS high-resolution electron energy loss spectroscopy
HRTEM high-resolution transmission electron microscopy
IINS inelastic incoherent neutron spectroscopy
IT intellectual technology
MD molecular dynamics
NGM necklaced graphene molecule
NPD neutron powder diffraction
PD powder diffraction
rGO reduce graphene oxide
SEM scanning electron microscopy
ShC shungite carbon
STEM scanning transmission electron microscopy
TE-rGO thermally exfoliated rGO
VFF Voigt fitting function
XRPD X-ray powder diffraction
XPS X-ray photoelectron spectroscopy

REFERENCES

1. Sheka, E.F.; Rozhkova, N.N. Shungite as the natural pantry of nanoscale reduced graphene oxide. *Int. J. Smart Nano Mat.,* 2014, 5:1-16.
2. Hoffmann, R. Small but strong lessons from chemistry for nanoscience. *Angew. Chem. Int. Ed.*, 2013, 52:93-103.
3. Elliot, S.R. *Physics of Amorphous Materials.* Longman: London, UK; New York, NY, USA, 1983.
4. Raman, C.V. Molecular structure of amorphous solids. *Nature,* 1922, 109:138-139.
5. Natkaniec, I.; Sheka, E.F.; Drużbicki, K.; Hołderna-Natkaniec, K.; Gubin, S.P.; Buslaeva, E.Y.; Tkachev, S.V. Computationally Supported Neutron Scattering Study of Parent and Chemically Reduced Graphene Oxide. *J. Phys. Chem. C*, 2015, 119:18650-18662.
6. Donet, J.-B.; Bansal, R.C.; Wang, M.-J. (Eds.). *Carbon Black. Science and Technology.* Marcel Dekker: New York, NY, USA; Basel, Switzerland, 1993.
7. Rozhkova, N.N.; Rozhkov, S.P.; Goryunov, A.S. Natural graphene-based shungite nanocarbon. In: *Carbon Nanomaterials Sourcebook*; Sattler, K.D., Ed.; CRC Press: Roca Raton, FL, USA; London, UK; New York, NY, USA, 2016; Volume 1, pp. 151-174.
8. Filippov, M.M. *Anthraxolites*. VNIGRI: St. Petersburg, Russia, 2013, (in Russ.).
9. Skripchenko, G.B. Structure, properties and use of anthracytes of the Donetsk basin. *Chem. Solid Fuel,* 2010, 2:3-13, (in Russ.).
10. Tkachev, S.V.; Buslaeva, E.Y.; Naumkin, A.V.; Kotova, S.L.; Laure, S.V.; Gubin, S.P. Reduced graphene oxide. *Inorg. Mat.*, 2012, 48:796-802.
11. Sheka, E.F.; Natkaniec, I.; Mel'nikov, V.; Druzbicki, K. Neutron scattering from graphene oxide paper and thermally exfoliated reduced graphene oxide. Nanosyst. Phys. Chem. Math. 2015, 6, 378–393.
12. SIGMA-ALDRICH. Synthesis of mesoporous materials. *Mat. Matt*, 2008, 3:17-18.
13. Sheka, E.F.; Golubev, E.A. Technical graphene (reduced graphene oxide) and its natural analog (schungite). *Tech. Phys.*, 2016, 61:1032-1038.

14. Sheka, E.F. Digital Twins in the graphene technology. *arXiv 2022*, https://doi.org/10.48550/arXiv.2208.14926.
15. Radovic, L. (Ed.). *Chemistry and Physics of Carbon*. Marcel Dekker: New York, NY, USA, 2001.
16. Setton, R.; Bernier, P.; Lefrant, S. (Eds.). *Carbon Molecules and Materials*. Taylor and Francis: London, UK; New York, NY, USA, 2002.
17. Filippov, M.M. *Shungite-Bearing Rocks of the Onega Structure*. Karelian Science Centre of RAS: Petrozavodsk, Russia, 2002, (in Russ.).
18. Silva, R.; Silva, S.R.P. (Eds.). *Properties of Amorphous Carbon*. INSPEC: London, UK, 2003.
19. Marsh, H.; Rodriguez-Reinoso, F. (Eds.). *Activated Carbon*. Elsevier Science & Technology Books: Amsterdam, The Netherlands, 2006.
20. Gogotsi, Y. (Ed.). *Carbon Nanomaterials*. Taylor and Francis Group, LLC: Boca Raton, FL, USA, 2006.
21. Radovic, L. (Ed.). *Chemistry and Physics of Carbon*. Taylor and Francis Group, CRC Press: Boca Raton, FL, USA, 2008.
22. Serp, P.; Figueiredo, J.L. (Eds.). *Carbon Materials for Catalysis*. Wiley: Hoboken, NJ, USA, 2009.
23. Colombo, L.; Fasolino, A. (Eds.). *Computer-Based Modeling of Novel Carbon Systems and Their Properties, Carbon Materials: Chemistry and Physics 3*. Springer Science + Business Media B.V.: Berlin/Heidelberg, Germany, 2010.
24. Oberlin, A.; Bonnamy, S. A realistic approach to disordered carbons. In: *Chemistry and Physics of Carbon*. Radovic, L., Ed.; CRC Press: Boca Raton, FL, USA, 2013.
25. Serp, P.; Machado, B. (Eds.). *Nanostructured Carbon Materials for Catalysis*. RSC: Croydon, UK, 2015.
26. Putz, M.V.; Ori, O. (Eds.). *Exotic Properties of Carbon Nanomatter. Advances in Physics and Chemistry. Carbon Materials: Chemistry and Physics*. Springer Science + Business Media: Dordtrecht, The Netherlands, 2015.
27. Sattler, K.D. (Ed.). *Carbon Nanomaterials Sourcebook*. CRS Press: Boca Raton, FL, USA; London, UK; New York, NY, USA, 2016.
28. Sheka, E. *Spin Chemical Physics of Graphene*. Pan Stanford: Singapore, 2018.
29. Kharisov, B.I.; Kharissova, O.V. *Carbon Allotropes: Metal-Complex Chemistry, Properties and Applications*. Springer Nature: Cham, Switzerland, 2019.
30. Ray, S.C. *Magnetism and Spintronics in Carbon and Carbon Nanostructured Materials*. Elsevier: Dodrecht, The Netherlands, 2020.
31. Borghi, F.; Soavi, F.; Milani, P. (Eds.). *Nanoporous Carbons for Soft and Flexible Energy Devices. Carbon Materials: Chemistry and Physics*. Springer Nature: Cham, Switzerland, 2022.
32. Uspensky, V.A.; Radchenko, O.A.; Glebovskaya, E.A. *Basics of Genetic Classification of Bitumen*. USSR, Leningrad, Nedra Publ., 1964, (in Russ.).
33. Cornelius, C.D. Classification of natural bitumen: A physical and chemical approach. In: *Exploration for Heavy Crude Oil Fnd Natural Bitumen*. Meyer, R.F., Ed.; AAPG Studies in Geology: Tulsa, OK, USA, 1987; Volume 25, pp. 165–174.
34. Jakob, H. Nomenclature, classification, characterization and genesis of natural solid bitumen (Migrabitumen). In: *Bitumen in Ore Deposits*. Parnell, J., Kucha, H., Landais, P., Eds.; Springer: Berlin/Heidelberg, Germany, 1993; pp. 11-27.
35. Mossman, D.J.; Nagy, B. Solid bitumens: An assessment of their characteristic, genesis, and role in geological processes. *Terra Nova,* 1996, 8:114-128.
36. Sheka, E.F.; Golubev, Y.A.; Popova, N.A. Amorphous state of sp^2 solid carbon. FNCN, 2021, 29:107-113.
37. Shumilova, T.G. *Mineralogy of Native Carbon*. Ural Dept RAS: Yekaterinburg, Russia, 2003, (in Russ.).
38. Shumilova, T.G.; Isaenko, S.I.; Divaev, F.K. Mineralogical features of diamond, amorphous diamond like carbon and graphite from Chagatay carbonatites (Uzbekistan). *Mineral. J.,* (Ukr.) 2013, 35:81-89.
39. Robertson, J. Diamond-like amorphous carbon. *Mater. Sci. Eng. R Rep.*, 2002, 37:129-281.
40. Zhang, L.; Wei, X.; Lin, Y.; Wang, F. A ternary phase diagram for amorphous carbon. *Carbon*, 2015, 94:202-213.
41. Harris, P.J.F. New perspectives on the structure of graphitic carbons. *Crit. Rev. Solid State Mat. Sci.*, 2005, 30:235-253.
42. Chua, C.K.; Pumera, M. Chemical reduction of graphene oxide: A synthetic chemistry viewpoint. *Chem. Soc. Rev.,* 2014, 43:291-312.
43. Krishnan, D.; Kim, F.; Luo, J.; Cruz-Silva, R.; Cote, L.J.; Jang, H.D.; Huang, J. Energetic

graphene oxide: Challenges and opportunities. *Nanotoday*, 2012, 7:137-152.
44. Chyan, Y.; Ye, R.; Li, Y.; Singh, S.P.; Arnusch, C.J.; Tour, J.M. Laser-induced graphene by multiple lasing: Toward electronics on cloth, paper, and food. *ACS Nano*, 2018, 12:2176-2183.
45. Luong, D.X.; Bets, K.V.; Algozeeb, W.A.; Stanford, M.G.; Kittrell, C.; Chen, W.; Salvatierra, R.V.; Ren, M.; McHugh, E.A.; Advincula, P.A.; et al. Gram-scale bottom-up flash graphene synthesis. *Nature*, 2020, 577:647-651.
46. Seal, M. The effect of surface orientation on the graphitization of diamond. *Phis. Stat. Sol.*, 1963, 3:658.
47. Sheka, E.F.; Hołderna-Natkaniec, K.; Natkaniec, I.; Krawczyk, J.X.; Golubev, Y.A.; Rozhkova, N.N.; Kim, V.V.; Popova, N.A.; Popova, V.A. Computationally supported neutron scattering study of natural and synthetic amorphous carbons. *J. Phys. Chem. C*, 2019, 123:15841-15850.
48. Golubev, Y.A.; Rozhkova, N.N.; Kabachkov, E.N.; Shul'ga, Y.M.; Natkaniec-Hołderna, K.; Natkaniec, I.; Antonets, I.V.; Makeev, B.A.; Popova, N.A.; Popova, V.A.; Sheka, E.F. sp^2 Amorphous carbons in view of multianalytical consideration: Normal, expected and new. *J. Non-Cryst. Solids,* 2019, 524:119608.
49. Sheka, E.F.; Natkaniec, I.; Ipatova, E.U.; Golubev, Y.A.; Kabachkov, E.N.; Popova, V.A. Heteroatom necklaces of sp^2 amorphous carbons. XPS supported INS and DRIFT spectroscopy. FNCN, 2020, 28:1010-1029; https://doi.org/10.1080/1536383X.2020.1794849.
50. Sheka, E.F.; Golubev, Y.A.; Popova, N.A. Graphene domain signature of Raman spectra of sp2 amorphous carbons. *Nanomaterials*, 2020, 10:2021.
51. Razbirin, B.S.; Rozhkova, N.N.; Sheka, E.F.; Nelson, D.K.; Starukhin, A.N. Fractals of graphene quantum dots in photoluminescence of shungite. *J. Exp. Theor. Phys.*, 2014, 5:838-850.
52. Avdeev, M.V.; Tropin, T.V.; Aksenov, V.L.; Rosta, L.; Garamus, V.M.; Rozhkova, N.N. Pore structures in shungites as revealed by small-angle neutron scattering. *Carbon*, 2006, 44:954-961.
53. Broude, V.L.; Klimusheva, G.V.; Prikhotjko, A.F.; Sheka, E.F.; Yatcenko, L.P. *Absorption Spectra of Molecular Crystals*. Polysubstituted Benzene Compounds; Naukova Dumka: Kiev, USSR, 1972, (in Russ.).
54. Sheka, E.F. Spectroscopy of amorphous substances with molecular structure. *Sov. Phys. Usp.*, 1990, 33:147-166.
55. Golubev, Y.A.; Ulyashev, V.V.; Veligzhanin, A.A. Porosity and structural parameters of Karelian shungites according to the data of small-angle synchrotron radiation scattering and microscopy. *Crystallgr. Rep.,* 2016, 61:66-77.
56. Rozhkova, N.N. Aggregation and stabilization of shungite carbon nanoparticles. *Ecol. Chem.*, 2012, 4:240-251.
57. Duan, X.; Ao, Z.; Zhang, H.; Saunders, M.; Sun, H.; Shao, Z.; Wang, S. Nanodiamonds in sp2 /sp3 configuration for radical to nonradical oxidation: Core-shell layer dependence. *Appl. Cat. B: Envirom.*, 2018, 222:176-181.
58. Sadovnichii, R.V.; Rozhkov, S.S.; Rozhkova, N.N. The use of shungite processing products in nanotechnology: Geological and Mineralogical Justification. *Smart Nanocomp.*, 2016, 7:111-119.
59. Garvie, L.A.J.; Buseck, P.R. Carbonaceous materials in the acid residue from the Orgueil carbonaceous chondrite meteorite. *Meteor. Planet. Sci.*, 2006, 41:633-642.
60. Taskaev, S.; Skokov, K.; Khovaylo, V.; Donner, W.; Faske, T.; Dudorov, A.; Gorkavyi, N.; Muratov, D.S.; Savosteenko, G.; Dyakonov, A.; et al. Exotic carbon microcrystals in meteoritic dust of the Chelyabinsk superbolide: Experimental investigations and theoretical scenarios of their formation. *Eur. Phys. J. Plus,* 2022, 137:562.
61. Povarennykh, M.Y.; Matvienko, E.N.; Knot.ko, A.V.; Shatalova, T.B. Characteristic of natural carbon nanominerals and their aggregates from the Dzhaharduk area (Uzbekistan). *Mineral,* 2018, 4:85-97.
62. Allen, K.D.; Wegener, G.; Matthew Sublett, D., Jr.; Bodnar, R.J.; Feng, X.; Wendt, J.; White, R.H. Biogenic formation of amorphous carbon by anaerobic methanotrophs and select methanogens. *Sci. Adv.*, 2021, 7:eabg9739.
63. Melezhik, V.A.; Filippov, M.M.; Romashkin, A.E. A giant Palaeoproterozoic deposit of shungite in NW Russia: Genesis and practical applications. *Ore Geol. Rev.*, 2004, 24:135-154.

64. Sheka, E.F.; Popova, N.A. Virtual vibrational analytics of reduced graphene oxide. *Int. J. Mol. Sci.*, 2022, 23:6978.
65. Sheka, E.F. sp2 Carbon stable radicals. C 2021, 7, 31.
66. Deng, D.; Yu, L.; Pan, X.; Wang, S.; Chen, X.; Hu, P.; Sunb, L.; Bao, X. Size effect of graphene on electrocatalytic activation of oxygen. *Chem. Commun.*, 2011, 47:10016-10018.
67. Sheka, E.F. Graphene oxyhydride catalysts in view of spin radical chemistry. *Materials,* 2020, 13:565.
68. Jurkiewicz, K.; Pawlyta, M.; Burian, A. Structure of carbon materials explored by local transmission electron microscopy and global powder diffraction probes. *Carbon*, 2018, 4:68.
69. Warren, B.E. X-ray diffraction in random layer lattices. *Phys. Rev.*, 1941, 59:693-698.
70. Biscoe, J.; Warren, B.E. An X-ray study of carbon black. *J. Appl. Phys.*, 1942, 13:364-371.
71. Busek, P.R.; Galdobina, I.P.; Kovalevski, V.V.; Rozhkova, N.N.; Valley, J.W.; Zaidenberg, A.Z. Shungites: The C-rich rocks of Karelia, Russia. *Can. Mineralog.*, 1997, 35:1363-1378.
72. Kovalevskii, V.V. The Structure of Carbon Matter and the Genesis of Shungite Rocks. *Dr. Sci. Dissertation, Geology and Mineralogy*, Petrozavodsk, Russia, 2007.
73. Golubev, E.A. Globular structure of higher anthraxolites according to scanning probe microscopy. *Dokl. Ak. Nauk.*, 2009, 425:519-521, (in Russ.).
74. Golubev, E.A. Electrophysical properties and structural features of shungite. *Phys. Solid State,* 2013, 55:1078.
75. Available online: http//rsb.info.nih.gov/ij (accessed on).
76. Osváth, Z.; Deák, A.; Kertész, K.; Molnár, G.; Vértesy, G.; Zámbó, D.; Hwang, C.; Biró, L.P. The structure and properties of graphene on gold nanoparticles. *Nanoscale*, 2015, 7:5503-5509.
77. Klug, H.P.; Alexander, L.E. X-Ray *Diffraction Procedures for Polycrystalline and Amorphous Materials*, 2nd Ed.; John Wiley: New York, NY, USA, 1974.
78. Ingham, B. X-ray scattering characterization of nanoparticles. *Cryst. Rev.,* 2015, 21:229-303.
79. Kisi, E.H.; Howard, C.J. *Applications of Neutron Powder Diffraction.* Oxford University Press: New York, NY, USA, 2008; 384 p.
80. Sheka, E.F.; Rozhkova, N.N.; Holderna-Natkaniec, K.; Natkaniec, I. Nanoscale reduced-graphene-oxide origin of shungite in light of neutron scattering. *Nanosyst. Phys. Chem. Math.*, 2014, 5:659-676.
81. Lobzova, R.V. *Graphite and Alkaline Rocks of the Botogol'sk Massif.* Moscow, Nauka Publ., 1975, (in Russ.).
82. Langford, J.I.; Wilson, A.J.C. Scherrer after sixty years: A survey and some new results in the determination of crystallite size. *J. Appl. Cryst.,* 1978, 11:102-113.
83. Vorokh, A.S. Scherrer formula: Estimation of error in determining small nanoparticle size. *Nanosyst. Phys. Chem. Mat.*, 2018, 9:364-369.
84. Sofer, Z.; Šimek, P.; Jankovsky, O.; Sedmidubsky, D.; Beran, P.; Pumera, M. Neutron diffraction as a precise and reliable method for obtaining structural properties of bulk quantities of graphene. *Nanoscale*, 2014, 6:13082-13089.
85. Opalev, S.V.; Belenkov, E.A. Experimental study of graphites structure change under mechanical grinding. *Bull. Chelyabinsk. Sci. Cent.*, 2004, 3:27-30. (in Russ.).
86. Klancnik, G.; Medved, J.; Mrvar, P. Differential thermal analysis (DTA) and differential scanning calorimetry (DSC) as a method of material investigation. *RMZ Mat. Geoenv.*, 2010, 57:127-142.
87. Mitchel, P.C.H.; Parker, S.F.; Ramirez-Cuesta, A.J.; Tomkinson, J. Vibrational Spectroscopy with Neutrons. In: *With Application in Chemistry, Biology, Materials Science and Catalysis.* World Scientific: Singapore, 2005.
88. Huang, H.; Sun, G.; Hu, J.; Jiao, T. Low temperature synthesis of MnO2/graphene nanocomposites for supercapacitors. *J. Chem.,* 2015, 2015, 629362.
89. Goldstein, J.; Newbury, D.E.; Echlin, P.; Joy, D.C.; Romig, A.D.; Lyman, C.E. Scanning Electron Microscopy and X-Ray Microanalysis. In: *A Text for Biologists, Materials Scientists, and Geologists*, 2nd Ed.; Plenum Press: New York, NY, USA, 1992.
90. CasaXPS User's Manual; Casa Software Ltd.: San Diego, CA, USA, 2001.
91. Plyusnina, L.P.; Likhoidov, G.G.; Kuzmina, T.V. Graphitization and naphthide-ore genesis. *Litosphere*, 2011, 5:111-116. (in Russ.).

92. Shumilova, T.G.; Shevchuk, S.S.; Isayenko, S.I. Metal concentrations and carbonaceous matter in the black shale type rocks of the Urals. *Dokl. Earth Sci.,* 2016, 469:695-698.
93. Moldoveanu, S.C. *Pyrolysis of Organic Molecules with Application to Health and Enviromental Issues*, 2nd ed. Elsevier: Amsterdam, The Netherlands, 2018.
94. Darmstadt, H.; Roy, C.; Kaliaguine, S. ESCA characterization of commercial carbon blacks and of carbon blacks from vacuum pyrolysis of used tires. *Carbon*, 1994, 32:1399-1406.
95. Cheng, C.-H.; Lehmann, J.; Thies, J.E.; Burton, S.D.; Engelhard, M.H. Oxidation of black carbon by biotic and abiotic processes. *Org. Geochem.*, 2006, 37:1477-1488.
96. Shao, Y.; Yin, G.; Zhang, J.; Gao, Y. Comparative investigation of the resistance to electrochemical oxidation of carbon black and carbon nanotubes in aqueous sulfuric acid solution. Electrochim. Acta 2006, 51, 5853–5857.
97. Nikitin, A.; Li, X.; Zhang, Z.; Ogasawara, H.; Dai, H.; Nilsson, A. Hydrogen storage in carbon nanotubes through the formation of stable C−H bonds. *Nano Lett.,* 2008, 8:162-167.
98. Yan, J.; Wei, T.; Shao, B.; Ma, F.; Fan, Z.; Zhang, M.; Zheng, C.; Shang, Y.; Qian, W.; Wei, F. Electrochemical properties of graphene nanosheet/carbon black composites as electrodes for supercapacitors. *Carbon*, 2010, 48:1731-1737.
99. Schuster, M.E.; Havecker, M.; Arrigo, R.; Blume, R.; Knauer, M.; Ivleva, N.P.; Su, D.S.; Niessner, R.; Schlogl, R. Surface sensitive study to determine the reactivity of soot with the focus on the European emission standards IV and VI. *J. Phys. Chem. A,* 2011, 115:2568-2580.
100. Chen, W.; Zhu, Z.; Li, S.; Chen, C.; Yan, L. Efficient preparation of highly hydrogenated graphene and its application as a high-performance anode material for lithium ion batteries. *Nanoscale*, 2012, 4:2124-2129.
101. Kalazhokov, Z.K.; Naumkin, A.V.; Zhansitov, A.;, Khashirova, S.Yu.; Kalazhokov, K.H.; Karamurzov, B.S. Investigation of carbon fiber/polyphenylenesulfone composites by method of X-ray photoelectron spectroscopy. *Key Engin. Mat.*, 2019, 816:37-42.
102. Komarova, N.S.; Krivenko, A.G.; Ryabenko, A.G.; Naumkin A.V. Active forms of oxygen as agents for electrochemical functionalization of SWCNTs. *Carbon,* 2013, 53:188-196.
103. Wang, J.; Chen, Z.; Chen, B. Adsorption of polycyclic aromatic hydrocarbons by graphene and graphene oxide nanosheets. *Environ. Sci. Technol.*, 2014, 48:4817-4825.
104. Gusmjo, R.; Sofer, Z.; Bouša, D.; Pumera, M. Synergetic metals on carbocatalyst shungite. *Chem. Eur. J.*, 2017, 23:18232-18238.
105. Beamson, G.; Briggs, D. High Resolution XPS of Organic Polymers. In: *The Scienta ESCA300 Database.* Wiley: Chichester, UK, 1992.
106. Acik, M.; Lee, G.; Mattevi, C.; Chhowalla, M.; Cho, K.; Chabal, Y.J. Unusual infrared-absorption mechanism in thermally reduced graphene oxide. *Nat. Mater.,* 2010, 9:840-845.
107. Acik, M.; Lee, G.; Mattevi, C.; Pirkle, A.; Wallace, R.M.; Chhowalla, M.; Cho, K.; Chabal, Y. The role of oxygen during thermal reduction of graphene oxide studied by infrared absorption spectroscopy. *J. Phys. Chem. C,* 2011, 115:19761-19781.
108. Kim, S.; Zhou, S.; Hu, Y.; Acik, M.; Chabal, Y.J.; Berger, C.; De Heer, W.; Bongiorno, A.; Riedo, E. Room-temperature metastability of multilayer graphene oxide films. *Nat. Mater.*, 2012, 11:544-549.
109. Radovich, L.R.; Bockrath, B. On the chemical nature of graphene edges: origin of stability and potential for magnetism in carbon materials. *JACS,* 2005, 127:5917-5927.
110. Serp, P.; Machado, B. (Eds.). *Nanostructured Carbon Materials for Catalysis*. Royal Society of Chemistry: Croydon, UK, 2015.
111. Villa, A.; Dimitratos, N. (Eds.) *Metal-free Functionalized Carbons in Catalysis: Synthesis, Characterization and Applications.* Royal Society of Chemistry: Croydon, UK, 2018.
112. Larciprete, R.; Lacovig, P.; Gardonio, S.; Baraldi, A.; Lizzit, S. Atomic oxygen on graphite: Chemical characterization and thermal reduction. *J. Phys. Chem. C,* 2012, 116:9900-9908.
113. Yamada, Y.; Yasuda, H.; Murota, K.; Nakamura, M.; Sodesawa, T.; Sato, S. Analysis of heat-treated graphite oxide by X-ray photoelectron spectroscopy. *J. Mater. Sci.,* 2013, 48:8171-8198.
114. Alternative Asymmetric Line-Shapes. Available online: http://www.casaxps.com/

help_manual/line_shapes.htm (accessed on 1 January 2023).
115. Coates, J. *Encyclopedia of Analytical Chemistry. In Application, Theory and Instrumentation,* 2nd ed. Meyers, R.A., Ed.; Wiley: Chichester, UK, 2006; pp. 1–23.
116. Varsanyi, G. *Assignments for Vibrational Spectra of Seven Hundred Benzene Derivatives.* Hilger, A.: London, UK, 1974.
117. Baskir, E.G.; Maltsev, A.K.; Korolev, V.A.; Khabashesku, V.N.; Nefedov, O.M. Generation and IR spectroscopic study of benzyl radical. *Russ. Chem. Bull.*, 1993, 42:1438-1440.
118. Crespo-Otero, R.; Bravo-Rodriguez, K.; Roy, S.; Benighaus, T.; Thiel, W.; Sander, W.; Sánchez-García, E. Interactions of aromatic radicals with water. *Chem. Phys. Chem.,* 2013, 14:805-811.
119. Wilmshurst, J.K.; Bernstein, H.J. The infrared and Raman spectra of toluene, toluene –alfa-d4, m-xylene, and m-xylene = alfaalfa'-d6. *Can. J. Chem.*, 1957, 35:911-925.
120. Gardner, A.M.; Green, A.M.; Tamé-Reyes, V.M.; Wilton, V.H.K.; Wright, T.G. Vibrations of the low energy states of toluene (1A1 and 1B2) and the toluene cation (2B1). *J. Chem. Phys.*, 2013, 138:134303.
121. Sheka, E.; Natkaniec, I.; Rozhkova, N.; Buslaeva, E.; Tkachev, S.; Gubin, S.; Mel'Nikov, V. Parent and reduced graphene oxide of different origin in light of neutron scattering. *Nanosyst.: Phys. Chem., Math.*, 2016, 7:71-80.
122. Fillaux, F.; Papoular, R.; Lautié, A.; Tomkinson, J. Inelastic neutron-scattering study of the proton dynamics in coals. *Fuel,* 1995, 74:865-873.
123. Fuente, E.; Menndez, J.A.; Diez, M.A.; Montes-Moran, M.A. Infrared spectroscopy of carbon materials: A quantum chemical study of model compounds. *J. Phys. Chem. B,* 2003, 107:6350-6359.
124. Sheka, E.F. Digital Twins solve the mystery of Raman spectra of parental and reduced graphene oxides. *Nanomaterials*, 2022, 12:4209.
125. Singh, S.K.; Peeters, F.M. Vibrational properties of nanographene. *NanoMMTA,* 2013, 2:10-29.
126. Sheka, E.F. Virtual vibrational spectrometry of stable radicals—Necklaced graphene molecules. *Nanomaterials*, 2022, 12:597.
127. Jorio, A.; Dresselhaus, M.S.; Saito, R.; Dresselhaus, G. *Raman Spectroscopy in Graphene Related Systems.* Wiley-VCH: Weinheim, Germany, 2011.
128. Merlen, A.; Buijnsters, J.G.; Pardanaud, C. A guide to and review of the use of multiwavelength Raman spectroscopy for characterizing defective aromatic carbon solids: From graphene to amorphous carbons. *Coatings*, 2017, 7:153.
129. Tuinstra, F.; Koenig, J.L. Raman spectrum of graphite. *J. Chem. Phys.,* 1970, 53:1126.
130. Pimenta, M.A.; Dresselhaus, G.; Dresselhaus, M.S.; Cançado, L.G.; Jorio, A.; Saito, R. Studying disorder in graphite-based systems by Raman spectroscopy. *Phys. Chem. Chem. Phys.,* 2007, 9:1276-1290.
131. Venezuela, P.; Lazzeri, M.; Mauri, F. Theory of double-resonant spectra in graphene.: Intensity and line shape of defect-induced and two-phonon bands. *Phys. Rev. B.,* 2011, 84:1-25.
132. Ramos, S.L.; Pimenta, M.A.; Champi, A. Multiple-excitation study of the double-resonance Raman bands in rhombohedral graphite. *Carbon,* 2021, 179:683-691.
133. Ferrari, A.C.; Robertson, J. Raman spectroscopy of amorphous, nanostructured, diamond–like carbon, and nanodiamond. *Philos. Trans. R. Soc. A: Math. Phys. Eng. Sci.,* 2004, 362:2477-2512.
134. Mallet-Ladeira, P.; Puech, P.; Toulouse, C.; Cazayous, M.; Ratel-Ramond, N.; Weisbecker, P.; Monthioux, M. A Raman study to obtain crystallite size of carbon materials: A better alternative to the Tuinstra and Koenig law. *Carbon*, 2017, 80:629-639.
135. Mapelli, C.; Castiglioni, C.; Meroni, E.; Zerbi, G. Graphite and graphitic compounds: Vibrational spectra from oligomers to real materials. *J. Mol. Struct.*, 1999, 480-481, 615-620.
136. Mapelli, C.; Castiglioni, C.; Zerbi, G.; Müllen, K. Common force field for graphite and polycyclic aromatic hydrocarbons. *Phys. Rev. B,* 1999, 60:12710-12725.
137. Castiglioni, C.; Mapelli, C.; Negri, F.; Zerbi, G. Origin of the D line in the Raman spectrum of graphite: A study based on Raman frequencies and intensities of polycyclic aromatic hydrocarbon molecules. *J. Chem. Phys.,* 2001, 114:963-974.

138. Negri, F.; Castiglioni, C.; Tommasini, M.; Zerbi, G. A computational study of the Raman spectra of large polycyclic aromatic hydrocarbons: Toward molecularly defined subunits of graphite. *J. Phys. Chem. A,* 2002, 106:3306-3317.
139. Di Donato, E.; Tommasini, M.; Fustella, G.; Brambilla, L.; Castiglioni, C.; Zerbi, G.; Simpson, C.D.; Müllen, K.; Negri, F. Wavelength-dependent Raman activity of D2h symmetry polycyclic aromatic hydrocarbons in the D-band and acoustic phonon regions. *Chem. Phys.*, 2004, 301:81-93.
140. Negri, F.; di Donato, E.; Tommasini, M.; Castiglioni, C.; Zerbi, G.; Müllen, K. Resonance Raman contribution to the D band of carbon materials: Modeling defects with quantum chemistry. *J. Chem. Phys.*, 2004, 120:11889-11900.
141. Tommasini, M.; Castiglioni, C.; Zerbi, G. Raman scattering of molecular graphenes. *Phys. Chem. Chem. Phys.,* 2009, 11:10185-10194.
142. Golubev, Y.A.; Sheka, E.F. Peculiarities of the molecular character of the vibrational spectra of amorphous sp2 carbon: IR absorption and Raman scattering. *Proceedings of the 14th Intrnational Conference Carbon: Fundamental Problems of Material Science and Technology*, Moscow, Troitzk, 7-9 June 2022; pp. 59–60, (in Russ.).
143. Yang, X.; Han, D.; Fan, H.; Wang, M.; Du, M.; Wang, X. First-principles calculations of phonon behaviors in graphether: A comparative study with graphene. *Phys. Chem. Chem. Phys.*, 2020, 23:123-130.
144. Savosteenko, G.; Taskaev, S.; Avramov, P. Structure and Raman spectra of exotic carbon microcrystals from meteoritic dust of Chelyabinsk superbolide. *Nanomaterials,* 2023, 13:73.
145. Sheka, E.F. Molecular theory of graphene chemical modification. In: *Graphene Science Handbook: Mechanical and Chemical Properties*; Aliofkhazraei, M., Ali, N., Miln, W.I., Ozkan, C.S., Mitura, S., Gervasoni, J., Eds.; CRC Press: Boca Raton, FL, USA; Taylor and Francis Group: Abingdon, UK, 2016; pp. 312–338.
146. Rasheed, A.; San, O.; Kvamsdal, T. Digital twins: Values, challenges and enablers from a modeling perspective. *IEEE Access,* 2020, 8:21980-22012; https://doi.org/0.1109/ACCESS.2020.2970143.
147. Belousova, I.M.; Videnichev, D.A.; Kislyakov, I.M.; Krisko, T.K.; Rozhkova, N.N.; Rozhkov, S.S. Comparative studies of optical limiting in fullerene and shungite nanocarbon aqueous dispersions. *Opt. Mat. Expr.*, 2015, 5:169-175.
148. Skrypnik, L.; Babich, O.; Sukhikh, S.; Shishko, O.; Ivanova, S.; Mozhei, O.; Kochish, I.; Nikonov, I. A Study of the Antioxidant, Cytotoxic Activity and Adsorption Properties of Karelian Shungite by Physicochemical Methods. *Antioxidants,* 2021, 10:1121.
149. Sheka, E.F.; Popova, N.A.; Popova, V.A. Virtual spectrometer for sp2 carbon clusters. 1. Polycyclic benzenoid-fused hydrocarbons. *FNCN,* 2021, 29:703-715.
150. Bloino, J. A VPT2 route to near-infrared spectroscopy: The role of mechanical and electrical anharmonicity. *J. Phys. Chem. A,* 2015, 119:5269-5287.
151. Dewar, M.J.S.; Ford, G.P.; McKee, M.-L.; Rzepa, H.S.; Thiel, W.; Yamaguchi, Y. Semiempirical calculations of molecular vibrational frequencies: The MNDO method. *J. Mol. Struct.,* 1978, 43:135-138.
152. Dolganov, V.K.; Kroo, N.; Rosta, L.; Sheka, E.F.; Szabort, J. Multimode polymorphism of solid MBBA. *Mol. Cryst. Liq. Cryst.*, 1985, 127:187-194.
153. Sharma, N.; Sharma, V.; Jain, Y.; Kumari, M.; Gupta, R.; Sharma, S.K.; Sachdev, K. Synthesis and characterization of graphene oxide (GO) and reduced graphene oxide (rGO) for gas sensing application. *Macromol. Symp.,* 2017, 376:1700006.

DOI: 10.17725/rensit.2023.15.295

Temperature influence on the formation of Langmuir monolayers with Ni arachidic acid and Ni arachidate clusters

Iliya A. Gorbachev, Andrey V. Smirnov, Iren E. Kuznetsova, Vladimir V. Kolesov

Kotelnikov Institute of Radioengineering and Electronics of Russian Academy of Science, http://www.cplire.ru/
Moscow 125009, Russian Federation

E-mail: iliyagor36@gmail.com, andre-smirnov-v@yandex.ru, kuziren@yandex.ru, kvv@cplire.ru

Received September 07, 2023, peer-reviewed September 14, 2023, accepted September 21. 2023

Abstract: **Changing the temperature of the aqueous subphase makes it possible to control the absorption rate of metal ions dissolved in the aqueous subphase by the Langmuir monolayer. This affects the morphology of the Langmuir monolayers formed at an elevated temperature of the aqueous subphase. An adsorption of metal ions by a monolayer leads to the formation of nanoclusters under it. In the present work the process of formation of nickel arachidate (NiArch) clusters under a Langmuir monolayer of arachidic acid (AA) at different temperatures was studied. The process of adsorption of Ni^{2+} ions and formation of clusters of nickel salts under a Langmuir monolayer of arachidic acid (AA) at different temperatures was studied. The subphase temperature was changed in the range of 10 to 30°C with a step of 4°C. The formed films were transferred on the solid substrates. The morphology of the corresponding LB films transferred onto a solid substrate was analyzed by atomic force microscopy. It was found that an increase in the subphase temperature leads to changing in the process of Ni^{2+} ions adsorption by Langmuir monolayer of AA. It was shown that subphase temperature influenced the compressibility of a monolayer, the area occupied by one molecule in the Langmuir monolayer of NiArch, and the morphology of Langmuir-Blodgett (LB) films formed on their basis. An increasing of subphase temperature leads to increase in the number of NiArch clusters in the LB AA film and a decrease in their size. This is due to a change in the rate of growth and dissolution of NiArch clusters with a temperature change. The distribution of NiArch clusters in the resulting film was random. The results obtained are of great importance for the possibility of the creation of multilayer composite coatings with controlled characteristics.**

Keywords: **Langmuir monolayers, Ni arachidate clusters, arachidic acid, monolayer morphology, atomic force microscopy, Langmuir-Blodgett films**

UDC 539.23, 544.032.7

Acknowledgments: The work was carried out with the financial support of the Russian Science Foundation, grant No. 22-29-20317.

For citation: Iliya A. Gorbachev, Andrey V. Smirnov, Iren E. Kuznetsova, Vladimir V. Kolesov. Temperature influence on the formation of Langmuir monolayers with Ni arachidic acid and Ni arachidate clusters. *RENSIT: Radioelectronics. Nanosystems. Information Technologies,* 2023, 15(3):295-306e. DOI: 10.17725/rensit.2023.15.295.

Contents

1. INTRODUCTION

The Langmuir-Blodgett (LB) technology is a promising method for the formation of thin highly organized films based on amphiphilic molecules or nanoparticles stabilized by them [1-3]. The use of surfactants with selectivity to various agents makes it possible to create thin films with sensory properties [4-6]. As is known, the developed surface of LB films allows them to be used, among other things, as sensitive adhesive coatings [7]. In this case, the problem of increasing the specific surface area of such a film is of particular relevance. One of the approaches to the creation of LB films with a developed morphology is the formation of mixed Langmuir monolayers with embedded nanoscale objects [8,9]. Two approaches are used to form such films. The first approach is used in the formation of mixed layers with nanoparticles synthesized in a separate technological cycle [10,11]. The second one is to obtain nanoparticles during the formation of the film itself [12]. A monolayer of surfactant molecules is modified by metal ions dissolved in the aqueous subphase to reach this purpose. The adsorption of metal ions by a Langmuir monolayer leads to the appearance and growth of clusters under its surface. In this case, an exchange reaction occurs between the polar part of the surfactant molecule and ions dissolved in the aqueous subphase [13,14]. As is known, the physicochemical properties of the formed monolayers depend on the acidity and temperature of the subphase, as well as on the concentration of metal ions in the subphase [15]. This is clearly seen in the analysis of the compression isotherms of the created monolayers. The effect of Cu^{2+}, Ca^{2+}, and Ni^{2+} ions on phase transitions and the morphology of fatty acid monolayers was studied in [16-20]. The effect of the adsorption of Ba^{2+} ions on the morphology and phase transitions in mixed monolayers of behenic and stearic acids was studied in [21]. It was shown that the adsorption of metal ions can lead to the disappearance of the liquid phase of the monolayer [16,17], an increase in its length [18], and a change in the shape of the compression isotherm after the collapse of the monolayer [21,22]. The effect of temperature and acidity on the stability of monolayers of oleic acid and bovine serum albumin in the presence of Ca^{2+} ions was studied in [23]. It should be noted that the adsorption of metal ions from the subphase should affect the morphology of the Langmuir-Blodgett film transferred onto a solid substrate. In particular, the authors of [19, 24] studied the effect of the adsorption of Ni^{2+} and Cd^{2+} ions on the morphology of the Langmuir–Blodgett film of arachidic acid. It was shown that in this case the area occupied by arachidic acid molecules in the film changes. The possibility of forming a multilayer film structure during the collapse of a monolayer on the subphase surface was also demonstrated [21,22].

The morphology and surface-active properties of monolayers can also be affected by external electric and magnetic fields. For example, an external magnetic field applied to a monolayer of arachidic acid during the adsorption of iron ions makes it possible to control the growth direction of iron nanoparticles under the monolayer [25]. Thus, by changing the adsorption parameters of metal ions, it is possible to influence the morphology of Langmuir-Blodgett films.

The formation of metal nanoparticles under the surface of a monolayer leads to the creation of inhomogeneity in the morphology of films obtained on its basis. Similar inhomogeneities are formed during the synthesis of nanoparticles in a mixed monolayer [14]. It should be noted that based on the above-mixed monolayers doped with metal ions, it is possible to create composite coatings with different properties.

An analysis of the literature showed that temperature is the least studied factor influencing the properties of Langmuir monolayers and the growth dynamics of nanoparticles under them. This is because temperature affects both the

monolayer formation process and the dynamics of the nanoparticle formation reaction. It is a challenge to study these processes separately from each other. It should also be noted that controlling the number of nanoclusters of metals and their compounds in Langmuir monolayers is an important problem for their practical application as conductive or sensor coatings. However, the effect of temperature on this parameter has not yet been practically studied.

The ordered films with incorporated magnetic nanoparticles made of such materials as nickel, iron, and cobalt have the particular interest. It should be noted that nickel nanoparticles have a noticeable antibacterial effect against resistant bacterial cultures [26]. Using the effect of temperature on the properties of LB films based on fatty acids containing similar nanoparticles, it is possible to form films with a more developed surface. Such films can be further used as sensor coatings in various sensors and can be effectively used in food safety technologies.

Thus, the purpose of this work was to study the mechanism of the formation of nickel arachidate (NiArch) clusters under a Langmuir monolayer of arachidic acid (AA) at different temperatures and to investigate the morphology of LB films based on the resulting mixed monolayers.

2. EXPERIMENTAL PART

2.1. Formation of Langmuir monolayers

AA [$CH_3(CH_2)_{18}COOH$, 99%], chloroform (PAI, filtered), chloride nickel powder [$NiCl_2 \times 6H_2O$, 99.9%], sodium citrate [$Na_3C_6H_5O_7 \times 2H_2O$], and citric acid [$C_6H_8O_7 \times H_2O$] were purchased from Sigma Aldrich. Deionized water (electrical resistivity of 18 MΩ·cm) was obtained by means of ultrapure water purification system Milli-*Q* plus (Millipore Corp.).

All LB monolayers were produced with an automated LB KSV NIMA 622 (KSV Instruments Ltd., Finland) with a work square of 1200 cm^2. An aqueous solution of $NiCl_2$ (4 mM) was used as a subphase. The pH value of the subphase was fixed at pH = 5.8 to prevent the creation of $Ni(OH)_2$ and nickel-based tetranuclear hydrocomplex. The formation process of these compounds was a pH-dependence process that took a flow at pH value of more than 7 [27]. An acetate buffer (0.1 M; 22.67 g sodium citrate and 4.402 g citric acid ratio per liter of water) was used to adjust the acidity.

In the Langmuir-Blodgett technology, a continuous monomolecular layer is preliminarily formed on the subphase surface. Then, using a movable barrier, the monolayer is compressed to obtain a continuous film with close packing of molecules. Here the molecule mean area A is approximately equal to the cross-sectional area of the molecule, and hydrophobic hydrocarbon chains are oriented almost vertically. At the final stage, the formed monolayer was transferred onto the surface of the substrate at a constant surface pressure of 35 mN/m by using the Langmuir-Schaeffer method. The transferring ratio was equal to 0.9.

The influence of time on the process of nickel ion binding with an arachidic acid monolayer was studied in [19]. It has been shown that the incorporation of Ni^{2+} ions into the AA monolayer occurs even in the gas phase before the barriers begin to move. In the present work, the formation time of NiArch clusters was constant for each of the chosen temperatures and amounted to 75 minutes. In particular, the solvent evaporated from the water surface for 15 minutes, and then, for 60 minutes, the monolayer was compressed until a transfer pressure of 35 mN/m was reached.

A solution of arachidic acid (1 mM) in chloroform was used to form a monolayer. An aliquot of the solution (50 μL) was dropped onto the surface of the subphase, kept for 15 min, and compressed by movable barriers at a constant compression rate. The barrier compression rate was 20 cm^2/min. The influence of temperature on the properties of the Langmuir monolayer was studied in the range from 10 to 30°C with a step of 4°C. The subphase temperature was controlled by a Brinkmann Lauda RC6 RCS thermostat with an accuracy of ± 0.1°C.

2.2. Analysis of the compression isotherms

In the Langmuir-Blodgett technology, the state of the monolayer is described by the compression isotherm π-A, which reflects the ratio between the surface pressure of the barrier π and the molecule mean area A at a constant temperature T. It should be noted that the phase state of the amphiphilic substance monolayer localized at the "subphase-gas" interface is determined by the adhesive-cohesive balance of forces in the "subphase-monolayer"

system and depends on the nature of the substance and the structure of its molecules, temperature T, and subphase composition [28]. The linear sections on the π-A compression isotherm, corresponding to the compression of the monolayer in different phase states, are characterized by the area per molecule in the monolayer obtained by extrapolating the linear section to the abscissa axis (π = 0 mN/m). Thus, gaseous, liquid-expanded, tilted-condensed, and untilted-condensed phases of the monolayers are distinguished on the compression isotherm. These monolayers are in different states of aggregation.

The next parameters were used to assess the effect of temperature on the compression isotherms [15,29]:

A_{C0} and A_{L0} are the molecule mean area of AA molecule in the untilted-condensed, and tilted-condensed phases of a pure monolayer, respectively, and A_{C0} = 20.1 Å, A_{L0} = 23.5 Å at T = 22°C;

A_{CN} and A_{LN} are the molecule mean area of AA molecule in a monolayer formed on a subphase with dissolved Ni^{2+} ions in the untilted-condensed, and tilted-condensed phases, respectively, and $\perp A_d = A_{CN} - A_{C0}$;

$\perp A_0$ is the length of the area of the tilted-condensed phase of the AA monolayer on the compression isotherm. It is determined as $\perp A_0 = A_{L0} - A_{C0}$, $\perp A_N = A_{LN} - A_{CN}$;

k_C and k_L are the compression modulus of the monolayer in the untilted-condensed, and tilted-condensed phases, respectively.

The approach proposed by Vollhardt and Feinerma was used for quantitative assessment of k_C and k_L [28]. This approach is based on the assumption that the change in the slope of the linear sections of the compression isotherm corresponds to phase transitions in the monolayer. In this case, the change in compression modulus (k) of the monolayer can be estimated from:

$$k = -A_0 \frac{d\pi}{dA}. \quad (1)$$

Here A_0, A, π, are the area occupied by the molecule in the corresponding phase, the molecule mean area, the surface pressure, respectively.

The phase transition points appearing at the formation of a monolayer and the values of the corresponding molecule mean areas per molecule are usually determined using the dependence of the change in k versus A [30].

2.3. Morphology studies of the monolayers transferred onto the solid surface

Monolayers formed at a surface pressure of 35 mN/m were transferred using the Langmuir-Schaeffer method onto the surface of a hard glass coverslip with a size of 24 mm×24 mm and a roughness of ~0.6 nm (Carl ROTH Gmbh & Co, Germany). In this case, the monolayer is in the untilted-condensed phase at any temperature. Atomic force microscopy (AFM) Integra Spectra probe station (NT-MDT, Russia) was used to study the morphology of AA monolayers modified with NiArch clusters. Before AFM measurements, the samples were stored in a desiccator for 24 h at room temperature to evaporate water. AFM scans of 40 μm×40 μm and 5 μm×5 μm were used for the estimation of the NiArch cluster average area and its thickness, respectively. AFM images were analyzed using the ImageJ v.1.53e and Gwyddion v.2.61 programs. It allowed to perform statistical processing and determining the average geometric parameters of the cluster.

3. RESULTS AND DISCUSSION

3.1. Influence of Ni^{2+} ions

Compression isotherms of AA monolayers formed on the surface of the aqueous subphase at T = 22°C in the presence and the absence of dissolved Ni^{2+} ions are shown in **Fig. 1.** Adsorption of

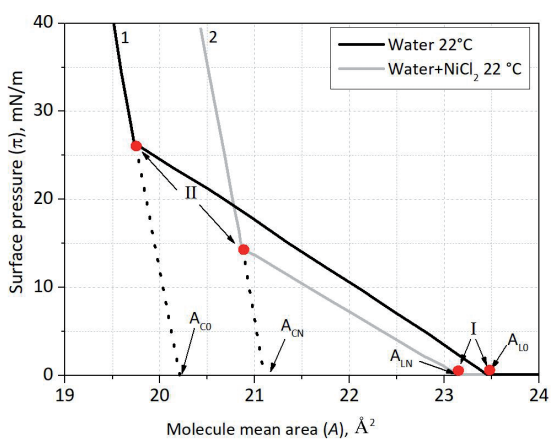

Fig. 1. *Typical compression isotherms of AA monolayer on the surface of aqueous subphase consisted of (1) pure water and (2) aqueous solution of $NiCl_2$ (4mM) obtained at T = 22°C. Points (I) and (II) indicate the phase transitions from coexisting of the gaseous and liquid-expanded phases to tilted-condensed phase (I) and from tilted-condensed to untilted-condensed phase (II) of the film, respectively.*

Ni^{2+} ions from the subphase with a $NiCl_2$ powder concentration not exceeding 1 mM affects the behavior of compression isotherms but does not lead to significant changes in the morphology of AA monolayers at any temperature of the subphase [30,31]. In this regard, the concentration of Ni^{2+} ions in the subphase was fixed at the level of 4 mM. It is necessary to note that the incorporation of nickel ions into the monolayer is as follows. The water-soluble salt $NiCl_2$ dissociates into Ni^{2+} and $2Cl^-$ ions. This process leads to the formation of water-insoluble hydroxide $Ni(OH)_2$ at an acidity above 7 [32]. At lower acidities, the complex compound $Ni(OH)_2$ is formed, which was observed in the present work. Negatively charged AA-ions are formed as a result of the polarization of the hydrophilic parts of AA molecules at their interaction with water molecules. This leads to the formation of a nickel arachinate salt (NiArch) and an increase in the area occupied by one AA molecule in the untilted-condensed phase (A_0) [32]. For this reason, Ni can be attributed to the group of metals, the use of which has an expanding effect when it is adsorbed by a Langmuir monolayer.

Points (I) and (II) correspond to the phase transitions in the AA monolayer coexisting of the gaseous and liquid-expanded phases – "tilted-condensed phase" (I) and "untilted-condensed phase" (II). The adsorption of Ni^{2+} ions in the LB film from the subphase leads to an increase in the area occupied by the AA molecule by 3.6% (from 20.1 Å^2 to 20.9 Å^2) and decrease in the length of the tilted-condensed phase region by 32%. The decrease in the length of the liquid phase region on the compression isotherm during the adsorption of Ni^{2+} ions agrees with the results of [18,30].

The presence of Ni^{2+} ions affects the average area occupied by an AA molecule in the untilted-condensed phase of a monolayer (A_{C0}). This change is more noticeable than the change in the molecule mean area in the tilted-condensed phase of the monolayer (A_{L0}). The change in the areas occupied by the AA molecule in the pure monolayer and the monolayer modified with NiArch clusters is 0.8 Å^2 and 0.2 Å^2 for the untilted-condensed and tilted-condensed phases of the AA monolayer, respectively.

3.2. Influence of temperature on the isotherms

Compression isotherms of AA monolayers formed on the subphase without dissolved Ni^{2+} ions at different subphase temperatures are shown in **Fig. 2**. It can be seen that a change in the subphase temperature from 10°C to 26°C leads to a change in the monolayer collapse pressure from 60 to 52 mN/m, and the molecule mean area (A_0) does not change. An increase in temperature to 30°C leads to a decrease in A_0 to 20.0 Å^2 and an increase in the length of the tilted-condensed phase of the AA monolayer from 1.9 Å^2 to 4.4 Å^2. A similar effect of decreasing the monolayer collapse pressure and the A_0 value was described earlier for monolayers of CdSe quantum dots stabilized with oleic acid. This effect was explained by a decrease in monolayer stability due to an increase in the thickness of the quiescent layer [33].

Compression isotherms of AA monolayers formed on the subphase in the presence of Ni2+ ions (a) and the dependences of changes in their compressibility modulus on the area occupied by one AA molecule (b) at various temperatures are shown in **Fig. 3**. Two linear segments corresponding to the transition of the AA monolayer from the coexisting of the gaseous and liquid-expanded phases to the tilted-condensed phase (I-II) and from the tilted-condensed to the untilted-condensed phase (III-IV) are shown in Fig. 3*b*. The line segment II-III in Figures 3*a* and 3*b* has corresponded to the

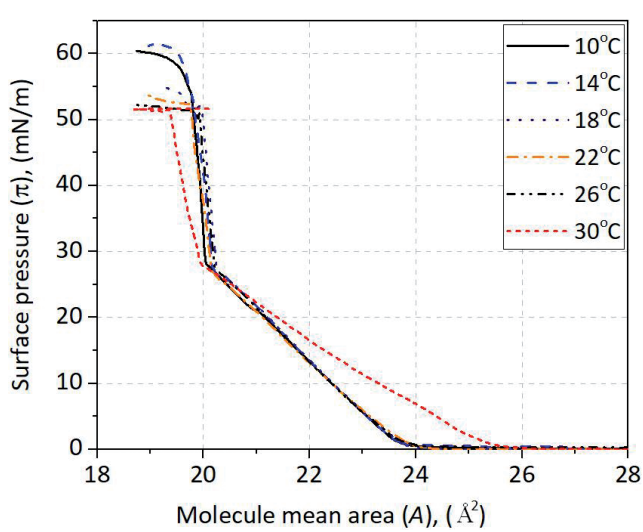

Fig. 2. *Compression isotherms of arachidic acid monolayers formed at the different subphase temperature in the absence of dissolved Ni^{2+} ions.*

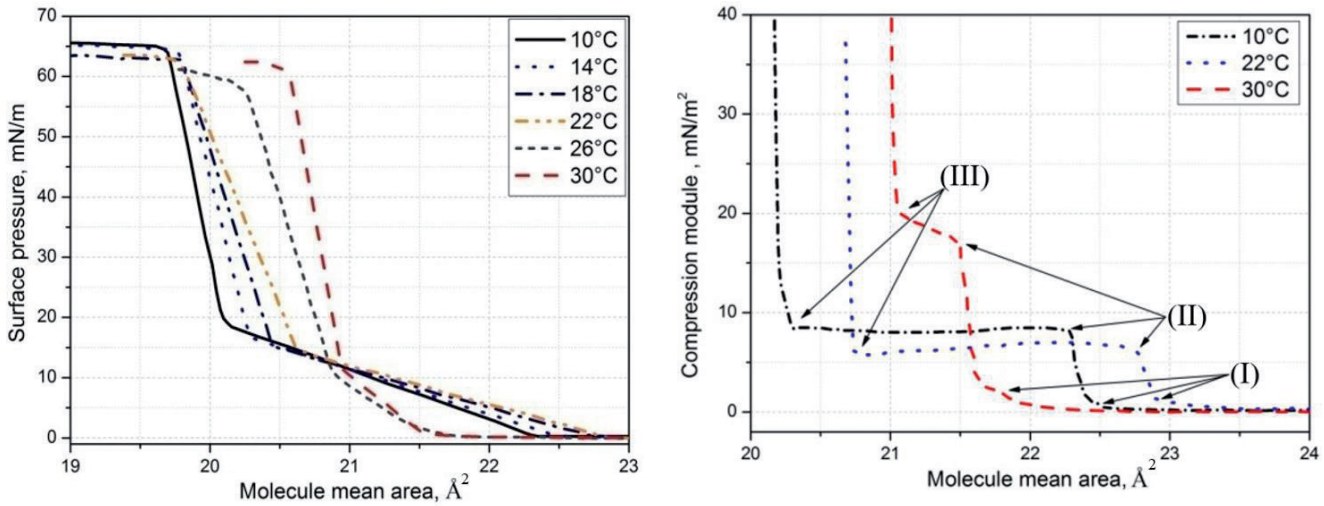

Fig. 3. (*a) Influence of the subphase temperature on the compression isotherms of AA monolayer in the presence of Ni^{2+} ions in the subphase (4mM). (b) The compression isotherms were obtained using the subphase with 10°C, 22°C, and 30°C temperatures. The segments I-II and III-IV in Fig. 3b are corresponded to the transition of the AA monolayer from the phase of coexisting of the gaseous and liquid-expanded phases to the tilted-condensed phase and from the tilted-condensed to the untilted-condensed phase, respectively. The linear segment II-III in Figures 3a and 3b is corresponded to the tilted-condensed phase of the AA monolayer.*

tilted-condensed phase of the AA monolayer. The temperature influence on the AA monolayers with embedded NiArch nanoparticles is presented in **Table 1.** It is possible to see that an increase in the subphase temperature reduces the length of the tilted-condensed phase region and the difference between the molecule mean areas of AA molecules in the monolayer. In this case, the compression modulus of the tilted-condensed and untilted-condensed phases of the AA monolayer increases.

From Fig. 3*b* it is possible to see that an increase in the temperature of the subphase leads to an increase in the slope of the section of the II-III compression isotherm at the T = 30°C. This is due to the change of the monolayer phase from the tilted-condensed phase of the AA monolayer at the subphase temperature T = 10°C and 22°C to the liquid-expanded phase at T = 30°C. Such behavior can be associated with an increase in the contribution from the interaction of the head groups of surfactant molecules with each other to the intermolecular interaction in the monolayer during its compression [34-36] and a decrease in the length of the tilted-condensed phase region of the monolayer on the compression isotherm ($\perp A_0$) [37,38]. The described effect is associated with the appearance of NiArch clusters under the AA monolayer [39]. Compression of the AA monolayer leads to a change in the distance between Ni clusters and the formation of their aggregates under the surface of the subphase. This, in turn, leads to the appearance of inhomogeneity in the distribution of surface pressure. As a result of the subphase heating, the number of new points of NiArch clusters growth increases, and the type of the liquid phase of the AA monolayer changes.

A change in the temperature of the subphase also affects the untilted-condensed phase of the AA monolayer. Thus, an increase in the temperature of the subphase leads, on the whole, to a change in the properties of the AA monolayer itself. It can be seen that the A_{CN} reaches the maximum value at 30°C and

Table1

The temperature influence on the AA monolayers with embedded NiArch nanoparticles: the difference between mean area of AA in the pure monolayer and in the monolayer modified by NiArch (ΔA_d), length of liquid phase (ΔA_0), monolayer compressibility modulus in untilted-condensed (k_C) and tilted-condensed (k_L) phases.

Temperature, °C	Condensed phase		Liquid phase		ΔA_0, Å^2	ΔA_d, Å^2
	A_{CN}, Å^2	$k_C \times 10^3 mN/m$	A_{LN}, Å^2	$k_L \times 10^3 mN/m$		
10	20.2	0.4	22.3	5.5	2.1	0.8
14	20.4	0.5	22.5	5.9	2.1	1.0
18	20.6	0.7	22.7	6.7	2.1	1.2
22	20.9	0.8	22.9	6.7	2.0	1.5
26	20.9	0.6	21.6	3.5	0.7	1.6
30	21.0	0.4	21.5	2.5	0.5	1.6

k_C reaches the minimal value at 22°C (Table 1). For the untilted-condensed and tilted-condensed phases, the values of k_C and k_L take maximal values at temperatures of 10°C and 30°C (Table 1). This can be explained as follows. It is well known that the rate of a chemical reaction has an exponential temperature dependence [40]. In our case, a decrease in the temperature of the subphase leads to a slowdown in the reaction rate of the formation of NiArch. In this regard, the properties of the NiArch monolayer slightly differ from the properties of the AA monolayer. An increase in the subphase temperature leads to an increase in the efficiency of the exchange reaction and an increase in the homogeneity of the monolayer due to the appearance of new centers of growth of NiArch clusters [34,41].

3.3. Morphology of LB films based on AA monolayers with NiArch clusters

The images of the AA LB film and its profile line height are shown in **Fig. 4**. The film has a homogeneous morphology with alterations in profile height close to 2 nm that is comparable with the length of the AA molecule 2.25 nm. The defects in the film are explained by the structural rearrangements in the film during its drying.

The length of the tilted-condensed phase region on the compression isotherm (ΔA_0) is one of the most important parameters of a monolayer. Its analysis makes it possible to judge the intensity and efficiency of the salt formation reaction in the monolayer. From Table 1 it can be seen that the most dramatic change in ΔA_0 occurs at a subphase temperature above 26°C. This may be related both to the appearance of new growth centers of NiArch clusters and to a change in their size with an increase in the subphase temperature. The investigation of the surface morphology of LB films based on AA with NiArch clusters formed at different subphase temperatures was performed to this effect study.

The typical images of the surface of the obtained LB films based on AA monolayers with NiArch nanoparticles formed at different subphase temperatures are shown in **Fig. 5***a*. The right part of Fig. 5*a* shows an enlarged image of a group of NiArch clusters. The inset of Fig. 5*a* shows the surface profile of one NiArch cluster. The NiArch cluster is a cylindrical particle with a large aspect ratio between height and width.

An increase in the subphase temperature leads to an increase in the total number of NiArch clusters (Fig. 5*b*). The series of 7 images of the film surface morphology with dimensions of 40×40μm were obtained to construct a histogram of the distribution of the number of particles by size. Series were obtained for the films formed at subphase temperatures of 10°C, 14°C, 18°C, 22°C, 26°C, and 30°C. The histograms were constructed by using mathematical processing each of the obtained images. Such a histogram

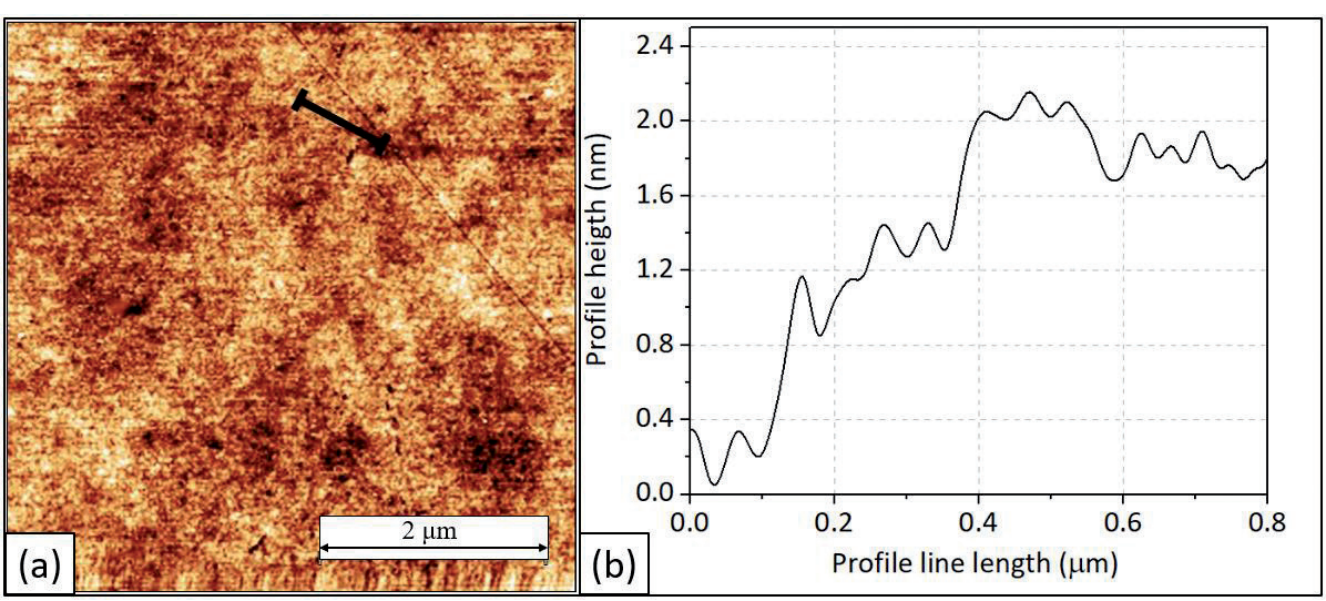

Fig. 4. *An AFM image of AA LB film formed at 22°C on the water subphase in the absence of Ni^{2+} ions (a) and the film profile line (b).*

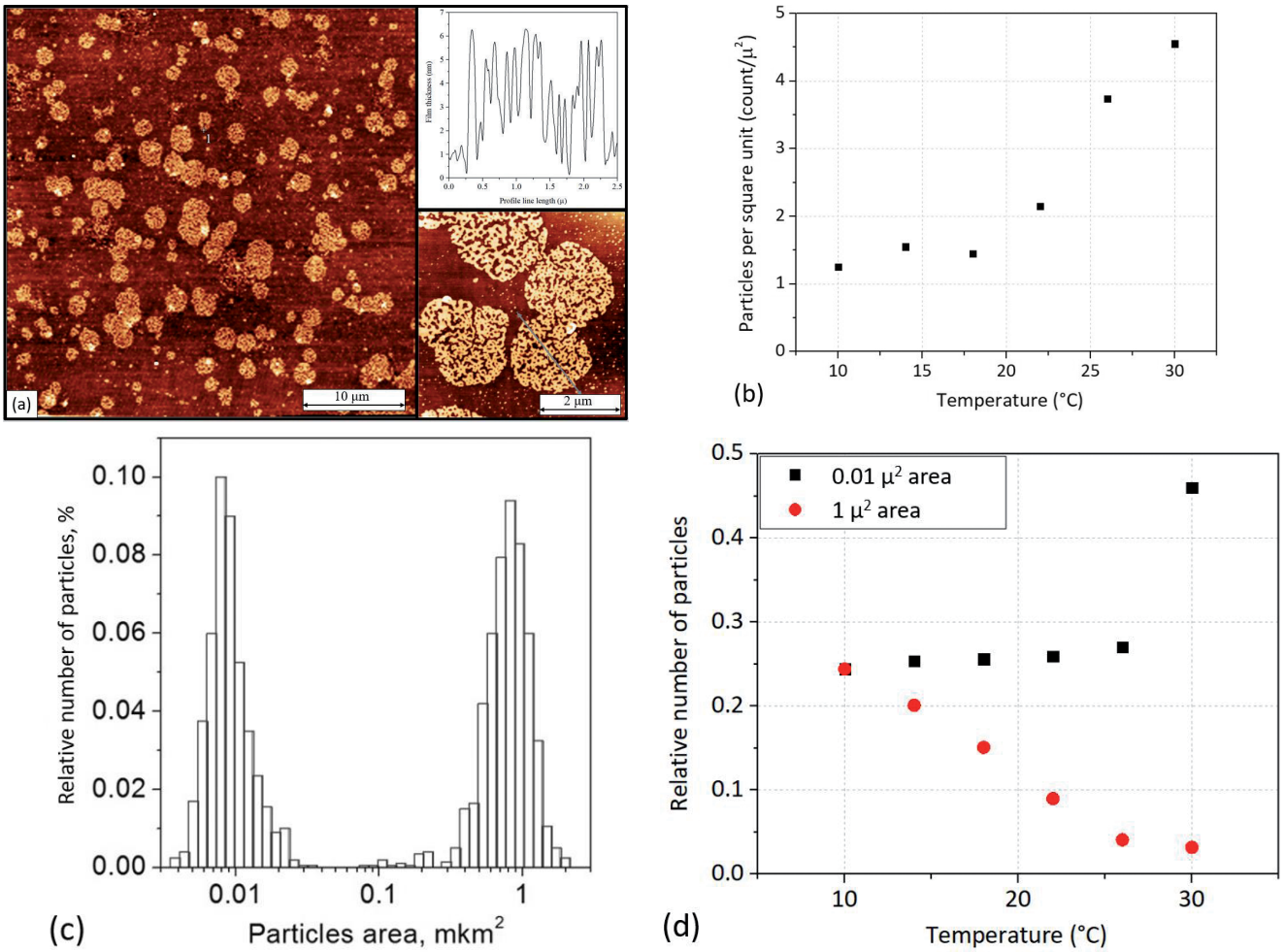

Fig. 5. *(a) An example of AFM image of LB film with NiArch clusters formed at the subphase temperature of 22°C; (b) influence of subphase temperature on numbers of particles per one area init; (c) typical histogram of particles size distribution; (d) Changing of the relative number of NiArch clusters with an occupied area of 0.01 μm².*

for T = 22°C is shown in Fig. 5*c*. There are two peaks corresponding to NiArch clusters with an area of 1 and 0.01 μm². The number of particles with an area of more than 1 μm² and less than 0.01 μm² was less than 0.05%.

In this regard, NiArch clusters with an area of only 1 μm² and 0.01 μm² were analyzed. The histograms were fitted with a Gaussian distribution (Fig. 5*d*). It can be seen that at a subphase temperature of 10°C, the number of NiArch clusters with an area of 1 μm² and 0.01 μm² is the same. An increase in the subphase temperature leads to an increase in the number of NiArch clusters with an area of 0.01 μm² and a decrease in the number of NiArch clusters with an area of 1 μm². At a subphase temperature of 30°C, the number of NiArch clusters with an area of 1 μm² becomes minimal.

The temperature dependences of the geometric dimensions and areas occupied by NiArch clusters in the formed LB films are presented in **Fig. 6.** Despite an increase in the number of the NiArch clusters upon subphase heating (Fig. 5*b*), the area occupied by NiArch clusters decreases (Fig. 6*a*). As the subphase temperature increases, the average thickness of the NiArch cluster first increases, reaches a maximum at 22°C, and then decreases (Fig. 6*b*). The average area of NiArch clusters also decreases monotonically with temperature increasing (Fig. 6*c*).

The change in the number and average size of NiArch clusters with an increase in the subphase temperature can be explained by the next reasons. As the temperature rises, the efficiency of the exchange reaction between the Ni^{2+} ions in the subphase and the polar part of the AA molecule (carboxyl group) increases. Consequently, the number of new cluster growth centers increases. In this case, the dissolution rate of clusters also

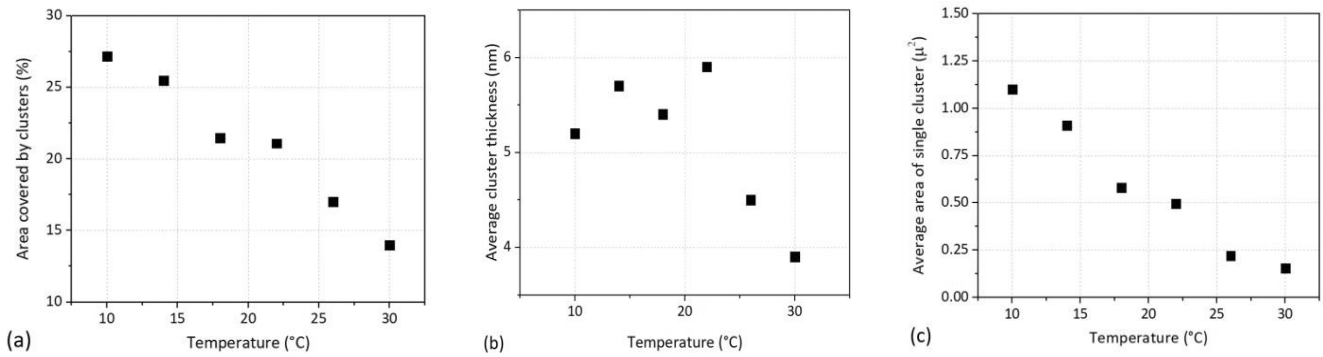

Fig. 6. *The dependencies of (a) film area covered by NiArch clusters, (b) average thickness of NiArch clusters, and (c) average NiArch clusters area (c) on subphase temperature.*

increases at high temperatures, which leads to a decrease in their average area. The subphase heating leads to decreasing cluster sizes (area and thickness). It was found that the horizontal and vertical dissolution rates of the cluster are different. During growth, the cluster is assembled from nuclei of different sizes; therefore, the cluster assembled from them will have a dendrite-like structure with a non-uniform thickness. For this reason, when a cluster is dissolved, the fine fractions located on its periphery first dissolve. This explains the decrease in the area of clusters and the change in the ratio of the number of clusters with areas of 0.01 μm^2 and 1 μm^2. The dissolution rate of the cluster in thickness is lower, which is explained by the presence of a highly porous dendrite-like structure of the cluster.

These effects can be described by the theory of homogeneous nucleation, which is used to analyze the growth of clusters [36]. This approach implies the existence of a minimum lifetime of clusters during which they dissolve or aggregate to form a stable particle. In this work, the concentration of Ni^{2+} ions in the subphase is far from the saturated concentration. This leads to an insignificant probability of the appearance of nickel derivatives in the volume of the subphase. At the same time, the change in the concentration of Ni^{2+} ions in the interfacial layer occurs as a result of the compression of the AA monolayer with NiArch clusters by movable barriers. This process leads to the formation of NiArch aggregates at the layer boundary. The described effect allows us to consider the system "Langmuir monolayer – the surface layer of the interface" as a supersaturated solution (**Fig. 7**) [40].

In the near-surface layer, due to the adsorption of Ni^{2+} ions by an AA monolayer and its further compression, conditions for an increase in the local concentration of nickel are created. Due to this effect, surface NiArch aggregates are formed at the water-air interface. These aggregates are the seeds for the further growth of clusters. The reaction of the formation of NiArch clusters proceeds continuously from the moment the solution of AA is placed on the surface of the aqueous subphase. At that, an increase in the temperature of the subphase leads to an increase in the rate of the above reaction. In this regard, there is an increase in the number of points of growth of NiArch clusters.

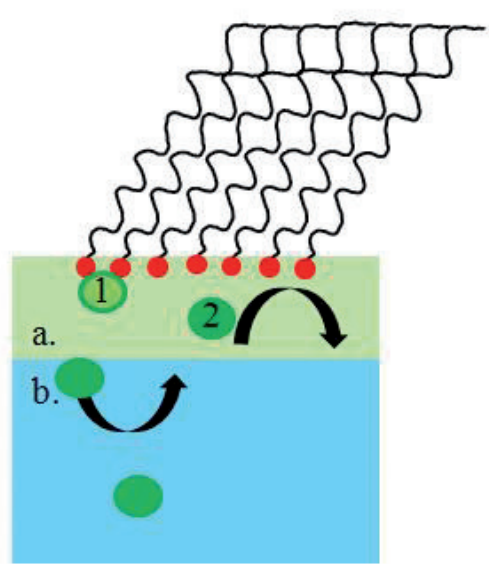

Fig. 7. *Schematic illustration of volume and interfacial layer of water subphase. "a." is an interfacial layer, "b." is a volume of subphase, 1 are Ni^{2+} ions that were reacted with AA molecule and formed a NiArch cluster, 2 are Ni^{2+} ions that were not reacted with acid molecules and could diffuse from interfacial layer to the subphase.*

A decrease in the temperature of the subphase leads to a decrease in the limiting solubility of the nickel chloride salt and a decrease in the dissolution rate of nickel arachidate in the subphase. In this case, the compression of barriers leads to an increase in the average area of NiArch clusters due to their aggregation. The simultaneous influence of these factors leads to the achievement of the critical size of NiArch nuclei when the dissolution process stops.

4. CONCLUSION

The process of formation of clusters of nickel salts under a Langmuir monolayer of arachidic acid (AA) at different temperatures was studied, and the morphology of the corresponding LB films transferred onto a solid substrate was analyzed. It was shown that the change in the number of growth centers of nickel arachidate (NiArch) clusters under the Langmuir AA monolayer can be controlled by the subphase temperature change. It was found that an increase in the subphase temperature in the range from 10°C to 30°C leads to a change in the type of the liquid phase of the AA monolayer with included NiArch clusters and to a decrease in the length of the liquid phase region of the AA monolayer on the compression isotherm. An AA monolayer with incorporated NiArch clusters is in a tilted-condensed phase at a subphase temperature of 10°C. An increase in the temperature of the subphase to 30°C leads to a change in the monolayer phase condition from the tilted-condensed phase to the liquid-expanded phase. This effect can be associated with an increase in the number of growth points of NiArch clusters under the AA monolayer with an increase in the subphase temperature to 30°C.

It was found that an increase in the subphase temperature leads to an increase in the number of NiArch clusters in the LB AA film and a decrease in their size. An increase in the number of NiArch clusters can be associated with an increase in the number of points of their growth with an increase in the temperature of the subphase. Reducing the cluster size, i.e. its average area and thickness is associated with an increase in the dissolution rate of NiArch nuclei in the subphase during its heating. The process of changing the size of a cluster can be described in terms of the theory of nucleation in colloidal solutions. This theory can be applied to our case, taking into account that the nucleation process was localized directly under the monolayer. The factor initiating the process of cluster formation is the change in the intermolecular distance upon compression of the monolayer by barriers. This leads to a change in the local concentration of NiArch molecules in the surface layer and the appearance of NiArch clusters with different sizes. Some of these clusters do not dissolve completely, because their size is large enough and they can to absorb smaller clusters. In general, this leads to an increase in the number and average size of NiArch clusters. However, an increase in the subphase temperature accelerates the dissolution of both large and small clusters. The distribution of NiArch clusters in the formed film was random. However, using the magnetic properties of nickel, they can be structured using external magnetic fields. Using the magnetic properties of NiArch clusters will make it possible to purposefully control the distribution of NiArch clusters in a Langmuir monolayer by an external magnetic field during its formation.

The results obtained are of great importance for the creation of multilayer composite coatings with controlled properties. These coatings can be further used as sensitive coatings for acoustic and electronic sensors.

REFERENCES

1. Kondalkara VV, Yang SS, Patil PS, Choudhury S, Bhosale PN, Lee KK. Langmuir-Blodgett assembly of nanometric WO_3 thin film for electrochromic performance: A new way. *Materials Letters,* 2017, 194:102-106.
2. Li T, Lilja K, Morris RJ, Brandani GB. Langmuir-Blodgett technique for anisotropic colloids: Young investigator perspective. *Journal of Colloid and Interface Science*, 2019, 540:420-438. DOI:10.1016/j.jcis.2019.01.044.
3. Xu L, Tetreault AR, Khaligh HH, Goldthorpe IA, Wettig SD, Pope MA. Continuous Langmuir–Blodgett Deposition and. Transfer by Controlled Edge-to-Edge Assembly of Floating 2D Materials. *Langmuir,* 2019, 35:51-59.
4. Avramov ID, Ivanov GR. Layer by Layer Optimization of Langmuir–Blodgett Films for Surface Acoustic Wave (SAW) Based Sensors for

Volatile Organic Compounds (VOC) Detection. *Coatings,* 2022, 15:669.
5. Silva EA, Braunger ML, Gregori A, Olivati CA. Volatile organic compounds detection by electrical sensors using polyalkylthiophene-based Langmuir–Blodgett films. *Applied Sciences,* 2019, 1(3):1-9. DOI: 10.1007/s42452-019-0187-z.
6. Sołoducho J, Cabaj J, Swist A. Structure and Sensor Properties of Thin Ordered Solid Films. *Sensors,* 2009, 9:7733-7752.
7. L. Caseli. Enzymes immobilized in Langmuir-Blodgett films: Why determining the surface properties in Langmuir monolayer is important? *An Acad Bras Cienc.*, 2018, 9:631-644.
8. Gorbachev IA, Smirnov AV, Glukhovskoy EG, Kolesov VV, Ivanov GR, Kuznetsova IE. Morphology of Mixed Langmuir and Langmuir–Schaefer Monolayers with Covered CdSe/CdS/ZnS Quantum Dots and Arachidic Acid. *Langmuir,* 2021, 37:14105-14113. DOI: 10.1021/acs.langmuir.1c02345.
9. Thampi A, Babu K, Verma S. Large scale solvothermal synthesis and a strategy to obtain stable Langmuir–Blodgett film of CoFe2O4 nanoparticles. *Journal of Alloys and Compounds,* 2013, 564:143-150.
10. Villanueva ME, Lanterna AE, Vico RV. Hydrophobic silver nanoparticles interacting with phospholipids and stratum corneum mimic membranes in Langmuir monolayers. *Journal of Colloid and Interface Science,* 2019, 543:247-255. DOI: 10.1016/j.jcis.2019.02.069.
11. Justo Y, Moreels I, Lambert K, Hens Z. Langmuir–Blodgett monolayers of colloidal lead chalcogenide quantum dots: morphology and photoluminescence. *Nanotechnology,* 2010, 21:295606-295612.
12. Hupfer ML, Kaufmann M, Roussille L, Preish J, Weish D, Hinrichs K, Deckert V, Dietzek B, Beckert R, Presselt M. Arylic versus Alkylic-Hydrophobic Linkers Determine the Supramolecular Structure and Optoelectronic Properties of Tripodal Amphiphilic Push-Pull Thiazoles. *Langmuir*, 2019, 35:2561-2570.
13. Al-Ali F, Dejugnat C, Etemad-Moghadam G, Rico-Lattes I. Langmuir films of (alpha-amino) phosphorus amphiphiles on various ion-containing subphases. *Journal of Colloid and Interface Science,* 2004, 273(2):512–516.
14. Protasov DY, Jian WB, Svit KA, Duda TA, Teys SA, Kozhuhov AS, Sveshnikova LL, Zhuravlev KS. Formation of Arrays of Free-Standing CdS Quantum Dots Using the Langmuir–Blodgett Technique. *J. Phys. Chem. C*, 2011, 115:20148-20152.
15. Yanklovich MA, Ivanov NS, Sukhodolov NG, Zhukov AN. A study of the properties and composition of stearic acid monolayers on an aqueous subphase containing cadmium ions. *Colloid Journal,* 2016, 78(2):277-280.
16. Capistran BA, Blanchard GJ. Effects of Cu(II) on the Formation and Orientation of an Arachidic Acid Langmuir-Blodgett Film. *Langmuir,* 2019, 35:3346-3353. DOI: 10.1021/acs.langmuir.9b00022.
17. Vaknin D, Bu W, Satija SK, Travesset A. Ordering by Collapse: Formation of Bilayer and Trilayer Crystals by Folding Langmuir Monolayers. *Langmuir,* 2007, 23:1888-1897.
18. Khomutov GB, Bykov IV, Gainutdinov RV, Polyakov SN, Sergeyev-Cherenkov AN, Tolstikhina AL. Synthesis of Ni-containing nanoparticles in Langmuiur-Blodgett films. *Colloids and Surfaces A: Physicochemical and Engineering Aspects*, 2002, 198:559-567. DOI: 10.1016/S0927-7757(01)00961-X.
19. Chumakov A, Al-Alwani1 AJ, Ermakov A, Shinkarenko J, Begletsova N, Glukhovskoy E, Santer S. The Formation of arachidic acid Langmuir monolayers on the NiCl2 solution. *Journal of Physics: Conference Series,* 2018, 1124:081009.
20. Al-Alwani AJ, Mironyuk VN, Pozharov MV, Gavrikov MV, Glukhovskoy EG. Formation and phase behavior of porphyrin/arachidic acid mixed systems and morphology study of Langmuir-Schaefer thin films. *Soft Materials,* 2022, 20:310-321. DOI:10.1080/1539445X.2022.2028829.
21. Sah BK, Kundu S. Ccollapse of langmuir monolayer formed by the mixture of short- and long-tailed fatty acid molecules. *Colloid and Interface Science Communications,* 2020, 36:100261.
22. Klimova SA, Sreij R, Bratashov D, Bookhold J, Teichert N, Gorobets AS, Hellweg T. Pb arachidate Langmuir-Blodgett coatings of silicon wafers: relation between Pb particle density and

subphase composition *Colloid and Polymer Science*, 2018, 296:771-780.
23. Krajewska M, Dopierała K, Prochaska K. Lipid-protein interactions in langmuir monolayers under dynamically varied conditions. *J. Phys. Chem. B.*, 2020, 124:302-311; doi: 10.1021/acs.jpcb.9b10351.
24. Klimova SA, Stetsyura SV, Venig SB, Kaya M, Dincer I, Elerman Y, Skaptsov AA. The effect of Langmuir arachidic acid layers on surface morphology and electrical properties of a polycrystalline CdS film. *Int. J. Nanotechnol.,* 2018, 15:402-416. DOI: 10.1504/IJNT.2018.094797.
25. Khomutov GB. Two-dimensional synthesis of anisotropic nanopartocles. *Colloids and Surfaces A: Physicochemical and Engineering Aspects,* 2002, 202:243-267.
26. Zarenezhad E, Abdulabbas HT, Marzi M, Ghazy E, Ekrahi M, Pezeshki B, Ghasemian A, Moawad AA. Nickel Nanoparticles: Applications and Antimicrobial Role against Methicillin-Resistant Staphylococcus aureus Infections. *Antibiotics*, 2022, 11(9):1208.
27. Betts JJ, Pethica BA. The ionization characteristics of monolayers of weak acids and bases. *Trans. Farad.Soc.,* 1956, 52:1581-1589.
28. Vollhardt D, Fainerman VB. Progress in characterization of Langmuir monolayers by consideration of compressibility. *Advances in Colloid and Interface Science,* 2006, 127:83-97.
29. Podolskaya EP, Serebryakova MV, Krasnov KA, Grachev SA, Gzgzyane AM, Sukhodolov NG. Application of Langmuir–Blodgett technology for the analysis of saturated fatty acids using the MALDI-TOF mass spectrometry. *Mendeleev Commun*., 2018, 28:337-339.
30. Khomutov GB, Gainutdinov RV, Gubin SP, Kislov VV, Khanin VV, Rakhnyanskaya AA, Sergeev-Cherenkov AN, Soldatov ES, Suyatin DB, Taranov IV, Tolstikhina AL. Organized planar nanostructures from ligand-stabilized nanoclusters: a route to molecular nanoelectronic devices. *Applied Surface Science,* 2004, 566-568, 396–401.
31. Khomutov GB, Gubin SP. Interfacial synthesis of noble metal nanoparticles. *Materials Science and Engineering C,* 2002, 22(2):141-146. DOI: 10.1016/S0928-4931(02)00162-5.
32. Ellis JW, Pauley JL. The infrared determination of the composition of stearic acid multilayers deposited from salt substrata of varying pH. *J. Colloid Sci*., 1964, 19:755.
33. Gorbachev IA, Shtykov SN, Brezesinski G, Glukhovskoy EG. Studying of Quantum Dots Langmuir Monolayers Stability at the Different Subphase Temperature. *BioNanoSci*, 2017, 7:686-691.
34. Johann R, Brezesinski G, Vollhardt D, Möhwald H. The effect of headgroup interactions on structure and morphology of arachidic acid monolayers. *J. Phys. Chem. B,* 2001, 105: 2957-2965.
35. Gaines GL. I*nsoluble Monolayers at Liquid-Gas Interfaces*. New York, Interscience Publ., 1966, 386 p.
36. Adamson AW. *Physical chemistry of surfaces*. New York, Wiley Publ., 1983, 698 p.
37. Koerner RM, Lord AE, Hsuan YH. Arrhenius modeling to predict geosynthetic degradation. *Geotext Geomembr.,* 1992, 11(2):151-183; doi: 10.1016/0266-1144(92)90042-9.
38. Smith IWM. The temperature-dependence of elementary reaction rates: beyond Arrhenius. *Chem. Soc. Rev.*, 2008, 37:812-826.
39. Dhanabalan A, Riul AJr, Mattoso LCH, Oliveira ONJr. Composite Langmuir monolayers and Langmuir-Blodgett films from 16-mer polyaniline. *Langmuir,* 1997, 13:4882-4886.
40. Carvalho-Silva VH, Coutinho ND, Aquilanti V. Temperature Dependence of Rate Processes Beyond Arrhenius and Eyring: Activation and Transitivity. *Front. Chem*., 2019, 7:1-11.
41. Andelman D, Brochard F, Knobler C, Rondelez F. Structures and Phase Transitions in Langmuir Monolayers. In: Gelbart W.M., Ben-Shaul A., Roux D. (eds) *Micelles, Membranes, Microemulsions, and Monolayers, Partially Ordered Systems*. New York, Springer, 1994.
42. Ter-Minassian-Saraga L. Recent work on spread monolayers, adsorption and desorption. *Journal of Colloid Science,* 1956, 11:398-418.

DOI: 10.17725/rensit.2023.15.307

Biosensor based on Langmuir-Blodgett film with alcohol oxidase enzyme

Iliya A. Gorbachev, Andrey V. Smirnov

Kotelnikov Institute of Radioengineering and Electronics of RAS, http://www.cplire.ru/
Moscow 125009, Russian Federation

E-mail: iliyagor36@gmail.com, andre-smirnov-v@yandex.ru

Received September 08, 2023, peer-reviewed September 13, 2023, accepted September 18, 2023

Abstract: **The work examined the sensor properties of a biofilm based on phospholipid molecules 1,2-dipalmitoyl-sn-glycero-3-phosphoethanolamine with immobilized molecules of the enzyme alcohol oxidase to vapors of ethyl and isopropyl alcohols. The immobilization of alcohol oxidase enzyme molecules was carried out using a Langmuir monolayer process of phospholipid molecules. The sensor coating was obtained using the Langmuir-Schaeffer technology, in which the substrate is oriented parallel to the monolayer. The analysis of microimages of the film surface obtained by atomic force microscopy, allows to present of enzyme molecules in it was established. The study of the sensory properties of the formed coatings was carried out using acoustoelectronic technology. The presence of the enzyme in the sensor coating led to an increase in the amplitude and phase responses of the acoustic delay line when interacting with vapors of the detected substance. The maximum amplitude and phase responses were recorded when the film interacted with ethanol vapor and were 1.5 dB and 19°, respectively. The work showed that the formed sensor coating has selective sensitivity to ethanol vapor. This allows us to conclude that it is possible to use this sensor coating to create an acoustoelectronic ethanol biosensor. Increasing the sensitivity of such biosensors can be achieved by varying technological parameters such as the number of layers in the film, as well as the amount of immobilized enzyme in each layer.**

Keywords: **Langmuir-Blodgett films, monolayers with immobilized enzyme, acoustoelectronic sensor, biosensor, ethanol sensor**

UDC 539.23, 544.032.7

Acknowledgments: The work was carried out with the financial support of the Russian Science Foundation, grant No. 22-29-20317.

For citation: Iliya A. Gorbachev, Andrey V. Smirnov. Biosensor based on Langmuir-Blodgett film with alcohol oxidase enzyme. *RENSIT: Radioelectronics. Nanosystems. Information Technologies*, 2023, 15(3):307-316e. DOI: 10.17725/rensit.2023.15.307.

Contents

1. INTRODUCTION

The active development of the medical and chemical industry requires the creation of new effective systems of technological parameters process flow monitoring. The slightest change in the concentration of precursors and chemical reagents can take a significant influence on the result of the technological process. In addition, the slightest leakage of certain chemicals can have toxicological effects on plant personnel and the environment. Such substances include saturated monohydric alcohols, which have a wide variability of effects on the human body [1,2]. In this regard, the task of determining the concentration of alcohol vapors in the environment becomes particularly relevant.

There are two types of most commonly used sensors for determining alcohol vapors in the gas phase. The first is an optical type of sensor, based on changes in the absorption and refractive coefficients of the sample being studied. The second type of sensors is based on changes in the electrical conductivity of the system. The main disadvantage of both types of sensors is their low selectivity and difficulty in determining the elemental composition of a mixture of different alcohols [3,4]. Carrying out enzymatic reactions on a touch coating is one of the ways to solve this problem [5].

There are a number of techniques that allow the immobilization of enzyme molecules in the sensor layer [6-8]. One of the effective approaches is the Langmuir-Blodgett method, which allows the formation of a highly ordered film of surfactant molecules with the simultaneous immobilization of enzyme molecules in it [9,10]. Such films can be used as a sensitive touch coating in the manufacture of various types of sensors [11]. A promising direction in sensors is the use of acoustoelectronic technologies, which are based on changes in the characteristics of an acoustic wave when interacting with the external environment.

In an acoustoelectronic device, an acoustic wave propagates in a sound pipe, the surface of which is in contact with the environment. With a certain change in the gas composition in the environment, the characteristics (amplitude, phase, speed) of the acoustic wave in the sound pipeline change, which are recorded by the measuring device [12]. A fairly common acoustoelectronic device is an acoustic delay line (ALD), in which a gas-sensitive sensor coating is located on the surface of a piezoelectric sound pipe between an electrode system of interdigital transducers (IDTs) [13,14]. The parameters of the acoustic wave in the delay line (amplitude, frequency, phase, speed) depend quite strongly on the properties of the sensor coating. Almost all acoustoelectronic sensors are based on this principle. Thus, changes in the properties of the sensor coating when interacting with the external environment, for example, such as density, elasticity, viscosity, conductivity, are the basis for the development of acoustoelectronic sensors for various purposes.

The use of this technology using LB films with immobilized proteins as a sensor coating, which biochemically selectively interact with various organic and inorganic substances, makes it possible to create a whole family of various new generation enzymatic biosensors [15-18].

The purpose of this work was to study the sensory properties of a film of phospholipid molecules (1,2-dipalmitoyl-sn-glycero-3-phosphoethanolamine – DPPE) with the immobilized enzyme alcohol oxidase (AO) to vapors of ethyl and isopropyl alcohol.

2. EXPERIMENTAL PART

2.1. Creation of sensor cover based on the Langmuir-Blodgett films with immobilized enzyme alcoholoxidaze

To form Langmuir-Blodgett films and immobilize the enzyme in them, a solution of 1,2-dipalmitoyl-sn-glycero-3-phosphoethanolamine (DPPE, 99%, Sigma Aldrich) in chloroform (99%, Sigma Aldrich) with a concentration of 10^{-3} was used M/l. The formation of a multilayer DPPE film with immobilized AO enzyme was performed on an LB Trough Nima KSV KN2001 installation (Nima KSV, Finland) at an aqueous subphase temperature of 22°C. An aqueous solution of AO molecules with an enzyme concentration of 0.015 mg/ml was used as a subphase.

The formation of a sensor coating based on a Langmuir-Blodgett multilayered films of DPPE phospholipid molecules with an immobilized enzyme occurred according to the following procedure. A 60 μL aliquot of a DPPE solution in chloroform was dropped onto the surface of the aqueous subphase. After 120 minutes allocated for the adsorption of the enzyme on the surface of the aqueous subphase [19], the DPPE monolayer was compressed by movable barriers with a constant rate of area decreasing equal to 1.5 cm^2/min. During the compression of the monolayer by movable barriers, the dependence of the surface pressure on the area occupied by one molecule in the monolayer (compression isotherm) was automatically recorded. Compression isotherms of DPPE monolayers formed on the aqueous subphase in the presence and absence of dissolved AO molecules are shown in **Fig. 1**. To assess the effect of AO enzyme adsorption on the surface properties of monolayers, parameters such as specific area per molecule in the liquid-condensed phase were used monolayer (A_0) and monolayer compression modulus (k) [20]. The quantity A_0 is numerically equal to the

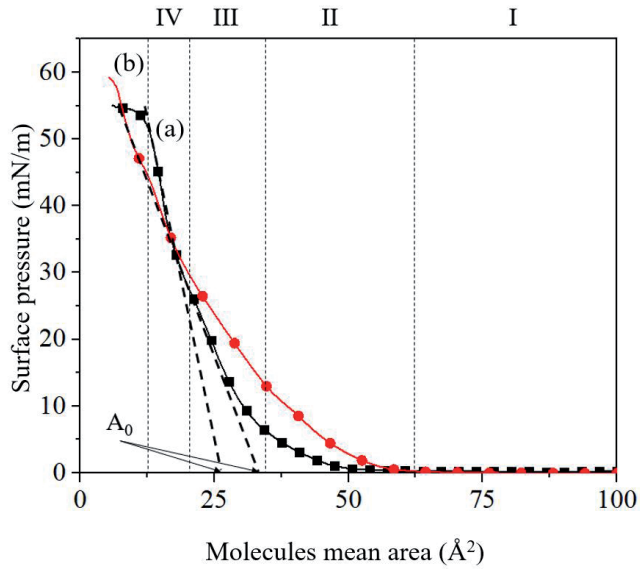

Fig. 1. *Compression isotherms of a DPPE monolayer on a subphase in the absence (a) and at the presence of dissolved AO enzyme molecules (b), where I, II, III and IV are the gas, liquid-expanded, liquid-condensed and condensed phases of the monolayer, respectively.*

coordinate of the intersection point of the straight line drawn through the condensed phase of the monolayer and the abscissa axis. The monolayer compression modulus (k) is determined from the following relation:

$$k = -A_0 \frac{d\pi}{dA}, \quad (1)$$

where A_0, A, π are the specific area per molecule in the non-tilted condensed phase of the monolayer, the specific area per molecule and surface pressure, respectively.

The transfer of the formed monolayers to solid substrates was carried out using the Langmuir-Schaeffer method (horizontal lift) at the surface pressure value of 40 mN/m. The substrate oriented parallel to the monolayer was take into a contact with the water surface, and the monolayer was adsorbed on the surface of the substrate. The process of monolayer transfer was repeated after the drying of the formed films during the 10 minutes. So a six-layer film with immobilized enzyme molecules was formed. The plates of lithium niobate plates and mica

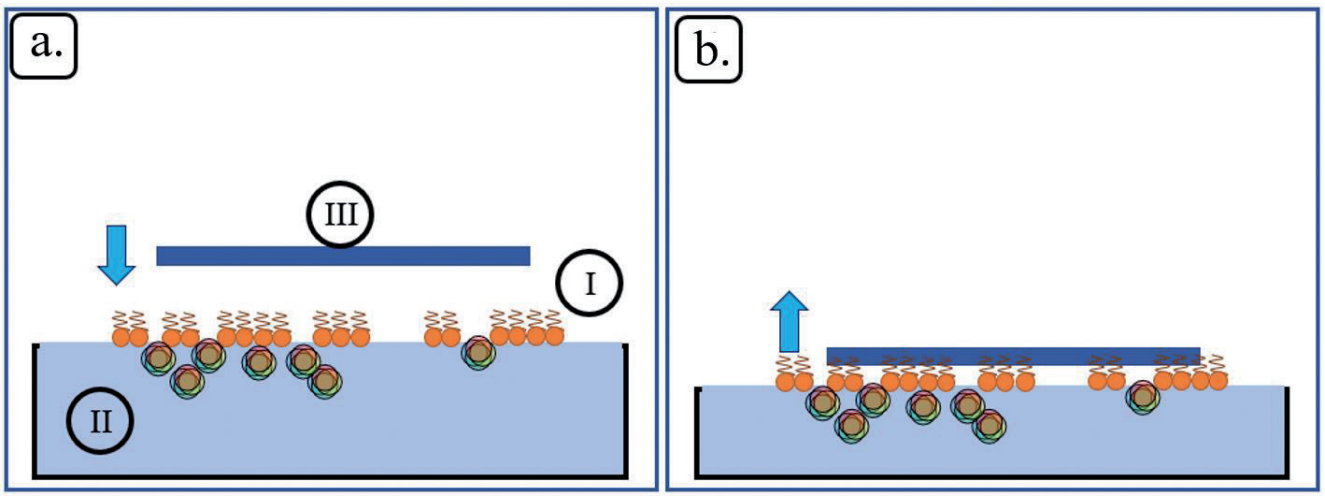

Fig. 2. *Schematic representation of the process of forming a sensor film using the Langmuir-Schaeffer technology (a. – immersion of the substrate, b – separation of the substrate from the surface of water with an adsorbed monolayer), where I is a monolayer with immobilized AO enzyme molecules, II is an aqueous subphase with a dissolved enzyme AO, III–substrate.*

plates were used as substrates. The process of transferring a Langmuir monolayer onto a solid substrate is schematically shown in **Fig. 2**.

Drying of the sensor coatings was carried out for 2 hours in a desiccator. Since the sensitive film was formed on the entire surface of the plate, after the LB film had dried, the electrode structures of the acoustic delay line were mechanically cleaned using chloroform (99% Sigma Aldrich) and ethyl alcohol (95% Sigma Aldrich). The formed coating was localized in the space between the transducers and did not affect the process of excitation and recording of the acoustic wave.

2.2. Studying by atomic force microscopy of the formed sensor covering morphology

The morphology of DPPE films with immobilized AO enzyme transferred onto mica substrates was studied by atomic force microscopy using an NT-MDT Solver setup (Russia, Zelenograd, NT-MDT). Scanning was carried out in intermittent contact mode with a frequency of 1 Hz. NSG10 probes (NT-MDT, Russia) with a radius of curvature of the probe tip of 10 nm were used for scanning. Surface images obtained from studying the films are shown in **Fig. 3**.

To quantify the properties of the film surface, the average film roughness (R_a) was

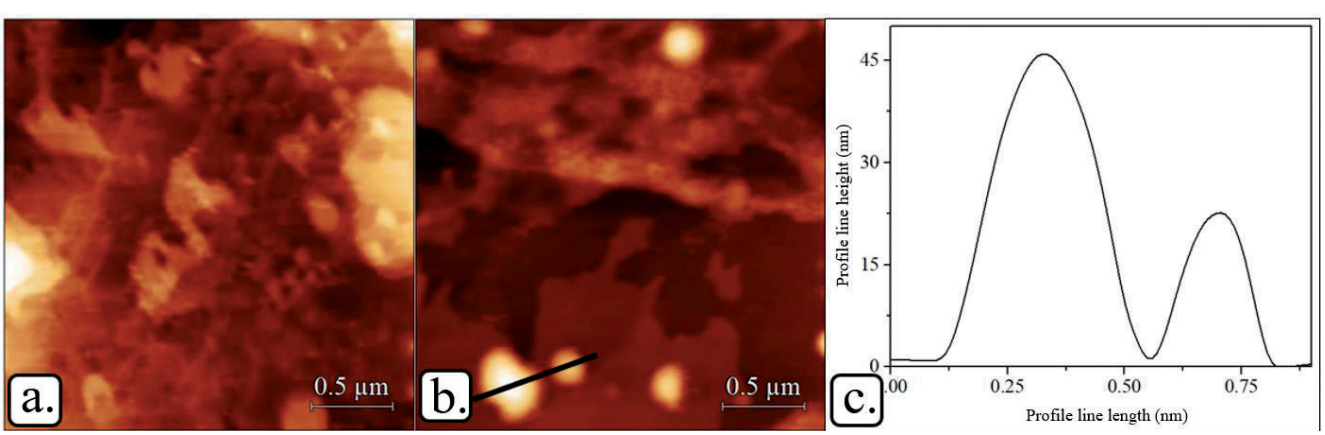

Fig. 3. *Images of the surface of the DPPE film formed in the absence (a) and in the presence (b) of AO enzyme molecules dissolved in the subphase, and the profile line of the film surface with included aggregates of enzyme molecules (c).*

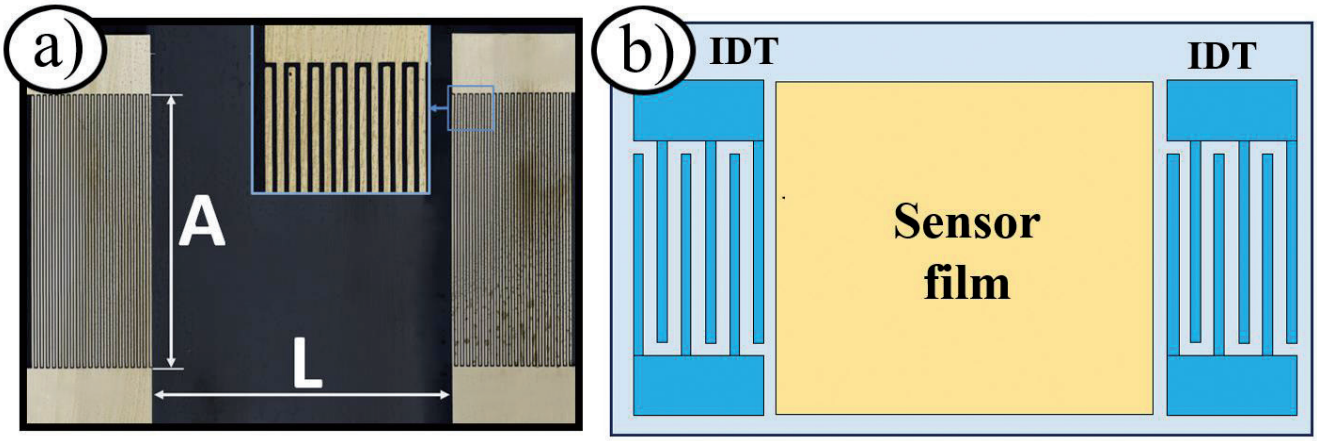

Fig. 4. *Optical image of the electrode structures of the created delay line (a), schematic image of the location of the sensitive sensor coating on the surface of the lens (b).*

calculated. The calculation was performed automatically using software Gwyddion 2.62 [21,22].

2.3 Studying of the sencoric properties of the created films by acoustic electronic method

2.3.1. Creating an Acoustic Delay Line

The acoustic delay line was formed on a piezoelectric substrate made of lithium niobate 128YX, dimensions 25×15 mm and thickness 2 mm. Electrode structures in the form of interdigitated converters (IDTs) were manufactured using maskless photolithography and magnetron sputtering of aluminum. **Fig. 4***a* shows an optical image of the formed electrode structures of the acoustoelectronic delay line obtained using an OlympusLext laser confocal scanning microscope. Transducer aperture A = 9 mm, distance between transducers L = 10 mm. The operating wavelength is determined by the distance between adjacent IDT electrodes and was 200 μm. Each interdigitated transducer contained 20 pairs of pin electrodes. Fig. 4*b* shows a schematic representation of the area where the sensitive coating is located on the surface of the delay line.

Fig. 5 shows the amplitude-frequency dependences of the S_{12} parameters of the acoustic delay line in the absence of a coating, with a DPPE coating formed, and with a DPPE+enzyme coating.

It is clear from the graphs that the coating does not have a significant effect on the type and level of the acoustic signal.

2.3.2. Measuring stand for biosensor research

The study of the gas-sensitive properties of the formed coatings was carried out using an automatic measuring complex. It schematic

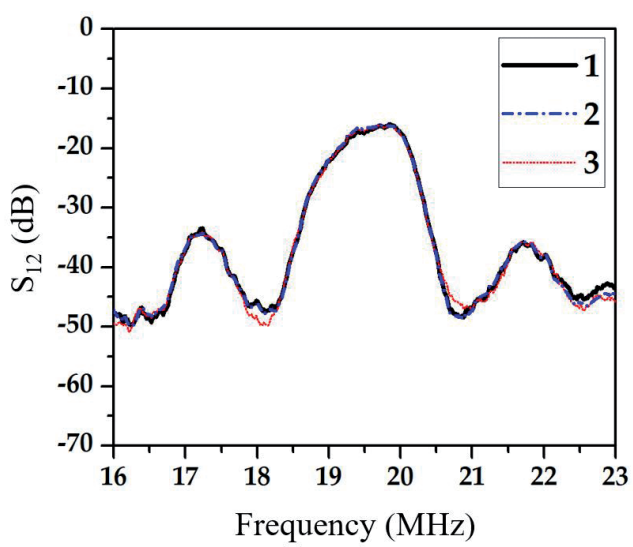

Fig. 5. *Frequency dependences of the S_{12} delay line parameters in the absence of a coating (1), with a formed DPPE coating (2) and a DPPE+enzyme coating (3).*

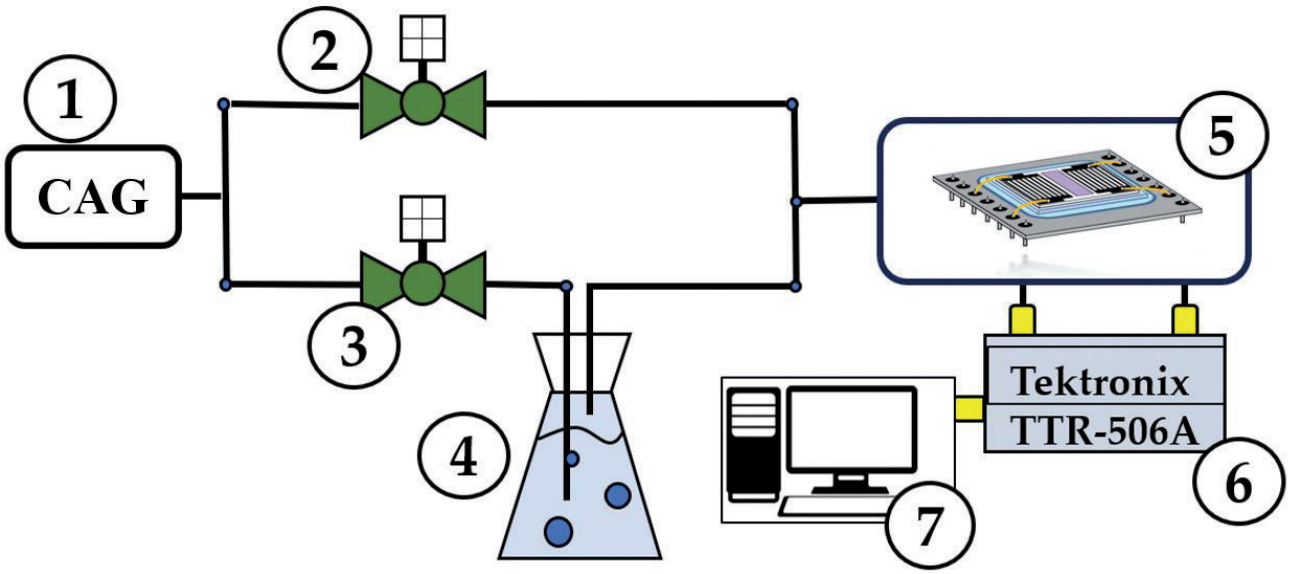

Fig. 6. *Schematic representation of the measuring stand (1) clean air generator (2) dry air flow meter (3) dry air flow meter for supply to the bubbler (4), measuring chamber (5), vector network analyzer (6) and personal computer (7).*

representation is provided in **Fig. 6.** The flow of clean, dried air from the clean air generator (1) is supplied through stainless steel lines to flow meters (2) and (3), the flow meter (2) regulates the flow of dry air used to purge the measuring chamber and diluting the test gas mixture flow. The flow meter (3) regulates the flow of dry air supplied to the aerator (pore size 20 microns) of the bubbler (4). When bubbling, dry air is saturated with vapors of the test liquid (propanol and ethanol) and at the outlet of the bubbler a mixture of dry air and vapors of the test substance is obtained at a concentration close to saturated. Adjusting the ratio of gas flows passing through flow meters (2) and (3) made it possible to supply a gas mixture with the desired concentration of the test substance into the measuring chamber (5). Using a Tektronix TTR-506A vector network analyzer and a personal computer, changes in the acoustic signal were recorded when exposed to different concentrations of the tested substances.

Detailed information on the measuring stand is presented in the works: [15,23].

3. RESULTS AND DISCUSSION

3.1. Effect of adsorption of the enzyme alcohol oxidase on the surface properties of DPPE monolayers

Fig. 1 shows compression isotherms of DPPE monolayers formed on the subphase in the absence and presence of dissolved AO enzyme. In the absence of AO enzyme molecules dissolved in the subphase, phospholipid DPPE molecules form a stable monolayer. On the compression isotherm, gaseous, liquid-expanded (II), liquid-condensed (III) and condensed phases (IV) can be distinguished. In the condensed phase, the values of A_0 and k take values of 25.2 Å^2 and 106.68 mN/m, respectively. The addition of dissolved AO enzyme molecules to the subphase affects the surface properties of the DPPE monolayer, so A_0 increases to 35.7 Å^2, and k decreases to 68.5 mN/m. There is a shift in the compression isotherm towards larger areas occupied by one molecule. This effect is explained by the incorporation of AO enzyme molecules into the Langmuir monolayer of DPPE. In the presence of AO molecules dissolved in

the subphase, the gas phase-liquid-expanded phase phase transition occurs at large areas per molecule. This effect is associated with the adsorption of AO molecules on the surface of water, which leads to an increase in the total number of molecules located on it [19]. A decrease in k and an increase in A_0 shows that the adsorption of AO molecules has an expanding effect on the structure of the DPPE monolayer.

3.2. Morphology of Langmuir-Blodgett DPPE films with immobilized alcohol oxidase (AO) enzyme

Fig. 3 shows images of the surface of a DPPE film formed in the absence and presence of AO enzyme molecules dissolved in the subphase, obtained by studying it using atomic force microscopy. Multilayer Langmuir-Blodgett films have a developed morphology. This is due to the formation of pores in the film during the evaporation of water captured during the transfer of monolayers [15] on a solid substrate. In Fig. 3*a* it is seen the 6-layer DPPE film, formed on the subphase in the absence of dissolved AO molecules, has a developed surface with an average roughness of about 3 nm. The surface roughness of a six-layer DPPE film with immobilized AO enzyme molecules is on the order of 5 nm. On the surface of the film, individual aggregates of AO enzyme molecules are visible with heights from 15 to 40 nm and occupied areas of the order of 0.2 μm^2. The minimum heights of the observed aggregates are values comparable to the dimensions of the AO molecule, which are 10 nm×10 nm×10.5 nm [24]. The presence of adsorbed aggregates of AO enzyme molecules leads to structural changes in the film, which leads to an increase in the roughness of the film surface.

3.3. Sensor properties of Langmuir-Blodgett DPPE films with immobilized enzyme alcohol oxides (AO)

The alcohol oxidase enzyme catalyzes the oxidation of short-chain aliphatic alcohols to their corresponding aldehydes according to the following scheme [25]:

$$RCH_2OH + O_2 \xrightarrow{\text{alcohol oxidase}} RCHO + H_2O_2. \quad (2)$$

During reaction (2), a change in conductivity occurs in the region where the AO enzyme is localized. In the samples under study, the en enzyme is localized in the LB layer up to 15 nm thick, and a change in its conductivity will affect the electrical properties of the acoustic wave probing it. **Fig. 7** shows the concentration dependences of the change in the amplitude of the acoustic wave (ΔS_{12}) in the acoustic delay line at a frequency of 19.7 MHz during the interaction of an air mixture containing

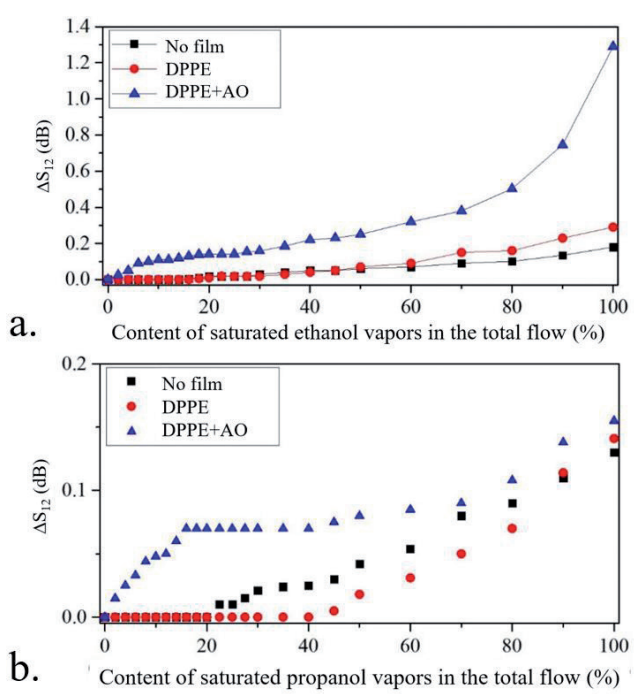

Fig. 7. *Concentration dependences of the change in the amplitude of the acoustic wave in the acoustic delay line at a frequency of 19.7 MHz for ethanol (a) and propanol (b) vapors for pure LZ, LZ with a deposited DPPE film and LZ with a deposited DPPE film with immobilized AO enzyme.*

various concentrations of ethanol or propanol vapor with the formed sensor coatings.

The attenuation of an acoustic wave in an acoustic laser without and with an applied coating that does not contain immobilized AO enzyme molecules when interacting with ethanol and propanol vapors is 0.15 dB. The presence of immobilized AO enzyme molecules in the film coating leads to an increase in the attenuation of the acoustic wave from 0.2 dB to 1.3 dB at 100% ethanol vapor content in the sample flow. The attenuation of an acoustic wave in an acoustic laser coated with a film coating with an immobilized AO enzyme upon interaction with propanol vapor is also 0.15 dB.

Fig. 8 shows the concentration dependences of the change in the phase of the acoustic wave in the acoustic delay line at a frequency of 19.7 MHz for ethanol and propanol vapors for pure LZ, LZ with a deposited DPPE film, and LZ with a deposited DPPE film with immobilized AO enzyme. The impact of propanol vapor on the LZ with an applied sensor coating without an enzyme and with an enzyme leads to a phase shift of the acoustic wave by 2 and 3, respectively. Thus, the formed sensor coating has virtually no phase sensitivity to propanol vapor.

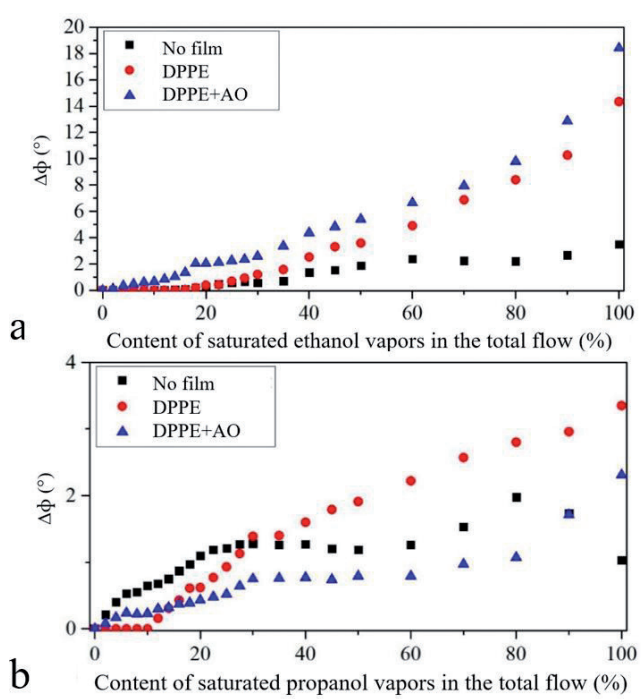

Fig. 8. *Concentration dependences of the change in the phase of the acoustic wave in the acoustic delay line at a frequency of 19.7 MHz for ethanol (a) and propanol (b) vapors for pure LZ, LZ with an applied DPPE film and LZ with a deposited DPPE film with immobilized AO enzyme.*

The effect of ethanol vapor on a laser without a film coating leads to a change in the phase of the acoustic wave by 3°. The presence of a film coating on the surface of the LZ without and with an immobilized enzyme leads to an increase in the maximum phase shift to 14° and 19°, respectively. In this case, in the range of ethanol vapor concentrations in the total sample flow from 0 to 20%, the presence of a DPPE film with an immobilized enzyme leads to an increase in the phase response to 2. Thus, it was shown that the formed sensor coating has selective sensitivity to ethanol vapor. The selectivity of the formed sensor coating is based on the differences in the catalytic activity of the AO enzyme used in relation to the alcohols used [26].

CONCLUSION

The work studied the morphology and sensory properties of Langmuir-Blodgett films of phospholipid DPPE molecules with immobilized AO enzyme molecules to vapors of ethyl and isopropyl alcohols. The presence of the AO enzyme in the formed film coatings was demonstrated using atomic force microscopy. In the course of studying the gas sensitivity of the formed sensor coatings, it was shown that LB films have the greatest sensory response to ethyl alcohol vapor. Thus, the maximum change in the amplitude and phase of the acoustic wave in the acoustic delay line in the presence of ethanol vapor was 1.5 dB and 19°, respectively. In this case, in the range

of ethanol concentrations in the sample flow from 10 to 70%, the amplitude response has a character close to linear.

This allows us to conclude that it is possible to use this sensor coating to create an acoustoelectronic ethanol biosensor. Increasing the sensitivity of such biosensors can be achieved by varying technological parameters such as the number of layers in the film, as well as the amount of immobilized enzyme in each layer.

REFERENCES

1. Ernstgard L, Shibata E, Johanson G. Uptake and Disposition of Inhaled Methanol Vapor in Humans. *Toxicological Sciences,* 2005, 88(1):30-38.
2. Kim Y-S, Park K-Y, Cho E-S. Thirteen-week inhalation toxicity study of 1-propanol in F344 rats. *Toxicology Reports*, 2021, 8:1839-1845.
3. Fong JK, Dansby-Sparks RN, Lamb AC, Owen TW, Mushfiq M, Sampathkumaran U, Goswami K, Jensen SL, Xue ZL. Fluorescent-Dye Doped Thin-Film Sensors for the Detection of Alcohol Vapors. *Am. J. Anal. Chem.*, 2014, 5(9):566-580.
4. Dalstein O, Tabo M, Alvarez E, Roux L, Garuz R, Pasquinelli M, Azzi L, Bendahan M, Aguir K, Loizillon J, Abbarchi M, Grosso D. Method to detect ethanol vapour in high humidity by direct reflection on a xerogel coating. *ACS Appl. Mater. Interfaces,* 2019, 11(4):4439-4446.
5. Kashin VV, Kolesov VV, Krupenin SV, Parshintsev AA, Reshetilov AN, Soldatov ES, Azev VN. Molecular nanobiosensor based on the enzyme glucose oxidase. *RENSIT: Radioelectronics. Nanosystems. Information Technology,* 2013, 5(2):45-61.
6. Reshetilov AN, Kitova AE, Tarasov SE, Plekhanova YuV, Bykov AG, Sandramorti AK, Kuznetsova IE, Kolesov VV, Gotovtsev PM. Highly conductive polymer PEDOT:PSS – application in biomedical and bioelectrochemical systems. *RENSIT: Radioelectronics. Nanosystems. Information Technology,* 2020, 12(4):471-482. DOI: 10.17725/rensit.2020.12.471.
7. Abolpour A, Sariri HR, Vianello F, Stevanato R. Enzyme immobilization: an update. *J. Chem Biol,* 2013, 6:185-205.
8. Nguyena HH, Kim M. An Overview of Techniques in Enzyme Immobilization. *Appl. Sci. Converg. Technol.*, 2017, 26(6):157-163.
9. Li J, Rosilio V, Boissonnade M-M, Baszkin A. Adsorption of glucose oxidase into lipid monolayers: effect of a lipid headgroup charge. *Colloids and Surfaces B: Biointerfaces,* 2003, 29:13-20.
10. Ohnuki H, Saiki T, Kusakari A, Endo H, Ichihara M, Izumi M. Incorporation of Glucose Oxidase into Langmuir-Blodgett Films. *Langmuir,* 2007, 23(8):4675-81.
11. Bie J, Sepodes B, Fernandes PCB, Ribeiro MHL. Enzyme Immobilization and Co-Immobilization: Main Framework. *Advances and Some Applications Processes,* 2022, 10:494
12. Vellekoop MJ. Acoustic wave sensors and their technology. *Ultrasonics,* 1998, 36:7-14.
13. Jahanshahi P, Wei Q, Jie Z, Zalnezhad E. Three-dimensional analysis of surface acoustic resonator for ultra-high sensitive ethanol disclosure as non-invasive biosensor. *MOJ App Bio Biomech.*, 2017, 1(4):150-151.
14. Guz L. Technical aspects of SAW gas sensors application in environmental measurements. *MATEC Web of Conferences*, 2019, 252:06007.
15. Gorbachev I, Smirnov A, Ivanov G, Avramov I, Datsuk E, Venelinov T, Bogdanova E, Anisimkin V, Kolesov V,

Kuznetsova I. Langmuir-Blodgett Films of Arachidic and Stearic Acids as Sensitive Coatings for Chloroform HF SAW Sensors. *Sensors*, 2023, 23:100.

16. Ivanov GR, Avramov I. Langmuir-Blodgett Films from Fluorescently Labelled Phospholipids Deposited on Surface Acoustic Wave Devices. *Journal of Physics: Conference Series*, 2019, 1186(1):012007.
17. Gorbachev I, Smirnov A, Ivanov GR, Venelinov T, Amova A, Datsuk E, Anisimkin V, Kuznetsova I, Kolesov V. Langmuir–Blodgett Films with Immobilized Glucose Oxidase Enzyme Molecules for Acoustic Glucose Sensor Application. *Sensors*, 2023, 23:5290.
18. Giffney TJ, Ng YH, Aw KC. A Surface Acoustic Wave Ethanol Sensor with Zinc Oxide Nanorods. *Smart Materials Research*, 2011, 2012:5.
19. Caseli L, Perinotto AC, Viitala T, Zucolotto V, Jr Oliveira ON. Immobilization of Alcohol Dehydrogenase in Phospholipid Langmuir-Blodgett Films to Detect Ethanol. *Langmuir,* 2009, 25:3057-3061.
20. Vollhardt D, Fainerman VB. Progress in characterization of Langmuir monolayers by consideration of compressibility. *Advances in Colloid and Interface Science*, 2006, 127:83-97.
21. Necas D, Klapetek P, Valtr M. Estimation of roughness measurement bias originating from background subtraction. *Measurement Science and Technology*, 2020, 31:094010.
22. Necas D, Valtr M, Klapetek P. How levelling and scan line corrections ruin roughness measurement and how to prevent it. *Scientific Reports,* 2020, 10:15294.
23. Smirnov A, Anisimkin V, Krasnopolskaya L, Guliy O, Sinev I, Simakov V, Golyshkin A, Almyasheva N, Ageykin N, Kuznetsova I. Features of the formation of sensitive films based on mycelium of higher fungi for surface and plate acoustic waves gas sensors. *Sensors*, 2023, 23(4):2216.
24. Vonck J, Parcej DN, Mills DJ. Structure of Alcohol Oxidase from Pichia pastoris by Cryo-Electron Microscopy. *PLoS ONE*, 11(7):e0159476.
25. Mizgunova UM, Tesker AE, Krasnoslobodtseva EA, Dolmanova IF. Enzymatic determination of methanol impurities in water-ethanol solutions using alcohol oxidase. *Moscow University Bulletin, Ser. 2 Chemistry,* 1998, 39(6):378-382.
26. Zakhari S. Overview: How Is Alcohol Metabolized by the Body? *Alcohol Research & Health*, 2006, 29(4):245-254.

DOI: 10.17725/rensit.2023.15.317

Holographic Method for Localization of a Moving Underwater Sound Source in the Intense Internal Waves Presence

Venedikt V. Kuz'kin

Prokhorov Institute of General Physics, Russian Academy of Sciences, http://www.gpi.ru/
Moscow 119991, Russian Federation
E-mail: kumiov@yandex.ru

Sergey A. Pereselkov, Sergey A. Tkachenko, Nikolay V. Ladykin, Mikhail V. Kutsov

Voronezh State University, http://www.vsu.ru/
Voronezh 394006, Russian Federation
E-mail: pereselkov@yandex.ru, sega-th@mail.ru, ladykin.edu@yandex.ru, mkutsov.edu@yandex.ru

Vladimir I. Grachev

Kotelnikov Institute of Radioengineering and Electronics of RAS, http://www.cplire.ru/
Moscow 125009, Russian Federation
E-mail: grachev@cplire.ru

Received July 04, 2023, peer-reviewed July 11, 2023, accepted July 18, 2023

Abstract: **Within the numerical experiment framework, the holographic processing of noise emission from a moving underwater sound source in the intense internal waves presence, which cause horizontal refraction of sound field waves, is considered. The interference of the undisturbed and disturbed fields forms a moiré interference pattern (interferogram) that masks the noise source interferogram. Registration of a moiré interferogram using a two-dimensional Fourier transform makes it possible to separate the spectral densities of the unperturbed and perturbed fields. This makes it possible to reconstruct the interferogram of the unperturbed field in the intense internal waves presence. The relative error of its reconstruction is estimated. The errors in reconstructing the range and source radial velocity due to horizontal refraction are analyzed.**

Keywords: **shallow sea, moving sound source, intense internal waves, horizontal refraction, interferogram, hologram**

UDC 004.052.34

Acknowledgments: The study was supported by the Russian Science Foundation grant No. 23-61-10024, https://rscf.ru/project/23-61-10024/. Numerical calculations of the sound field interferogram were carried out by S.A. Tkachenko with the support of the grant of the President of the Russian Federation MK-4846.2022.4.

For citation: Venedikt M. Kuz'kin, Sergey A. Pereselkov, Vladimir I. Grachev, Sergey A. Tkachenko, Nikolay V. Ladykin, Mikhail V. Kutsov. Holographic Method for Localization of a Moving Underwater Sound Source in the Intense Internal Waves Presence. *RENSIT: Radioelectronics. Nanosystems. Information Technology,* 2023, 15(3):317-326e. DOI: 10.17725/rensit.2023.15.317.

Contents

1. INTRODUCTION

Recently, of increasing interest in ocean acoustics are works on holographic interferometry using the two-dimensional Fourier transform (2D-FT) of the interferogram, which makes it possible to solve a wide range of new problems in the hydroacoustic information processing field [1-3]. An interferogram is understood as the modulus square of the received signal in frequency-time variables. The interferogram is characterized by a waveguide invariant [4], which determines the interference fringes slope. The slope establishes a relationship between the frequency shift of the interference maxima of the sound field and time (distance) while maintaining the phase difference between the interfering modes. The location geometry of the localized bands is determined by the waveguide parameters, the speed and trajectory of the sound source. At the output of the integral transformation (hologram), the spectral density is localized in a narrow band in the form of focal spots corresponding to the interference of different numbers modes. The hologram records the amplitudes of the interfering modes and the phase difference between them in all intermediate states that the source successively passes during the observation time.

In [1-3], it was assumed that the oceanic environment is homogeneous, i.e. its characteristics in the space-time domain are unchanged. In the hydrodynamic perturbations presence, the interferogram can be represented as the sum of the unperturbed and perturbed waveguide interferograms. The 2D-FT transformation is a linear process, which allows the hologram to be considered as a linear superposition of the unperturbed and perturbed waveguide holograms. If the spectral densities of the unperturbed and perturbed holograms are separated, then the inverse 2D-FT transformation to the selected spectral densities makes it possible to observe the unperturbed and perturbed fields interferograms.

For the first time, successful separation of the unperturbed and perturbed holograms was demonstrated by processing the data of the SWARM-95 full-scale experiment on stationary paths [5,6], when intense internal waves (IIWs) caused horizontal refraction and interaction of source acoustic field modes [7]. In [8,9], this effect was theoretically described and confirmed by the numerical simulation results, and the errors in reconstructing the unperturbed fields interferograms were estimated.

In this paper, generalizing the results of [8], within the numerical simulation framework, we consider the holographic processing of a moving source in the IIWs field, which determine the horizontal mode refraction. The IIWs effect on the error in reconstructing the distance, the radial velocity (velocity projection towards the receiver) of the source, and the interferogram of the undisturbed field is estimated.

2. EXPERIMENTAL CHARACTERISTICS OF INTENSE INTERNAL WAVES IN SHALLOW WATERS

Intense internal waves are a hydrodynamic phenomenon that is widespread in the oceanic environment. In shallow water areas, they are trains of intense short-period fluctuations of the constant density water surface, interpreted as solitons trains that propagate in the coastline direction. The reason for their occurrence is due to internal tides [10]. According to experimental data, soliton trains are characterized by the following parameters: velocity u ~ 0.5-1 m/s, periods of calm δL ~ 5-10 km, length L ~ 2-4 km, period D ~ 200-400 m (distance between crests of adjacent solitons), half-width η ~ 50-150

m, amplitude B ~ 10-30 m [11-13]. Soliton trains are characterized by: *a*) anisotropy in the horizontal plane, radius of front curvature r = 15-25 km; *b*) quasi-sinusoidality in the propagation direction, i.e. spatial narrow spectrum; *c*) synchronism of vertical displacements in depth, which indicates the dominance of the first gravity mode. These properties determine the horizontal refraction of source sound waves if the acoustic path is located at a small angle to the wave front of the soliton train [14,15].

3. DESCRIPTION OF INTENSE INTERNAL WAVES

Let us assume that the velocity of the soliton train is directed along the normal to the path located along the horizontal axis X. The soliton wavefront is assumed to be flat. In the absence of oceanic medium perturbation, the waveguide is considered to be horizontally homogeneous with depth H. Unperturbed values are denoted by an overline, and perturbed ones by a tilde. With the notation made, the refractive index square

$$n^2\left(x,y,z_q,t\right)=\overline{n}^2\left(z\right)+\tilde{n}^2\left(x,y,z,t\right), \quad (1)$$

where z_q is the receiver depth, t is time, and the y-axis is perpendicular to the x-axis (right-handed Cartesian coordinate system). The refractive index is understood as the ratio of the sound speeds on the surface z = 0 to the value of the sound speed at the depth under consideration. According to [16]

$$\tilde{n}^2\left(x,y,z_q,t\right)=-2QN^2\left(z_q\right)\left(z\right)\left(y,t\right). \quad (2)$$

Here $Q \approx 2.4$ s^2/m is a constant determined by the water physical properties; $N(z)$ is the buoyancy frequency; $\Phi(z)$ is the eigenfunction of the first gravity mode, normalized to the eigenvalue at the reception depth; $\zeta(y,t)$ is the deviation of the surface from the depth, where $\Phi(z)$ = 1. Due to the chosen geometry of the problem, the right side of expression (2) does not depend on the x coordinate. We write the envelope of the soliton train $\zeta(y,t)$ when crossing the path as a sequence of N different solitons with amplitudes B_n shifted relative to each other by a period D_n and propagating with velocities u_n

$$\varsigma\left(y,t\right)=\sum_{n=1}^{N}-B_n\operatorname{sech}^2\left[\left(y-D_n-u_nt\right)/\eta_n\right], \quad (3)$$

where η_n is the half-width of the n-th soliton at a level of 0.42 from the maximum [10]. The minus sign means that the perturbation of the refractive index is directed towards the bottom.

Taking into account the smallness $\tilde{n}^2$ with respect to $\overline{n}^2$, $\tilde{n}^2 \ll \overline{n}^2$, the real part of the horizontal wave number $h_m(x,z,t)$ (propagation constant) of the sound field of mode number m can be represented as

$$h_m\left(y,z,t\right)=\overline{h}_m+\tilde{h}_m\left(y,z,t\right), \quad (4)$$

where the linear correction within the framework of perturbation theory [14] is determined by the expression

$$\tilde{h}_m\left(y,z,t\right)=\frac{\overline{k}_0^2}{2\overline{h}_m}\int_0^H\overline{\Psi}_m^2\left(z\right)\tilde{n}^2\left(y,z,t\right)dz. \quad (5)$$

Here, $\overline{k}_0^2=\omega^2/\overline{c}_0^2$ is the squared wavenumber at depth z = 0, $\omega = 2\pi f$ is the cyclic frequency; $\overline{\Psi}_m(z)$ is the eigenfunction of the mth mode. Substituting (2) into (5), we obtain

$$\tilde{h}_m\left(y,z,t\right)=-q_m\varsigma\left(y,t\right), \quad (6)$$

where form

$$q_m=\frac{Q\overline{k}_0^2}{\overline{h}_m}\int_0^H\overline{\Psi}_m^2\left(z\right)N^2\left(z\right)\Phi\left(z\right)dz \quad (7)$$

is the dependence of the propagation constant linear correction on the mode number. The applicability limits of the perturbation method are limited by the solitons amplitudes on the order of several tens of meters, which are typical for shallow water areas [14].

4. HOLOGRAM FORMATION

The field of a broadband source is understood as the sound pressure in frequency-time variables. Let us write the radiation interferogram of a moving source as a modes sum

$$\begin{aligned} &I(\omega,t)= \\ &=\left|S(\omega)\right|^2\sum_m\sum_n A_m(\omega,\,t)\,A_n^*(\omega,\,t)\exp\left[ih_{mn}(\omega)(r_0+wt)\right]= \\ &=\sum_m\sum_n I_{mn}(\omega,t),\quad m\neq n. \end{aligned} \tag{8}$$

where $h_{mn}(\omega) = h_m(\omega) - h_n(\omega)$. Here $S(\omega)$ is the signal spectrum; $A_m(\omega,t)$ is the amplitude of the m-th mode; r_0 is the initial distance at time $t_0 = 0$, w is the source radial velocity. The superscript "*" denotes the complex conjugate value. Cylindrical divergence, modal attenuation, and source depths z_s and receivers z_q are taken into account in the mode amplitude. The modes number is M. The condition $m \neq n$ means that the mean value has been subtracted from the interferogram. If this operation is not performed before applying the 2D-FT transformation, then an intense peak will appear on the hologram at the coordinates origin.

Let us apply to the interferogram (8) the 2D-FT transformation

$$\begin{aligned} &F(\tau,\tilde{\nu})=\sum_m\sum_n\int_0^{\Delta t}\int_{\omega_1}^{\omega_2} I_{mn}(\omega,t)\exp\left[i(\tilde{\nu}t-\omega\tau)\right]dtd\omega= \\ &=\sum_m\sum_n F_{mn}(\tau,\tilde{\nu}). \end{aligned} \tag{9}$$

Here τ and $\tilde{\nu}=2\pi\nu$ are the time and circular frequency of the hologram; $\omega_{1,2} = \omega_0 \pm \Delta\omega/2$, $\Delta\omega$ is the band, ω_0 is the spectrum average frequency; Δt is the observation time. We restrict ourselves to the linear approximation of the waveguide dispersion

$$h_m(\omega)=h_m(\omega_0)+\frac{dh_m(\omega_0)}{d\omega}(\omega-\omega_0). \tag{10}$$

Assuming the amplitude spectrum of the signal $|S|$ and the amplitude A_m with frequency ω varying slowly compared to the rapidly oscillating factor $\exp[ih_m(\omega)(r_0 + wt)]$, for the partial hologram $F_{mn}(\tau,\tilde{\nu})$ (9) we obtain [2]

$$\begin{aligned} &F_{mn}(\tau,\tilde{\nu})= \\ &=\left|S(\omega_0)\right|^2 A_m(\omega_0)A_n^*(\omega_0)\Delta\omega\Delta t\exp\left[i_{mn}(\tau,\tilde{\nu})\right]\times \\ &\times\frac{\sin\left\{\left[r_0\dfrac{dh_{mn}(\omega_0)}{d\omega}-\tau\right]\dfrac{\Delta\omega}{2}\right\}}{\left[r_0\dfrac{dh_{mn}(\omega_0)}{d\omega}-\tau\right]\dfrac{\Delta\omega}{2}}\,\frac{\sin\left\{\left[wh_{mn}(\omega_0)+\tilde{\nu}\right]\dfrac{\Delta t}{2}\right\}}{\left[wh_{mn}(\omega_0)+\tilde{\nu}\right]\dfrac{\Delta t}{2}}, \end{aligned} \tag{11}$$

where is the phase

$$\Phi_{mn}(\tau,\tilde{\nu})=\left(\frac{\tilde{\nu}\Delta t}{2}-\tau\omega_0\right)+h_{mn}(\omega_0)\left(\frac{\Delta t}{2}w+r_0\right). \tag{12}$$

In (11) the approximation $r_0 \gg w\Delta t$.

Spectral density (9) is localized in two narrow regions in the form of focal spots. They are located: in the first and third quadrants, if the source approaches the receiver, $w < 0$; in the second and fourth quadrants, if the source moves away from the receiver, w > 0. The localization region contains $(M - 1)$ main maxima with coordinates $(\tau_\mu,\tilde{\nu}_\mu)$, located on a straight line $\tilde{\nu}=\tilde{\varepsilon}\tau$. Here, $\mu=\overline{1,M-1}$ is the focal spot number. At points with coordinates $(\tau_\mu,\tilde{\nu}_\mu)$ $(M - \mu)$ of the main peaks are summarized. The slope coefficient $\tilde{\varepsilon}=2\pi\varepsilon$ can also be represented in the form $\tilde{\varepsilon}=-\delta\omega/\Delta t$, where $\delta\omega$ is the frequency shift of the interferogram maximum over time δt. The linear dimensions of focal spots $\delta\tau$, $\delta\tilde{\nu}$ along the axes τ, $\tilde{\nu}$ do not depend on their numbers and are equal: $\delta\tau = 4\pi/\Delta\omega$, $\delta\tilde{\nu}=4\pi/\Delta t$ [2].

From the first focal spot closest to the origin, the radial velocity and initial distance are estimated as

$$\dot{w}=-\kappa_{w1}\tilde{\nu}_1,\quad \dot{r}_0=\kappa_{r1}\tau_1, \tag{13}$$

where

$$\begin{aligned} &\kappa_{w1}=(M-1)\left[h_{1M}(\omega_0)\right]^{-1}, \\ &\kappa_{r1}=(M-1)\left[dh_{1M}(\omega_0)/d\omega\right]^{-1}. \end{aligned} \tag{14}$$

The restored source parameters, in contrast to the true values, are indicated by a dot at the top.

Holographic processing is implemented as follows. During the observation time Δt in the emission band $\Delta\omega$, J independent realizations of duration t_1 with a time interval t_2 between them are quasi-coherently accumulated along the interference fringes: $J = \Delta t/(t_1 + t_2)$. Realizations are independent if $t_2 > 2\pi/\Delta\omega$. An interferogram $I(\omega,t)$ is formed and the 2D-FT transformation is applied to it.

In general, the transformation of a 2D-FT function is completely different from the function itself. However, a hologram is an unambiguous representation of an interferogram. The inversion, performed by inverse application of the 2D-FT transform, reconstructs the interferogram.

5. NUMERICAL SIMULATION

To be able to compare the holographic processing results for the cases of a stationary and moving source in the IIWs field, which determine the sound waves horizontal refraction, the simulation data are the same as in [8].

The depth distribution of the sound speed is shown in **Fig. 1**. Two frequency ranges were considered: f_1 = 100-120 Hz and f_2 = 300-320 Hz. Parameters of the liquid absorbing bottom: density ratio of soil and water ϱ = 1.8; for the first frequency range, the complex refractive index is $n = 0.84(1 + i0.03)$, for the second, $n = 0.84(1 + i0.05)$. In the f_1 frequency range, the field was formed by four modes, and in the f_2 frequency range, by ten modes. Mode propagation constants $h_m(\omega_0)$ and their frequency derivatives $dh_m(\omega_0)/d\omega$ at mid-range frequencies f_0 = 110, 310 Hz are given in **Tables 1, 2**.

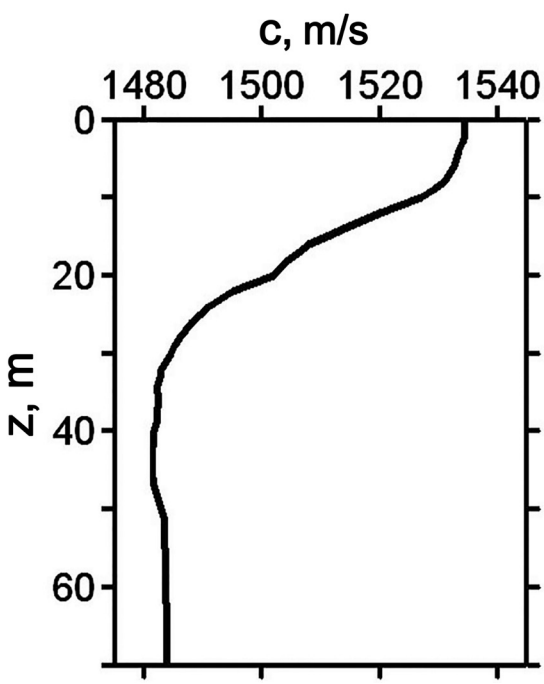

Fig. 1. *Unperturbed sound velocity profile.*

Table 1

Frequency f_0 = 110 Hz

Mod numbers, m	1	2	3	4
h_m, m^{-1}	0.4635	0.4557	0.4450	0.4310
$(dh_m/d\omega)\cdot10^{-4}$, s/m	6.7624	6.8085	6.9014	7.0912

Table 2

Frequency f_0 = 310 Hz

Mod numbers, m	1	2	3	4	5
h_m, m^{-1}	1.3123	1.3073	1.3006	1.2920	1.2826
$(dh_m/d\omega)\cdot10^{-4}$, s/m	6.7511	6.7619	6.7813	6.7973	6.8080
Mod numbers, m	6	7	8	9	10
h_m, m^{-1}	1.2730	1.2630	1.2525	1.2403	1.2258
$(dh_m/d\omega)\cdot10^{-4}$, s/m	6.8150	6.8312	6.8753	6.9703	7.0574

At the initial time $t_0 = 0$, the distance between the source and a single receiver x_0 = 10 km, the source approaches the receiver along the horizontal axis x. The source is located at a depth of z_s = 20 m, the receiver is at a depth of z_q = 45 m. The radial velocity of the source is $w = -1$ m/s. A uniform spectrum was set. Pulses with duration t_1 = 4 s (frequency sampling step 0.25 Hz) of sound pressure were recorded at intervals t_* = 5 s, ($t_* = t_1 + t_2$). As a perturbation model (3), we chose a train consisting of three identical solitons moving along the normal to the path. Soliton parameters: amplitude B = 20 m, width η = 200 m, velocity u = 0.7 m/s, period D = 250 m. The width of the perturbation front exceeds the path length. The observation time Δt = 20 min, during which time the soliton train completely crossed the path. With the chosen spectrum

model, the unperturbed field interferogram in the perturbation absence reproduces the transfer function of the waveguide up to a constant factor. The sound field at the receiving point was calculated using the approach of vertical modes and a parabolic equation in the horizontal plane [14].

The simulation results are shown in **Fig. 2-5**. The dotted line on the holograms shows the band in which the spectral density of the received signal is concentrated. Linear band dimensions: $\delta\tau \approx 0.15$ s, $\delta\nu \approx 0.002$ Hz, which agrees with the theoretical estimates of the sizes of focal spots $\delta\tau = 0.1$ s, $\delta\nu = 0.0017$ Hz [2].

On **Fig. 2** shows interferograms and moduli of unperturbed fields holograms in the absence of a path crossing by a solitons train. As the frequency increases, the irregularity of the interference pattern, which consists of localized inclined fringes, and the number of focal spots in the hologram increase, which is explained by an increase in the number of modes. Angular coefficients of interference fringes: $\delta f/\delta t \approx -0.015$ s^{-2} (frequency range f_1) and $\delta f/\delta t \approx -0.040$ s^{-2} (frequency range f_2).

Peak coordinates of the first focal spot: $\tau_1 = 1.30\cdot10^{-1}$ s, $\nu_1 = 1.79\cdot10^{-3}$ Hz (Δf_1); $\tau_1 = 4.08\cdot10^{-2}$ s, $\nu_1 = 1.54\cdot10^{-3}$ Hz (Δf_2). According to (15) and the data of Tables 1 and 2, the restored source parameters are:

$$\dot{w} = -1.0\ m/s,\ \dot{x}_0 = 11.8\ km\ (f_1);$$
$$\dot{w} = -1.0\ m/s,\ \dot{x}_0 = 12.0\ km\ (f_2).$$

Moiré interferograms and holograms modules when a solitons train crosses the path are shown in **Fig. 3**. Perturbation of the aquatic environment causes a change in the refractive index. This leads to a interference fringes transformation and a change in the configuration of the holograms spectral densities Moiré interferograms (Fig. 3*a,b*) show horizontal fringes with a width of $\Delta T_1 \approx 5.6$ min (f_1), $\Delta T_2 \approx 5.9$ min (f_2) with a quasi-periodic pattern of focal spots. Linear focal spots sizes: $\delta f_1 \approx 2.4$ Hz, $\delta t_1 \approx 1.1$ min (f_1) and $\delta f_2 \approx 2.8$ Hz, $\delta t_2 \approx 1.1$ min (f_2). Periodicity scales for focal spot maxima: $\delta\Lambda_1 \approx 5.6$ Hz, $\delta T_1 \approx 8.3$ min (f_1) and $\delta\Lambda_2 \approx 6.8$ Hz, $\delta T_2 \approx$

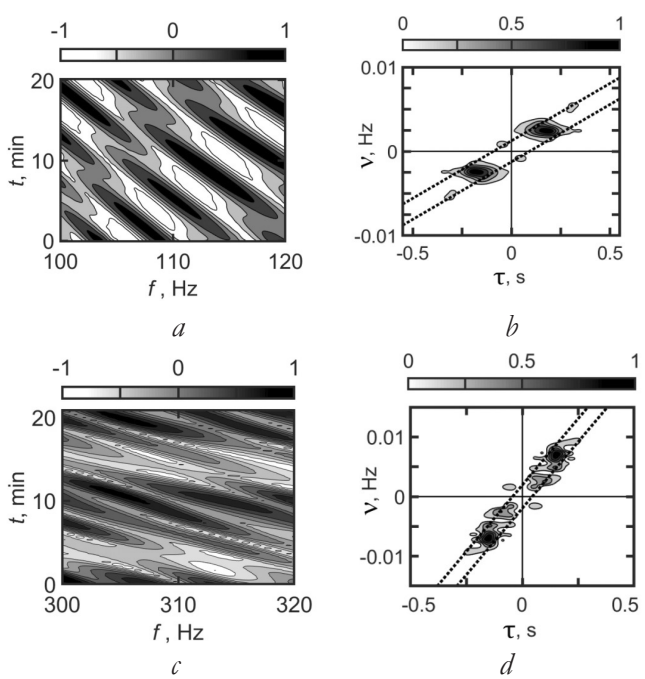

Fig. 2. *Normalized interferograms (a, c) and holograms (b, d) in the absence of perturbation: (a, b) – frequency range f_1, (c, d) – frequency range f_2.*

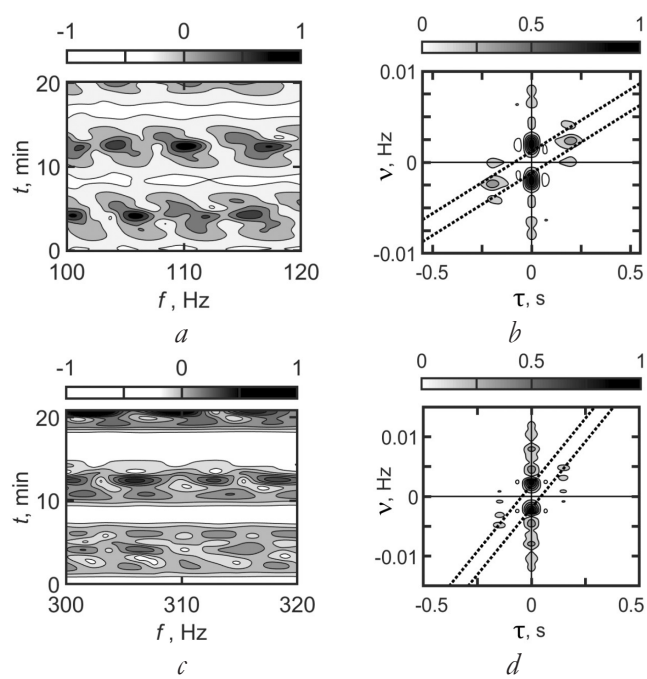

Fig. 3. *Normalized moiré interferograms (a, c) and holograms (b, d) in the presence of a disturbance: (a, b) – frequency range f_1, (c, d) – frequency range f_2.*

8.1 min (f_2). Although the values of the focal spots parameters in the interferograms are approximately the same as in the case of a stationary source, the interferograms noticeably differ in contrast and symmetry of the horizontal interference fringes arrangement [8]. In the holograms (Fig. 3*b,g*), the spectral density in the form of focal spots is concentrated mainly on the frequency axis, which gives an idea of the refracted signal influence.

In contrast to moiré interferograms, the location configuration of focal spots on holograms makes it possible to separately observe the spectral densities of the unperturbed and perturbed fields. The undisturbed and disturbed fields in the IIWs presence are understood to mean the fields formed by direct and refracted signals. Under natural conditions, when the train consists of solitons of different shapes and different parameters, this will naturally lead to a decrease in the contrast of the interference pattern and an expansion of the region of location of focal spots on the hologram.

The cleaning results the holograms spectral densities from the perturbed field in the frequency axis ν vicinity and their Fourier image are shown in **Fig. 4.** The shape of the spectral densities arrangement on the holograms of the unperturbed waveguide (Fig. 2*b,g*) and reconstructed in the IIWs presence (Fig. 4*b,g*) are close to each other. The peak coordinates of the first focal spot are estimated as follows: $\tau_1 = 1.50 \cdot 10^{-1}$ s, $\nu_1 = 2.05 \cdot 10^{-3}$ Hz (f_1); $\tau_1 = 4.08 \cdot 10^{-2}$ s, $\nu_1 = 1.54 \cdot 10^{-3}$ Hz (f_2). According to (15) and the data of Tables 1, 2, the restored source parameters

$$\dot{w} = -1.2\ m/s,\ \dot{x}_0 = 13.7\ km\ (f_1);$$
$$\dot{w} = -1.0\ m/s,\ \dot{x}_0 = 12.0\ km\ (f_2).$$

For the frequency range f_1, the perturbation leads to an increase in the error in restoring the source parameters;

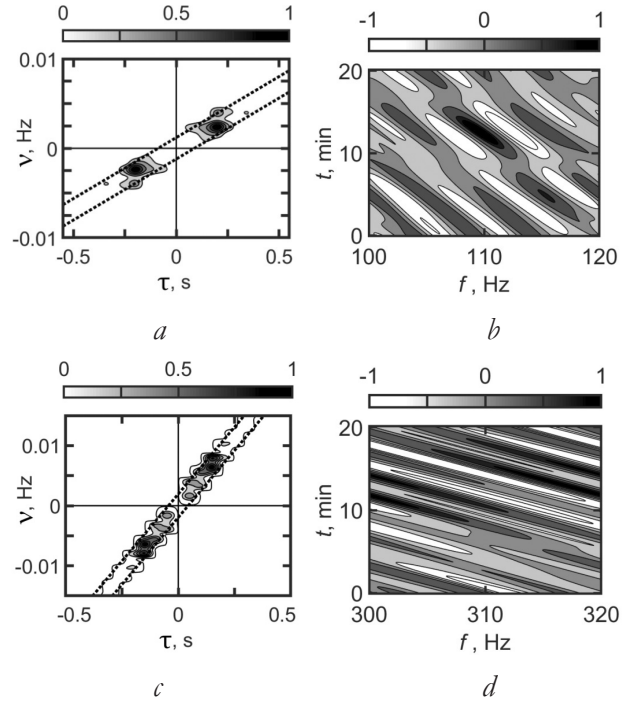

Fig. 4. *Normalized filtered modules of holograms (a, c) of the unperturbed field and interferograms (b, d) reconstructed from them: (a, b) – frequency range Δf_1, (c, d) – frequency range Δf_2.*

for the frequency range f_2, the perturbation presence does not affect the error in restoring the source parameters. This is explained by the increased influence of waves horizontal refraction on the formation of the source sound field with decreasing frequency [14]. The reconstructed interferograms of the unperturbed field in the presence of a train of solitons are shown in Fig. 4*b,d*. The angular coefficients of the interference fringes are estimated as $\delta f/\delta t \approx -0.017$ s^{-2} (Δf_1) and $\delta f/\delta t \approx -0.042$ s^{-2} (Δf_2), which is close to their values in the absence of medium disturbance.

The closeness degree of two-dimensional interferograms of unperturbed fields in the IIWs absence and presence will be estimated from the proximity of their one-dimensional interferograms, which are a horizontal section for a fixed time moment. With the chosen model of a uniform signal spectrum, one-dimensional interferograms, up to a constant factor, are equal to the transfer functions of

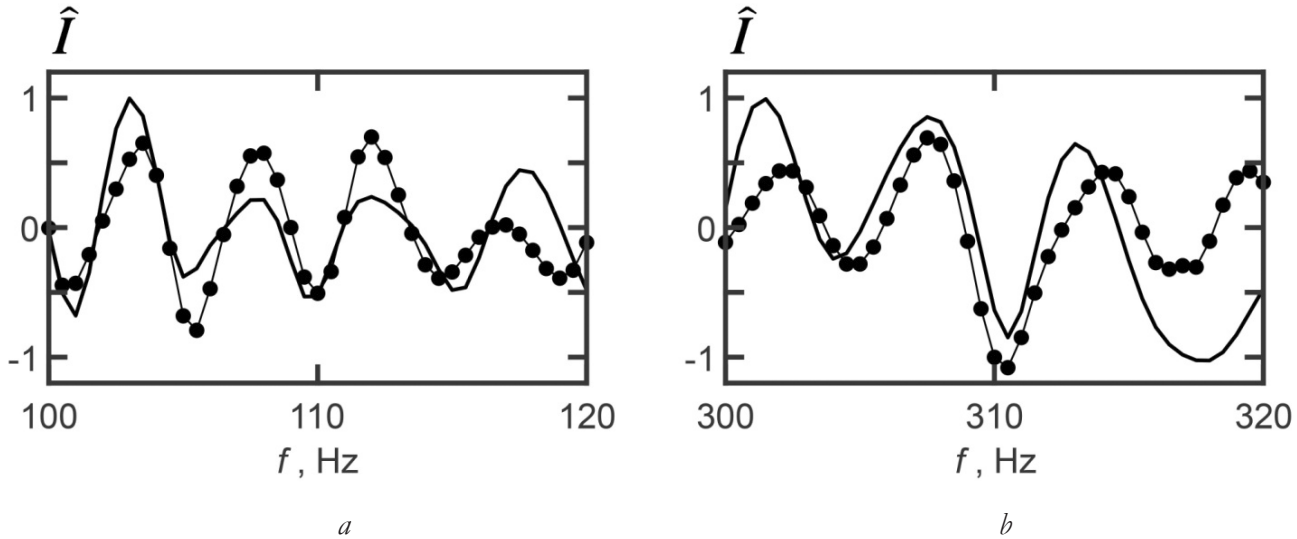

Fig. 5. *Dependences of normalized one-dimensional interferograms of unperturbed fields* $\hat{I}$ *on frequency f in the absence of a disturbance (solid line) and reconstructed in its presence (points): (a) frequency range* f_1*, (b) frequency range* f_2*.*

the waveguide in the absence and presence of a disturbance. On **Fig. 5** shows the one-dimensional normalized spectral densities of the unperturbed fields interferograms in the absence of a disturbance (solid line) and those reconstructed in its presence (points) for the time instant t = 10 min. The normalized value is indicated at the top with the "lid" icon. The error in reconstructing the interferograms was estimated as

$$d(t) = \frac{\sum_{j=1}^{J} \left| I_1(f_j, t) - I_2(f_j, t) \right|}{\sum_{j=1}^{J} \left| I_1(f_j, t) \right|}, \qquad (15)$$

where the readings number is J = 80. Here $I_{1,2}$ is the one-dimensional interferogram of the unperturbed field for time t in the disturbance absence and reconstructed in its presence, respectively. For the frequency range f_1, the error is d = 0.45; for the frequency range f_2, d = 0.60. Compared to a stationary source [8], the error increased by a factor of 3.7 and 6.2 for the frequency ranges f_1 and f_2, respectively. The indicated difference in the error values is explained by the different medium variability character. With a stationary source, there is a temporal variability of the medium, and with a moving source, there is a spatio-temporal variability. Note that the error (16) depends on the chosen moment of time.

6. CONCLUSION

Within the numerical simulation framework, the holographic method stability of localization of a moving broadband sound source in the IIWs presence, which determine the sound waves horizontal refraction, is demonstrated. The processing stability is based on the fact that the spectral densities of the unperturbed and perturbed fields do not overlap in the hologram, so that each of them can be observed separately. The filtering of these regions makes it possible, with minimal distortion, to reconstruct the unperturbed field hologram of a moving source in the IIWs presence in order to estimate its parameters. With an increase in the frequency range, the error in reconstructing the distance and the source radial velocity decreases. The inverse 2D-FT transformation application to the unperturbed hologram makes it possible to reconstruct the unperturbed field interferogram in the IIWs presence. The unperturbed field interferograms in

the absence and presence of IIWs differ in contrast, but their angular interference fringes coefficients are comparable in magnitude.

REFERENCES

1. Cockrell KL, Schmidt H. Robust passive range estimation using the waveguide invariant. *Acoust. Soc. Am.*, 2010, 127(5):2780-2789; https://doi.org/10.1121/1.3337223.
2. Kuznetsov GN, Kuz'kin VM, Pereselkov SA, Kaznacheev IV. Noise source localization in shallow water. *Phys. Wave Phenom.,* 2017, 25(2):156-163; https://doi.org/10.3103/S1541308X17020145.
3. Emmetiere R, Bonnel J, Gehant M, Cristol X, Chonavel T. Understanding deep-water striation patterns and predicting the waveguide invariant as a distribution depending on range and depth. *Acoust. Soc. Am.*, 2018, 143(6):3444-3454; https://doi.org/10.1121/1.5040982.
4. Chuprov SD. *Interference structure of a sound field in a layered ocean. Ocean Acoustics. Current State.* Moscow, Nauka Publ., 1982, pp. 71-91.
5. Apel J, Badiey M, Chiu C, Finette S, Headrick RH, Kemp J, Lynch J, Newhall A, Orr M, Pasewark B, Tielburger D, Turgut A, Heydt KVD, Wolf S. An overview of the SWARM 1995 shallow-water internal wave acoustic scattering experiment. *IEEE J. Ocean. Eng.*, 1997, 22:465-500; https://doi.org/10.1109/48.611138.
6. Frank SD, Badiey M, Lynch J, Siegmann W. Analysis and modeling of broadband airgum data influenced by nonlinear internal waves. *J. Acoust. Soc. Am.*, 2004, 116(6):3404-3422; https://doi.org/10.1121/1.1819499.
7. Badiey M, Kuz'kin VM, Pereselkov SA. Interferometry of hydrodynamics of oceanic shelf caused by intensive waves. *Fundam. Prikl. Gidrofiz.*, 2020, 13(1):45-55; https://doi.org/10.7868/S2073667320010050.
8. Kaznacheeva ES, Kuz'kin VM, Pereselkov SA. Interferometric processing of hydroacoustic information in the presence of intense internal waves. *Phys. Wave Phenom.*, 2021, 29(3):278-284; https://doi.org/10.3103/S1541308X21030067.
9. Kuz'kin VM, Lyakhov GA, Pereselkov SA, Kaznacheeva ES. The information transmission through random-inhomogeneous ocean environment. *Fundam. Prikl. Gidrofiz.,* 2021, 14(2):54-64; https://doi.org/10.7868/S2073667321020052.
10. Konyae KV, Sabinin KD. *The Waves within the Ocean.* St. Petersburg, Gidrometeoizdat Publ., 1992.
11. Zhou J, Zhang XZ, Rogers PH. Resonant interaction of sound wave with internal solitons in the coastal zone. *Acoust. Soc. Am.*, 1991, 90(4):2042-2053; https://doi.org/10.1121/1.401632.
12. Hsu MK, Liu AK, Liu C. An study of internal waves in the China seas and yellow sea using SAR. *Continental Shelf Research*, 2000, 20(4-5):389-410; https://doi.org/10.1016/S0278-4343(99)00078-3.
13. Li X, Clemente-Colon P, Friedman KS. Estimating jceanic mixed-layer depth from internal wave evolution observed from Radarsat-1 SAR. *Johns Hopkins APL Technical Digest.*, 2000, 21(1):130-135.
14. Katsnel'son BG, Pereselkov SA. Low-frequency horizontal acoustic refraction caused by internal wave solitons in a shallow sea. *Acoust. Phys.* 2000, 46(6):684-691; https://doi.org/10.1134/1.1326723.

15. Oba R, Finette S. Acoustic propagation through anisotropic internal wave fields: transmission loss, cross-range coherence, and horizontal refraction. *Acoust. Soc. Am.*, 2002, 111(2):769-784; https://doi.org/10.1121/1.1434943.

16. Flatte SM (ed.). *Sound transmission through a fluctuating ocean*. Cambridge University Press, 1979, 299 p.

DOI: 10.17725/rensit.2023.15.327

Evaluation of images quality obtained by remote sensing

Alexander V. Kokoshkin, Evgeny P. Novichikhin

Kotelnikov Institute of Radioengineering and Electronics of RAS, Fryazinsky branch, http://fireras.su/
Fryazino 141190, Moscow region, Russian Federation

E-mail: shvarts65@mail.ru, epnov@mail.ru

Received March 28, 2023, peer-reviewed April 03, 2023, accepted April 10, 2023

Abstract: **Testing of digital images restoration by methods of sequentially calculated Fourier spectrum interpolation, spline interpolation, projections onto convex sets and amplitude iterations is proposed. The task is a sparseness reconstruction modeled according to the randomly uniform law (90 percent of the information is missing). In addition to the well-known image quality estimates, new ones are introduced - a measure of histogram similarity, the rms deviation of the difference in phase spectra. It is shown that the proposed criteria are effective for assessing the images quality obtained by remote sensing.**

Keywords: **remote sensing, image processing, objective evaluation of the efficiency of reconstruction methods, measure of histogram similarity, standard deviation of phase spectrum difference**

UDC 621.397

Acknowledgments: The work was supported by a state task of the Kotelnikov Institute of Radioengineering and Electronics, Fryazino Branch, Russian Academy of Sciences № 075-01110-23-01.

For citation: Alexander V. Kokoshkin, Evgeny P. Novichikhin. Evaluation of images quality obtained by remote sensing. *RENSIT: Radioelectronics. Nanosystems. Information Technology*, 2023, 15(3):327-334e. DOI: 10.17725/rensit.2023.15.327.

Contents

1. INTRODUCTION

In remote sensing systems, in various ranges of electromagnetic waves, the data obtained are often presented in the form of digital images. When solving practical problems, these images are processed by one method or another. The tasks can be extremely diverse: restoring a defocused partially shaded image, combating noise, increasing spatial resolution, searching for information about a distorting hardware function, reconstructing lost data (lacunae), etc. [1-5]. Thus, an objective assessment of the effectiveness of recovery methods is extremely relevant, since it is an important part of image processing systems obtained with remote sensing.

In this paper, new criteria are proposed for an objective estimate of the quality of reconstructed images relative to the original "ideal" (undistorted). The use of well-known and new objective estimate of image quality makes it possible to assess the competitiveness of image processing methods in remote sensing systems. Here, reconstruction algorithms are applied to sparse images (from unevenly spaced samples). I.e., to such images, over the entire field of which only a certain number of elements are available, while most of the elements are missing. A high degree of sparsity is simulated (90 percent of the information is

missing). To restore digital images, methods developed at the V.A. Kotelnikov IRE of the Russian Academy of Sciences are used. In [6,7,8,9], algorithms for the Interpolation Method of Sequential Computation of the Fourier spectrum (IMSCS), the method of projections onto convex sets (POCS) and the method of amplitude iterations (MAI) adapted for the reconstruction of sparse two-dimensional signals were described in detail.

Additionally, as an ideological alternative to methods operating in the frequency domain, spline interpolation is used in our study [10,11]. The physical meaning of this method is that for an arbitrary set of reference points (nodes), a system of linear equations is solved that models the behavior of a curved elastic plate. The result is a relation describing a two-dimensional spline surface. This approach has a certain versatility and can be applied for comparative analysis.

2. APPLICATION OF RESTORATION METHODS TO SPARSE IMAGES

As an example, to illustrate the effectiveness of the methods of reconstruction of sparse images, we use an aerospace image of the aircraft carrier "Midway" moored in the port of San Diego (USA), turned into a museum ship since 1998 (size 1296 by 558 pixels) **Fig. 1**. For this purpose, a public Yandex map is used.

Directly during sparsity modeling and subsequent processing, a fragment of the original image is used in Fig. 1 – the area

Fig. 1. *The original aerospace image (size 1296 by 558 pixels).*

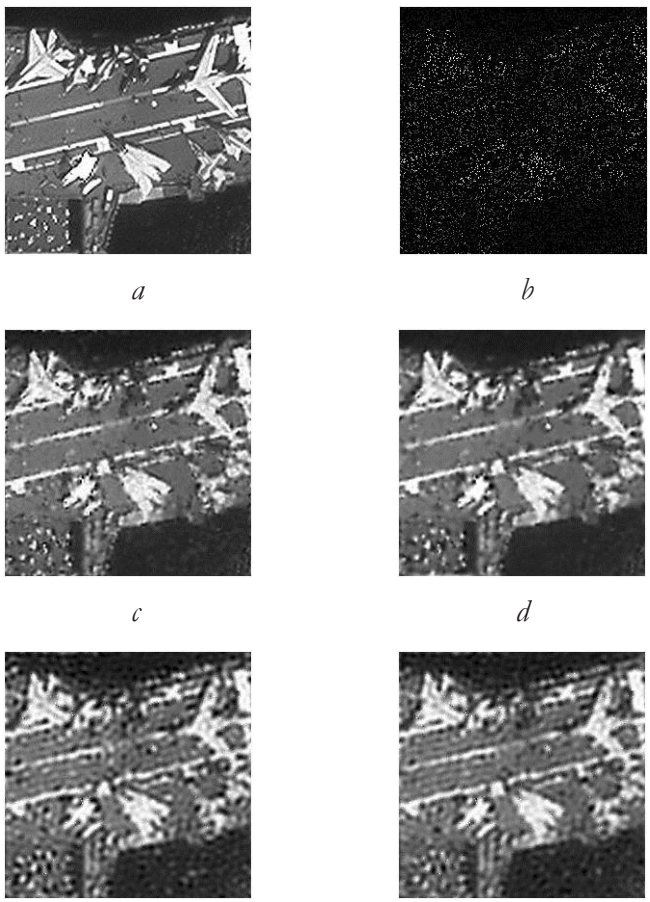

Fig. 2. *Fragment of the original image Fig.1 (size 256 by 256 pixels) – (a); Sparse image (90 percent of the information in Fig. 2a is missing) – (b); Restoration of Fig. 2b) using IMSCS – (c); Restoration of Fig. 2b) using a spline – (d); Restoration of Fig. 2b) using POCS – (e); Restoration of Fig. 2b) using MAI – (f).*

near the stern of the aircraft carrier with a size of 256 by 256 pixels (**Fig. 2***a*). Fig. 2*b* shows a sparse image, where 90 percent of the information is deleted according to a randomly uniform law (black color). Unlike previous works, here, for sparsity modeling (in a Delphi program), a "mask" is used. This makes it possible not to shift the brightness up in order to reserve the "zero" intensity for "places of lack of information", and thus not to make, albeit a small, but compression of the brightness range. Fig. 2*c* shows the restoration of Fig. 2*b* using IMSCS (128 harmonics, 1 iteration). Fig. 2*d* demonstrates the reconstruction of Fig. 2*b* using a spline. The reconstruction of Fig. 2*b* using POCS

(a frequency window with a radius of 31 harmonics, 2500 iterations) is shown in Fig. 2*e*. And, finally, the sparsity interpolation of Fig. 2*b* using MAI (frequency window with a radius of 31 harmonics, 2500 iterations) can be seen in Fig. 2*f*.

3. ESTIMATES OF THE RECOVERY QUALITY OF SPARSE IMAGES

An expert observer can visually compare the effectiveness of the methods. The most "similar" to the "ideal" Fig. 2*a* are reconstructions using IMSCS (Fig. 2*c*) and using a spline (Fig. 2*d*). The recovery of a sparse image using POCS (Fig. 2*e*) and using MAI (Fig. 2*f*) is noticeably worse than the first two competing methods. This can be partially explained by a relatively small operating frequency window with a radius of 31 harmonics. The fact is that if you set the frequency window much wider, then on the reconstructed images, in addition to the apparent increase in sharpness, there are significantly more interfering artifacts.

In order to adequately estimate the effectiveness of the methods, it is necessary to calculate the quality criteria. **Table 1** shows objective estimates of the quality of reconstructed images [1,12]: SSIM – Structural Similarity Index Measure, image sharpness evaluation, the average contrast, SD1 is the standard deviation from its average value, SD2 is the standard deviation of the pixel difference between the reference and reconstructed image, excess, asymmetry.

Table 1

Objective estimates of the quality of reconstructed images.

	ideal	IMSCS	spline	POCS	MAI
SSIM	1	0.894	0.895	0.826	0.847
image sharpness evaluation	16.337	8.149	6.264	8.23	7.207
average contrast	0.144	0.114	0.093	0.154	0.13
SD1	66.709	61.19	62.269	63.522	61.719
SD2	0	29.553	29.519	38.44	35.52
excess	-0.101	-0.102	-0.114	-0.354	-0.253
asymmetry	0.88	0.773	0.77	0.643	0.666

The Structural Similarity Index Measure is maximal when comparing the original "ideal" image with itself – it is equal to 1. For all four methods of reconstruction of sparsity, the SSIM are quite close. IMSCS and spline SSIM are almost the same, while POCS and MAI have slightly lower indicators (the worst of all POCS). Nevertheless, POCS shows the "best" result in terms of sharpness estimates. According to this indicator, only IMSCS is nearby. This can be explained by the fact that the assessment of sharpness is strongly influenced by parasitic artifacts (brightness differences compare Fig. 2*c* and Fig. 2*e*). For the same reason, POCS surpasses even the original "perfect" image in "average contrast". Similarly, both estimates of SD systems for POCS are higher than those of competing methods. SD2 (deviation of the pixel difference between the reference and reconstructed image) in MAI noticeably exceed SD2 with IMSCS and spline. This indicates that there are more significant structural differences with the "ideal" images of restored POCS and MAI than in IMSCS and spline reconstructions. The excess of the brightness values for a digital image indicates how flat or insular the distribution is when compared with the normal distribution. The fact that the calculated excess values for all images are less than zero indicates that all distributions are flat-topped (relative to the normal, whose excess is zero). As for the absolute values of the excess for the studied methods, IMSCS is the closest to the original one.

The asymmetry of the brightness values for a digital image measures the asymmetry of the distribution near the average. Positive values of asymmetry for all four methods indicate that the "tail" of the distribution is stretched in the direction of positive values. If the asymmetry of the image brightness

values were zero, then the distribution would be symmetrical about its average (as in the case of normal). According to this indicator, the method of interpolation of the sequentially calculated Fourier spectrum surpasses competitors in this study – it is closer to the "ideal" one.

After analyzing the data in Table 1, it can be stated that according to the objective estimates of the quality of reconstructed images calculated above, IMSCS has some advantage over competing methods. The expert assessment also leans towards the interpolation method of the sequentially calculated Fourier spectrum. In [13], another objective quality criterion was introduced. As can be seen from the Table.1 some of the assessments may produce contradictory results. It is proposed to compare the forms of brightness distributions of reconstructed images with a similar distribution for the reference. This is practically implemented on histograms. Moreover, the histograms need to be "coarsened" a little, i.e. not to take them for all brightness gradations (256), but to calculate averaged, for example, 8 (we get 32 columns in each histogram). This is due to the fact that the pixels of some of the brightness gradations may be physically absent from certain images [13]. **Fig. 3** illustrates the normalized brightness histograms of the images under discussion.

Fig. 3*b* indicates an extremely small amount of significant information (10 percent) present in the sparse image. Upon closer examination of Fig. 3, it can be seen that the type of histograms varies significantly for different sparsity interpolation methods. And if each of them is numerically compared with the "standard" (Fig. 3*a*), then an objective criterion for evaluating the quality of images will be obtained. By analogy with the already known structural similarity index measure (SSIM), we will call it "histogram similarity index measure" (HSIM) [13].

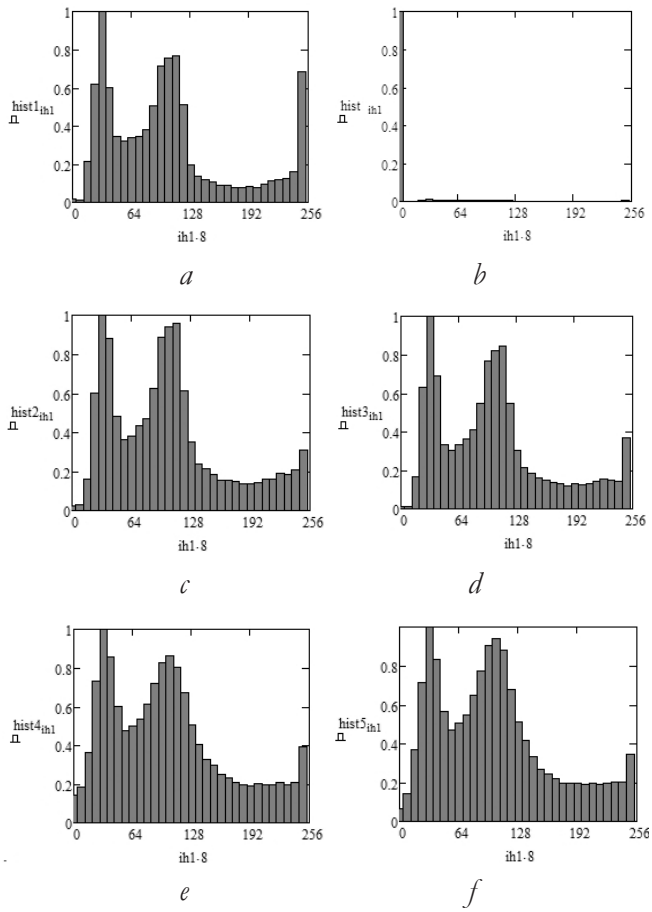

Fig. 3. *Brightness histograms for: the original image Fig. 2a) – (a); sparse image Fig. 2b) – (b); restored Fig. 2c) using IMSCS – (c); restored Fig. 2d) using a spline - (d); restored Fig. 2b) using POCS – (e); restored Fig. 2b) using MAI – (f).*

It is proposed to calculate the measure of histogram similarity as follows [13]:

$$\mathbf{HSIM} = \frac{\sum_{\mathbf{ih1}=0}^{31} \left| \mathbf{hist1}_{\mathbf{ih1}} - \mathbf{hist2}_{\mathbf{ih1}} \right|}{32}.$$

In this formula: $\mathrm{hist1}_{\mathrm{ih1}}$ – values along the columns of the reference normalized histogram (Fig. 3*a*); $\mathrm{hist2}_{\mathrm{ih1}}$ – values for the columns of the normalized histogram under test (Fig. 3*c*). The averaged modulus of the difference is calculated for each pair of histogram bars. In the proposed example, 32 is equal to the number of bars in the histograms (256 divided by 8). So the above formula calculates the HSIM for IMSCS. Similar are calculated histogram similarity index measure to the spline while substituting in the formula as a test histogram values $\mathrm{hist3}_{\mathrm{ih1}}$ (Fig. 3*d*), for POCS, substituting in the formula $\mathrm{hist4}_{\mathrm{ih1}}$ (Fig.

Table 2

Histogram similarity index measure

	ideal	IMSCS	spline	POCS	MAI
HSIM for normalized histograms	0	0.094	0.049	0.153	0.157
HSIM for non-normalized histograms	0	360.625	266.875	583.688	547.875

3*e*), or $hist5_{ih1}$ (Fig. 3*f*) when calculating the HSIM to MAI. **Table 2** shows the histogram similarity index measure calculated according to the proposed method for the studied images. HSIM for the original (reference) image, in our case, means comparison with itself, so the difference in values is zero [13].

When evaluating sparsity reconstructions by various methods, spline has an advantage over competitors, IMSCS is in second place. Most significantly (in percentage terms) this is manifested if data from normalized histograms are used for calculations.

Fig. 4 shows the amplitude spatial spectra on a logarithmic scale: the original ("ideal") image (Fig. 2*a*) – Fig. 4*a*; sparse image (Fig. 2*b*) – Fig. 4*b*; sparsity reconstruction using IMSCS (Fig. 2*c*) – Fig. 4*c*; sparsity reconstruction using a spline (Fig. 2*d*) – Fig. 4*d*; sparsity reconstruction using POCS (Fig. 2*e*) – Fig. 4*e*; reconstruction of sparsity using MAI (Fig. 2*f*) – Fig. 4*f*. Vertically Fig. 4 the values of the amplitudes of the spatial spectra are postponed (on a logarithmic scale), along the other axes – the values of the indices of brightness pixels in the image field.

In [1] it is stated: the amplitude of a two-dimensional discrete Fourier transform is an array whose components set the intensities in the image, and their corresponding phases make up an array of offsets, which contains a significant part of the information about where visible objects are placed in the image. Thus, the basic information about the contours (details) of objects in the images is contained in the phase spectrum. In this connection, the idea arises of

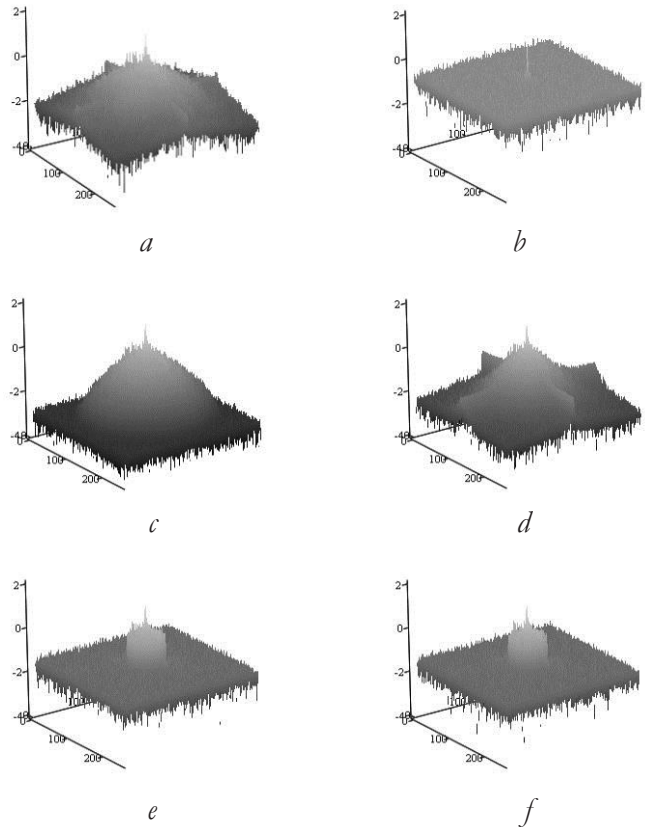

Fig. 4. *Amplitude spatial spectra in logarithmic scale for: the original image Fig. 2a) – (a); sparse image Fig. 2b) – (b); restored Fig. 2b) using IMSCS – (c); restored Fig. 2b) using a spline - (d); restored Fig. 2b) using POCS – (e); restored Fig. 2b) using MAI – (f).*

creating some kind of objective criterion for assessing the quality of the phase spectrum of the reconstructed images. Visually, the phase spectrum of images is difficult to interpret in any way. **Fig. 5***a* shows the phase spectrum of the original "ideal" image, and Fig. 5*b* shows the spectrum of a sparse image. Vertically, Fig. 5 shows the values of the phase of spatial spectra

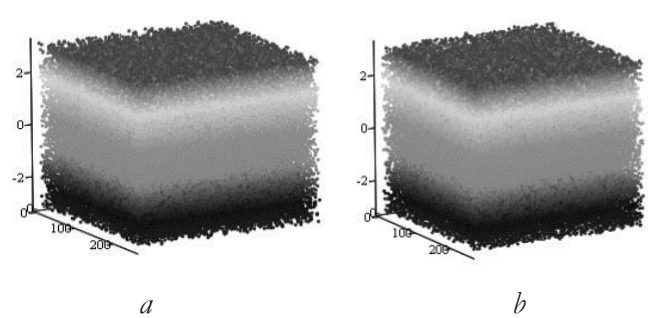

Fig. 5. *The phase spatial spectra of the value are in the range (-π , π]: of the original image Fig. 2a) – (a); of the sparse image Fig. 2b) – (b).*

(in the interval (–π, π]), along the other axes – the values of the indices of brightness pixels in the image field.

We propose to calculate pixel-by-pixel the differences in the phase spatial spectra between the original ("ideal") and sparse images (see Fig. 5). The array of values of the result of the operation is in the range (-2π , 2π]. All similar arrays for the difference of phase spatial spectra between the original ("ideal") and any of the four images reconstructed by the methods studied here should have a smaller spread of values. **Fig. 6** shows sections of arrays of values: the phase spectrum of the "ideal" image minus the phase spectrum of the sparse image Fig. 6*a*, and the phase spectrum of the "ideal" undistorted source image minus the phase spectrum of sparsity restoration using IMSCS Fig. 6*b*. Vertically Fig. 6, the values of the phase difference of spatial spectra are postponed (in the interval

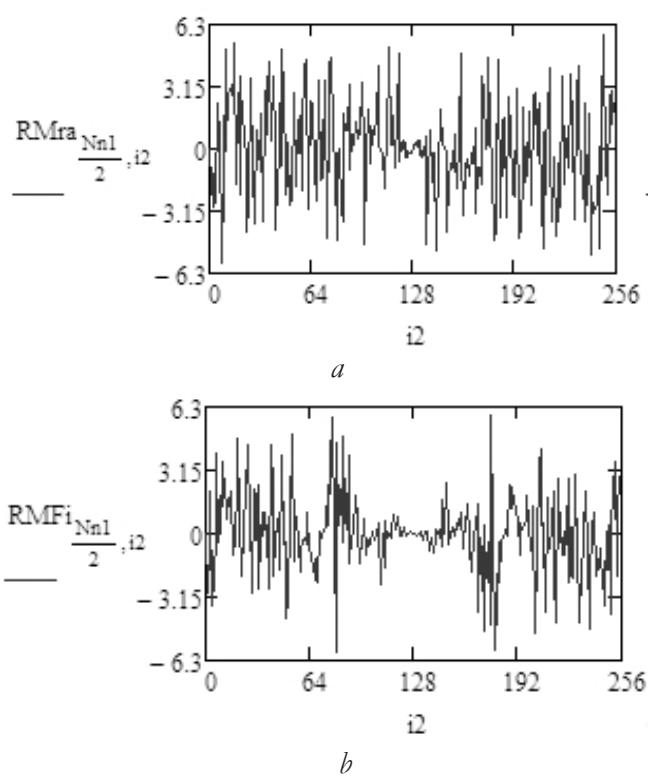

Fig. 6. *Sections of the difference of the full phase spatial spectra: the "ideal" undistorted source image (Fig. 2a) minus the phase spectrum of the sparse image (Fig. 2b) – (a); the "ideal" undistorted source image (Fig. 2a) minus the phase spectrum of sparsity recovery using IMSCS (Fig. 2c) – (b).*

Table 3

SD of the difference of phase spectra (in rad.) between the "ideal" and reconstructed images

	ideal	sparse	IMSCS	spline	POCS	MAI
SD for the full spectrum	0	2.529	2.423	2.362	2.442	2.438
SD for the central part of the spectrum (with a radius of 31 harmonics)	0	0.893	0.63	0.641	0.714	0.701

(–2π, 2π]), horizontally – the values of pixel brightness indices in the image field.

Fig. 6 shows that near the central frequency of the spectrum (corresponding to the average brightness of the image), the phase differences are relatively small. But as we move away into the high frequency region, the values of the phase difference increase on average. In the first row of **Table 3**, the phase differences for the full spectrum between the "ideal" and the reconstructed images considered here by the methods are given.

The results for a sparse image are obviously the worst. The ratio of the difference of the phase spectra (in rad.) of the "ideal" image with itself is an array of zeros (the first column of Table 3), i.e. the best result. In order to put competing methods in more equal conditions, we limit the calculation of the difference between the phase spectra to a region near the central frequency with a radius of 31 harmonics. This corresponds to the frequency window size chosen in this paper for POCS and MAI.

Fig. 7 shows the corresponding sections for the central zones (with a radius of 31 harmonics) of the difference in the phase spatial spectra.

Table 3, in the second line, shows the values of the SD for the central part of the spectrum (with a radius of 31 harmonics) of the difference in phase spectra (in rad.) between the "ideal", sparse and reconstructed images. According to this indicator, IMSCS takes the first place, the second is spline, the third is MAI, and the last is POCS.

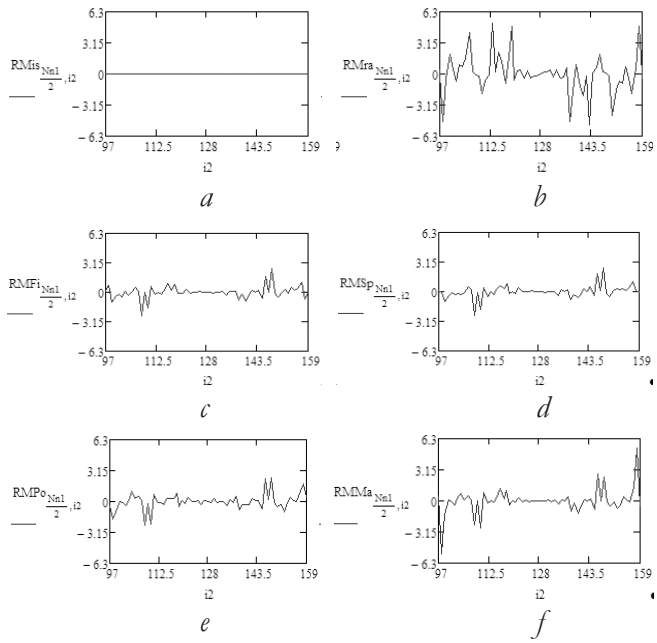

Fig. 7. *Sections for the central zones (with a radius of 31 harmonics) of the difference in the phase spatial spectra: the "ideal" undistorted source image (Fig. 2a) minus the phase spectrum of itself – (a); the "ideal" undistorted source image (Fig.2a)) minus the phase spectrum of the sparse image (Fig. 2b) – (b); "ideal" undistorted source image (Fig. 2a) minus the phase spectrum of sparsity recovery using IMSCS (Fig. 2b) – (c); "ideal" undistorted source image (Fig. 2a) minus the phase spectrum of sparsity restoration using a spline (Fig. 2d) – (d); "ideal" undistorted source image (Fig. 2a) minus the phase spectrum of sparsity restoration using POCS (Fig. 2e) – (e); "ideal" undistorted source image (Fig. 2a) minus the phase spectrum of sparsity recovery using MAI (Fig. 2f) – (f).*

4. CONCLUSION

The paper proposes new objective assessments of the quality of images obtained by remote sensing (the histogram similarity index measure, the SD of the difference in phase spectra). The following methods are used as tested methods: the Interpolation Method of Sequential Computation of the Fourier Spectrum (IMSCS), spline interpolation, the method of projections onto convex sets (POCS) and the method of amplitude iterations (MAI). Competing methods reconstructed the sparsity modeled according to a randomly uniform law (90 percent of the information is missing). IMSCS showed the best performance in almost all estimates. The conducted research allows us to conclude that the proposed criteria can be applied in principle to assess the quality of images obtained by remote sensing. This allows you to check the effectiveness of digital image recovery methods used to solve various practical problems.

REFERENCES

1. Gonzalez RC, Woods RE. *Digital Image Processing*. International Version 3rd Edition. NJ, Prentice Hall, 2012, 1071p.
2. Huang H, Makur A. A new iterative reconstruction scheme for signal reconstruction. *Proceedings of the IEEE Asia Pacific Conference on Circuits and Systems* (*APCCAS '08*). 2008; https://doi.org/10.1109/APCCAS.2008.4746028.
3. Zrazhevsky AY, Kokoshkin AV, Korotkov VA, Korotkov KV. Vosstanovlenie defokusirovannogo zatenennogo izobrazheniya [Recovery of defocusing partially shaded image]. *Zhurnal radioelektroniki* [*Journal of Radioelectronics*] [online]. 2014, №10, http://jre.cplire.ru/jre/oct14/9/text.html (in Russ.).
4. Kokoshkin AV. Features of an Application of the Constrained Renormalization Method to Images with Speckle Noise. *J. of Communications Technology and Electronics*, 2022, 67(12):1419-1429. DOI: 10.1134/S1064226922120075.
5. Kokoshkin AV, Korotkov VA, Novichikhin EP. Comparison of interpolation methods when achieving super-resolution of images based on the analysis of several frames. *RENSIT: Radioelectronics. Nanosystems. Information Technologies*, 2019, 11(1):85-91. DOI: 10.17725/rensit.2019.11.085.
6. Kokoshkin AV, Korotkov VA, Korotkov KV, Novichikhin EP. Retouching and restoration of missing image fragments by means of the iterative calculation of their spectra. *Computer Optics,* 2019; 43(6):1030-1040. DOI: 10.18287/2412-6179-2019-43-6-1030-1040.
7. Kokoshkin AV, Korotkov VA, Novichikhin EP. Reconstruction of Acoustic Signals

According to Incomplete Data. *J. of Communications Technology and Electronics,* 2020, 65(12):1399-1406. DOI: 10.1134/S1064226920120104.

8. Kokoshkin AV, Novichikhin EP. Application of the Interpolation Method of Sequential Computation of the Fourier Spectrum to Sparse Images. *RENSIT: Radioelectronics. Nanosystems. Information Technologies*, 2022, 14(2):165-174e. DOI: 10.17725/rensit.2022.14.165.
9. Kokoshkin AV. Algoritmy metoda amplitudnykh iteratziy i POCS dlya rekonstruktsii razrezhennykh dvumernykh signalov [Algorithms of the method of amplitude iterations and POCS for the reconstruction of sparse two-dimensional signals]. *Zhurnal radioelektroniki* [*Journal of Radioelectronics*] [online]. 2022, №9; https://doi.org/10.30898/1684-1719.2022.9.7 (in Russ.).
10. Ashkenazy AV. *Spline surfaces. Fundamentals of the theory and computational algorithms.* Tver, Tver State University Publ., 2003, p. 82.
11. Nesterenko EA. Vozmozhnost' ispol'zovaniya splainpoverkhnosti dlya postroeniya poverkhnostey po rezultatam c'emok [The ability to use spline surfaces for constructing surfaces based on the shooting results]. *Zapiski Gornogo Instituta,* 2013, 204:127-133 (in Russ.).
12. Kokoshkin AV, Korotkov VA, Korotkov KV, Novichikhin EP. Sravnenie ob'ektivnykh metodov ozenki kachestva zifrovykh izobrazheniy [Comparison of objective methods of assessing quality of digital images]. *Zhurnal radioelektroniki* [*Journal of Radioelectronics*] [online]. 2015, №6; http://jre.cplire.ru/jre/jun15/15/text.html (in Russ.).
13. Kokoshkin AV. Metody interpolyatsii razrezhennykh izobrazheniy, rabotayushchie v chastotnoy oblasti [Sparse Image Interpolation Methods Working in the Frequency Domain]. *Zhurnal radioelektroniki* [*Journal of Radioelectronics*] [online]. 2023, №3; https://doi.org/10.30898/1684-1719.2023.3.10 (in Russ.).

DOI: 10.17725/rensit.2023.15.335

70 YEARS OF KOTELNIKOV INSTITUTE OF RADIOENGINEERING AND ELECTRONICS OF RAS

Editorial board RENSIT journal

Kotelnikov Institute of Radioengineering and Electronics of RAS, http://cplire.ru/
Moscow 125009, Russian Federation

E-mail: grachev@cplire.ru

Received September 18, 2023, peer-reviewed September 24, 2023, accepted September 28, 2023

Abstract: **Information is presented on the organization and activities of Kotelnikov Institute of Radioengineering and Electronics of Russian Academy of Sciences. Its scientific directions are covered, the main results of fundamental scientific, exploratory and applied research are noted, as well as the training of highly qualified personnel (candidates and doctors of science) and the presence of close international scientific ties.**

Keywords: **radiophysics, micro- and nanoelectronics, radio electronics, photonics, telecommunications, information technology**

UDC 621.396

For citation: Editorial board RENSIT journal. 70 years of Kotelnikov Institute of Radioengineering and Electronics of RAS. *RENSIT: Radioelectronics. Nanosystems. Information technologies*, 2023, 15(3):335-338e. DOI: 10.17725/rensit.2023.15.335.

Kotelnikov Institute of Radioengineering and Electronics of Russian Academy of Sciences, Moscow, Mokhovaya st., 11, building 7.

On September 28, 2023, the celebration of the 70th anniversary of the V.A. Kotelnikov Institute of Radioengineering and Electronics of RAS.

The Institute of Radioengineering and Electronics (IRE) was formed in the Department of Technical Sciences of the USSR Academy of Sciences by a resolution of the USSR Council of Ministers dated August 29, 1953 and the corresponding resolution of the Presidium of the USSR Academy of Sciences dated September 18, 1953.

The purpose of creating IRE was to develop 5 (at that time) main problems of radioelectronics:

- research of physical processes and development of a theory of phenomena occurring in electronic devices at radio frequencies;
- physical research and development of semiconductor materials, as well as the development of methods for using semiconductors in electronics and radio engineering;
- study of the propagation, radiation and channeling of high-frequency electromagnetic energy in free space, limited volumes and various environments;
- development of new methods for measuring electrical and magnetic quantities at high and ultrahigh frequencies;
- exploring new areas of application of radio engineering methods in science, the national economy and defense technology.

Academician and engineer-admiral Aksel Ivanovich Berg was appointed acting director of the IRE. At the end of October – beginning of November 1953, Vladimir

FOUNDERS OF THE IRE AS USSR

Aleksandrovich Kotelnikov, who had just been immediately elected as an academician, and at the same time Dmitry Vladimirovich Zernov, who was simultaneously elected to a corresponding member of the USSR Academy of Sciences, were appointed deputy directors of the IRE.

To house the IRE, the building of the Physics Faculty of Moscow State University was allocated on Mokhovaya st., 11.

To develop large-scale research, strengthen the material and technical base of the Institute and accelerate the implementation of development results in industry, in 1955 in the Fryazino city, Moscow region, by decree of the USSR Council of Ministers, the Fryazino part of the IRE was formed (now the Fryazino branch of the V.A. Kotelnikov IRE of RAS). In 1979, by the

Nikitov Sergey Apollonovich
Dr Phys Math Sci, Professor,
Academician of RAS

Gulyaev Yuri Vasil'evich
Dr Phys Math Sci, Professor,
Academician of RAS

decision of the State Committee for Science and Technology of the USSR and the resolution of the Presidium of USSR Academy of Sciences, the Saratov branch of the V.A. Kotelnikov IRE of RAS, and in 1990, by resolution of the Presidium of the USSR Academy of Sciences, the Ulyanovsk branch of the V.A.Kotelnikov IRE of RAS.

In order to perpetuate the memory of the outstanding Russian scientist Academician V.A. Kotelnikov – in 2006 the Institute was named after him.

From 1988 to 2014, the director of the Institute was Academician of the Russian Academy of Sciences Yu.V. Gulyaev. Now he is the scientific director of the Institute. Since 2015, the director of the Institute is Academician of the Russian Academy of Sciences S.A. Nikitov.

Currently, the Institute consists of 4 structural parts: the Moscow part of the IRE (22 laboratories), the Fryazino branch (29 laboratories and 2 thematic groups), the Saratov branch (9 laboratories), the Ulyanovsk branch (2 laboratories).

FRYAZINO BRANCH
Fryazino Moscow areas,
Vvedensky sq., 1

SARATOV BRANCH
Saratov, st. Zelyonaya, 38

ULYANOVSK BRANCH
Ulyanovsk, st. Goncharova, 48/2

The main task of the institute is to conduct fundamental, exploratory and applied research in the field of radiophysics, micro- and nanoelectronics, photonics, telecommunications, information technology, as well as the development and development of the physical, mathematical and technical foundations of a new element base of radio electronics and photonics.

The Institute conducts fundamental and applied scientific research in 15 scientific areas in the field of physical sciences, nano- and information technologies, which include radiophysical research of the Solar system, methods of remote sensing of the Earth, studying the propagation of radio waves in the Earth's atmosphere, near-Earth and outer space, development methods of generation, reception and conversion of electromagnetic waves, fundamental problems of radiophysical methods of communication, location and diagnostics, current scientific problems of optics and laser physics, research of nonlinear dynamic systems, creation of new materials and structures, including metamaterials, research in the field of quantum macrophysics, mesoscopics, physics nanostructures, spintronics and superconductivity, research in the field of biomedical radio electronics, etc. The results of the work are published in leading Russian and world scientific publications. The Institute trains highly qualified personnel (candidates and doctors of science) and has close international scientific connections.

The total number of the Institute is 930 people, including 587 scientists. Currently at the V.A. Kotelnikov IRE of RAS employs 5 academicians of the RAS: Yu.V. Gulyaev, S.A. Nikitov, N.A. Kuznetsov, V.A. Cherepenin and A.S. Bugaev, 6 professors of the Russian Academy of Sciences, 98 doctors of science, 220 candidates of science.

In 1969, the Institute was awarded the Order of the Red Banner of Labor. The Institute's works were awarded high awards: 2 prizes of the European Physical Society, 2 Lenin Prizes, 24 State Prizes of the USSR, 6 State Prizes of the Russian Federation, 4 Prizes of the Council of Ministers of the USSR, 3 Prizes of the Government of the Russian Federation, 3 Lenin Komsomol Prizes, 2 State Prizes of the Ukrainian SSR, 1st Prize of the Government of the Russian Federation in the field of education, 1st State Prize of the Russian Federation named after Marshal of the Soviet Union G.K. Zhukov in the field of military science, 4 awards from the Moscow Government for young scientists.

The main major achievements of the Institute, awarded with international and state awards:

– The world's first radar studies of the planets Venus, Mercury and Mars (Lenin Prize, 1964)

– The world's first detailed radar survey of the surface of the planet Venus from the spacecraft "Venera-15", "Venera-16" (Lenin Prize, 1986; USSR State Prizes, Lenin Komsomol Prize, 1985)

– Development of methods and equipment for remote sensing of the Earth using radiophysical methods (2 USSR state prizes)

– Experimental detection of electron-hole drops and multiparticle exciton-impurity complexes in semiconductors (European Physical Society Prize, 1975, USSR State Prize, 1988)

– Development of the scientific foundations of acoustoelectronics and acoustoelectronic information processing devices (European Physical Society Prize, 1979; IEEE W.G. Cady Award, 6 USSR State Prizes, 2 Russian Federation State Prizes, Lenin Komsomol Prize, 1984)

– Creation of the scientific foundations of spin-wave electronics (USSR State Prize, 1988, Lenin Komsomol Prize 1984, State Prize of the Ukrainian SSR, 1986).

– Development of THz superconductor receivers with quantum sensitivity (the

Van Duzer Prize awarded by the IEEE Superconductivity Council, 2012).

– Creation of a unique scientific installation "Cryointegral" - a technological and measuring complex for the creation of superconducting nanosystems based on new materials.

– Development of the scientific foundations of biomedical radio electronics (Russian Federation State Prize, 2000).

The total level of financing is 1.2 billion rubles, of which 0.7 billion rubles. allocated by the budget for the implementation of 16 topics of the state task.

Within the framework of the national project "Science and Universities", 3 youth laboratories have been created and are successfully operating, the average age of whose employees does not exceed 35 years. In addition, as part of integration with leading Russian universities, 8 basic departments have been created at the Institute. The Institute also has its own graduate school and two dissertation councils. In the graduate school of the IRE named after. V.A. There are 40 people studying at Kotelnikov RAS. In recent years, a number of young scientists from the Institute have been awarded prizes from the Moscow Government in the field of science. In 2021-2023 more than 20 researchers of the Institute were awarded state and departmental awards.

The Institute's staff annually publishes more than 350 articles in highly rated foreign and Russian journals, indexed in Web of Science and Scopus; more than 1000 articles and theses indexed in the RSCI. About 10 monographs and textbooks are published annually, Russian and international patents are registered. The results obtained by the Institute's staff have received unconditional international recognition. In 2022, the number of citations to articles published by Institute staff amounted to more than 28 thousand.

The editorial staff and editorial board of the journal "RENSIT: Radioelectronics. Nanosystems. Information Technologies" wish the V.A. Kotelnikov IRE of RAS prosperity and further scientific and production achievements, congratulate all employees, scientists and engineers on the anniversary and wish new creative successes on the path of technical progress of our country.

The editorial team and editorial board of RENSIT journal